VILNIUS UNIVERSITY
CENTER FOR PHYSICAL SCIENCES AND TECHNOLOGY

Jonas
Nekrasovas

Investigation and development of fluorene based organic charge transport materials for organic and inorganic solar cells applications

DOCTORAL DISSERTATION

Technology Sciences,
Materials Engineering (T 008)

VILNIUS 2021

This dissertation was prepared between 2014 and 2020 at Vilnius University, Chemical Physics Institute.

Academic supervisor: Prof. Dr.**Vygintas Jankauskas** (Vilnius University, Technology Sciences, Materials Engineering – T 008).
Academic consultant: Habil. Dr. Valentas Gaidelis (Vilnius University, Technology Sciences, Materials Engineering – T 008).

This doctoral dissertation will be defended in a public meeting of the Dissertation Defence Panel:
Chairman – Prof. Habil. Dr. Nerija Žurauskienė (Center for Physical Sciences and Technology, Technology Science, Materials Engineering – T 008).
Members:
Prof. Habil. Dr. Gytis Juška (Vilnius University, Technology Science, Materials Engineering, – T 008);
Dr. Rokas Kondrotas (Center for Physical Sciences and Technology, Technology Science, Materials Engineering, – T 008);
Dr. Gediminas Kreiza (Vilnius University, Natural Sciences, Physics – N 002);
Prof. Dr. Vincas Tamošiūnas (Vilnius University, Technology Science, Materials Engineering – T 008).

The dissertation shall be defended at a public meeting of the Dissertation Defence Panel 14:00 on 24 September 2021 in Room B336 of the National Center for Physical Sciences and Technology. Address: Saulėtekio ave. 3 10257, Vilnius, Lithuania
Tel. +37052234560; e-mail: jonas.nekrasovas@ff.vu.lt
The text of this dissertation can be accessed at the libraries of the Center for Physical Sciences and Technology, as well as on the website of Vilnius University: www.vu.lt/lt/naujienos/ivykiu-kalendorius

https://orcid.org/0000-0002-3810-4257

VILNIAUS UNIVERSITETAS
FIZINIŲ IR TECHNOLOGIJOS MOKSLŲ CENTRAS

Jonas
NEKRASOVAS

Krūvį pernešančių fluoreno darinių tyrimai organinių ir neorganinių saulės celių taikymams

DAKTARO DISERTACIJA

Technologijos mokslai,
Medžiagų inžinerija (T 008)

VILNIUS 2021

Disertacija rengta 2014– 2020 metais Vilniaus universitete, Cheminės fizikos institute.

Mokslinis vadovas: prof. dr. Vygintas Jankauskas (Vilniaus universitetas, technologijos mokslai, medžiagų inžinerija – T 008).
Mokslinis konsultantas: habil. dr. Valentas Gaidelis (Vilniaus universitetas, technologijos mokslai, medžiagų inžinerija – T 008).
Gynimo taryba:
Pirmininkė – **Prof. habil. dr. Nerija Žurauskienė** (Fizinių ir technologijos mokslų centras, technologijos mokslai, Medžiagų inžinerija – T 008).
Nariai:
Prof. habil. dr. Gytis Juška (Vilniaus universitetas, technologijos mokslai, Medžiagų inžinerija – T 008);
Dr. Rokas Kondrotas (Fizinių ir technologijos mokslų centras, technologijos mokslai, medžiagų inžinerija – T 008);
Dr. Gediminas Kreiza (Vilniaus universitetas, gamtos mokslai, fizika – N 002) ;
Prof. dr. Vincas Tamošiūnas (Vilniaus universitetas, technologijos mokslai, medžiagų inžinerija – T 008).

Disertacija ginama viešame Gynimo tarybos posėdyje 2021 m. rugsėjo mėn. 24 d. 14 val. Nacionalinio fizinių ir technologijos mokslų centro B336 auditorijoje. Adresas: Saulėtekio al. 3 10257, Vilnius, Lietuva, tel. +37052234560; el. pastas jonas.nekrasovas@ff.vu.lt .

Disertaciją galima peržiūrėti Vilniaus universiteto fizinių mokslų centro bibliotekose ir VU interneto svetainėje adresu: https://www.vu.lt/naujienos/ivykiu-kalendorius

Contents

6

Padėka

Mamai ir Tėčiui…

List of Acronyms

$\langle \varepsilon_\infty \rangle$ - a carrier located at mean carrier energy of DOS

CBD - chemical bath deposition

CELIV - charge extraction by linearly increasing voltage

CV - cyclic voltammetry

CZTS - copper zinc tin sulfide

CZTSSe - $Cu_2ZnSn(S_xSe_{1-x})_4$

d - the thickness of the sample

DOS - density of states

DSC - differential scanning calorimetry

$E, T(E)$ - surface escape function

E_0 – applied electric field

EC - electron counter

eN_i – generated charge

E_t - threshold energy

E_{VAC} - energy of vacuum level

FET - field effect transistor

FF – fill factor

H_2Pc - metal-free phthalocyanine

HOMO - highest occupied molecular orbital level

HTM – hole transport material

$h\nu$ - photon energy

I_p – ionization potential

J_{sc} - short-circuit current

LEDs - light emitting diodes

LUMO - lowest unoccupied molecular orbital

N_i^{opt} - initial optical density of state

N_f^{opt} - final optical density of state

$P(E, h\nu)$ - probability of exciting an electron to a state of energy E with photon energy $h\nu$

P3HT - regioregular polyhexyltiophene

PCE - power conversion efficiency

PC-Z - polycarbonate

PES - photoemission spectroscopy

PYS - photoelectron yield spectroscopy

PYSA - photoelectron yield spectroscopy in air

SC – solar cell

THF - tetrahydrofuran

TiOPc - titanyl phthalocyanine

TOF - time of flight

TPD - N,N'-is(3-methylphenyl)-N,N'-diphenylbenzidine

t_{tr} - transit time of charge carries

UPS - ultraviolet photoemission spectroscopy

VACh - Volt-Ampere characteristics

VB-UPS - valence band ultraviolet photoemission spectroscopy

V_{oc} - open circuit voltage

$X(E)$ - transmission probability for the electron at the level

XTOF - xerographic time-of-flight

Y - quantum yield of photoelectron

α - coefficient of μ dependence on electric field (E)

$\delta(\lambda)$ - absorption depth

μ - charge carries mobility

μ_0 - drift mobility without electric field ($E=0$)

$\varSigma$ - Gaussian width of DOS

$\varSigma$ - parameter that describes the degree of off-diagonal disorder

$\varPhi$ - wok function

1 Introduction

In recent years organic/inorganic hybrid structures, such as perovskite, attracted a lot of attention. Huge variety of potential combinations of materials and tunability of a band gap and other elsewhere described properties [1], continuously improving efficiency of perovskite solar cells (SCs) [2]. However, perovskite films are still unstable and often contains toxic elements, such as lead. Nevertheless, fabrication techniques for perovskite SCs might be complicated, especially, when considering large scale fabrication techniques such as spray coating [3]. Moreover, an expensive hole transport material (HTM) is required, which is usually sensitive to oxygen and water vapor interaction and even interacts with metal contact on a top [4].

One of possible alternatives to perovskite for SCs could be the quaternary direct bandgap semiconductors such as copper zinc tin sulfide (CZTS), selenide (CZTSSe) and mixed chalcogenide ($Cu_2ZnSn(S_xSe_{1-x})_4$) (CZTSSe). These materials are considered to be promising materials for the production of efficient and inexpensive solar cells [5], [6]. These Earth-abundant and non-toxic chemical composition of elements and possess excellent intrinsic properties, such as high absorption coefficients of about $10^4\,cm^{-1}$, tunable band-gap (1−1.5 eV) and easy processability [7]. Usually, CZTS SC structure contains semiconductor absorber between Mo back contact and the top buffer layer (CdS or ZnS) and transparent conducting oxide bi-layer [8], [9]. However, this structure has some limitations: it is costly, poor stability and incompatible for tandem SCs application. To overcome these drawbacks, kesterite SCs can be processed in superstrate configuration as an alternative. For non-kesterite SCs a superstrate configuration is often referred as an inverted configuration. In this architecture, back contact is transparent conductive glass (FTO or ITO) electrode, onto which all electron transporting, photoactive CZTS and HTM layers are deposited [10], [11].

One of the most common HTM for organic/inorganic SC is Spiro-OMeTAD, however, it is relatively unstable and expensive [4]. The cheaper HTM replacement for Spiro- OMeTAD would make organic/inorganic SCs more attractive to develop. i.e., a developed HTM should be compatible with CZTS and perovskite SC, as these light harvesting materials have similar energy levels of the highest occupied molecular orbital level (HOMO) and the lowest unoccupied molecular orbital (LUMO) levels [12]. Fluorene based HTMs are promising charge transport substance -relatively cheap synthesis and tunability allows to develop cross-linking HTMs. Cross-linking enables

multilayered structures without orthogonal solvents, higher stability, longevity [13].

However, finding out the right molecular structure and synthesis processes are time consuming tasks and, moreover, testing all these HTMs in the real device would be an ordeal. Straightforward and reliable techniques to select compatible HTMs materials are to evaluate charge transport properties by the xerographic time-of-flight (XTOF) and ionization potential by photoelectron emission spectroscopy in air (PYSA) in bulk layer. These methods allow to determine two important properties of HTM: charge carrier mobility (μ) and HOMO energy level. These parameters impact power conversion efficiency (PCE) of SC, open circuit voltage (V_{oc}) and short-circuit current (J_{sc}) [14].

A depositions technique plays important role for CZTS. CZTS layer can be formed employing vacuum or non-vacuum deposition technique. Both techniques have their merits and demerits. The vacuum deposition techniques allow to obtain a high quality CZTS films, but they are expensive, some materials are unstable at high deposition temperatures, it is also difficult to control the ratio of elements in CZTS composition. On the other hand, non-vacuum growing techniques, such as spray pyrolysis [15], spin coating [16], ink printing [17] and electrochemical deposition [18] are versatile, straightforward and inexpensive. Thus, currently the challenge is to fabricate high quality CZTS films for the superstrate configuration using non-vacuum deposition technique. Furthermore, the other difficulty is the fabrication of complete CZTS SC using scalable deposition technique, such as spray coating.

The combination of straightforward and reliable characterization methods of organic materials, the creation of preeminent HTMs and development of scalable, non-toxic SCs active layer in effect can lead towards next generation of organic/inorganic SCs.

1.1 Aim and objectives

The aim of the dissertation is to evolve fluorene based HTMs, that would be suitable for organic/ inorganic structures used in photovoltaic applications. Desired features of HTMs can be achieved by improving characterization methods for organic materials, enhancing development of HTMs and development of inorganic SC fabrication technique. The following tasks were set to achieve introduced aim of the work:

1. To develop the new high sensitivity ($\sim 10^{-19}$A) apparatus for ionization potential (I_p) measurements in organic and inorganic materials.

2. To develop the new method of photoemission spectrum analysis that would allow a detailed study of the structure of energy levels in organic semiconductors.
3. To evaluate I_p and $\boldsymbol{\mu}$ for fluorene based organic HTMs in order to identify HTMs suitable for organic/inorganic SCs.
4. To develop SC, consisting of inorganic light harvesting layers, suitable for cross-linkable fluorene based HTMs and estimate the main parameters of developed SC.

1.2 Novelty and relevance

In a search of new, cheap, efficient and reliable organic HTMs for SCs fabrication, there is a need for straightforward, informative and simple characterization methods to estimate I_p and μ. I_p parameter gives important information about compatibility of different materials in terms of energy levels. The absence of accurate I_p value would lead to insufficient engineering of SC – as I_p can be approximated as HOMO level; incompatible HOMO levels between different materials would lead to inefficient charge extraction towards contacts in SC. PYSA for organic materials is relatively well known method [19]. If electrometer is used to estimate photocurrent like described in [20], it usually has a threshold of around 10^{-15}-10^{-16} A. It means, that the information about accurate value of I_p may be lost. On the other hand, commercial systems like Riken-Keiki's AC-2 [21] and AC-3 [22] are more sensitive than the systems based on electrometer, however, they use suppressor grids along with pulse generators for quenching and false pulse elimination. The above described systems cause 3ms dead time of the counter, which leads to less than 300 electrons per second of maximum possible detection rate. A new method was developed to overcome these defined issues.

Most of well performing and commercially available HTMs, i.e. Spiro-OMeTAD, are expensive to produce: multistep synthesis procedures, expensive reagents and costly purification methods [23]–[25]. Development of less costly and easier to synthesize HTMs with performance comparable or better than that of Spiro-OMeTAD is a leap towards more effective and cheaper organic/inorganic SCs. The development process is strongly connected with characterization methods of these materials. μ is important parameter of transport layers, as it directly impacts efficiency of SC. The higher μ is, the higher probability to extract more charge carries towards contacts of SC, leading to higher J_{sc}. Common techniques to estimate mobility

for organic materials are analysis of Volt-Ampere characteristics (VACh), field effect transistor (FET) transfer and output characteristics analysis, time of flight (TOF) and charge extraction by linearly increasing voltage (CELIV). However, VACh analysis is not accurate and reliable technique, FET fabrication requires specific sample structure, while a sample fabricated for TOF or CELIV will have at least two conductive contacts and one of the contacts will be thermally evaporated metal contact on top of an organic material. Since the evaporated contact will have specific geometry and placement, it will provide the information only from small portion of the sample. Moreover, evaporation process might defect whole sample or contact area, since increased temperature or evaporated metal might accelerate a crystallization process of HTM. XTOF examines whole surface of a sample (cm^2 range) without second metal contact, the results are less affected by defects of the surface, in comparison to relatively small area of evaporated metal contact (mm^2 range).

As the production of any SC consist of many steps, therefore the main goals are to make the production as simple, safe and cheap as possible. CZTSSe is perspective composition of materials and has potential to fulfill desired goals – it is non-toxic, spray coating is applicable for layer deposition, preparation of a solution is simple and materials are relatively cheap [5], [26]. A cross-linkable fluorene based HTM could be used on top, because CZTSSe films can withstand high temperature. Fluorene based HTMs have relatively high cross-linking temperature point, which is too high for perovskite films or requires inverted architecture [27].

The use of all improvements and techniques mentioned above, enables the search of the new generation of SCs devices.

1.3 Statements of dissertation

1. The developed apparatus for the estimation of ionization potential in the mixture of air with Ar and CH$_4$ allows to register up to 10^4 times weaker current in comparison to electrometer measurements.
2. Photoemission yield spectrum plotted as $(dY/d(h\nu))^{1/2}$ allows to detect more energy levels than just HOMO level, in comparison with most frequently used $Y^{1/n}$ plot.
3. Methoxydiphenylamine-substituted fluorene derivatives HTM4 and HTM5 with alkyl groups at para positions of the triphenylamine moiety have similar hole mobility, ionization potential values and performance

13

in perovskite solar cells in comparison with Spiro-OMeTAD, however the synthesis of them requires only two steps instead of five.

4. Fluorene-based cross-linkable enamines HTM6 and HTM7 are suitable for multilayered structure without usage of orthogonal solvents. HTM6 and HTM7 demonstrate comparable to or higher hole mobility values than Spiro-OMeTAD. These HTMs have suitable ionization potential and cross-linking temperature for CZTSSe solar cells.

5. The solar cell of superstrate configuration $FTO/TiO_2/Cu_2ZnSnSe_{3.2}S_{0.8}$/Spiro-OMeTAD /Ag demonstrated power conversion efficiency of 3.1%, so far it is the highest reported value for the spray pyrolysis deposited superstrate solar cells up to date.

1.4 Publications related to dissertation

1. R. Tiazkis, P. Sanghyun, M. Daškevičienė, T. Malinauskas, M. Saliba, J. Nekrasovas, V. Jankauskas, Sh. Ahmad, V. Getautis, M. K. Nazeeruddin. "Methoxydiphenylamine-substituted fluorene derivatives as hole transporting materials: role of molecular interaction on device photovoltaic performance", *SCIENTIFIC REPORTS*, Volume 7, 150, DOI: 10.1038/s41598-017-00271-z (2017).

2. M. Franckevičius, V. Pakštas, G. Grincienė, E. Kamarauskas, R. Giraitis, J. Nekrasovas, A. Selskis, R. Juškėnas, G. Niaura. "Efficiency improvement of superstrate CZTSSe solar cells processed by spray pyrolysis approach", *Solar Energy*, Volume 185, June 2019, Pages 283-289. DOI: 10.1016/j.solener.2019.04.072 (2019).

3. J. Nekrasovas, V. Gaidelis, E. Kamarauskas, M. Viliūnas, V. Jankauskas. "Photoemission studies of organic semiconducting materials using open Geiger-Muller counter", *Journal of Applied Physics*, 126, 015501. DOI: 10.1063/1.5096070 (2019).

4. D. Vaitukaitytė, A. Al-Ashouri, M. Daškevičienė, E. Kamarauskas, J. Nekrasovas, V. Jankauskas, A. Magomedov, S. Albrecht, V. Getautis, "Enamine-Based Cross-Linkable Hole-Transporting Materials for Perovskite Solar Cells", *SOLAR RRL*, Volume: 5 Issue: 1, 2000597, DOI: 10.1002/solr.202000597 (2021).

1.5 Conference presentations

1. R. Tiazkis, P. Sanghyun, M. Daškevičienė, T. Malinauskas, M. Saliba, **J. Nekrasovas**, V. Jankauskas, Sh. Ahmad, V. Getautis, M. K. Nazeeruddin, "Charge-transporting properties of methoxydiphenylamine-substituted fluorene derivatives as hole transporting materials for PSC.", *E-MRS Fall Meeting 2017*, p. 146, Warsaw University of Technology, Warsaw, Poland, September 18-21, 2017.

2. **J. Nekrasovas**, V. Gaidelis, V. Jankauskas, E. Kamarauskas, M. Viliūnas, "Puslaidininkių jonizacijos potencialo matavimas Geigerio-Miulerio skaitikliu."ISBN: 9786094598807 ; DOI: 10.15388/proceedings/LNFK.42, *the 42nd Lithuanian national Physics Conference*, Vilnius, Lithuania, October 4-6, 2017.

3. **J. Nekrasovas**, E. Kamarauskas, V. Gaidelis, M. Steponaitis, T. Malinauskas,V. Getautis, V. Jankauskas, "Charge transport properties of novel enamines with different central group.", eISBN: 9786090216385 ; DOI: 10.5755/e01.9786090216385, *the 43th Lithuanian national Physics Conference*, Kaunas, Lithuania, October 3-5, 2019.

4. **J. Nekrasovas**, Š. Daškevičiūtė, M. Daškevičienė, V. Getautis, V. Gaidelis, V. Jankauskas, "Charge-transporting properties of enamine-based fluorene derivatives as hole transporting materials for PSC", *nanoGe Fall Meeting19*, Berlin, Germany, November 3-8, 2019.

1.6 Participation in scientific projects

Research Council of Lithuania, the scientist's groups project "Investigation of the charge carriers transport features in thin multilayered hybrid structures, Project No. MIP-091/2015, 2015-2018.

1.7 Contribution of author

The author participated in the development and construction processes of the new PYSA system and performed all experiments and data analysis using PYSA and XTOF methods. The author developed I_p determination using $(dY/d(h\nu))^{1/2}$ dependence. The author designed the new spray coating system and participated in the development of spray coating technique for the new CZTSSe SCs and performed VACh measurements of CZTSSe SCs. The

author actively participated in the discussions of the results as well as the preparation of the related publications.

Differential scanning calorimetry (DSC) measurements and synthesis of HTM1-HTM7 were carried out in Kaunas University of Technology in the research group led by prof. Vytautas Getautis. Prof. Sanghyun Paek and prof. Michael Saliba performed fabrication and characterization of SCs with HTM1-HTM5. Dr. Amran Al-Ashouri and prof. Steve Albrecht performed fabrication and characterization of SCs with HTM6-HTM7. The preparation of solutions for CZTS layers, chemical bath deposition (CBD) of CdS, CZTS films formation by hand spraying, selenization processes of CZTS films and Spiro-OMeTAD deposition for CZTS SC were perfomed by dr. Marius Franckevičius, dr.Vidas Pakštas, dr. Giedrė Grincienė, dr. Raimondas Giraitis, dr. Algirdas Selskis.

1.8 Layout of the dissertation

In chapter 1 the introduction of the dissertation is presented, in which the importance of the development of new organic and inorganic structures and significance of their characterization methods are pointed out. This is followed by the aim and objectives, novelty and relevance and statements of the dissertation, the list of publications related to the dissertation, the list of presentations in the conferences, the list of scientific projects, where author participated and the contribution of the author to the dissertation.

In chapter 2 the principal of the photoemission spectroscopy and estimation methods of I_p are overviewed. The results of PYSA measurements of the new fluorene based HTMs are presented. I_p estimation plot as the dependence of $(dY/d(hv))^{1/2}$ and the new system for PYSA measurements is presented. Four well known organic materials were investigated to show capabilities of the new system and the new way to estimate I_p.

In chapter 3 the principal of charge carries transport dynamics in organic materials and μ estimation method using XTOF are overviewed. The results of XTOF measurements of the new fluorene based HTMs are presented. VACh results of five materials performance with perovskite SC are shown.

In chapter 4 theoretical principal of organic materials cross-linking and the results of new cross-linkable fluorene-based HTMs of PYSA, XTOF and VACh in perovskite SCs are presented.

In chapter 5 the formation and deposition techniques for CZTSSe SCs are explained. Results of VACh of SCs are presented.

In chapter 6 the conclusions of the dissertation are formulated.

2 Determination of I_p

The electron photoemission is an important tool to investigate energetic levels of metals, semiconducting materials, especially organic compounds, which are widely used in the development of electronic devices, as SCs, light emitting diodes (LEDs), FETs. In all the cases mentioned, the knowledge of the energetic levels of the materials is essential for making right choice from the wide variety of existing materials or to synthesize new materials with desired characteristics. The key question in the evaluation of energetic levels is the measurement of I_p. Various methods are used for this purpose, such as ultraviolet photoemission spectroscopy (UPS) [28]–[37] and its modification valence band UPS (VB-UPS) [32],[33] electrochemical method of cyclic voltammetry (CV) [34],[35], the photoelectron yield spectroscopy (PYS) [36], [42]–[46] technique and dual-mode Kelvin probe ambient pressure photoemission spectroscopy (PES) technique, which enables to measure both contact potential difference between the material investigated and the tip electrode of the apparatus as well as ionization potential[47] . It should be noted that physical process for PYS is the same as PES, where photoelectrons are emitted from the sample surface upon UV irradiation. The photoemission event is common for both methods, but the photon energy range and detection scheme of photoelectrons are different. The UPS technique is widely used for investigations of both metals and non-metals. However, this technique has some drawbacks related to the need of performing experiments in high vacuum and charging-up of the sample as discussed in [48], [49] . Another problem arises from the light sources used in the UPS equipment. The cold cathode capillary discharge in He light source UV illumination with the quanta energy of 21.2 and 40.8 eV is usually used, which may cause negative effects on the specimens investigated. The bond dissociation energy in organic molecules is around 6.4 eV (or around 618 kJ/mol in the case of the C-H bonds and around 338 kJ/mol for C-C bonds)[50], therefore, the energy of the light quanta in the UPS apparatus far exceeds the dissociation of the molecules limit and may cause photochemical reactions to change the characteristics of samples. In the case of TiO_2 the work function change of 0.5 eV was found as the result of UV illumination during measurement by UPS technique [48]. The electrochemical technique is performed with the materials dissolved in organic solvent, while in the electronic devices – the same materials are used as solids. Therefore, the CV measurements are useful for comparison of

different materials among themselves, but in fact they give little information on possible behavior of the materials in the devices.

PYS is based on the measurement of the quantity of photoelectrons released from the sample as a function of the light quanta energy. PYS experiments may be performed either in vacuum or in a gas atmosphere, including air. The technique based on the photoemission in air are relatively easy to perform and are widely used for the evaluation of the ionization potential of semiconducting materials or work function of metals[42], [51]–[54].
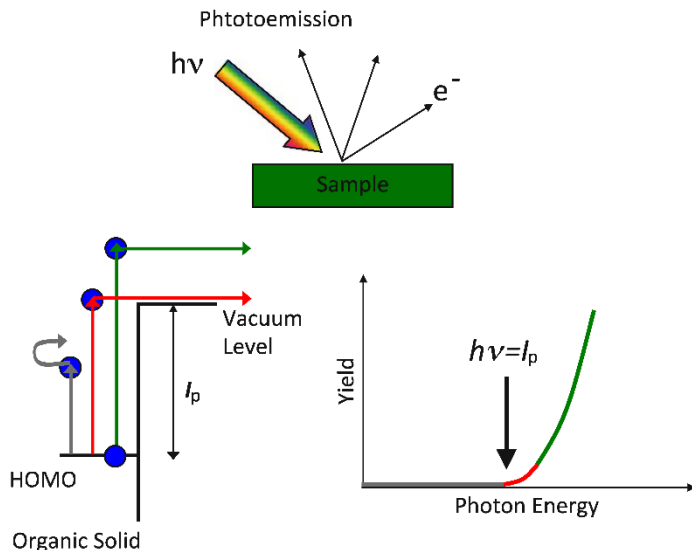
Fig. 1. Principle of photoelectron yield spectroscopy in the case of organic materials. Adapted from [55], [56].

In Fig. 1 the principle of PYS is showed. The quantum yield of photoelectron (Y), which is the number of emitted photoelectrons per photon absorbed, is detected as a function of incident photon energy ($h\nu$). When photon energy is lower than threshold ionization energy, the first region of spectra is observed - "0" level (grey). The second region starts at the point, where $h\nu$ becomes slightly greater than ionization energy (red). The third region is registered, when $h\nu$ clearly excess ionization energy (green). After all, $Y^{1/n}(h\nu)$ is plotted, selecting the most suitable value of n to achieve the best linearity, as further will be explained in more details. However, the second region is hardly to be approximated linearly, even when data is plotted as $Y^{1/n}$. This might lead to some deviation of observed results in literature.

In three *step* model, which is presented in [57] and described in simplified form in [29], [55], Photoemission event consists of three steps; (I) optical excitation of an electron at initial energy E, (II) electron transport towards the surface, and (III) escape through the surface to vacuum. During the steps (II) and (III), primary photoelectron suffers from inelastic scattering and secondary electrons with lower kinetic energy are produced. Scattering processes such as electron–electron and electron–phonon scattering should be considered. However, if we focus on the threshold region of PYS plot, photoelectrons are mainly primary, and the contribution of secondary electrons could be neglected. If distribution of photoelectrons is isotropic, the photoemission yield for $h\nu$ expressed as:

$$Y(h\nu) \propto \frac{\int_{E_{\text{vac}}}^{h\nu} P(E,h\nu)X(E)T(E)\mathrm{d}E}{\int_0^{h\nu} N_i^{\text{opt}}(E-h\nu)N_f^{\text{opt}}(E)\mathrm{d}E}, \tag{2.1}$$

where $P(E,h\nu)$ is the probability of exciting an electron to a state of energy E with photon energy $h\nu$, $X(E)$ is the transmission probability for the electron at the level E, $T(E)$ is a surface escape function, N_i^{opt} and N_f^{opt} are initial and final optical density of states, E_{vac} is the energy of vacuum level of the sample.

However, determination of the threshold energy is not straightforward, because the observed yield shows finite intensity even far below the ionization energy. To overcome this issue and to detect the threshold energy E_t, the threshold region can be fitted by a function form. Fowler showed how to estimate work function for metals using the yield function of photoemission [58]. For metals photoemission yield shows Fowler function curve [58] and yield curve can be approximated as:

$$Y \propto (h\nu - \Phi)^2, \tag{2.2}$$

where Φ is wok function. The yield curve is usually analyzed by using power dependence as:

$$Y \propto (h\nu - E_{\text{T}})^n. \tag{2.3}$$

The rule of this method is to find the n value, in order to achieve the best linearity of plotted curve. For metals $n = 2$, however, depending on surface properties it can vary among $n = 1, n = 3/2, n = 5/2$ [59]. For organic materials $n = 3$ is recommended. However, n could vary from 1 to 5 to

achieve the proper linear fitting [36], [60]–[62]. Kochi and etl. reported the results of experiment for tetracene, where good linearity was achieved for the values $n = 1; 2; 3; 4$ [43]. The number of n should be considered as empirical value [42].

2.1 I_p determination using an electrometer and $Y^{1/n}$ dependence

HTMs, which are less costly and easier to synthesize with performance comparable or better than Spiro-OMeTAD, were investigated by photoelectron yield spectroscopy in air (PYSA) technique [63]. This method was first used in [52]. The chemical formulas are shown in Fig. 2. These materials were chosen, because in the recent years pervoskite have tremendous amount of interest for SCs applications. Many of high efficiency SCs were using Spiro-OMeTAD as HTM [64]–[67]. However, Spiro-OMeTAD is expensive material to produce: multistep synthesis procedures, expensive reagents and costly purification methods [23]–[25] are required.

Prof. Vytautas Getautis and his work group prepared 5 materials based on methoxydiphenylamine-substituted fluorene and triphenylamine fragments (Fig. 2): 4-{[2,7-bis(4,4'-dimethoxydiphenylamino)-9*H*-fluoren-9-ylidene]methyl}-*N,N*-diphenylaniline (HTM1), 4-{[2,7-bis(4,4'-dimethoxydiphenylamino)-9*H*-fluoren-9-ylidene]methyl}-*N,N*-diphenyl-2-methylaniline (HTM2), 4-{[2,7-bis(4,4'-dimetoxydiphenylamino)-9*H*-fluoren-9-ylidene]methyl}-*N,N*-diphenyl-3-methylaniline (HTM3), 4-{[2,7-bis(4,4'-dimethoxydiphenylamino)-9]-fluoren-9-ylidene]methyl}-*N,N*-bis(4-methylphenyl)aniline (HTM4), 4-{[2,7-bis(4,4'-dimethoxydiphenylamino)-9*H*-fluoren-9-ylidene]methyl}-*N,N*-bis(4-butylphenyl)aniline (HTM5).
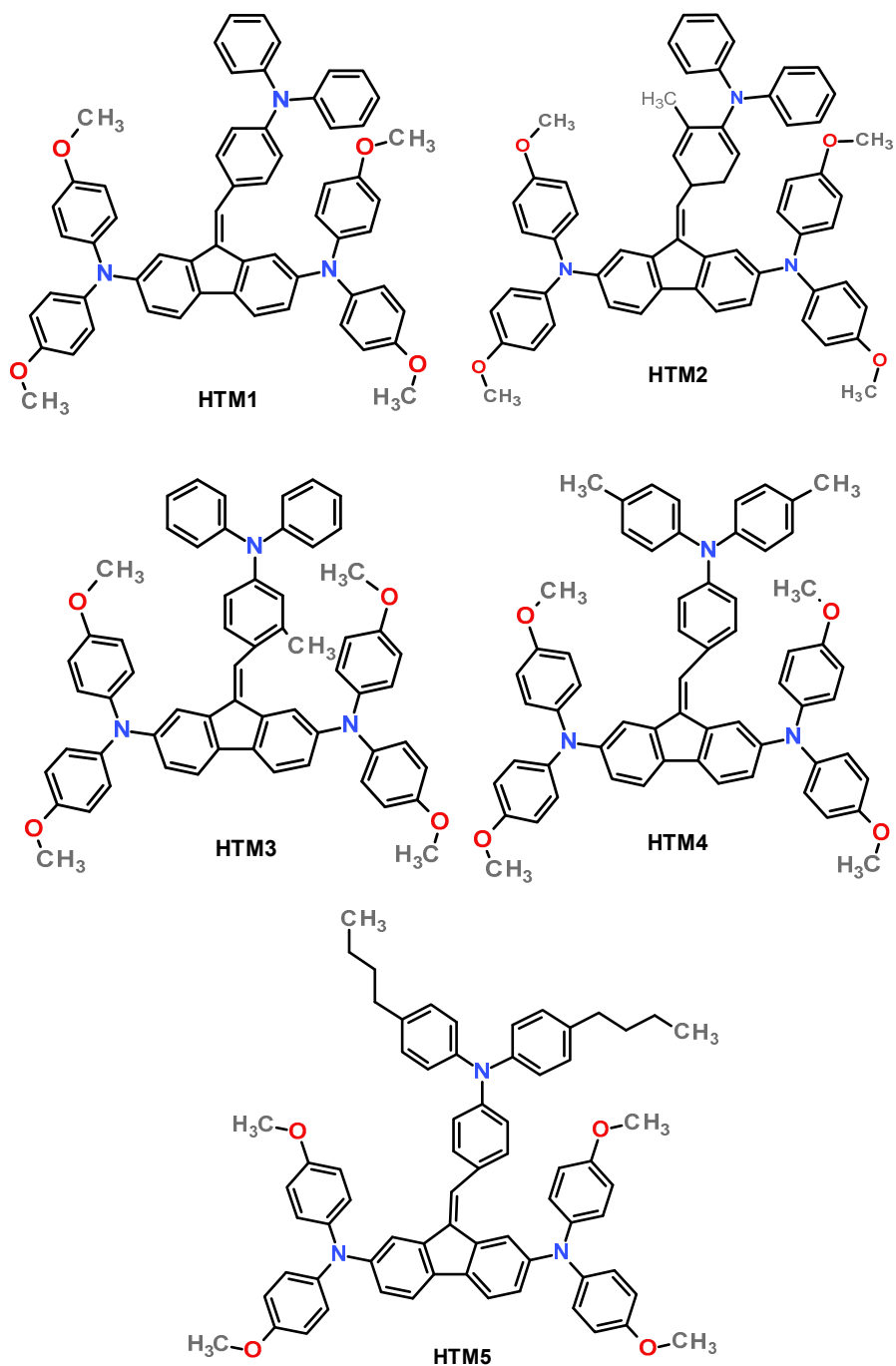
Fig. 2. Structures of the investigated fluorene-based hole transporting materials HTM1 - HTM5.

All materials were designed to have I_p around 5 eV. The solid state I_p of the layers of the synthesized compounds was measured by PYSA technique using the electrometer, as described further. The samples for the ionization potential measurement were prepared by dissolving materials in tetrahydrofuran (THF) and were coated on Al plates pre-coated with ~0.5 μm thick methylmethacrylate and methacrylic acid copolymer adhesive layer. The thickness of the transporting material layer was 0.5-1 μm. The samples were illuminated with monochromatic light from the quartz monochromator with deuterium lamp. The power of the incident light beam was $(2\text{-}5)x10^{-8}$ W. The negative voltage of –300 V was supplied to the sample substrate. The counter-electrode with the 4.5×15 mm^2 slit for illumination was placed at 8 mm distance from the sample surface. The counter-electrode was connected to the input of the BK2-16 type electrometer. The setup is described in [52] at length. The $10^{-15} – 10^{-12}$ A photocurrent was flowing in the circuit under illumination. The photocurrent I is strongly dependent on the incident light photon energy $h\nu$. The $Y^{0.5} = f(h\nu)$ dependence was plotted. The dependence of the photocurrent on incident light quanta energy is well described by linear relationship between $Y^{0.5}$ and $h\nu$ near the threshold. The linear part of this dependence was extrapolated to the $h\nu$ axis and I_p value was determined as the photon energy at the interception point. It has to be noted, that the results were plotted as a square, not a cubic root, as explained in the beginning of section 2.1. The results are shown in Fig. 3 and summarized in Table 1. In Fig. 3 red line is fit line for Spiro-OMeTAD data points. Intersection point of red line with abscissa is considered as I_p.

Table 1. Estimated I_p values of HTM1-HTM5 and Spiro-OMeTAD.

Material	I_p, (eV±0.1eV)
HTM1	5.05
HTM2	5.00
HTM3	5.00
HTM4	4.92
HTM5	5.03
Spiro-OMeTAD	5.00
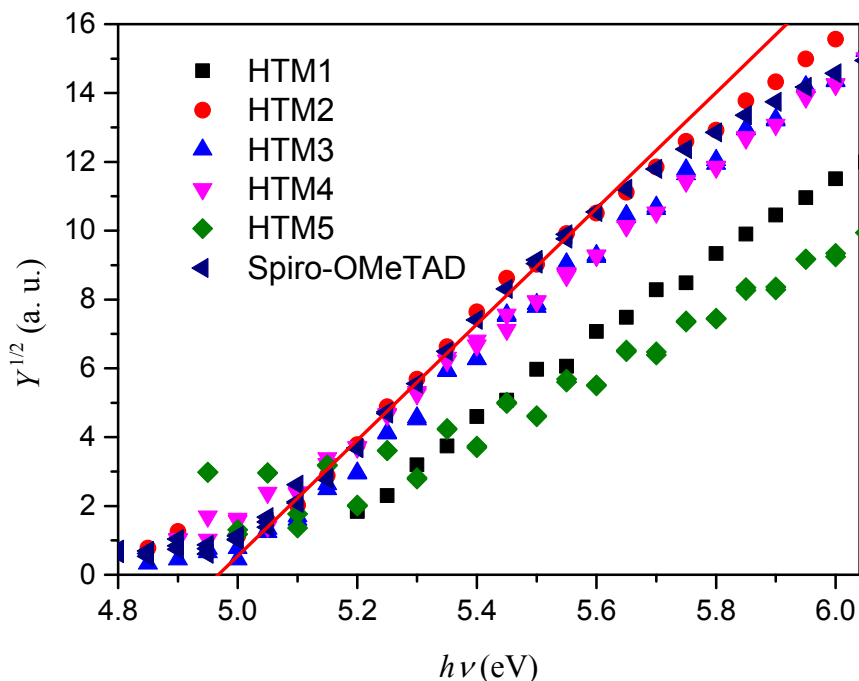
Fig. 3. Photoemission in air spectra of HTM1-5 and Spiro-OMeTAD. Measured with electrometer.

All HTMs demonstrated similar I_p as Spiro-OMeTAD, as all of them share the same methoxydiphenylamine-substituted fluorene main fragment. HTM4 has slightly lower I_p, which might be diminished by adding two methyl groups in *para* positions of the triphenylamine moiety. The structure/energy level dependency is less clearly defined in tightly packed films compared with the solvated molecules. I_p values of the HTMs containing alkyl substituents in the triphenylamine fragment are lower as compared to the parent derivative HTM1.

Spectrum of HTM2 is depicted in Fig. 4. Linear approximation crosses *x*-axis and the crossing point indicates I_p value with assumption that *x*-axis is "0" level. However, if the spectrum is analyzed more carefully, it is visible, that it has 3 regions:

1. ~4.8 - 5eV – dark signal region
2. ~5 – 5.4 eV – 1st photoemission region
3. ~5.4 - 6eV– 2nd photoemission region

Fig. 4. Photoemission spectrum of the HTM2. Measured with electrometer.

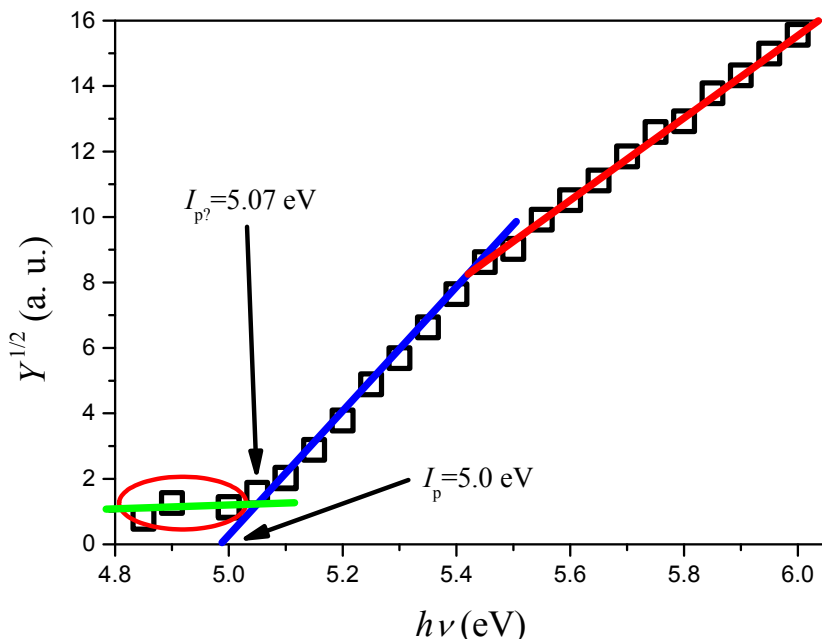Published literature reveals that, there are two methods, how to estimate the intersection point - I_p value: 1) spectrum's fit line and abscissa intersection point; 2) "0" level's fit line and spectrum fit line intersection point [36], [61]. If to consider the green line as true "0" level, the value of I_p changes by 0.07eV. Moreover, it is visible that, there is kind of transition between 1st and 2nd photoemission regions. There are two main reasons for loosing track of "0" level or slope changes: low photosensitivity of organic material and low sensitivity of electrometer. Fig. 4 shows the slope change of spectrum at ~5.4 eV, which on regular basis can be ignored and linear approximation is made using whole 5 – 6 eV range. It explains, why it is possible to find various publicized I_p values in literature for the same material, e.g. for H_2Pc values I_p of ranges from 4.95 to 5.1 eV[29], [32], [68].

To overcome these issues the home built slow electron counter (EC) was made to be used with other supplementary equipment (as described below).

2.2 I_p determination using open Geiger-Müller counter and $(dY/d(h\nu))^{1/2}$ dependence

PYS technique is widely used for the evaluation of the ionization potential of semiconducting materials or work function of metals [42], [51]–[54]. The

most common technical implementations to measure I_p in air is by using electrometer or open electron counter. The authors of the article [51] for the measurement of the photoemission yield used an open EC, however, the setup has drawbacks as described in more detail in 2.2.1. The authors of the article [52] used an electrometer, which measured the electric potential build-up as a result of incoming photoelectrons in the capacitance of the input of the electrometer. The practice shows that the sensitivity of the available electrometers is around 10^{-16}A and it is too low to detect photoemission current near the threshold. In such cases the quanta energy, at which the current reaches the noise level, may be regarded as the photoemission threshold, and this leads to inaccurate evaluation of the ionization potential. In order to increase the sensitivity of the measurement, the experiments with an open ionization cell working on the principal of Geiger–Müller counter were conducted [69]. A photoemission current as low as about one electron per second, or around 10^{-19}A, may be detected. The set-up for the I_p measurement was developed. Investigations of the photoemission yield in a gas mixture under atmospheric pressure were performed for a number of materials, some of which are described further.

2.2.1 An open Geiger-Müller counter for I_p determination

Fast ionized particles like α and β, thus γ rays, are counted using gas counters: ionization camera, proportional counter, Geiger–Müller counter [70]–[72]. While photoemission occurs during ionization potential measurement, emitted electrons are slow, however, they share similar effects as fast particles do. In case of slow electron detection, the gases between anode and cathode are not ionized and electrons are emitted straight from investigated material. Moreover, electric field in ionization camera should be kept relatively low to avoid undesirable electron multiplication effects.

Plasma is formed in the vicinity of anode of Geiger–Müller counter. In this area electron multiplication happens, however, some UV light might be generated here. If UV light will reach cathode, it will free up new electrons and they will continue this loop further. To avoid this, the material of the cathode is to be insensitive to the light emitted, for example it may be coated with a layer of material not emitting photoelectrons. The other problem is created by the positive gas ions reaching the cathode. There are two ways how positive ions can act when cathode is reached: 1) single-atom or double-atom molecules usually will become excited and eventually will emit undesirable light quanta, which may cause emission of electrons from cathode, which is

not desirable 2) multi-atom gases or halogen molecules can lose energy by dissociation [71], which is preferable. The other option to avoid these unnecessary electrons is to diminish applied voltage on counter for short period of time. This method is used in the Riken-Keiki's spectrometer [21], [22], however it slows down the electron counting process.

Voltage applied to Geiger–Müller counter is sufficient to initiate impact ionization processes, this means, that independently to initiative electron energy, a signal will be amplified enough to generate strong current, after impact ionization occurred. As electrons generated by photoemission won't have enough energy to go through mica window to counter, it should be performed in air or gas mixture.

For the investigation of photoemission at the atmospheric pressure we used the scheme working on the principal of Geiger–Müller counter [71]. Our home built slow EC consists of the cylinder shape ionization cell with a slit along one side of the cylinder for the electrons to enter from the surrounding space (Fig. 5). A thin wire runs along the axis of the cylinder, a high positive voltage is applied to the wire during cell operation. The voltage of the wire is maintained somewhat lower than the corona discharge initiation voltage. The voltage creates electric field of ~10^5 V/cm on the wire surface. When slow electron enters the interior of the cylinder, it is affected by the electric field and drifts toward the wire. The avalanche develops in the vicinity of the wire, where ionization of the gas molecules takes place in a strong electric field. The swift multiplication of the charge carriers increases their number up to around 10^9. The avalanche process ends, when the positive ions form space charge in the vicinity of the wire, thus electric field is weakened. Subsequently, positive ions drift toward the cathode, where they lose their charge. The molecules become neutral and excited [71]. Some of gases, as Ar or N_2 loose the excitation energy emitting quanta of UV light [71]; these quanta may ionise other gas molecules thus creating secondary free electrons, which approach the anode and initiate new undesirable avalanches. In order to diminish these avalanches, we used high purity mixture of gases, containing 5 % methane and 95 % argon together with air at a ratio around 1:1. The molecules of methane lose the energy by dissociation, working as effective quencher of the formation of secondary electrons and false signal pulses.
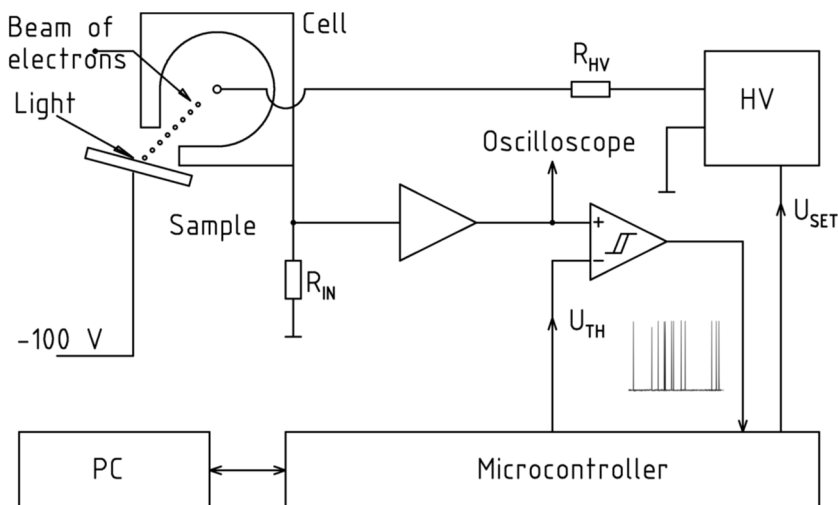
Fig. 5. Electric scheme of electron counter.

The electric scheme of the EC is shown in Fig. 5. It consists of high voltage source (HV), ionization cell and special sample's holder placed in a closed measurement camera as well as amplifier and comparator with optional threshold level adjustment. The pulse counter and the experiment are controlled by microcontroller, which is operated by PC. The monochromatic light enters into the camera through quartz window. If light quanta is absorbed by the sample and electron is emitted into the cell the avalanche discharge takes place. A short current pulse runs through the cell and the input resistor of the amplifier R_{IN}. The rising part of the pulse less than 1 µs long is determined by the processes inside the cell and bandwidth of amplifier while the falling part, which lasts around 25 µs, is determined by the capacitances of the cell, connecting wires, input capacitance of amplifier and resistor R_{IN}. After the pulse, the voltage in the cell increases up to the initial value. The duration of the voltage recovery is limited by R_{HV} and the capacitance of the cell and connecting wires, with the time constant close to 20 µs. The registration of the number of signal pulses is mostly limited by the time of the electric field redistribution in the cell and other phenomena, such as warming up of the gases in the vicinity of the wire. Therefore, the upper limit is around 1000 pulses per second. The magnitude of the signal pulses depends on the atmospheric pressure, high voltage and gas mixture composition. Typical signal height of registered pulses was around 4 V and the threshold of the minimum signal height was set to 2 V (U_{TH}). The sample was illuminated with monochromatic light from the deuterium light source through the Newport

CS260 grating monochromator. The slit width of the monochromator was 0.2 mm, the reciprocal resolution was 6.4 nm/mm. The calculation gave the spectral width of the light beam 0.040 eV at 6.2 eV quanta energy and 0.026 eV at 5.0 eV.

In comparison with commercially available photoelectron spectrometers, like Riken-Keiki's AC-2 and AC-3 [22], our system does not use quenching and suppressor grids along with pulse generators; instead, we use commercially available 95% of argon and 5% methane mixture and this solves the problem of quenching and false pulses. An absence of the quenching pulses is one of the merits of our counter. The electrons, reaching the counter, cannot be detected while these pulses are applied; thus, 3 ms long waiting periods arise; as a result, considerably less than 300 electrons can be detected per second [21], [22]. These 3 ms are dead time of the counter. In our case, the counter recovers with the time constant 25 μs, hence in about 100 μs. This enables to detect up to 1000 electrons per second.

After the new system was ready, to show and compare capabilities of two systems, the new samples of HTM2 – HTM5 were made. Estimated I_p values are shown in Table 2. Estimated values of I_p are similar, however, higher sensitivity of EC and higher spectral resolution provided more precise results of the measurements.

Table 2. I_p values for HTM2-5 when measured with EC in comparison to measurements of HTM2-5 with electrometer.

Material	Electrometer (I_p (eV±0.1eV))	EC (I_p (eV±0.05eV))
HTM2	5.00	4.99
HTM3	5.00	4.96
HTM4	4.92	5.01
HTM5	5.03	5.00

In Fig. 6 photoemission spectra of HTM2 measured with EC is shown in comparison to the measurement of HTM2 with electrometer. In the theory, $Y^{1/3}$ plot (black squares) should be more preferable for organic materials, on the other hand, if the most linear plot should be chosen, then $Y^{1/2}$ plot (green empty squares) is more suitable to indicate I_p value. These experiments rise the problem – how to figure out, which n value is the right one?
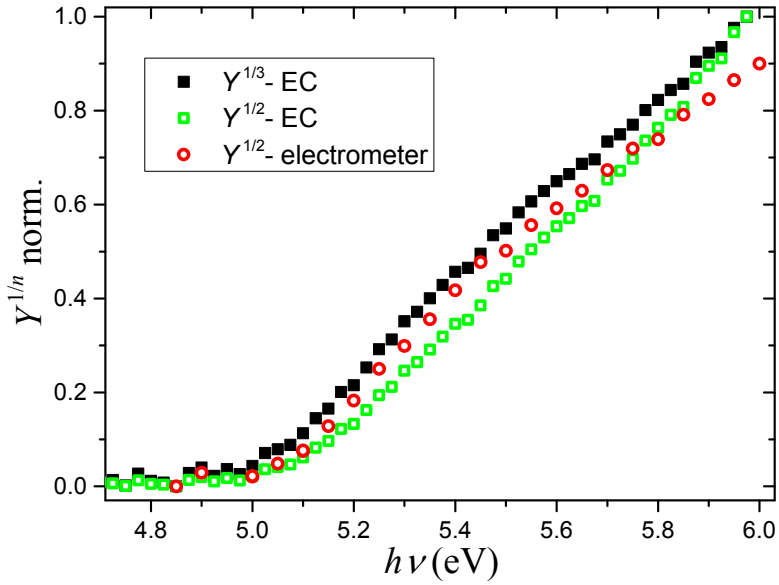
Fig. 6. I_p measurements for HTM2, performed with electrometer (red circles) and performed with the EC (black squares and green empty square). Data normalized to 1.

The new method of data processing and graphical presentation of the PYSA results are presented further. The method allows to study peculiarities of the photoemission spectra in detail.

2.2.2 I_p determination using $(\mathrm{d}Y/\mathrm{d}(h\nu))^{1/2}$ dependence

In literature the derivative of the yield spectrum is used to evaluate the density of states in the energy bands [51]. The first derivative of the yield with respect to energy, $\mathrm{d}Y/\mathrm{d}(h\nu)$, reflects an effective density of states around valence top region, however, the results strongly depend on the material [73]. After numerous experiments, it showed up that I_p estimation using the square root of the derivative of the yield dependence on the light quanta energy $(\mathrm{d}Y/\mathrm{d}(h\nu))^{1/2}$ plot is advantageous tool. As estimated I_p value considerably depends on n, $(\mathrm{d}Y/\mathrm{d}(h\nu))^{1/2}$ dependence diminishes chosen n value impact, as discussed further. The graphical representation of this function is more informative and straightforward and allows to distinguish more existing peculiarities of the plots.

Secondly, in publications on the UPS investigations of organic materials, as in [38], [39], [68], it is stated that the distribution of the density of states (DOS) is a Gaussian function. This function is used in both - theoretical

calculations and interpretation of experimental results, but in a sense of finding I_p value, it raises a question: how to define and to find experimentally photoemission threshold correctly? The Gaussian function smoothly decreases down toward zero. If a straight line is drawn, best fitting the slope of the Gaussian function, then it intersects the abscissa at the point, where the function value is about 10 % of the maximum value. The values below of 10 % are present in the results of UPS investigations [38], [39], [68]. Thus, the weak photoemission, present in the gap, may be caused by the tails of HOMO. $Y^{1/n}$ dependence eliminates detection of weak DOS in HOMO-LUMO energy gap. The weak photoemission below quanta energy lower than I_p is reported in literature [42], [51], [61].

Mathematical modeling helps to decide, which dependence of the graphical data presentation and data processing is better for the evaluation of I_p. It is assumed, that the dependence of the yield Y for semiconductors is proportional to the cube of the difference between the incident quanta energy $h\nu$ and ionization potential I_p [42], [55]. It is evident that, in the simple case, when there is only one photoemission band, the square root of the derivative of Y on the quanta energy is linear.

Let us consider a model, in which there are two photoemission bands: the first weak band and the second strong band accordingly characterized by the thresholds I_{pnR1} and I_{pnR2}. Further, if supposed, that there may be a weak nearly constant photoemission of the yield C, caused by the background radiation, scattered light or other phenomena, then the yield Y can be presented as follows:

$$Y = C, \text{ if } x < I_{pR1} \tag{2.4}$$

$$Y = C + A \cdot \left(x - I_{pR1}\right)^3, \text{if } I_{pR1} < x < I_{pR2} \tag{2.5}$$

$$Y = C + A \cdot \left(x - I_{pR1}\right)^3 + \left(x - I_{pR2}\right)^3, \text{if } x > I_{pR2} \tag{2.6}$$

Here x means the quanta energy. The parameter $A < 1$ means the intensity of the first band, while the intensity of the second band is 1.
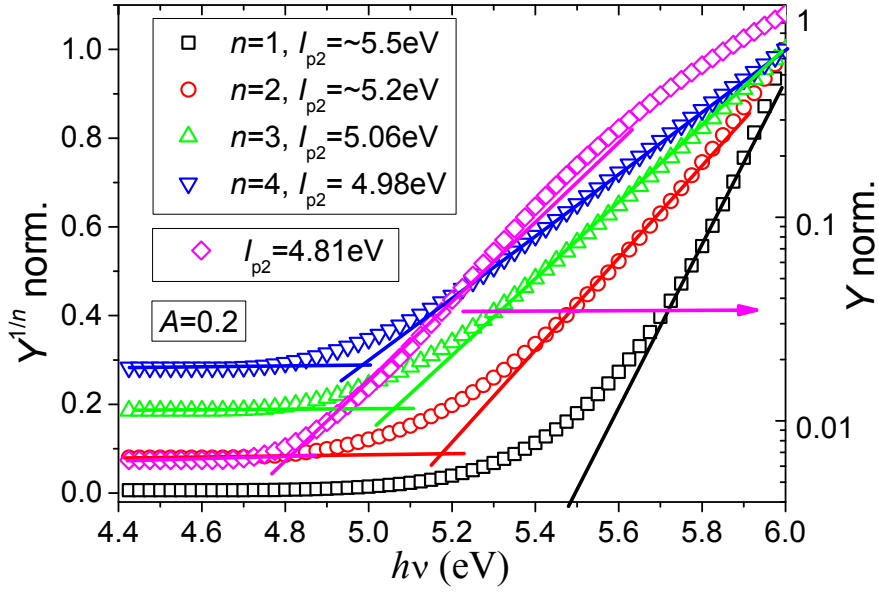
Fig. 7. Results of theoretical calculations plotted as $Y^{1/n}$ dependencies on x (representing light quanta energy) on linear and logarithm scales (pink diamond). The values of Y were calculated using formulas (2.4), (2.5) and (2.6) with these parameters: $I_{pR1} = 4.6$, $I_{pR2} = 5$, $C = 0.01$ and $A = 0.2$.

The plot of Y values is shown in Fig. 7 as $Y^{1/n}$ dependency on x. Y values were calculated using (2.4), (2.5) and (2.6) formulas. The straight lines approximating the sections of the curves were drawn in order to find the crossing points. The x coordinate of the intersection point considered as I_{p2}. It is necessary to note, that it is practically impossible to find satisfactory linear sections in the cases of $n = 1$ or 2, thus the "best visual fit" was chosen. The linearity of the curves improves at $n = 3$ or 4. In the case of $n = 1$, the dependence was plotted both in linear and logarithm scale.

The values of the parameter I_{p2} defined as x values at the crossing points are given in   Table 3. In the case of the linear plot, these values decrease with increasing of n, but the lowest value is estimated on the logarithm scale curve at $n = 1$. In majority of cases estimated I_{p2} value significantly differs from the real value $I_{pR2} = 5$. Moreover, it is problematic to find out the experimental I_{p1} value, which theoretically should be $I_{p1} = 4.6$ eV. The new way was explored to solve the issues described above, based on the calculation and plotting of the square root of the derivative of the dependence of Y on the quanta energy.

Table 3. Values of the parameter I_{p2} defined as x values at the crossing points.

n	I_{p2}, eV		
	$A = 0.05$	$A = 0.2$	$A = 0.5$
1	~5.6	~5.5	~5.5
2	~5.3	~5.2	~5.2
3	5.1	5.06	4.93
4	5.04	4.98	4.86
1, log scale	5.04	4.81	4.74
Derivative	5.05	5.08	5.11

Differentiation of (2.4) to (2.5) gives

$$\frac{dY}{dx} = 0, \text{if } x < I_{pR2} \tag{2.7}$$

$$\frac{dY}{dx} = 3A \cdot \left(x - I_{pR1}\right)^2, \text{if } x < I_{pR2} \tag{2.8}$$

$$\frac{dY}{dx} = 3A \cdot \left(x - I_{pR1}\right)^2 + 3\left(x - I_{pR2}\right)^2, \text{if } x > I_{pR2} \tag{2.9}$$

$$\frac{dY}{dx} = 3A \cdot \left(x - I_{pR1}\right)^2 + 3\left(x - I_{pR2}\right)^2, \text{if } x > I_{pR2}$$

Fig. 8 shows the dependencies of the square roots of Y calculated by the formulas from (2.7) to (2.9) at $I_{pR1} = 4.6$ eV and $I_{pR2} = 5$ eV. The derivatives were calculated digitally from Y data, similarly as it was done with the experiment results. Each dependence in Fig. 8 may be approximated by pairs of straight lines, the crossing points of these lines shift to higher x values with increment of parameter A, but this shift is less than in the power law presentations.
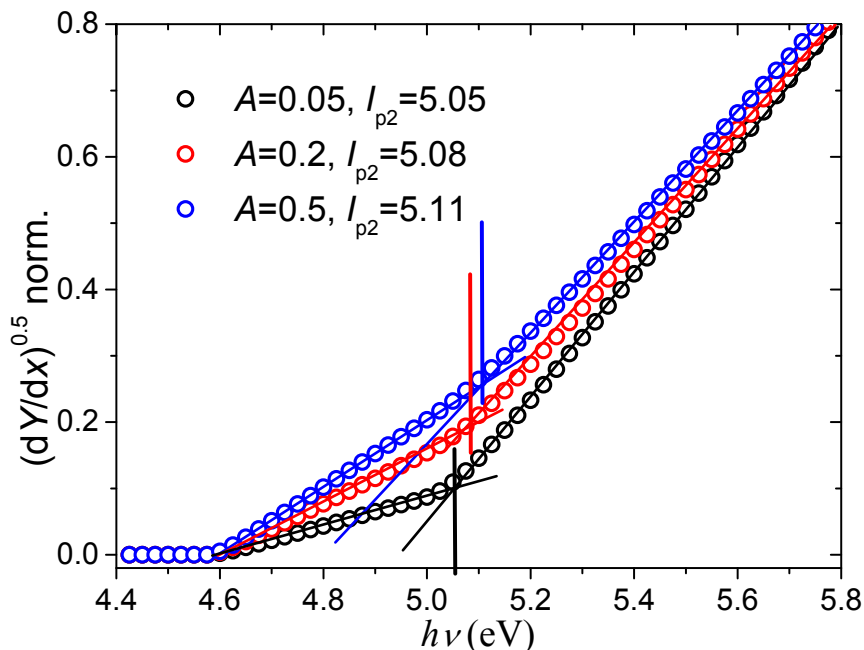
Fig. 8. Dependencies of the square root of the derivatives of Y according to the formulas (2.7) to (2.9).

Differentiation of the expression (2.6) is advantageous in comparison with calculation of the power law expressions or logarithm, because each component of the expression is differentiated individually and evaluated separately in the equation (2.9).

2.3 Measurements and data processing

In order to demonstrate the capabilities of the new method the photoemission spectra of some well-known materials were investigated: metal-free phthalocyanine (H_2Pc), titanyl phthalocyanine (TiOPc), N,N'-is(3-methylphenyl)-N,N'-diphenylbenzidine (TPD) from Sands Co., regioregular polyhexyltiophene (P3HT) from Sigma Aldrich. Chemical formulas of these materials are shown in Fig. 9. TiOPc and H_2Pc powders were dispersed in THF without any binding material, the dispersion was casted on the substrates consisting of polyester film coated with Al conductive layer and around 0.5 μm thick layer of copolymer of methylmetacrylate and metacrylic acid, coated from the 2.5 % solution in 1:1 mixture of ethanol and acetone. TPD was dissolved in THF and coated on the substrate. P3HT was dissolved in chloroform. The samples were dried at 60°C for 30 min.

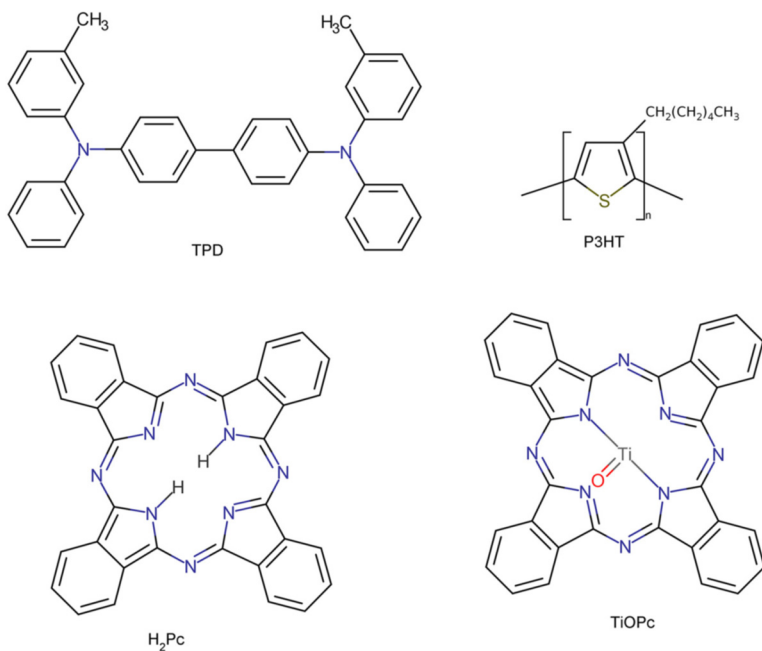Fig. 9. Investigated materials: TPD, P3HT, H_2Pc, TiOPc.
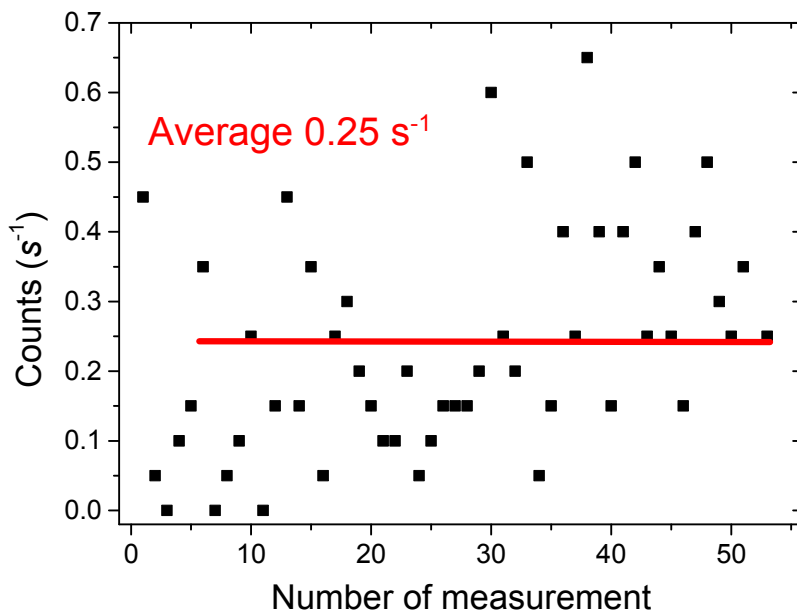
2.3.1 Background signal

Fig. 10. Numbers of the signal pulses, when a sample is not illuminated.

Some signal pulses are detected even in the case when the sample is not illuminated (Fig. 10). To evaluate the multitude of these pulses, series of the counting cycles were made, each lasting 20 s. The numbers of these pulses were from 0 to 17, the average was 4.9 pulses per 20 seconds, or 0.25 s^{-1}. In case of H_2Pc, the average numbers of the pulses of four experiments were 4.4 s^{-1} and 24.4 s^{-1}, when H_2Pc sample was illuminated with 4.95 eV and 5.15 eV monochromatic light respectively. The photo signal and the dark noise ratio was about 18 and 100 respectively. The pulses registered in the dark are caused by the humidity, the radiation background or other factors not related to the photoemission [61], [74]. However, the most of dark signal is related to humidity – the dark signal was considerably diminished, when measurement chamber was dried with pressured air. Relative humidity of pressured air was around 8-9%. The dark signal pulses can hinder the investigation of the photoemission spectrums near the threshold, where the numbers of pulses are relatively small. One of the ways to reduce false pulses is to filter and smooth them. When the numbers were considerably higher than the average of the near interval of the spectrum, such numbers were replaced by the average of the two adjacent counts. The smoothing by the 3 to 5 points methods made the results less scattered.

2.3.2 Data processing

After the photoemission spectrums were scanned for 2 to 4 times, the considerably higher numbers than the average of the near interval of the spectrum were replaced. The results for all scans were averaged, smoothed by the 3 or 5 points methods, divided by the normalized intensity of monochromatic light reaching the sample; thus, the corrected pulse numbers $N*$ were calculated for the case of equal energy spectrum and the result was considered as the photoemission yield Y. The yield was normalized by dividing its values by the highest value in the spectrum. The spectrums of the derivative Der of Y on the quanta energy $h\nu$ and the square root of derivative were calculated.

In order to retain the negative values of derivative in the square root of the derivative graphs, the following quantity was calculated:

$$(Der)^{0.5*} = (|Der|)^{0.5} \cdot |Der|/(Der), \qquad (2.10)$$

where (Der) is $(dN*/d(h\nu))$. In the cases of positive derivative, the $(Der)^{0.5*}$ coinciding with the usual square root, but at the negative (Der) the $(Der)^{0.5*}$ value is also negative.

2.4 Results

In Fig. 11. I_p of H_2Pc powder was estimated using $(dY/d(h\nu))^{1/2}$ dependence. There is linear part up to the quanta energy of $x_1 = 4.95$ eV (I_{p1}). There is second linear region between $x_1 = 4.95$ eV and $x_2 = 5.15$ eV (I_{p2}) and the third linear region follows above 5.15 eV.
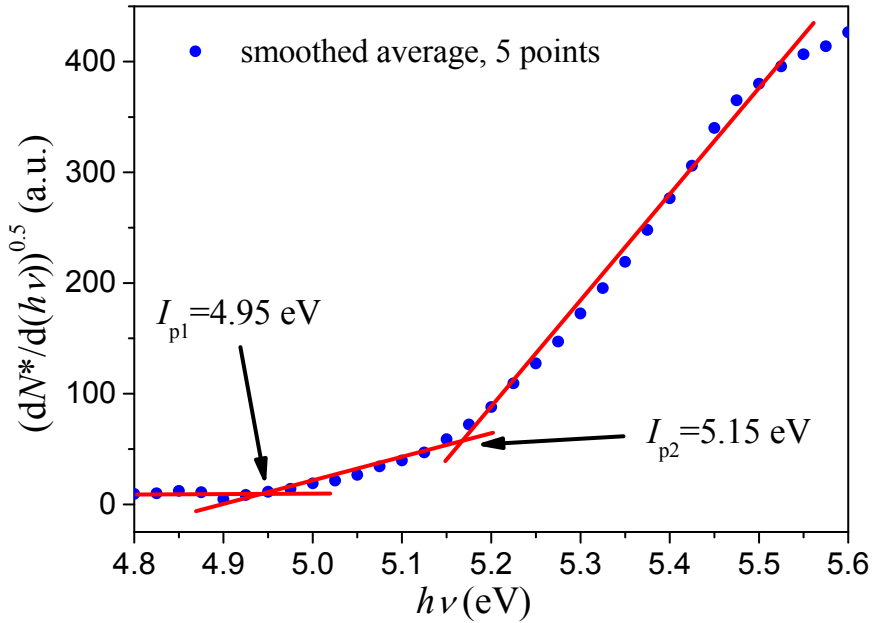
Fig. 11. Smoothed photoemission spectrum of H_2Pc.

In Fig. 12 the same data is plotted using $Y^{1/n}$ dependence and logarithm scale. Normalized photoemission spectrum of the metal-free phthalocyanine powder is presented. There are the regions, which may be approximated as straight lines; the crossing points of these lines may be considered as I_p values. If the power law function is used, then estimated values vary from 5.45 eV at $n = 1$ to 5.16 eV at $n = 4$. In Fig. 12 the case of $n = 1$ is also plotted in logarithm scale and the break point may be found on this plot at 5.06 eV. I_{p2} value of 5.15 eV found using $(dY/d(h\nu))^{1/2}$ plot is close to the values found using the $n = 3$ (5.17 eV) and $n = 4$ (5.16 eV) in power law plots (Fig. 12), but it only reveals one threshold of the spectrum and the value of

$I_{p1} = 4.95$ eV is lost. The square root of the derivative plot is preferable, because it reveals the peculiarities of the spectrum clearer and more break points are present on these plots.
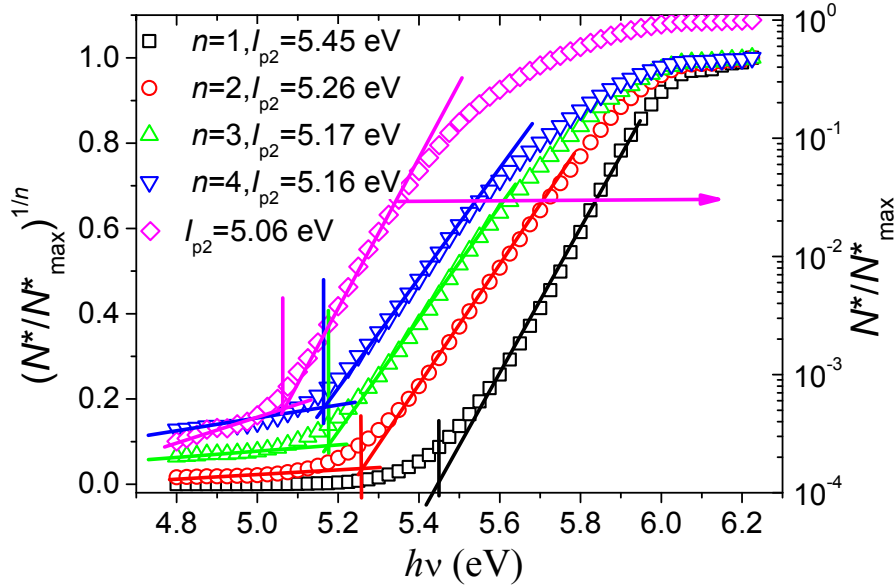

Fig. 12. Normalized photoemission spectrum of the H_2Pc in various presentations.

The results of investigated materials in this section are summarized in Table 4 and the graphs for other materials are shown in APPENDIX I. In all cases the breaking points shift to lower energies at increasing n. Usually I_p values estimated on the plots at $n = 3$ or 4 are close to the values found on the square root of derivative plot. The $n = 1$ plots in logarithm scale gives the lowest I_p value.

Table 4. Results of the I_p measurements in electronvolts (eV).

Material	I_p (eV±0.05eV), when				Log	$(Der)^{0.5}$	
	$n = 1$	$n = 2$	$n = 3$	$n = 4$	scale	I_{p1}	I_{p2}
TiOPc	5.61	5.47	5.40	5.36	5.3	5.25	5.41
H_2Pc	5.45	5.26	5.17	5.16	5.06	4.95	5.15
TPD	5.57	5.46	5.39	5.35	5.28	5.16	5.34
P3HT	4.83	4.72	4.67	4.65	4.61	4.40	4.66

The Table 5 shows the comparison of the results of performed experiments to those reported in literature. As seen on Table 4, estimated I_p values on

$(\mathrm{d}Y/\mathrm{d}(h\nu))^{1/2}$ plots correlate with the values estimated on $Y^{1/n}$ plots, when n is 3 or 4. The difference in I_p values can be caused by such factors: fabrication techniques, crystalline modification or amorphous state of the sample, apparatus error range or environment of the sample production and measurement (in atmosphere, in inert gases environment or in vacuum). In this experiment, if it is not mentioned otherwise, all samples were measured right after fabrication. In some published cases, it is not clear, how actually the final value of I_p was estimated or $n = 3$ was chosen by default. The errors of UPS measurements are up to 0.1 eV, in the case of H_2Pc [29]. The error of new system is around 0.05 eV. Additionally, some thermally evaporated Au samples were prepared and measured right after deposition and later – after one week and after two weeks. Estimated I_p values were 4.60 eV, 4.92 eV and 4.88 eV respectively. Au I_p value found using UPS is 5.10 eV [75]. When Au samples are measured in the air, estimated I_p value tends to decrease to 4.78 eV [76].

Table 5. Ionization potential values in electronvolts found in different literature sources.

Material	PES/PYS	UPS	CV	Kelvin probe	I_p1 /I_p2 (±0.05eV)
TiOPc	5.24* [61], [77]	5.2 [32]–[34]			5.25/5.41
H$_2$Pc	5.1* [78]	4.95-5.1 [29],[32],[70]		5.1 [80]	4.95/5.15
TPD	5.34** [43]	5.1-5.2 [29]–[31]	5.55 [41]		5.16/5.34
P3HT	4.54** [36], 4.75* [45]	4.6-4.85 [36], [37], [81], [82]	5.2 [83]		4.40/4.66
Au	4.78* [76]	5.10[75]			4.60***, 4.92****

*in air; **in vacuum; ***after deposition; ****1 week after deposition;

2.5 Meaning of I_p1 and I_p2 values

The first weak photoemission band with the start at $h\nu = I_\mathrm{p1}$ may be appear due to various factors, such as the presence of impurities in the investigated sample, crystallization or aggregation of the molecules, adsorbed gases. It also

may be caused by the tail of HOMO Gaussian function and, at least in some cases, represent the real value of the ionization potential. Comparison of attained results with the results of UPS studies helps to identify the meaning of I_{p1} and I_{p2} values. The value of ionization potential or HOMO level of TiOPc found using UPS technique [32]–[34] is 5.2 eV and it corresponds to evaluated $I_{p1} = 5.25$ eV value. Therefore, it can be concluded that, the value of I_{p1} corresponds to the HOMO value. Then the value $I_{p2} = 5.41$ eV may correspond to HOMO - 1. In the case of H$_2$Pc, the UPS value of 4.95 eV [35] matches with the $I_{p1} = 4.95$ eV and $I_{p2} = 5.15$ eV is close to the UPS value of 5.1 eV [79]. The ionization energy of 4.96 eV for H$_2$Pc found in [38] using the VB-UPS technique coincides with estimated value of $I_{p1} = 4.95$ eV. However, there is no indication of the presence of the second break point, found by us at 5.15 eV. The UPS measurements for TPD give the values of 5.1 - 5.2 eV, which are similar to the value $I_{p1} = 5.16$ eV, thus, the value represents the HOMO level. Then, the second value - $I_{p2} = 5.34$ eV, may be regarded as HOMO - 1. In the case of P3HT, the UPS value for HOMO is 4.6 - 4.85 eV, which is similar to $I_{p2} = 4.66$ eV value. If to regard this value as HOMO, then the photoemission band with the start at $I_{p1} = 4.40$ eV was absent or too weak to be detected in the UPS experiments. The absence of I_{p1} may be caused by different experiment conditions: high vacuum in UPS experiment and the gas mixture. Other factors to consider how the samples tend to change their surface properties in air environment, how initial materials where stored (in presented experiment, all materials except P3HT, where kept in air) or when sample was measured. As mentioned previously, I_p value from Au sample decrease up to 0.30 eV in one week. It is known, that Au samples are sensitive in terms of contamination [56]. In the case of TPD and H$_2$Pc and TiOPc, I_p values changed only within the error range after the samples were kept in air for one weak.

Fig. 13 shows unsmoothed spectra of HTM2 material (of two different samples). $(\mathrm{d}Y/\mathrm{d}(hv))^{1/2}$ dependence is depicted in black squares and circles. Spectrum without smoothing is "noisy", contrary to $Y^{1/n}$ dependence (red squares and circles). In   Fig. 14 the same spectrum of HTM2 is shown, but the data was smoothed by 5-point method. After the smoothing, $(\mathrm{d}Y/\mathrm{d}(hv))^{1/2}$ dependency shows some repeatable inclinations in spectra, while $Y^{1/n}$ dependence "polish" the spectra even without smoothing. If the range from 5 eV to 6 eV were used to estimate I_p, the results of both presentations would be very similar – ~$I_p = 5$ eV. However, if spectra are analyzed more precisely, I_p should be estimated from the range ~ 5-5.4 eV and the value of I_p would be different - 4.93 eV, in the case of $(\mathrm{d}Y/\mathrm{d}(hv))^{1/2}$ presentation. Ability to study

"unpolished" spectra is one of the most important merit of $(dY/d(h\nu))^{1/2}$ dependence.
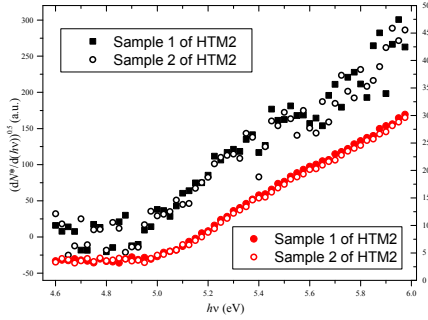

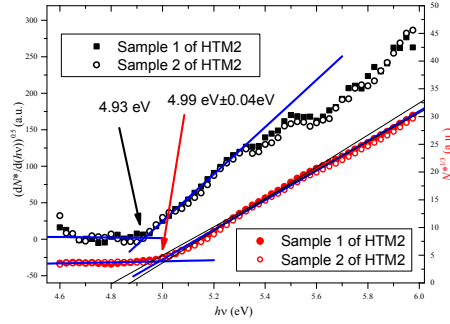Fig. 13. Unsmoothed spectra of HTM2 material.

Fig. 14. Smoothed spectra of HTM2 material.

It is difficult to approximate weak photoemission linearly on $Y^{1/n}$ plot and to choose the right n value, thus $(dY/d(h\nu))^{1/2}$ plot is advantageous and allows to analyze photoemission spectrum in more detail.

2.6 Summary

The apparatus to measure I_p of semiconductor materials and metals in a gas mixture at atmospheric pressure by using the PYSA technique was demonstrated. The apparatus is able to detect electron photoemission signals down to a single electron per second (10^{-19} A). The high sensitivity detector enabled to detect accurately weak electron emission out of the samples at photoemission spectrum threshold. The high sensitivity detector and the new method of data interpretation allowed to estimate I_p values more precisely in comparison to the PYS results, that were found in the literature. The new way of estimating I_p values is to calculate the square root of the derivative of the yield dependence on the light quanta energy $(dY/d(h\nu))^{1/2}$. This dependence is supported by the mathematical consideration and provides more precise estimation of I_p in comparison to the results plotted as $Y^{1/n}$ dependence on the quanta energy hν. The graphical presentation of this function is more informative than the other used presentations, and clearly shows multiply thresholds in photoemission spectrum. The experiments were carried out and I_p values measured for four well-known materials (TPD, TiOPc, H_2Pc, P3HT) and Au.

3 Determination of µ for organic materials

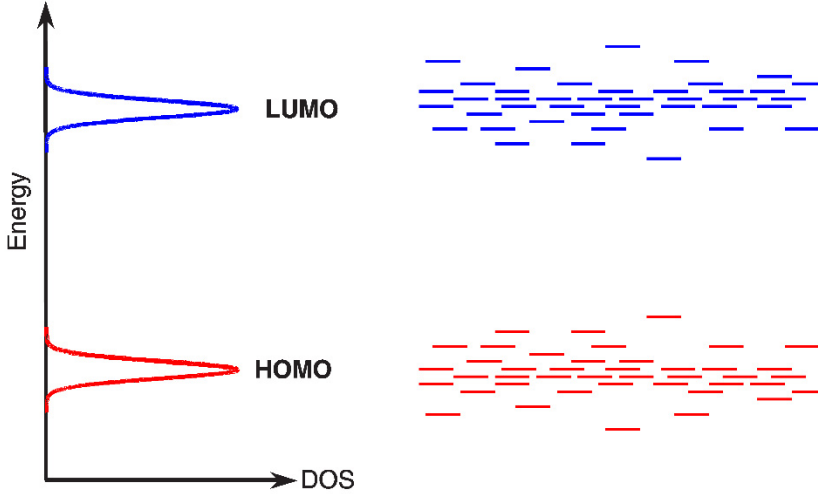## 3.1 Field and temperature dependent *µ*

Fig. 15. Distribution of HOMO and LUMO levels in amorphous organic semiconductors. Adapted from [84].

In fig. 16 (a) simplified illustration of DOS, HOMO and LUMO energy levels is shown. If no electric field is applied, a carrier located at mean carrier energy of DOS ($\langle \varepsilon_\infty \rangle$) moves only after thermal excitation. If all carriers would be located at $\langle \varepsilon_\infty \rangle$ and a transport level would exist at the center of DOS ($\varepsilon = 0$), the temperature dependence of the mobility should follow a non-Arrhenius dependence of the form $\exp\left[-(\sigma/kT)^2\right]$,where σ is Gaussian width of DOS [85]. This function is derived using Monte Carlo simulations. The predicted temperature dependence of the zero-field mobility is

$$\mu = \mu_0 \exp\left[-\left(\frac{2\sigma}{3kT}\right)^2\right],\qquad(3.1)$$

where μ_0 is drift mobility without electric field (*E*=0).

When the DOS is affected by an electrostatic potential, then the average barrier height is reduced for energetic jumps to higher energy states in the field direction. This leads to the change of charge carrier mobility and equilibrium energy $\langle \varepsilon_\infty \rangle$ depending as:

$$\langle \varepsilon_\infty \rangle = (\sigma/kT)\sigma + (E/E_0)^{3/2} ,\qquad(3.2)$$

41

where $E_0 = 1.8 \times 10^6$ V/cm and it is independent of σ/kT, assuming $\Sigma = 0$. Fig. 17(a) shows the field dependencies of the charge carrier mobility for different values of σ/kT. At low electric field charge carrier mobility is less field dependent and increases according to a Poole-Frenkel relation at high fields:

$$\mu = \mu_0 e^{\alpha\sqrt{E}}, \tag{3.3}$$

where α – coefficient of μ dependence on electric field and electric field strength (E).

In the case of $\sigma/kT = 0$, the mobility decreases in high fields, due to the saturation of the drift velocity. Where only positional disorder has effect (Fig. 17(b)), charge carrier mobility decreases over entire range of the fields. Fig. 17(c) shows mobility dependence in field, where both – energetic and positional disorder affects. Negative field dependence on the mobility in case of low fields could be explained as: this way a direct path for a charge carrier to move is impeded due to either poor overlap or large distance, than a charge carrier might take a detour that is faster because of improved coupling. A jump against the field is probable, when the field is low.

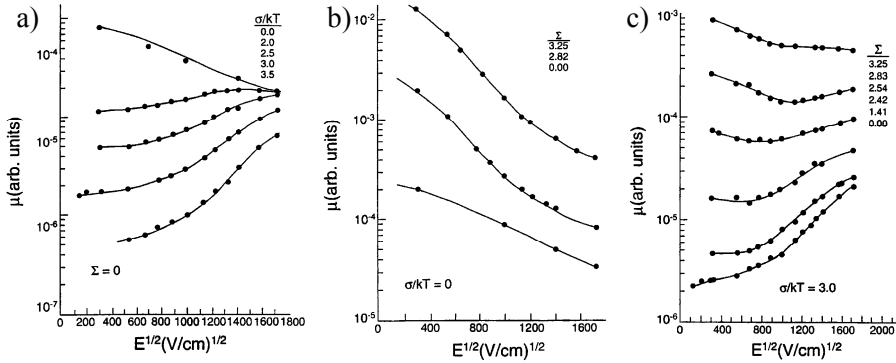Fig. 17. a - The field dependencies of the mobility for different values of σ/kT. b - The field dependencies of the mobility for different values of Σ. c - The field dependencies of the mobility, when both energetic and positional disorder are present. Figures are taken from [85].

Bässler formalism for disordered materials relates the mobility to σ/kT and Σ as [85]–[87]:

$$\mu(\sigma, \Sigma) = \mu_0 \exp\left[-\left(\frac{2\sigma}{3kT}\right)^2\right] \exp\left\{B\left[\left(\frac{2\sigma}{3kT}\right)^2 - \Sigma^2\right]E^{\frac{1}{2}}\right\}, \qquad (3.4)$$
$$\Sigma \geq 1.5$$

and

$$\mu(\sigma, \Sigma) = \mu_0 \exp\left[-\left(\frac{2\sigma}{3kT}\right)^2\right] \exp\left\{B\left[\left(\frac{2\sigma}{3kT}\right)^2 - 2.25\right]E^{\frac{1}{2}}\right\}, \qquad (3.5)$$
$$\Sigma \leq 1.5$$

where B is an empirical constant of 2.9×10^{-4} (cm/V)$^{1/2}$, Σ is parameter, that describes the degree of off-diagonal disorder. logμ versus $E^{1/2}$ is linear with slopes, that decrease with increasing temperature.

3.2 Xerographic time of flight (XTOF)

μ in organic semiconductors is low in comparison to inorganic semiconductors. Classic methods as Hall effect and magnetoresistance are not sufficient to estimate slow charge carriers. Other techniques, such as TOF of charge carries through the sample after they were generated by short light pulse, CELIV or other similar techniques are sufficient to estimate μ in organic materials. However, these techniques require two conductive contacts – usually, at least one metal contact, formed by a thermal evaporation. During a thermal evaporation, there is a chance to change a structure or to ignite crystallization of organic semiconductor beneath a metal contact or even to create a short circuit between the contacts. XTOF overcomes these issues – it allows to measure bulk layer with only one electrode and it is straightforward technique for charge carrier mobility evaluation in high resistivity semiconductors [88]. Another advantage to apply of XTOF is, that a sample can be prepared from solution by simple drop-casting method.

The principal of the technique: the floating surface of the sample resting on an earthed electrode is charged in the dark by a corona charging device. A short pulse of strongly absorbed light is used to generate a thin sheet of electron-hole pairs near the surface of the sample. The wavelength of the light is chosen this way, that the absorption depth $\delta(\lambda) << d$, where d is the thickness of the sample. For a positive applied field the free holes are pulled towards the conductive substrate, while the electrons neutralize some of the positive charges, or vice-versa [88], [89]. Fig.18 shows schematic illustration of the principle for the XTOF technique.
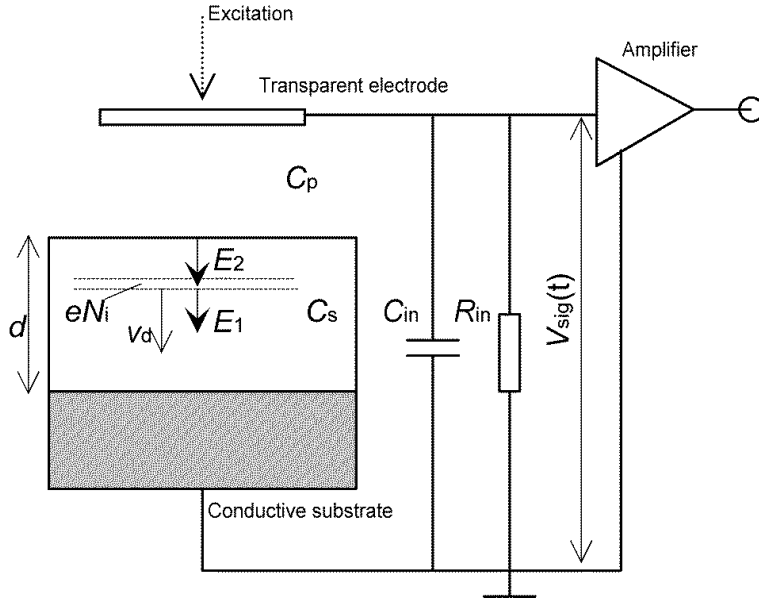
Fig.18 Schematic illustration of XTOF technique for the drift mobility estimation. Here, V_d – velocity of charge carriers, eN_i – generated charge, C_s – capacitance of a sample, C_p – capacitance of probe, C_{in} – input capacitance, R_{in} – input resistance, V_{sig} – voltage of registered signal, E_1 and E_2 – strength of electric field in front and behind charge carries package eN_i.

It is necessary condition that the number of generated/injected carrier N_i is much smaller than that of the surface charges - the drifting sheet of charges has negligible effect on the applied field, i.e. $E_1 \approx E_2$ and the internal field can be expressed as $E_0 = U_0/d$, where U_0 is the sample voltage. This condition is known as small signal operation and is a widely assumed case in theoretical work on transient photocurrent analysis. The injected charge sheet or cloud moves under the action of the applied field E_0 with a constant drift velocity $V_d = \mu_d E_0$, where μ_d is the drift mobility. The time taken for charge sheet to reach the substrate, where it is neutralized, is called the transit time t_{tr},

$$t_{tr} = \frac{d^2}{\mu_d\, U_0}. \tag{3.6}$$

In Fig. 19 typical waveforms of transient current and voltage are shown. Depending on presence of trapping, the charge carrier mobility can be calculated using experimental t_{tr} value and formula (3.6).
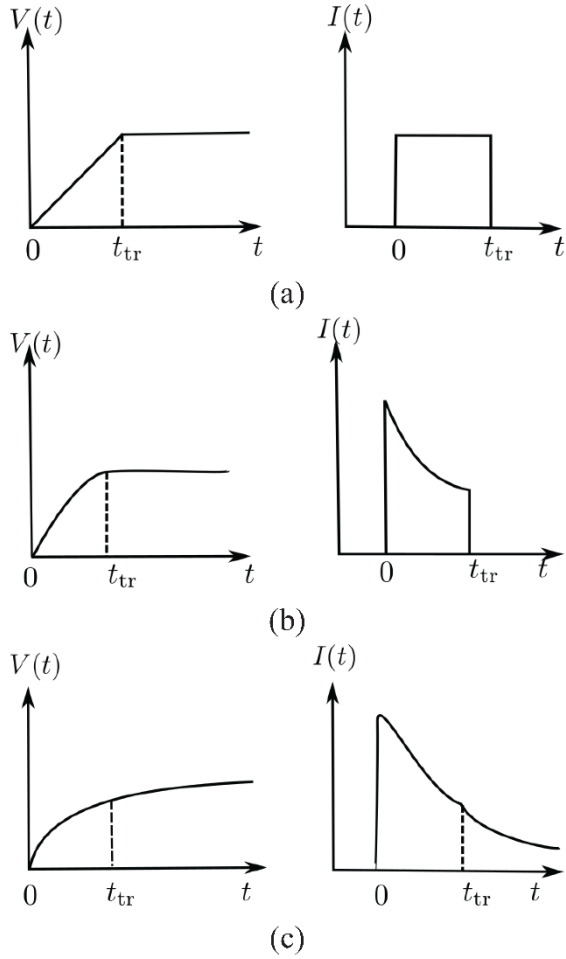
Fig. 19 Transient current and voltage waveforms showing effect of trapping and detrapping. (a) No trapping. (b) Trapping no detrapping. (c) Trapping and detrapping. Adapted from [90].

In the current-mode case, the transient current pulse produced by the drifting carriers is measured. The detected current is proportional to eN_i/d for $0 < t < t_{tr}$ and is zero for $t > t_{tr}$, as shown on Fig. 19. In the current-mode the measured potential difference will be longer than system's time constant $\tau = R_{in}(C_p + C_{in})$ and measured signal will be

$$U_{sig}(t) = R_{in}C_p \cdot \frac{dU(t)}{dt}. \qquad (3.7)$$

45

In the case of the voltage-mode, the potential $U(t)$ is developing across R and proportional to $eN_i vt/Cd$ during $0 < t < t_{tr}$, where $v = d/t_{tr}$ denotes the drift velocity. For $t > t_{tr}$, U remains constant and is proportional to eN_i/C_s as long as $t \ll CR$, as shown on Fig. 19. In this case, the signal will be

$$U_{sig}(t) = -\frac{C_p}{C_p + C_{in}} \cdot \Delta U(t). \tag{3.8}$$

If there are no trapping states and a short pulse of strongly absorbed light was applied, the potential could be determined as:

$$U(t) = U_0 - \frac{e\mu N_i U_0 t}{\varepsilon \varepsilon_0 d}, \text{ for } 0 < t < t_{tr}. \tag{3.9}$$

Thus, in the voltage-mode the registered signal is expressed as

$$U_{sig}(t) = \frac{C_p}{C_p + C_{in}} \cdot \frac{e\mu N_i U_0 t}{\varepsilon \varepsilon_0 d}, \text{ for } 0 < t < t_{tr}, \tag{3.10}$$

and in the current-mode the registered signal is expressed as

$$U_{sig}(t) = -R_{in} C_p \cdot \frac{e\mu N_i U_0}{\varepsilon \varepsilon_0 d}, \text{ for } 0 < t < t_{tr.} \tag{3.11}$$

While $t > t_{tr}$, $U_{sig} = 0$, as shown in Fig. 19(a).

The transport of charge carriers of most organic materials is dispersive. Thus, in most of the cases, in order to distinguish the slopes' changes, the *log-log* plot is used. In practice, the current-mode measurement is adopted, because the interpretation of results is relatively simple. On the other hand, the voltage-mode allows to detect slow charge carriers, because it is not limited by R_{in} (C_p+C_{in}) and allows to evaluate charge carries mobility, when weak signal is observed. To sum up, XTOF is simple and valuable technique to determine charge carries mobility, if these conditions are met:

- Absorption depth $\delta(\lambda) \ll d$
- Duration of excitation $t_{ex} \ll t_{tr}$
- Dielectric relaxation time $\rho \varepsilon_0 \varepsilon \gg t_{tr}$
- Charge carries life-time $\tau > t_{tr}$
- Small signal operation condition $eN_i \ll C_s U_0$, where C_s is sample's capacitance.

3.3 Results

Investigated materials HTM1 – HTM5 were described in section 2.1. The samples for the charge carrier's mobility measurements were prepared by drop casting method. The HTM was dissolved in THF. The solution of HTM formed layer on polyester film with conductive Al layer. Additionally, the samples were prepared by mixing HTM and polycarbonate (PC-Z) (Mitsubishi Gas Chemical Co., polycarbonate Iupilon Z-200) in 1:1 mass proportion in THF. It is taken into account, that quality of the prepared films can have significant impact on the results of mobility measurements [91]: every molecule has different film forming properties, therefore, in order to mitigate film quality influence on mobility results, additional XTOF measurements were performed with HTMs dispersed in PC-Z matrix, which minimizes HTM molecule dependent film quality variations. Absolute mobility values are lower in comparison to pure HTM due to the presence of large portion of nonconductive polymer, however, structure/properties relation are expressed better in this case.

The layer thickness ranged from of 2 μm to 6 μm. The drift mobility was measured using XTOF. Electric field was created by positive corona charging. The charge carriers were generated at the layer surface by illumination with pulses of nitrogen laser (pulse duration was 2 ns, wavelength 337 nm). The layer surface potential decrease as a result of pulse illumination was up to 1-5 % of initial potential before illumination. The capacitance probe, that was connected to the wide frequency band electrometer, measured the speed of the surface potential decrease dU/dt. The transit time t_{tr} was determined by the kink on the curve of the dU/dt transient in double logarithmic scale. The drift mobility was calculated using the equation (3.6).

Charge carriers drift kinetics in integral mode showed, that in all investigated organic materials the dominant charge carries were holes (including the samples with PC-Z), as it is shown in Fig. 20 (*a* and *b*), Fig. 21 (*a* and *b*) and in APPENDIX II. μ of these materials can be approximated by Pool-Frenkel relation (3.3).

Fig. 20(*c* and *d*) shows dU/dt hole-transients for the thin film of pure HTM2 and mix of HTM2+PC-Z. The curves exhibit a dispersive hole-transport, which, along with the strong electric-field mobility dependence, suggests the trap-dominant charge transport in HTM2 or HTM2+PC-Z layers. t_{tr} was estimated from the intersection points of two asymptotes of double-logarithmic plots and used to calculate hole-drift mobility at respective applied fields. The same dependencies for HTM3, HTM4, and HTM5 are

shown in APPENDIX II. Fig. 20 (*e*) shows field dependent μ values with and without PC-Z.

Fig. 20. a- Charge carriers drift kinetics in integral mode of HTM2 and b – in mixture in PC-Z. c- dU/dt hole-transients of HTM2. d- dU/dt hole-transients of HTM2 in mixture in PC-Z. e- field dependent μ values with and without PC-Z of HTM2.

The hole transport of HTM1 follows Gaussian distribution and transit time can be defined in linear plot of transients (Fig. 21 (*c*)). Fig. 21 (*e*) shows field dependent *μ* values with and without PC-Z.
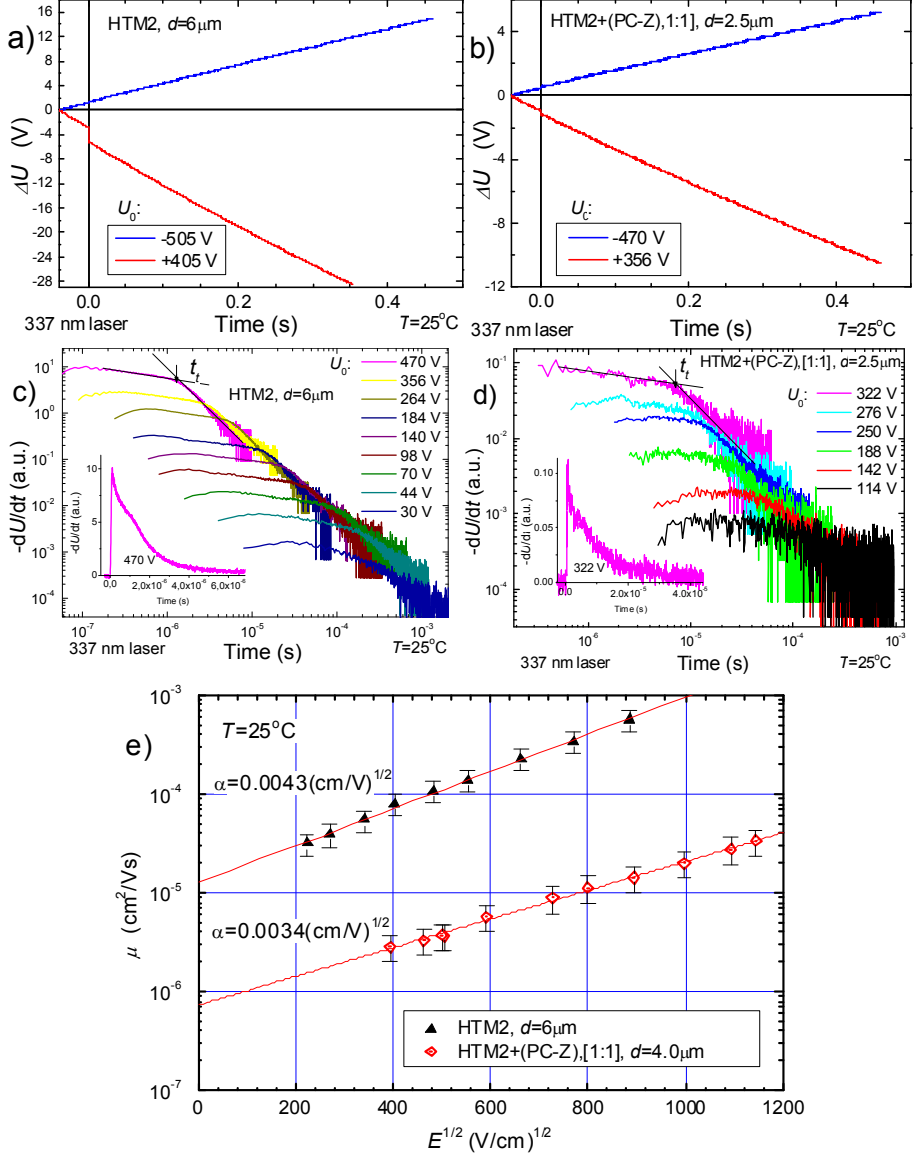

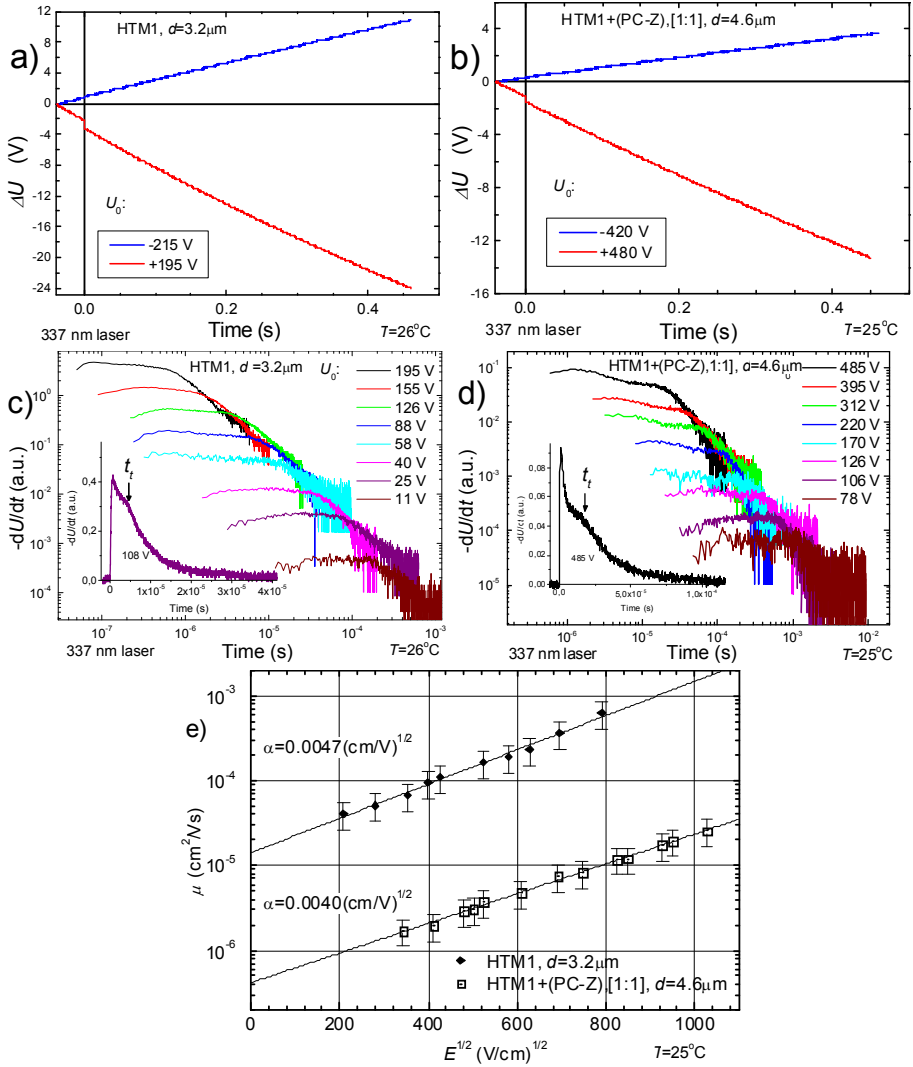
Fig. 21. a- Charge carriers drift kinetics in integral mode of HTM1 and b – in mixture in PC-Z. c- d*U*/d*t* hole-transients of HTM1. d- d*U*/d*t* hole-transients of HTM1 in mixture in PC-Z. e- field dependent *μ* values with and without PC-Z of HTM1.

As seen from the summarized results in Fig. 22 and Table 6, synthesized HTMs demonstrates competitive charge mobility. XTOF measurements of the

films prepared from HTM1, HTM2, HTM4, HTM5 indicate, that the hole-drift mobility is ~10^{-5} cm^2 V^{-1}s^{-1} at weak electric fields and ~3×10^{-4} cm^2 V^{-1}s^{-1} at field strength of 6.4×10^5 Vcm^{-1}. In Fig. 22 (b) XTOF measurements of HTM1-HTM5 in mixture in PC-Z (1:1)is shown and demonstrates around one magnitude lower values of μ at a field strength of 10^6 Vcm^{-1}. The hole mobility of these HTMs is comparable to that of Spiro-OMeTAD, while HTM3 demonstrates lower results of several orders of magnitude. Most likely, methyl group in the meta position of the triphenylamine fragment causes it to be more twisted out of the plain, which prevents tight packing of the molecules and makes it more difficult for the charge to hop between the sites. Methyl group in the meta position of the triphenylamine fragment in HTM3 causes significant negative changes in the molecule's conformation, which translates into lowest charge mobility. While mobility in HTM4, HTM5, with alkyl groups at para positions of the triphenylamine moiety, is up to two orders of magnitude higher μ due to better optimized structure.
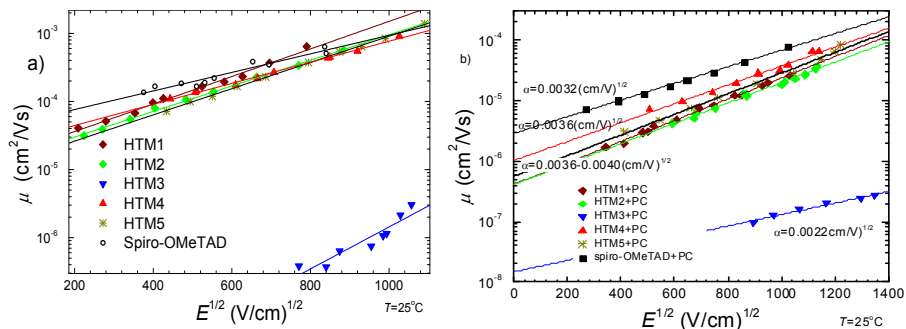

Fig. 22. Field dependent μ values of pure HTMs(*a*) and HTMs in mixture in PC-Z (*b*) of all HTM1 − 5, including Spiro-OMeTAD.

Table 6. I_p values for pure HTMs, μ_0 and μ for pure HTMs and in mixture with PC-Z (1:1).

Compound	I_p, (eV)	μ_0, (cm^2 V^{-1} s^{-1})	μ, (cm^2 V^{-1} s^{-1})
HTM1	5.05	1.4×10^{-5}	5.9×10^{-4}
HTM2	5.00	1.3×10^{-5}	3.8×10^{-4}
HTM3	5.00	1×10^{-9}	3×10^{-7}
HTM4	4.92	2.2×10^{-5}	3.8×10^{-4}
HTM5	5.03	1.1×10^{-5}	3.8×10^{-4}
Spiro-OMeTAD	5.00	4.1×10^{-5}	5×10^{-4}
HTM1 + PC	-	3.9×10^{-7}	2.3×10^{-5}
HTM2 + PC	-	4.0×10^{-7}	1.9×10^{-5}
HTM3 + PC	-	1.5×10^{-8}	1.3×10^{-7}
HTM4 + PC	-	1.1×10^{-6}	3.7×10^{-5}
HTM5 + PC	-	5.8×10^{-7}	2.8×10^{-5}
Spiro-OMeTAD+PC	-	2.9×10^{-6}	6.8×10^{-5}

In addition, prof. Sanghyun Paek and prof. Michael Saliba fabricated and analyzed perovskite SCs in order to investigate the relationship between the chemical structure of the HTMs and the photovoltaic performance. Structure of perovskites SC consisted of doped tin oxide (FTO)/compact TiO$_2$/ mesoporous TiO$_2$/ perovskite/ HTM/Au. Mixed perovskite precursor was prepared by mixing 1.15 m PbI$_2$, 1.10 m FAI, 0.2 m PbBr$_2$, 0.2 m MABr in a mixed solvent of DMF:DMSO (4:1 volume ratio) [63]. PCEs were in the range of 9% to 16.8% and measured utilizing these HTMs, highlighting the importance of the optimal chemical structure, since inappropriately placed methyl group could compromise device performance [63].
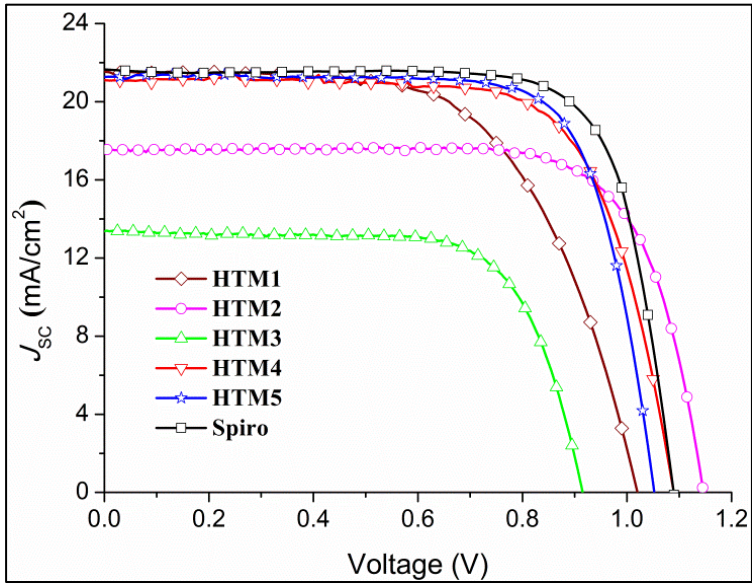
Fig. 23. VACh of the SCs with HTM1 - 5 and Spiro-OMeTAD, recorded under AM 1.5 conditions (100 mW/cm^2) [63].

Main parameters of SCs are presented in Table 7.

Table 7. J_{sc}, V_{oc}, fill factor (FF*)* and PCE of the best performing Spiro-OMeTAD, HTM1–HTM5 devices on perovskite.

Materials	J_{SC}, mA/cm²	V_{OC}, mV	FF(%)	PCE (%)
HTM1	19.075	1005	75.7	14.52
HTM2	17.526	1146	74.2	15.09
HTM3	13.371	915	70.7	9.15
HTM4	21.269	1052	75.0	16.79
HTM5	21.136	1029	75.7	16.45
Spiro-OMeTad	21.607	1092	75.3	17.88

Mobility measurements have correlation with SC performance. E.g., HTM3 demonstrated lowest mobility and lowest SC efficiency. SC with HTM3 showed ~5% lower value of *FF* to other HTMs. V_{OC} was lower by 10-15%, it might be caused by carriers trapping as XTOF measurements indicated dispersive charge transport, which can lead to internal electric field redistribution. J_{sc} was significantly lower, which limited overall performance of the devices. One of the factors of low J_{sc} could be the low mobility of HTM3. Low mobility indicates increased probability of recombination of generated charge carriers.

3.4 Summary

A new group of small-molecule HTM1-HTM5, based on methoxydiphenylamine-substituted fluorene and triphenylamine fragments was characterized using XTOF and PYSA. μ of HTM1, HTM2, HTM4, HTM5 ranged from 3.8×10^{-4} to 5.9×10^{-4} cm^2 V^{-1} s^{-1}. These values are similar to for Spiro-OMeTAD – 5.0×10^{-4} cm^2 V^{-1} s^{-1}. However, the synthesis of HTM1, HTM2, HTM4, HTM5 is easier in comparison to Spiro-OMeTAD [63] - synthesis of Spiro-OMeTAD requires 5 steps procedure [92], thus the synthesis of HTM1-5 requires only two. Aliphatic substituents in meta position of the triphenylamine fragment cause it to be more twisted out of the plain and severely reduce μ of the HTM3 to 3.0×10^{-7} cm^2 V^{-1} s^{-1} and overall device characteristics of the perovskite solar cells, while substitution at para position of the triphenylamine moiety has positive effect on the performance of the hole transporting materials. The overall efficiency of the investigated HTMs in perovskite SCs varies from 9% up to 16.8%.
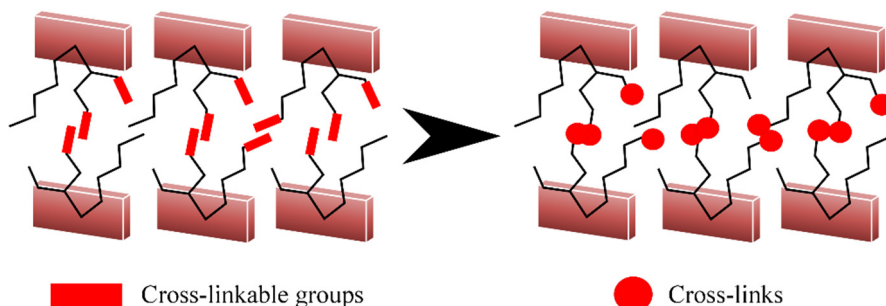
4 Cross-linkable HTMs

Fig. 24. Conjugated soluble polymer with cross-linkable side groups (on left side) and cross-linked insoluble conjugated polymer network (on the right side).

Fig. 24 shows basic cross-linking principle of conjugated polymers. Cross-linking "freezes" the initial morphology. Initial conjugated polymer is soluble and solution processable (Fig. 24(a)). The new covalent bonds are created and the polymer chains are formed after cross-linking (Fig. 24(b)). Polymerization results cross-linked conjugated polymer network, "frozen" morphology and insolubility. Fig. 25 shows structural formulas of linear polymer polystyrene formation from styrene.
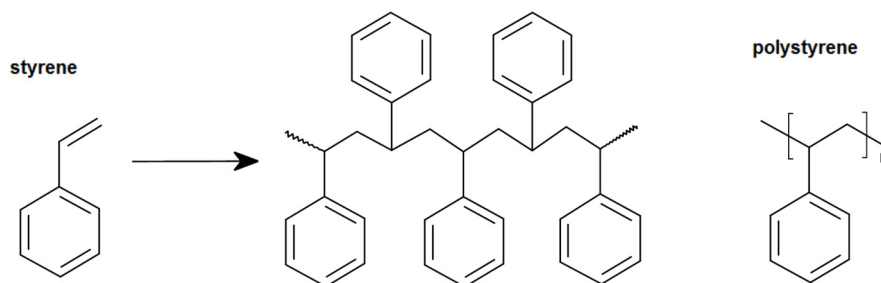

Fig. 25. Structural formulas of linear polymer polystyrene formation from styrene.

There are 3 main processes to initiate cross-linking process: initiator or photo initiator, exposure to ultraviolet light and thermal heating. Each method has it's applicability [93].

The main advantages of using cross-linkable polymers for organic or inorganic SCs are: a) stabilization of morphology [94], b) insolubility – no need for orthogonal solvent and it opens possibility of inverted organic SCs [27], c – increased water, oxygen, heat resistance and rigidity [95].

In a search of cheap and new SCs, cross-linking by thermal heating stands out of all other cross-linking methods. It is straightforward method without any additives or particular setup and allows the production of large scale SCs. However, it has one drawback – the cross-linking temperature often exceeds highest possible annealing temperature for perovskite [96]. The workaround can be done by fabricating perovskite SCs with inverted structure. Two fluorene-based cross-linkable enamines were synthesized at Kaunas Technology University. Structure formulas of these enamines are presented in Fig. 26.
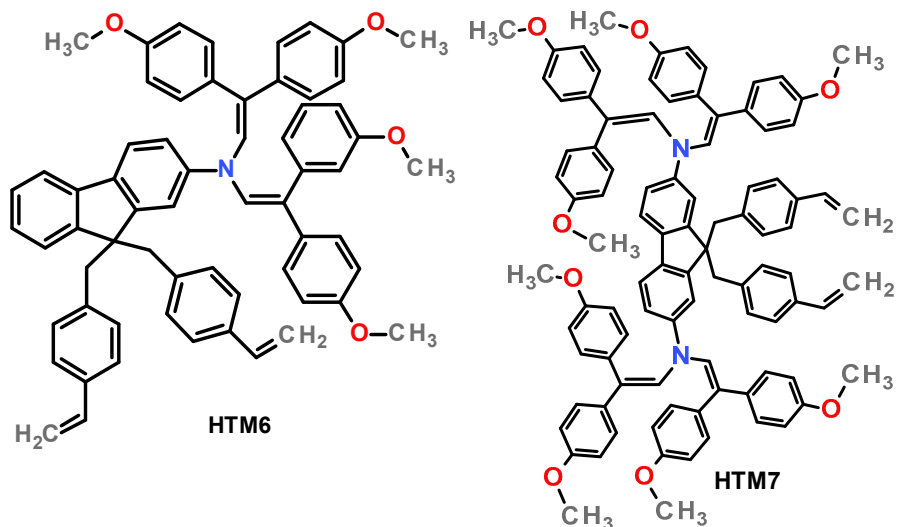
Fig. 26. Molecular structures of the synthesized cross-linkable HTM6 and HTM7.

N,N-bis[2,2-bis(4-methoxyphenyl)vinyl]-9*H*-fluorene-2-amine (HTM6) and N^2,N^2,N^7,N^7-tetrakis[2,2-bis(4-methoxyphenyl)vinyl]-9*H*-fluorene-2,7-diamine (HTM7) materials were investigated using XTOF and PYSA methods. The cross-linking temperatures were chosen according to DSC measurements results (see APPENDIX III).The cross-linking of HTM6 and HTM7 occurs after 45 minutes at 230-240 ºC.
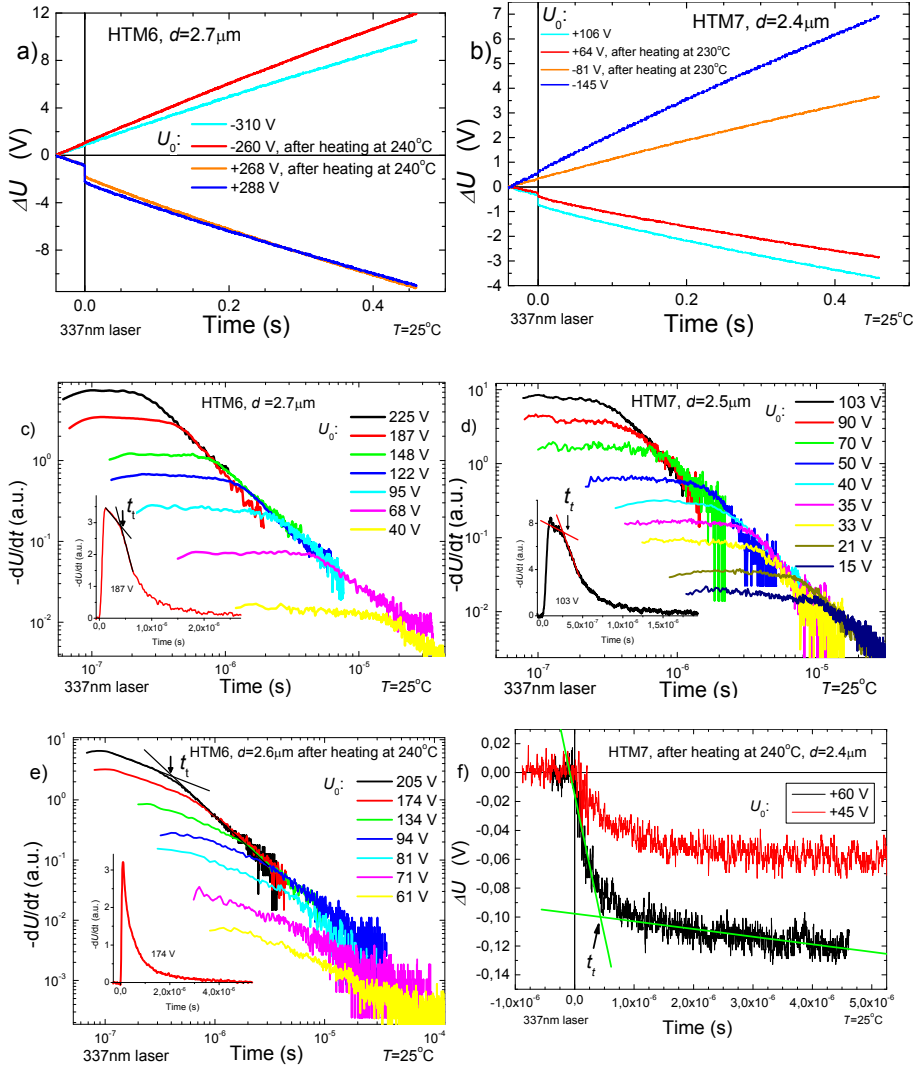
Fig. 27. a- Charge carrier drift kinetics in integral mode of HTM6 before and after heating. b – charge carriers drift kinetics in integral mode of HTM7, before and after heating. c- dU/dt hole-transients of HTM6. d- dU/dt hole-transients of HTM7. e- dU/dt hole-transients of HTM6 after the heating. f- dU/dt hole-transients of HTM7.

In Fig. 27 (*a*) and (*b*) charge carrier drift kinetics in integral mode of HTM6 and HTM7 before and after the heating, are shown. HTM6's charging voltage after the heating remain similar, however, charging voltage of HTM7 reduced after the heating.
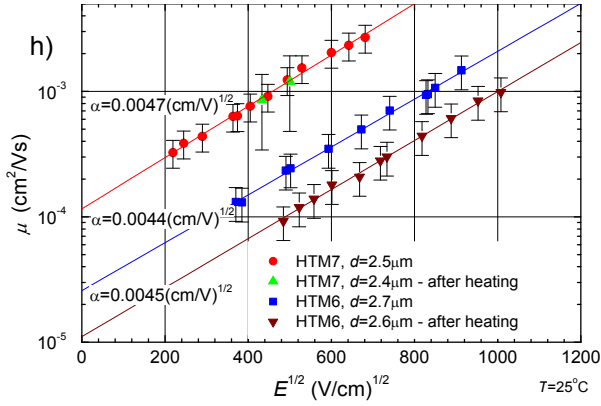
Fig. 28. Field dependent μ values before and after the heating of HTM6 and HTM7.

Fig. 28 shows the summary of the measurements. HTM7 showed good charge-transporting properties, reaching 10^{-3} cm^{2}V^{-1}s^{-1}, at a field strength of 3.6×10^5 Vcm^{-1} before and after heating. HTM6 showed slightly lower hole drift mobility – 3.5×10^{-4} cm^{2}V^{-1}s^{-1} in neat layer and 1.75×10^{-4} cm^{2}V^{-1}s^{-1} in cross-linked layer, at a field strength of 3.6×10^5 Vcm^{-1}, yet still comparable to those of popular HTMs for perovskite SCs.

  PYSA results for HTM6 and HTM7 are shown in Fig. 29. The values of I_p were 5.26 and 5.11 eV for HTM6 and HTM7 before the heating and 5.39 and 5.30 eV after the heating, respectively. Measured values are consistent with the values reported for other HTMs used in perovskite SCs.
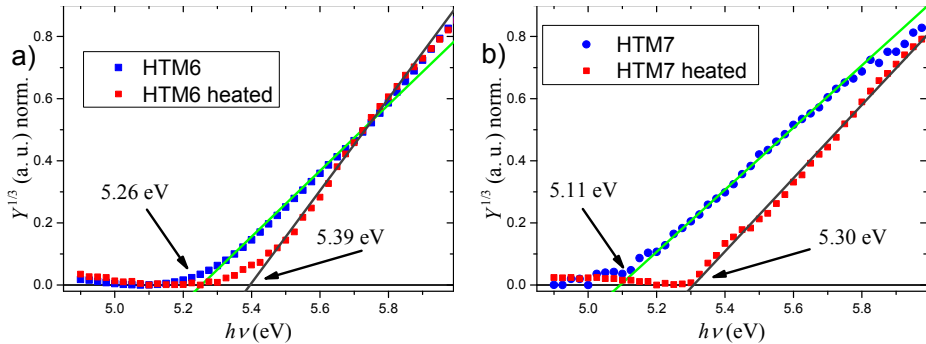

Fig. 29. Photoemission spectra of HTM6 (a) and HTM7 (b) before and after the heating.

  As it was mentioned before, $(\mathrm{d}Y/\mathrm{d}(h\nu))^{1/2}$ dependence has advantages in comparison to $Y^{1/n}$ dependence, however, usually $(\mathrm{d}Y/\mathrm{d}(h\nu))^{1/2}$ dependence

requires data smoothing. The nature of derivative requires as smooth measurement as possible. In case of HTM6 and HTM7, the measurements were relative unstable and $Y^{1/n}$ dependence was chosen for presentation.

The devices with the inverted architecture were fabricated and characterized by dr. Amran Al-Ashouri and prof. Steve Albrecht, in order to evaluate the performance of the materials acting as hole selective layers in perovskite SCs. HTM6 achieved PCE of ~14% before and after cross-linking, while HTM7 recorded PCE was ~15% before the heating and increased up to 16% after the heating. Structure of perovskites SC consisted of ITO/HTM6-7/perovskite/C60/BCP/Ag. Triple cation perovskite was used, with a nominal precursor solution composition of $Cs_{0.05}(FA_{0.83}MA_{0.17})_{0.95}Pb(I_{0.83}Br_{0.17})_3$ [27].
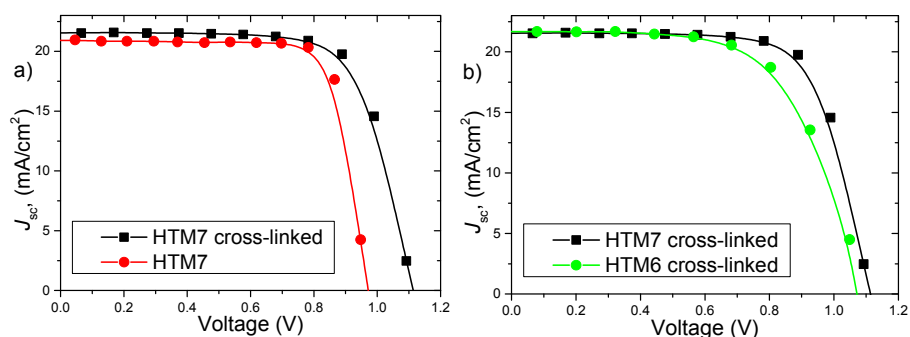

Fig. 30. VACh measurements of the perovskite SCs prepared with HTM6 and HTM7. a) comparison of the devices, prepared with the neat HTM7 vs cross-linked HTM7; b) comparison of the performances of cross-linked HTM6 and HTM7 [27].

Fig. 30 shows VACh measurements of the perovskite SCs prepared with the HTM6 and HTM7. The comparison of the devices, prepared with the neat HTM7 vs cross-linked HTM7 indicates that cross-linking improves the performance of the SC. In general, cross-linking improves overall mechanical and resistance properties of organic layers, as was mention before, and such cross-linkable HTMs should be advantageous over regular or neat HTMs. Fig. 30 (b) shows comparison of the performances of cross-linked HTM6 and HTM7. All results are summarized in [27].

After the cross-linking, the increment of V_{OC} was detected in both HTMs. This might be explained that, as I_p of materials increased or neat layer of HTM was damaged during solution- processing of perovskite and increased interfacial recombination, which reduced V_{OC} [97], [98]. Higher FF and PCE

can be attributed to higher hole drift mobilities – improved transport of the charge carriers through the film [99].

4.1 Summary

New hole transporting materials HTM6 and HTM7 were investigated using XTOF and PYSA methods. Due to the presence of two vinyl groups, materials HTM6 and HTM7 are able to undergo thermal cross-linking during the heating at 230-240 $^{\circ}$C. After 45 minutes the deposited films became resistant toward organic solvents. Polymerization leads to minor changes in hole drift mobility: HTM7 showed good charge-transporting properties, reaching 10^{-3} cm^{2}V^{-1}s^{-1} at strong electrical fields before and after heating. HTM6 showed slightly lower hole drift mobility – 3.5×10^{-4} cm^{2}V^{-1}s^{-1} in neat layer and 1.75×10^{-4} cm^{2}V^{-1}s^{-1} in cross-linked layer, yet still comparable to those of popular HTMs for perovskite SCs. I_p values for HTM6 and HTM7 were 5.26 and 5.11 eV before the heating and 5.39 and 5.30 eV after the heating, respectively. Due to cross-linking, the materials became suitable for application in p–i–n perovskite SCs. As the result, devices with the thermally cross-linked films have shown advantageous performance, mainly due to the higher open-circuit voltage. Perovskite SCs have shown over 18% power conversion efficiency, the HTMs are up to five times cheaper in comparison to Spiro-OMeTAD [27].

5 CZTS SC

Perovskite SCs demonstrate the highest efficiency among third generation solar technologies [100], however, perovskite usually contains toxic elements, such as Sb and , moreover, the longevity of the cells is still the problem. Alternatively, CZTSSe SCs are more environmentally friendly, not containing any toxic chemical elements. However, it is a challenge to fabricate high quality CZTSSe films, especially, for the superstrate configuration using non-vacuum deposition technique. Furthermore, if requirements for a deposition technique were scalability, low price and fabrication under heated substrates – spray coating would be one of the suitable techniques.

Further CZTSSe SCs fabrication using spray coating technique will be presented [101]. One of the goals of this work was to present inorganic SC structure, which would be compatible with materials like HTM1-HTM7, however, well known and commercially available HTMs should be used. Spiro-OMeTAD, as HTM, was chosen in the first stage of the experiment.

Fabrication technique of CZTS active layer was developed using hand automated spray coating system and hand carried spray coating. It has to be noted, that the best CZTS films were made using hand carried spray coating.

The main purpose of using automated spray coating machine was to test many different solutions with controllable and repeatable parameters, which is hard to do with hand carried apparatus. After the films were deposited with automated spray coating machine and the films examined using different techniques, further adjustments were done for hand carried spray coating.

However, the main disadvantages of hand carried spraying are that the parameters, such as the distance between nozzle and sample, movement speed of nozzle over the sample, flow rate of sprayed solution and etc., are difficult to control. Therefore, the main purpose of automated spray coating system was to test different fabrication parameters with ability to modify them or fabricate layers from different solutions using identical parameters, which is almost impossible to do using hand carried spray coating. According to the estimated spray coating parameters using automated machine, the further hand carried spray coating parameters were set.
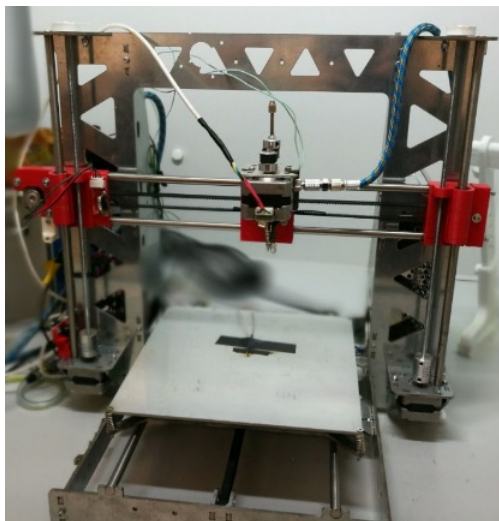
5.1 Automated spray coating system

Fig. 31. Spray coating apparatus used to fabricate CZTS films.
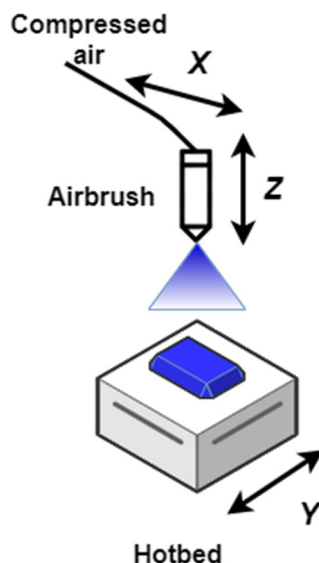
Fig. 32. Simplified working scheme of spray coating apparatus.

Spray coating system based on "RepRap" style 3D printer [102], tweaked "Marlin" firmware [103] and is controlled through "Arduino Mega 2560" by sending G-CODE [104] to the controller. The modified "Harder & Steenbeck" airbrush was used to distribute a solution on substrates. Photo of the system and simplified working scheme of spray coating apparatus are shown in Fig. 31 and Fig. 32, respectively. The system has movable platform in y axis, which carries hot plate. The airbrush can move along x and z axes. Work of airbrush is based on Bernoulli's principle. An air flow creates pressure differential, which sucks out a solution from reservoir and solution is disintegrated into droplets. The droplets are carried to substrate by initial air flow. Air flow is adjusted by the needle in airbrush by moving it, in this apparatus, it was attached to stepper motor, which was controlled by PC.

5.2 Fabrication of CZTS SC

Fig. 33. Schematic structure of investigated CZTSSe SC.

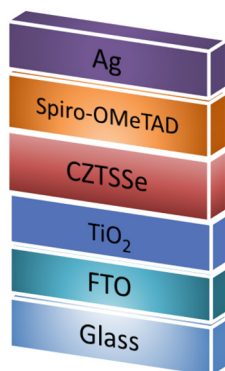In Fig. 33 the structure of the solar cells. The devices were prepared on conductive fluorine-doped tin oxide (FTO) coated glass substrates. The substrates were cleaned using sonication for 30 min in Hellmanex (2% water solution) and then rinsed using deionized water and isopropanol. A compact titanium dioxide (TiO_2) layer of about 30−50 nm was deposited as described in [105]. On top of this layer, CdS was deposited as a buffer layer at 65 ºC for 15 min using CBD method. Thereafter, the CZTS thin films were formed out of stock solution containing mixture of copper chloride 0.08 M, tin chloride 0.04 M, zinc chloride 0.06 M, and thiourea 0.4 M in dimethylformamide (DMF using spray pyrolysis) at 340 ºC. The solution was sprayed through the glass nozzle (0.25 mm) using compressed air as a carrier of gas with a constant flow rate (~1 ml/min). The spraying procedure was repeated several times in a 30 s drying interval to build up a precursor film thickness of approximately 1.5 μm. The formed layer was heated at 340 ºC for 1 hour. Then CZTS films were annealed in a graphite box (volume 20 cm^3) with different content of Se and 5 mg of Sn under atmospheric pressure of Ar (99,999 %) gas. The selenization process consisted of two annealing steps and was completed in 20 min at temperature of 540 °C. Subsequently, hole transporting material was deposited on the top of CZTSSe film by spin coating of Spiro-OMeTAD, dissolved in chlorobenzene at the concentration of 0.06 M at spinning rate of 3000 r.p.m. for 20 s, while keeping solutions at ambient environment during the whole procedure. The devices were finalized using thermal evaporation of 50 nm thick silver layer on the top of hole transporting material.
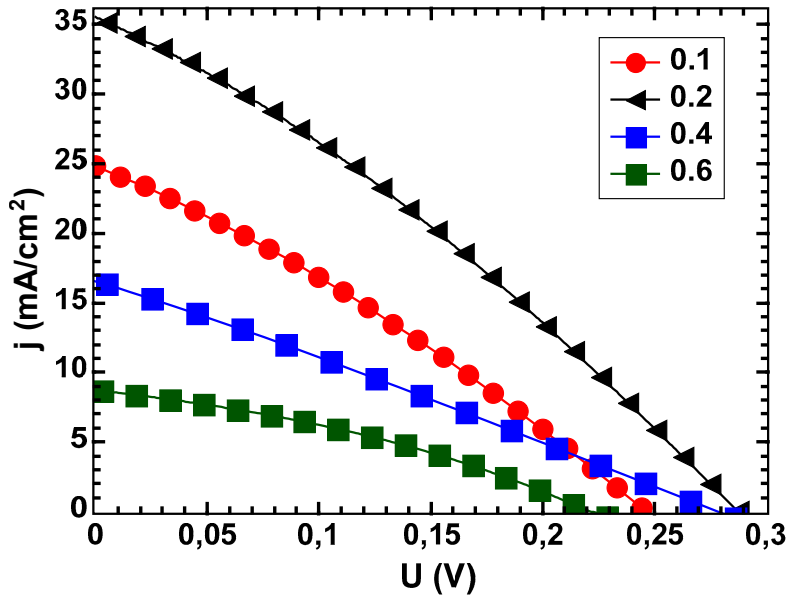
Fig. 34. CZTSSe SC *J-V* characteristics under illumination with different ratio of S/(S+Se).

The devices with different ratio of S/(S+Se) were made. Fig. 34 (*a*) shows VACh characteristics of SC's. *FF*, J_{sc}, PCE, V_{oc} were extracted, calculated from data and depicted in Fig. 35 (a-d). The champion cell was made with ratio of S/(S+Se)=0.2, showing PCE of 3.1%. Cells with ratio of S/(S+Se)=0.1 performed reasonably well, too. The solar cell of superstrate configuration FTO/TiO$_2$/Cu$_2$ZnSnSe$_{3.2}$S$_{0.8}$/ Spiro-OMeTAD/Ag demonstrated a record PCE of 3.1%, which is the highest reported value for the spray pyrolysis deposited superstrate solar cells up to date.
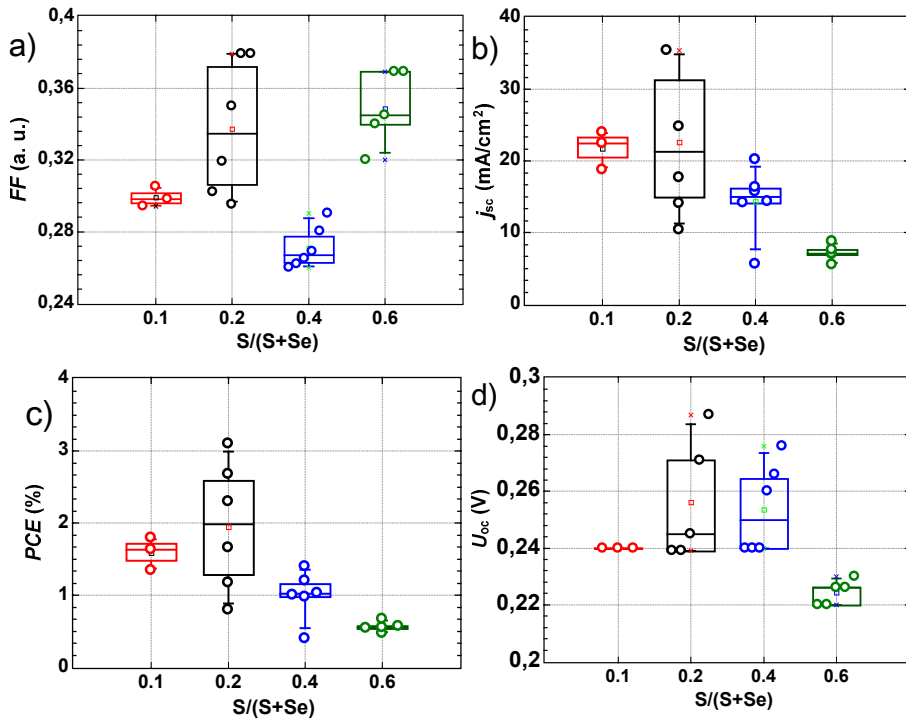
Fig. 35. The main parameters of SC, depending on ratio of S/(S+Se): a- fill factor, b- short circuit current density, c- power conversion efficiency, d- open circuit voltage.

In Fig. 36 energy diagram of typical perovskite SCs layers including CZTSSe and cross-linked HTM6 and HTM7 films is depicted. The diagram shows that HTM6 and HTM7 are completely suitable for CZTSSe SCs, in terms of energy levels. Moreover, these HTMs are up to 5 times cheaper than Spiro-OMeTAD [27], which makes CZTSSe SCs even more attractive to develop.
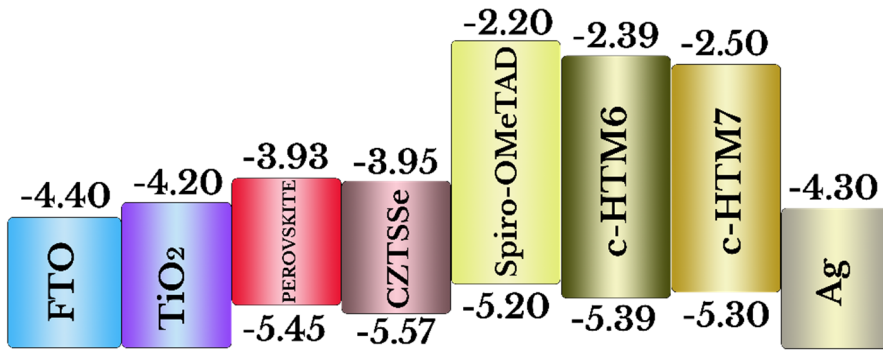
Fig. 36. Energy diagram of typical perovskite SCs layers including CZTSSe and cross-linked HTM6 and HTM7films [12], [106], [107].

5.3 Summary

The role of Se content ratio in CZTSSe on the structural and optical characteristics of CZTSSe films and the superstrate SCs performance were investigated. The new spray coating system allowed quicker and repeatable development of CSTSSe layers. The development led to achieve the solar cell of superstrate configuration $FTO/TiO_2/Cu_2ZnSnSe_{3.2}S_{0.8}$/ Spiro-OMeTAD /Ag, which demonstrated power conversion efficiency of 3.1% and was the highest reported value for the spray pyrolysis deposited superstrate solar cells up to date. Suitable photovoltaic structure for cross-linkable fluorene-based HTM6 and HTM7 was demonstrated during the experiment.

6 Conclusions

1. The apparatus to estimate ionization potential of semiconductor materials and metals in a gas mixture at atmospheric pressure by using the photoemission yield spectroscopy in air technique was demonstrated to allow more accurate estimation of photoemission threshold. The apparatus is able to detect electron photoemission signals down to a single electron per second (10^{-19} A).

2. Proposed method of plotting photoemission yield spectra as $(\mathrm{d}Y/\mathrm{d}(h\nu))^{1/2}$ is supported by the mathematical consideration and provides more precise estimation of ionization potential in comparison to $Y^{1/n}$ plot. The graphical presentation of this function is more informative than the other presentations in view of the fact that, it clearly shows multiple thresholds in photoemission yield spectrum. The new method of data interpretation allows estimation of ionization potential values more precisely in comparison to other PYS data presentations founded in the literature.

3. Hole drift mobility of methoxydiphenylamine-substituted fluorene derivatives HTM1, HTM2, HTM4, HTM5 research results ranged from 3.8×10^{-4} to 5.9×10^{-4} cm^2 V^{-1} s^{-1}. These values are almost the same or even higher in comparison with widely used Spiro-OMeTAD – 5.0×10^{-4} cm^2 V^{-1} s^{-1}. However, the synthesis of HTM1, HTM2, HTM4, HTM5 is easier and cheaper than Spiro-OMeTAD.

4. Ionization potential of HTM1-HTM5 ranged from 4.92-5.05 eV, which is suitable to substitute Spiro-OMeTAD (5.00 eV) in perovskite solar cells structure.

5. Polymerization of fluorene-based cross-linkable enamines HTM6 and HTM7 leads only to minor changes in hole drift mobility: HTM7 demonstrated hole drift mobility up to 10^{-3} cm^{2}V^{-1}s^{-1}, at a field strength of 3.6×10^5 Vcm^{-1} before and after heating. HTM6 showed slightly lower hole drift mobility – $3.5\mathrm{x}10^{-4}$ cm^{2}V^{-1}s^{-1} in neat layer and $1.75\mathrm{x}10^{-4}$ cm^{2}V^{-1}s^{-1} in cross-linked layer. Ionization potential values for HTM6 and HTM7 were 5.26 and 5.11 eV before the heating and 5.39 and 5.30 eV after the heating, respectively. These findings are compatible with CZTSSe SC structure. Due to cross-linking, the materials are suitable for application in inverted perovskite solar cells.

6. The solar cell of superstrate configuration FTO/TiO$_2$/Cu$_2$ZnSnSe$_{3.2}$S$_{0.8}$/ Spiro-OMeTAD /Ag demonstrated power conversion efficiency of 3.1%, which is the highest reported value for the spray pyrolysis deposited superstrate solar cells up to date.

1 Santrauka

1.1 Įvadas

Pastaraisiais metais daug dėmesio sulaukė organinės / neorganinės hibridinės struktūros, tokios kaip perovskitai. Didelė galimų medžiagų derinių įvairovė, draustinio juostos tarpo ir kitų savybių derinimas [1], nuolat didėjantis perovskito saulės elementų (SC) efektyvumas [2]. Tačiau, perovskito dariniai yra gan nestabilūs ir dažnai sudėtyje turi toksiškų elementų, tokių kaip švinas. Negana to, net ir mažo ploto perovskito SC gamybos metodikos yra gan preciziškos, nekalbant jau apie bandymus suformuoti didelio ploto bandinius, tokiomis metodikomis kaip purškimas [3]. Be to, reikalingos brangios skylių pernašos medžiagos (HTM), kurios paprastai yra jautrios deguonies ir vandens garų sąveikai ir gali sąveikauti su ant viršaus užgarintu metalo kontaktu [4].

Viena iš galimų perovskito SC alternatyvų yra vario cinko alavo sulfidas (CZTS), selenidas (CZTSe) ir mišrus chalkogenidas ($Cu_2ZnSn(S_xSe_{1-x})_4$) (CZTSSe) dariniai. Šios medžiagos yra perspektyvios, nes tinka efektyvių ir nebrangių SC gamybai [5], [6]. Dariniai susideda iš netoksiškų cheminių elementų ir pasižymi aukštu absorbcijos koeficientu ($\sim 10^4$ cm^{-1}), modifikuojamu draustinės energijos tarpu (1–1,5 eV) ir paprastu sluoksnių formavimu [7]. Paprastai CZTS SC struktūra yra su puslaidininkiniu absorberiu tarp Mo atgalinio kontakto ir viršutinio buferinio sluoksnio (CdS arba ZnS) ir permatomo laidaus dvisluoksnio oksido [8], [9]. Tačiau tokia struktūros gamyba yra santykinai brangi, mažiau stabili bei sunkiau pritaikoma tandeminėms SC, palyginti su iš kesteritų pagamintomis SC su invertuota struktūra. Šioje struktūroje galinis kontaktas yra skaidrus elektrodas nusodintas ant stiklo (FTO arba ITO), ant kurio toliau formuojami šie sluoksniai: elektronus pernešantis, foto aktyvus CZTS ir HTM sluoksnis [10], [11].

Viena iš dažniausiai naudojamų HTM organinėms / neorganinėms SC yra Spiro-OMeTAD, tačiau ši medžiaga yra santykinai nestabili ir brangi [4]. Pigesnė ir našesnė Spiro-OMeTAD alternatyva ir invertuotos CZTS SC būtų puikus derinys bei reikšmingas postūmis saulės energetikoje, turint omenyje, kad naujos HTM būtų suderinamos ir su CZTS ir su perovskitų SC: šie šviesą absorbuojantys sluoksniai turi palyginamus aukščiausios užimtos molekulinės orbitalėss lygius (HOMO) ir žemiausios neužimtos molekulinės orbitalės (LUMO) lygius[12]. Fluoreno pagrindu pagamintos HTM yra perspektyvios krūvį pernešančios medžiagos - palyginti pigi sintezė ir įvairios modifikacijos

galimybės leidžia sukurti skersaryšinamus HTM. Skersaryšinimas atveria galimybes daugiasluoksnėms struktūroms nenaudojant ortogonalių tirpiklių bei didesniam medžiagų stabilumui ir ilgaamžiškumui [13].

Tačiau norint atrasti tinkamą molekulinę struktūrą ir sintezės procesus, reikia tam skirti daug laiko bei pastangų, be to, visų šių HTM testavimas realiame įtaise pareikalautų dar daugiau išteklių. Vienas iš greičiausių ir paprasčiausių netinkamų HTM atmetimo būdų yra krūvio pernašos savybių įvertinimas kserografiniu krūvininkų lėkio trukmės metodu (XTOF) ir jonizacijos potencialo įvertinimo fotoelektronų emisijos spektroskopija ore (PYSA) metodas. Šie metodai leidžia nustatyti dvi svarbias HTM savybes: krūvininkų judrį (μ) ir HOMO energijos lygį. Šie parametrai yra susiję su SC efektyvumu (PCE), atviros grandinės įtampa (V_{oc}) ir trumpojo jungimo srove (J_{sc}) [14].

CZTS sluoksnis gali būti suformuotas naudojant vakuuminį arba nevakuuminį formavimo metodą. Abi technikos turi savo privalumų ir trūkumų. Vakuuminio nusodinimo metodai leidžia suformuoti aukštos kokybės CZTS plėveles, tačiau jos yra brangios, kai kurios medžiagos nestabilios esant aukštai nusodinimo temperatūrai, taip pat sunku kontroliuoti elementų santykį struktūroje. Kita vertus, nevakuuminio auginimo metodai, tokie kaip purškimo pirolizė [15], besisukančio stalelio metodas [16], rašalinis spausdinimas [17] ar elektrocheminis nusodinimas [18], yra pakankamai universalūs ir gana pigūs. Tačiau, yra didelis iššūkis pagaminti aukštos kokybės CZTS sluoksnius, kai SC struktūra yra invertuota naudojant ne vakuuminio formavimo techniką bei pagaminti pilną CZTS SC, naudojant sluoksnių formavimo metodiką, kuri leistų padengti didelio ploto padėklus, pvz.: purškimo būdu.

Greiti ir paprasti organinių medžiagų charakterizavimo metodai, naujų HTM sukūrimas, didelio ploto sluoksnių formavimo metodikos tobulinimas bei netoksiško SC aktyvaus sluoksnio vystymas paskatins naujos kartos organinių / neorganinių SC atsiradimą.

1.1.1 Darbo tikslas ir uždaviniai

Disertacijos tikslas buvo ištirti fluoreno pagrindu pagamintas skylių pernašos medžiagas, nustatyti jų tinkamumą organinėms / neorganinėms fotovoltinėms struktūroms, tobulinant organinių medžiagų charakterizavimo metodus, vystant skylių pernašos medžiagas bei plėtojant neorganinių SC gamybos būdus. Šiems tikslams pasiekti buvo nustatytos šios užduotys:

1. Sukurti naują didelio jautrumo (~10^{-19}A) jonizacijos potencialo (I_p) matavimo įrenginį, skirtą organinėms ir neorganinėms medžiagoms.

2. Sukurti naują fotoemisijos spektro analizės metodą, kuris leistų detaliau ištirti puslaidininkinių organinių medžiagų energetinių lygmenų struktūrą.

3. Įvertinti fluoreno pagrindu susintetintų skylių pernašos medžiagų I_p ir μ ir nustatyti, kurios medžiagos būtų tinkamos organiniams / neorganiniams SC.

4. Pagaminti SC, kurių šviesą absorbuojantis sluoksnis būtų neorganinis ir suderinimas su skersaryšinamomis fluoreno pagrindu susintetintomis skylių pernašos medžiagomis bei įvertinti pagrindinius šių SC parametrus.

1.1.2 Mokslinis naujumas

Ieškant naujų, pigių ir efektyvių organinių HTM, skirtų gaminti SC, reikia greitų, informatyvių ir paprastų medžiagų tyrimo metodų, leidžiančių įvertinti I_p ir μ. I_p parametras suteikia svarbios informacijos apie skirtingų medžiagų suderinamumą, kalbant apie energijos lygmenis. Netikslus I_p įvertinimas gerokai apsunkina SC architektūros kūrimą - kadangi I_p atitinka HOMO lygmenį, o nesuderinami HOMO lygmenys tarp skirtingų medžiagų lemtų neefektyvų krūvio atskyrimą ir ištraukimą link SC kontaktų. PYSA metodas organinių medžiagų I_p nustatymui yra palyginti gerai žinomas [19]. Jei foto srovei įvertinti naudojamas elektrometras, kaip aprašyta [20], jo jautrumo slenkstis yra apie 10^{-15}-10^{-16} A. Toks jautris gali būti nepakankamas tikslios I_p vertės nustatymui. Kita vertus, komercinės sistemos, tokios kaip Riken-Keiki AC-2 [21] ir AC-3 [22], yra jautresnės nei sistemos, pagrįstos elektrometru, tačiau jos naudoja slopinimo tinklelius ir impulsų generatorius, kad užgesintų ir neutralizuotų klaidingus impulsus. Tokia sistema turi 3ms nejautros trukmę, dėl kurios maksimali galima aptikimo sparta yra mažesnė nei 300 elektronų per sekundę. Šiame darbe yra pristatoma nauja I_p įvertinimo sistema, veikianti lavininio išlydžio pagrindu dujų mišinyje, kuri leidžia įveikti anksčiau minėtus trūkumus.

Daugelio komerciškai prieinamų HTM, pavyzdžiui, kaip Spiro-OMeTAD, sintezė yra brangi: daugiapakopės sintezės procedūros, brangūs reagentai ir gryninimo metodai [23]–[25]. Pigesnių ir lengviau sintetinamų HTM kūrimas, kurių savybės būtų panašios ar geresnis nei Spiro-OMeTAD, būtų postūmis link efektyvių ir pigių organinių / neorganinių SC. Sintezės procesas yra glaudžiai susijęs su šių medžiagų charakterizavimo metodais. μ yra svarbus HTM parametras, nes jis tiesiogiai veikia SC efektyvumą. Kuo didesnis μ yra, tuo didesnė tikimybė ištraukti daugiau krūvio link SC elektrodų, o tai lemia didesnę J_{sc}. Dažnai literatūroje minimos krūvio pernašos vertinimo metodikos

yra voltamperinių charakteristikų (VACh) analizė, lauko tranzistoriaus (FET) perdavimo ir išėjimo charakteristikų analizė, lėkio trukmės metodas (TOF) ir krūvio ištraukimas tiesiškai didėjančia įtampą (CELIV). Tačiau VACh analizė nėra labai tiksli ir patikima technika, FET gamybai reikalinga specifinė bandinio struktūra, o norint tirti bandinius TOF ar CELIV, reikia, kad bandinyje būtų bent du laidūs kontaktai, o vienas iš šių kontaktų paprastai būna termiškai užgarintas metalas ant organinės medžiagos. Kadangi užgarintas kontaktas turi specifinę geometriją ir išdėstymą, jis pateiks informaciją tik iš mažo bandinio ploto. Be to, garinimo procesas gali paveikti bandinį ar bandinio plotą po metaliniu elektrodu - padidėjusi temperatūra ar nusodintas metalas gali pagreitinti HTM kristalizacijos procesą. Kadangi XTOF tiria visą mėginio paviršių (cm^2 eilės) be užgarinto metalinio kontakto ant organinės medžiagos, paviršiaus defektai turi mažiau įtakos rezultatams, palyginti su santykinai nedideliu užgarinto metalo kontakto plotu (mm^2 eilės).

Kadangi, bet kurio SC gamyba susideda iš daugelio žingsnių, dažnai pagrindiniai tikslai yra padaryti SC gamybą kuo paprastesnę, saugesnę ir pigesnę. CZTSSe yra perspektyvus medžiagų derinys ir gali pasiekti šiuos tikslus - jis nėra toksiškas, galima formuoti sluoksnius purškimo būdu, tirpalo gamyba yra paprasta, medžiagos palyginti pigios [5], [26]. Kadangi CZTSSe sluoksniai gali atlaikyti aukštą temperatūrą, todėl ant jų galima formuoti skersaryšinamas HTM fluoreno pagrindu. Fluoreno pagrindu pagamintų HTM skersaryšinimo temperatūros yra gana aukštos ir dažniausiai yra per aukštos, kad būtų panaudotos perovskito SC.

Visų aukščiau paminėtų patobulinimų ir metodų naudojimas įgalina naujos kartos SC įrenginių paieškas.

1.1.3 Ginamieji teiginiai

1. Fotoemisijos spektro matavimo įrenginys veikiantis lavininio išlydžio principu oro, Ar ir CH_4 dujų mišinio aplinkoje, leidžia registruoti iki 10^4 karto silpnesnes foto sroves nei spektro matavimo sistema naudojanti elektrometrą.
2. Fotoemisijos spektro analizavimas naudojant $(dY/d(h\nu))^{1/2}$ priklausomybę, leidžia spektre išskirti daugiau nei vieną HOMO lygmenį, lyginant su dažniausiai naudojama $Y^{1/n}(h\nu)$ priklausomybe.
3. Metoksidifenilaminu pakeisti fluoreno dariniai HTM4 ir HTM5 su alkilo grupėmis trifenilamino para padėtyse turi panašias skylių judrio ir jonizacijos potencialo vertes bei efektyvumą perovskito saulės celėse,

lyginant su Spiro-OMeTAD, tačiau šių darinių. sintezė vykdoma dvejais etapais vietoje penkių.

4. Fluoreno pagrindu susintetinti ir skersaryšinami HTM6 ir HTM7 gali būti naudojami gaminant daugiasluoksnes struktūras nenaudojant ortogonalių tirpiklių. Skylių judriai yra palyginami arba didesni nei Spiro-OMeTAD. HTM6 ir HTM7 turi tinkamą jonizacijos potencialą ir skersaryšinimo temperatūrą CZTSSe saulės celėms.

5. Invertuotos struktūros saulės celė FTO/TiO$_2$/Cu$_2$ZnSnSe$_{3.2}$S$_{0.8}$/ Spiro-OMeTAD /Ag pasiekė 3,1% efektyvumą, kuris, tuo metu, buvo didžiausias tarp purškimo būdu suformuotų ir invertuotų CZTSSe saulės celių.

1.1.4 Publikacijos

1. R. Tiazkis, P. Sanghyun, M. Daškevičienė, T. Malinauskas, M. Saliba, J. Nekrasovas, V. Jankauskas, Sh. Ahmad, V. Getautis, M. K. Nazeeruddin. "Methoxydiphenylamine-substituted fluorene derivatives as hole transporting materials: role of molecular interaction on device photovoltaic performance", *SCIENTIFIC REPORTS*, Volume 7, 150, DOI: 10.1038/s41598-017-00271-z (2017).

2. M. Franckevičius, V. Pakštas, G. Grincienė, E. Kamarauskas, R. Giraitis, J. Nekrasovas, A. Selskis, R. Juškėnas, G. Niaura. "Efficiency improvement of superstrate CZTSSe solar cells processed by spray pyrolysis approach", *Solar Energy*, Volume 185, June 2019, Pages 283-289. DOI: 10.1016/j.solener.2019.04.072 (2019).

3. J. Nekrasovas, V. Gaidelis, E. Kamarauskas, M. Viliūnas, V. Jankauskas. "Photoemission studies of organic semiconducting materials using open Geiger-Muller counter", *Journal of Applied Physics*, 126, 015501. DOI: 10.1063/1.5096070 (2019).

4. D. Vaitukaitytė, A. Al-Ashouri, M. Daškevičienė, E. Kamarauskas, J. Nekrasovas, V. Jankauskas, A. Magomedov, S. Albrecht, V. Getautis, "Enamine-Based Cross-Linkable Hole-Transporting Materials for Perovskite Solar Cells", *SOLAR RRL*, Volume: 5 Issue: 1, 2000597, DOI: 10.1002/solr.202000597 (2021).

1.1.5 Pranešimai konferencijose

1. R. Tiazkis, P. Sanghyun, M. Daškevičienė, T. Malinauskas, M. Saliba, **J. Nekrasovas**, V. Jankauskas, Sh. Ahmad, V. Getautis, M. K. Nazeeruddin, "Charge-transporting properties of methoxydiphenylamine- substituted fluorene derivatives as hole transporting materials for PSC.", *E-MRS Fall Meeting 2017*, p. 146, Warsaw University of Technology, Warsaw, Poland, September 18-21, 2017.

2. **J. Nekrasovas**, V. Gaidelis, V. Jankauskas, E. Kamarauskas, M. Viliūnas, "Puslaidininkių jonizacijos potencialo matavimas Geigerio-Miulerio skaitikliu."ISBN: 9786094598807 ; DOI: 10.15388/proceedings/LNFK.42, *the 42nd Lithuanian national Physics Conference*, Vilnius, Lithuania, October 4-6, 2017.

3. **J. Nekrasovas**, E. Kamarauskas, V. Gaidelis, M. Steponaitis, T. Malinauskas,V. Getautis, V. Jankauskas, "Charge transport properties of novel enamines with different central group.", eISBN: 9786090216385 ; DOI: 10.5755/e01.9786090216385, *the 43th Lithuanian national Physics Conference*, Kaunas, Lithuania, October 3-5, 2019.

4. **J. Nekrasovas**, Š. Daškevičiūtė, M. Daškevičienė, V. Getautis, V. Gaidelis, V. Jankauskas, "Charge-transporting properties of enamine-based fluorene derivatives as hole transporting materials for PSC", *nanoGe Fall Meeting19*, Berlin, Germany, November 3-8, 2019.

1.1.6 Dalyvavimas moksliniuose projektuose

Lietuvos mokslo tarybos, mokslinių grupių projektas "Investigation of the charge carriers transport features in thin multilayered hybrid structures, Project No. MIP-091/2015, 2015-2018.

1.1.7 Autoriaus indėlis

Autorius dalyvavo kuriant ir konstruojant naująją PYSA sistemą, atliko visus su PYSA ir XTOF susijusius eksperimentus ir duomenų analize.

Autorius vystė I_p nustatymą naudojant $(\mathrm{d}Y/\mathrm{d}(h\nu))^{1/2}$ priklausomybę. Autorius suprojektavo naują purškimo sistemą ir dalyvavo naujų CZTSSe SC purškimo metodikos tobulinime ir atliko CZTSSe SC VACh matavimus. Autorius aktyviai dalyvavo rezultatų aptarime ir publikacijų rengime.

Diferencinės skenuojančios kalorimetrijos (DSC) matavimai ir HTM1-HTM7 sintezė buvo atlikti Kauno technologijos universitete, tyrėjų grupėje, kuriai vadovauja prof. Vytautas Getautis. Prof. Sanghyun Paek ir prof. Michael Saliba pagamino ir charakterizavo SC su HTM1-HTM5. Dr. Amran Al-Ashouri ir prof. Steve Albrecht pagamino SC su HTM6-HTM7 ir jas charakterizavo. Tirpalų paruošimą CZTS sluoksniams, cheminį CdS nusodinimą (CBD), CZTS sluoksnių formavimą purškiant rankiniu būdu, CZTS sluoksnių selenizaciją ir Spiro-OMeTAD dengimą ant CZTSSe SC atliko dr. Marius Franckevičius, dr.Vidas Pakštas, dr. Giedrė Grincienė, dr. Raimondas Giraitis, dr. Algirdas Selskis.

1.2 I_p charakterizavimas

I_p yra svarbus parametras tiriant metalų, puslaidininkių medžiagų, o ypač organinių junginių, energinius lygius, kuriuos reikia žinoti kuriant elektronikos prietaisus, SCs, šviesos diodus (LED), FET. Visais paminėtais atvejais, norint tinkamai pasirinkti iš daugybės esamų medžiagų arba sintetinti naujas medžiagas su norimomis savybėmis, būtina žinoti medžiagų energetinius lygmenis.
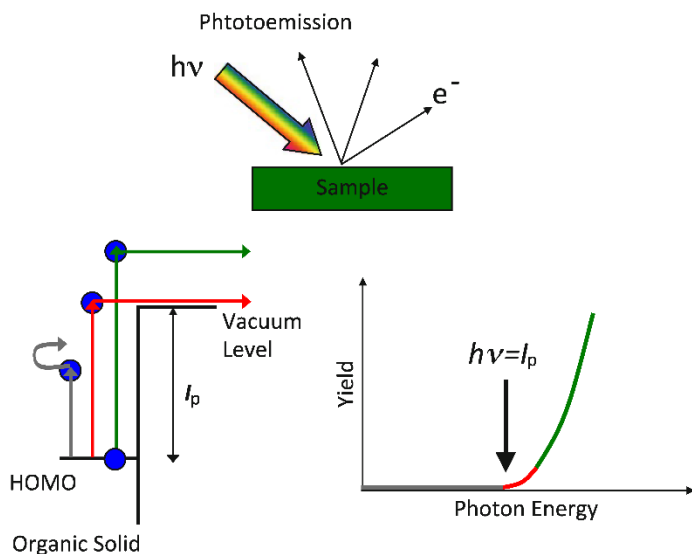
1 pav. Fotoemisijos spektroskopijos principas organinių medžiagų atveju. Adaptuota pagal [55], [56].

1 pav. parodytas PYS principas. Kvantinė fotoelektronų išeiga (Y), kuri yra emituotų fotoelektronų skaičius vienam absorbuotam fotonui, atidėta nuo fotono energijos ($h\nu$). Kai fotonų energija yra mažesnė už slenkstinę jonizacijos energiją, stebimas pirmasis spektro regionas – „0" lygyje (pilka tiesė). Antrasis regionas yra, kai $h\nu$ tampa šiek tiek didesnis už jonizacijos energiją (raudona kreivė). Trečiasis regionas, kai $h\nu$ gerokai viršija jonizacijos energiją (žalia kreivė). Duomenys atvaizduojami $Y^{1/n}(h\nu)$ grafike, parenkant tinkamiausią n vertę, kad žalioji ir raudonoji kreivės būtų kuo tiesiškesnė.

Fotoemisijos kreivė gali būti aprašoma pagal formulę:

$$Y \propto (h\nu - E_T)^n. \tag{1.1}$$

Šio metodo principas yra surasti *n* vertę, kad būtų pasiektas geriausias nubraižytos kreivės tiesiškumas. Metalams $n = 2$, priklausomai nuo paviršiaus savybių, jis gali skirtis tarp $n = 1, n = 3/2, n = 5/2$ [59]. Organinėms medžiagoms rekomenduojamas $n = 3$. Tačiau n gali svyruoti net nuo 1 iki 5 [36], [60]–[62].

### 1.2.1 I_p charakterizavimas naudojant elektrometrą ir $Y^{1/n}$ priklausomybę

Pigesnės ir lengviau sintetinamos HTM, kurių našumas saulės celėse yra panašus ar geresnis nei Spiro-OMeTAD, buvo tiriamos fotoemisijos spektroskopijos metodu ore (PYSA) [63]. Šis metodas pirmą kartą buvo panaudotas [52]. Struktūrinės cheminės formulės parodytos 2 paveiksle. Daugelis didelio efektyvumo SC naudojo Spiro-OMeTAD kaip HTM [64]–[67]. Tačiau Spiro-OMeTAD sintetinimas yra brangus: daugiapakopės sintezės procedūros, brangūs reagentai ir sudėtingesnės gryninimo procedūros [23]–[25].

Prof. Vytautas Getautis ir jo mokslinė grupė susintetino 5 naujas skylių pernašos medžiagas fluoreno pagrindu (2 pav.): 4 – {[2,7-bis (4,4'-dimetoksidifenilamino) -9*H*-fluoren-9-ilidene] metil} -*N*, *N*-difenilanilinas (HTM1), 4 – {[2,7-bis (4, 4'-dimetoksidifenilamino) -9*H*-fluoren-9-ilidene] metil} -*N*, *N*-difenil-2- metilanilinas (HTM2), 4 – {[2,7-bis (4,4'-dimetoksidifenilamino) -9*H*- fluoren-9-ilidene] metil} -*N*, *N*-difenil-3- metilanilinas (HTM3), 4 – {[2,7-bis (4,4'-dimetoksidifenilamino) -9] -fluoren-9-iliden] metilas } -*N*, *N*-bis (4-metilfenil) anilinas (HTM4), 4 – {[2,7-bis (4,4'-dimetoksidifenilamino) -9*H*-fluoren-9-ilidene] metil} -*N*, *N*- bis (4-butilfenil) anilinas (HTM5).
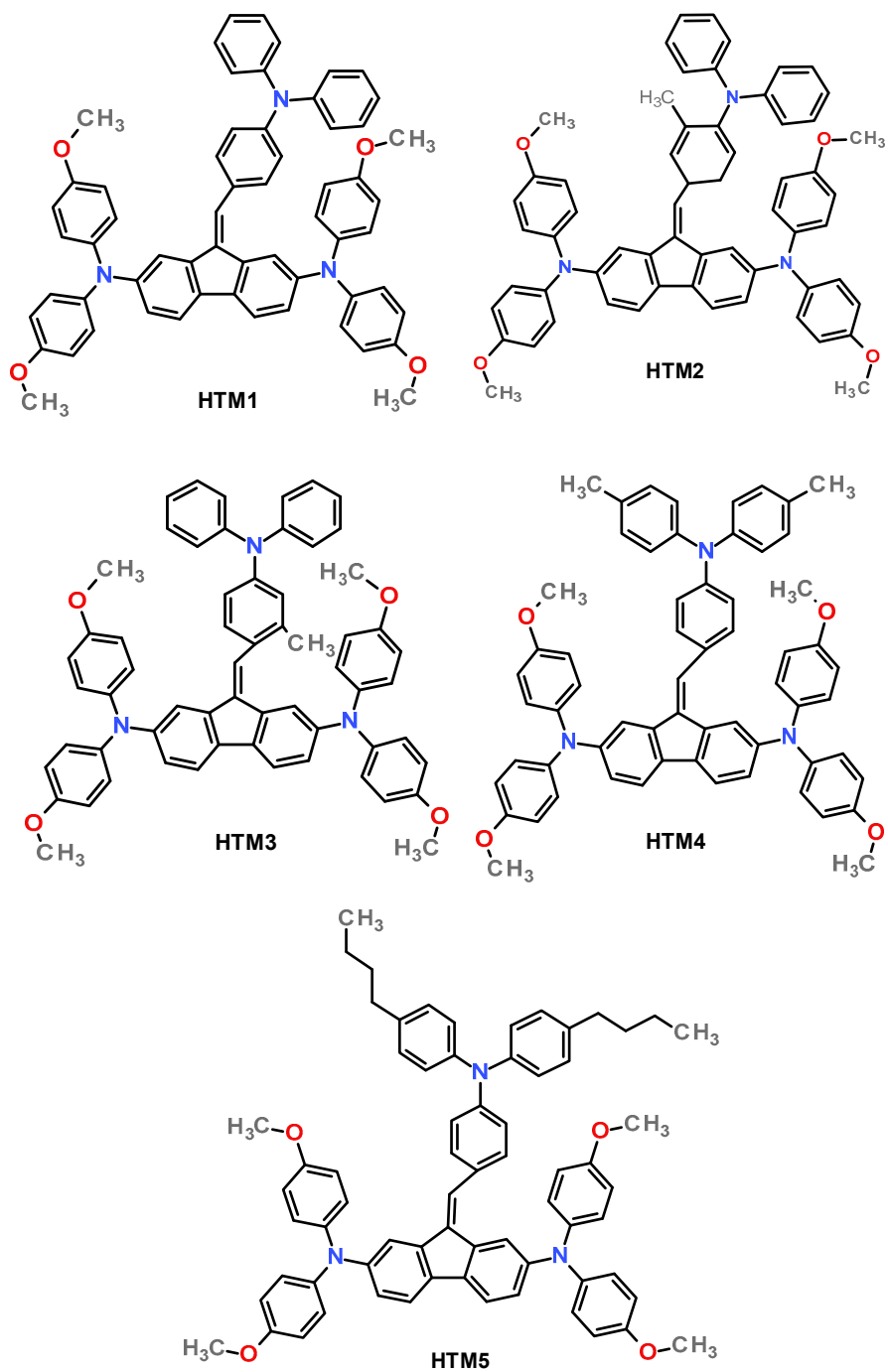
2 pav. Struktūrinės formulės tirtų skylių pernašos medžiagų HTM1 – HTM5.

Medžiagų I_p nustatytas naudojant PYSA metodiką ir elektrometrą. Matavimo metodika ir bandinių gamybos procesas detaliau aprašytas [52]. Rezultatai atvaizduoti 3 pav. ir apibendrinti lentelėje 1.
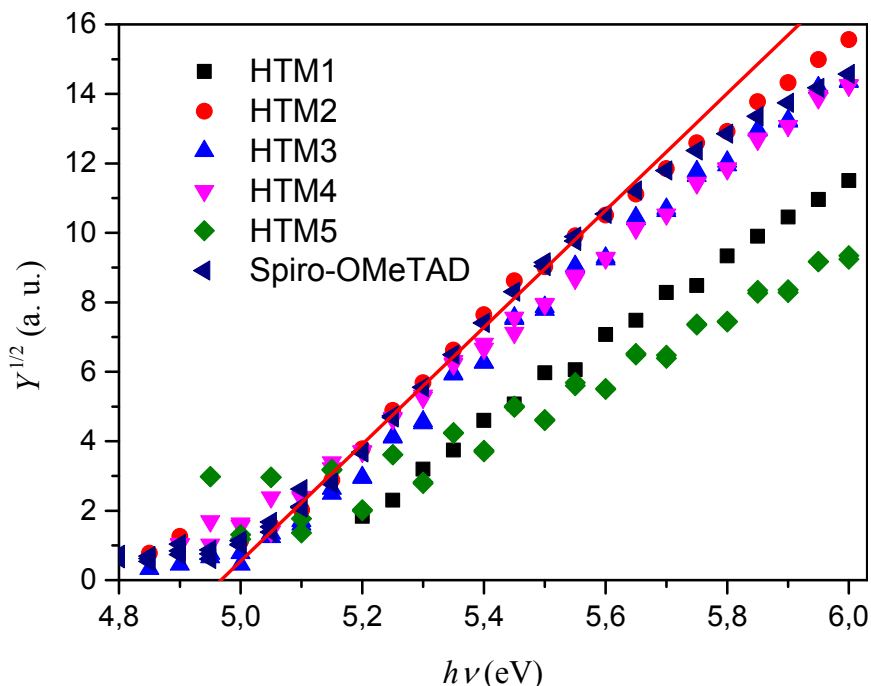
3 pav. HTM1-5 medžiagų fotoemisijos spektras ore. Spektras išmatuotas naudojant elektrometrą.

Lentelė 1. Nustatytos I_p vertės HTM1-HTM5 ir Spiro-OMeTAD medžiagoms.

Medžiaga	I_p, (eV±0.1eV)
HTM1	5.05
HTM2	5.00
HTM3	5.00
HTM4	4.92
HTM5	5.03
Spiro-OMeTAD	5.00

Visos HTM pademonstravo panašias I_p vertes, kaip ir Spiro-OMeTAD. HTM2 spektras pavaizduotas 4 pav. Naudojant tiesinį aproksimavimą, galima rasti tašką, kur spektras kerta x ašį ir nustatyti I_p vertę, darant prielaidą, kad x

ašis yra „0" lygyje. Tačiau, jei spektras analizuojamas atidžiau, matyti, kad jame yra 3 regionai:

1. ~4.8 – 5 eV – tamsinio signalo regionas
2. ~5 – 5.4 eV – pirmasis fotoemisijos regionas
3. ~5.4 – 6 eV– antrasis fotoemisijos regionas
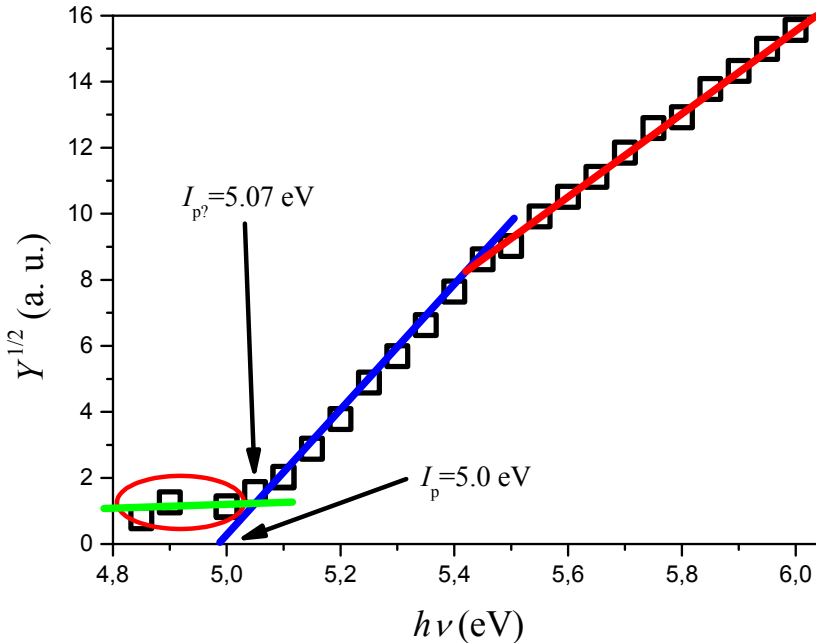
4 pav. HTM2 fotoemisijos spektras ore. Spektras išmatuotas naudojant elektrometrą.

Daugumoje publikuojamos literatūros nurodomi du metodai, kaip nustatyti I_p reikšmę: 1) spektro aproksimavimo tiesės ir abscisių ašies susikirtimo taškas; 2) „0" lygio aproksimavimo tiesės ir spektro aproksimavimo tiesės susikirtimo taškas [36], [61]. Jei laikytume, kad žalia linija yra tikrasis „0" lygmuo, I_p vertė pasikeičia per 0,07eV. Be to, matyti, kad vyksta perėjimas tarp 1 ir 2 fotoemisijos regionų. Atsižvelgiant į organinių medžiagų jautrumą šviesai, monochromatoriaus spektrinę skiriamąją gebą ir elektrometro jautrumą, gali būti pakankamai sunku nustatyti tikrąjį „0" lygį ar kreivės polinkio/lūžio taškus (pvz., kaip 4 pav., ties ~ 5,4 eV), ir tiesinis aproksimavimas būtų atliktas naudojant visą 5–6 eV diapazoną. Tai gali paaiškinti, kodėl literatūroje galima rasti įvairių publikuotų I_p verčių tai pačiai medžiagai, pvz. kaip H_2Pc – I_p reikšmės svyruoja nuo 4,95 iki 5,1 eV [29], [32], [68].

1.2.2 I_p charakterizavimas naudojant atvirą Geiger-Müller skaitiklį ir $(dY/d(h\nu))^{1/2}$ priklausomybę

Fotoemisijos atmosferos slėgyje tyrimui naudotos aparatūros supaprastinta schema pavaizduota 5 pav. Fotoelektronų detekcija veikia Geigerio – Müllerio skaitiklio pagrindu [71]. Elektronų skaitiklis (EC) susideda iš cilindro formos jonizacijos celės, kurios plyšys palei vieną cilindro pusę leidžia elektronams patekti į celę (5 pav.). Išilgai cilindro ašies eina plona vielelė, prie vielelės prijungta aukšta teigiama įtampa. Vielelės įtampa palaikoma šiek tiek mažesnė už vainikinio išlydžio įtampą ir vielelės paviršiuje sukuriamas $\sim 10^5$ V/cm elektrinis laukas. Lėtam elektronui patekus į cilindro vidų, jį veikia elektrinis laukas ir jis traukiamas link vielelės. Artėjant link vielelės vis didėja elektrinio lauko stipris ir prasideda dujų molekulių jonizacija bei griūtinio pramušimo procesas. Spartus krūvininkų dauginimasis padidina jų skaičių iki $\sim 10^9$ karto. Lavinos procesas baigiasi, kai teigiami jonai suformuoja erdvinį krūvį šalia vielelės, taip kompensuodami sudaryta elektrinį lauką. Vėliau teigiami jonai dreifuoja link katodo, kur jie praranda savo krūvį. Molekulės tampa neutralios ir sužadinamos [71]. Kai kurios dujos, pvz. kaip Ar arba N_2 praranda perteklinę energiją, išspinduliuodamos UV šviesos kvantus [71]; ši UV spinduliuotė gali jonizuoti kitas dujų molekules ir taip sukurti antrinius laisvuosius elektronus, kurie priartėję prie anodo vėl inicijuoja naujas nepageidaujamas lavinas. Norint neutralizuoti tokias lavinas, galima naudoti dujų mišinį, kuriame yra 5% metano ir 95% argono ir šį mišinį maišant su oru $\sim 1:1$ santykiu. Metano molekulės išlaisvina energiją disociacijos būdu, veikdamos kaip efektyvus antrinių elektronų ir klaidingų impulsų gesintojas.
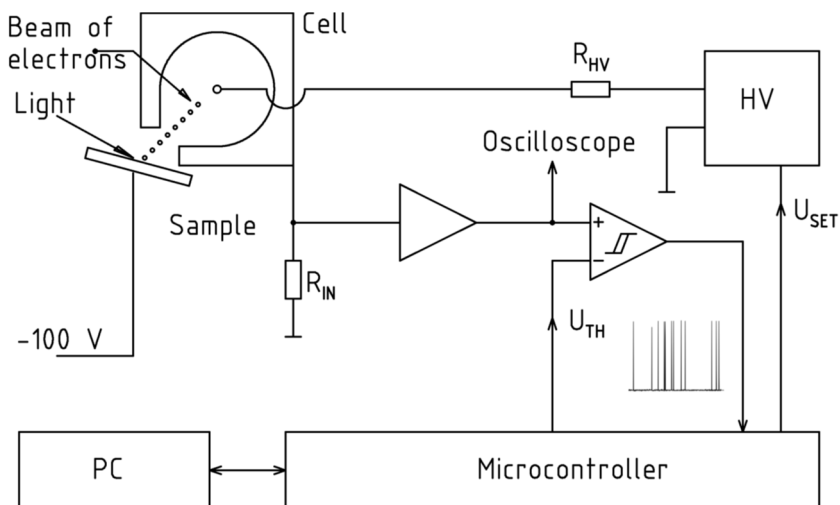
5 pav. Elektronų skaitiklio elektrinė schema.

Elektronų skaitiklio elektrinė schema parodyta 5 pav. Jį sudaro aukštos įtampos šaltinis (HV), jonizacijos celė ir specialus bandinio laikiklis, įdėtas į uždarą matavimo kamerą, taip pat stiprintuvas ir komparatorius, slenkstinės įtampos valdymui. Impulsų skaitiklį ir likusią eksperimentinę įrangą valdo kompiuteris per mikrovaldiklį. Monochromatinė šviesa į kamerą patenka pro kvarco langą. Jei bandinys sugeria šviesos kvantą ir į celę patenka elektronas, vyksta lavinos išlydis. Naudojant šią sistemą galima detektuoti iki 1000 elektronų per sekundę.

Parengus naują sistemą ir norint palyginti dviejų sistemų galimybes, buvo pagaminti nauji HTM2 - HTM5 bandiniai. Įvertinos I_p vertės pateiktos lentelėje 2. Nustatytos I_p vertės yra panašios, tačiau didesnis EC jautrumas ir aukštesnė spektrinė skiriamoji geba leidžia atlikti tikslesnius matavimus.

Lentelė 2. I_p vertės HTM2-5 medžiagoms. Matavimai atlikti su EC ir elektrometru.

Medžiaga	Elektrometras (I_p(eV±0.1eV))	EC (I_p(eV±0.05eV))
HTM2	5.00	4.99
HTM3	5.00	4.96
HTM4	4.92	5.01
HTM5	5.03	5.00

6 pav. pavaizduoti HTM2 fotoemisijos spektrai, išmatuoti naudojant EC ir elektrometrą. Teoriškai, $Y^{1/3}$ skalė (juodi kvadratai) turėtų būti labiau tinkama

organinių medžiagų I_p nustatymui, kita vertus, jei reikėtų pasirinkti kreivę, kuri būtų kuo artimesnė tiesei, reikėtų rinktis $Y^{1/2}$ atvaizdavimą (žali tušti kvadratai). Šie rezultatai iškėlė klausimą - kaip išsiaiškinti, kuri *n* reikšmė yra teisingesnė?
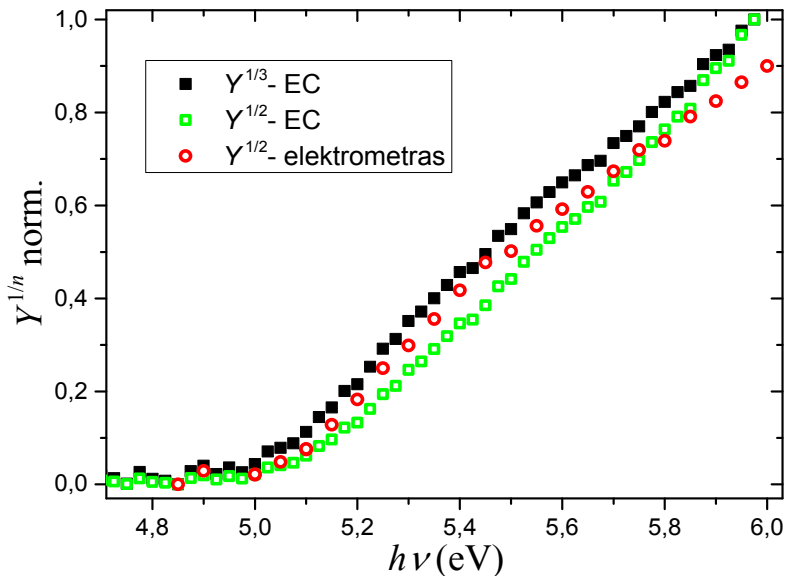
6 pav. HTM2 medžiagos I_p matavimai atlikti elektrometru (raudoni apskritimai) ir atlikti su EC (juodi kvadratai ir žali tušti kvadratai). Duomenys sunormuoti į 1.

Toliau pristatomas naujas PYSA matavimo rezultatų apdorojimo ir grafinio pateikimo metodas, siekiant išsamiau parodyti fotoemisijos spektrų ypatumus.

1.2.3 I_p charakterizavimas naudojant $(\mathrm{d}Y/\mathrm{d}(h\nu))^{1/2}$ priklausomybę

Publikacijose [38], [39], [68] apie organinių medžiagų tyrimus UPS metodiką, teigiama, kad būsenų tankio (DOS) pasiskirstymas yra Gausinė funkcija. Ši funkcija naudojama tiek atliekant teorinius skaičiavimus, tiek interpretuojant eksperimentinius rezultatus, tačiau, norint nustatyti I_p vertę, kyla klausimas - kaip teisingai apibrėžti ir eksperimentiškai nustatyti fotoemisijos slenkstį? Gauso funkcija tolygiai mažėja link nulio. Jei nubrėžta aproksimacijos tiesė, atitinkanti Gauso funkcijos polinkį, tai ji susikerta su abscisių ašimi taške, ten kur funkcijos vertė yra apie 10% nuo didžiausios funkcijos vertės. Panašūs UPS tyrimų rezultatai pateikti [38], [39], [68]. Šis

nuokrypis realiuose matavimuose praktiškai neįskaitomas, nors ir literatūroje yra minima silpna fotoemisija, kai sužadinimo energija yra mažesnėse nei I_p [42], [51], [61].

Matematinis modeliavimas padeda nuspręsti, kuri priklausomybė yra geresnė I_p vertinimui - $Y^{1/n}$ ar $(dY/d(hv))^{1/2}$. Pasinaudojant formule 1.1, galima daryti prielaidą, kad paprastu atveju, kai yra tik viena fotoemisijos juosta, Y išvestinės kvadratinė šaknis bus tiesė.

Aptarkime teorinį modelį, kuriame yra dvi fotoemisijos juostos: pirmoji silpnos fotoemisijos juosta ir antroji stiprios fotoemisijos juosta, atitinkamai apibūdinamos I_{pnR1} ir I_{pnR2} lūžio taškais. Taip pat egzistuoja pastovus foninis signalas C, kurį sukelia foninė spinduliuotė, išsklaidyta šviesa ar kiti reiškiniai, tuomet Y gali būti aprašytas taip:

$$Y = C, \text{ jei } x < I_{pR1} \tag{1.2}$$

$$Y = C + A \cdot \left(x - I_{pR1}\right)^3, \text{ jei } I_{pR1} < x < I_{pR2} \tag{1.3}$$

$$Y = C + A \cdot \left(x - I_{pR1}\right)^3 + \left(x - I_{pR2}\right)^3, \text{ jei } x > I_{pR2} \tag{1.4}$$

Čia x reiškia kvantinę energiją. Parametras $A < 1$ reiškia, kad pirmosios juostos intensyvumas yra mažesnis už antrosios, o antrosios intensyvumas yra 1.
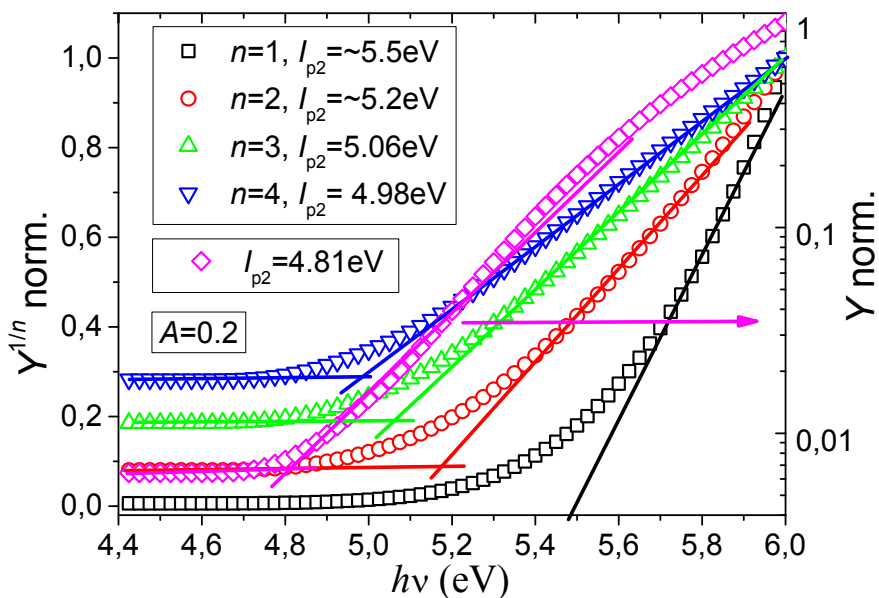
7 pav. Teorinių skaičiavimų rezultatai pavaizduoti kaip $Y^{1/n}$ priklausomybė nuo x (kvanto energija) tiesinėse ir logaritminėse skalėse (rožinis deimantas). Y reikšmės buvo apskaičiuotos pagal formules (1.2), (1.3) ir (1.4) naudojant tokius parametrus: $I_{pR1} = 4.6$, $I_{pR2} = 5$, $C = 0.01$ ir $A = 0.2$.

Y reikšmių diagrama parodyta 7 pav., kaip $Y^{1/n}$ priklausomybė nuo x. Y vertės buvo apskaičiuotos naudojant (1.2), (1.3) ir (1.4) formules. Norint rasti susikirtimo taškus, nubrėžtos aproksimavimo tiesės. Susikirtimo taškas tarp x ašies ir aproksimavimo tiesės, yra laikoms I_{p2}. Reikia pažymėti, kad $n = 1$ or 2 atvejais, praktiškai neįmanoma parinkti tinkamų aproksimavimo kreivių, todėl buvo pasirinktas „geriausiai atrodantis" variantas.

Lentelė 3. I_{p2} vertės susikirtimo taške, priklausomai nuo A parametro

n	I_{p2}, eV		
	$A = 0.05$	$A = 0.2$	$A = 0.5$
1	~5.6	~5.5	~5.5
2	~5.3	~5.2	~5.2
3	5.1	5.06	4.93
4	5.04	4.98	4.86
1, log skalė	5.04	4.81	4.74
Išvestinė	5.05	5.08	5.11

I_{p2} vertės vertės susikirtimo taške, priklausomai nuo A parametro pateiktos lentelėje 3. Beveik visais atvejais apskaičiuota I_{p2} vertė reikšmingai skiriasi nuo realiosios vertės $I_{p2} = 5$. Be to, problematiška nuspręsti, kaip šiuose grafikuose rasti tikrąją I_{p1} vertę, kuri yra 4,6 eV. Naujas būdas išspręsti aukščiau aprašytas problemas yra I_p nustatymas braižant $(\mathrm{d}Y/\mathrm{d}(h\nu))^{1/2}$ priklausomybę.
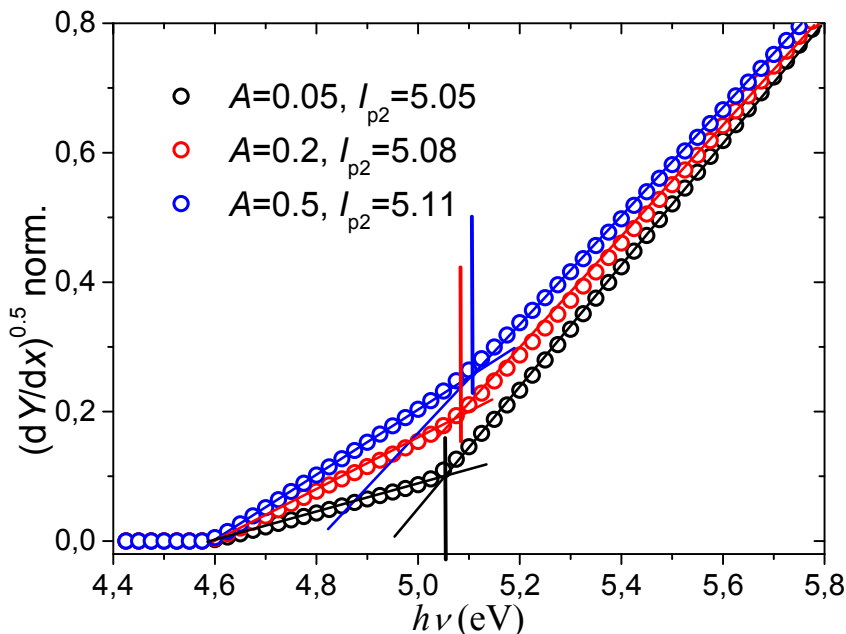
Diferencijuojant (1.2) - (1.4) gaunama

$$\frac{\mathrm{d}Y}{\mathrm{d}x} = 0, \text{jei } x < I_{pR2} \tag{1.5}$$

$$\frac{\mathrm{d}Y}{\mathrm{d}x} = 3A \cdot \left(x - I_{pR1}\right)^2, \text{jei } x < I_{pR2} \tag{1.6}$$

$$\frac{\mathrm{d}Y}{\mathrm{d}x} = 3A \cdot \left(x - I_{pR1}\right)^2 + 3\left(x - I_{pR2}\right)^2, \text{jei } x > I_{pR2} \tag{1.7}$$

8 pav. Y atvaizduota pagal $(\mathrm{d}Y/\mathrm{d}(h\nu))^{1/2}$, skaitmeninės vertės apskaičiuotos pagal formules (1.5) - (1.7), kai $I_{pR1} = 4.6$ eV ir $I_{pR2} = 5$ eV. 8 pav. kiekvienoje kreivėje galima nesunkiai išskirti tiesines dalis.

8 pav. Y priklausomybė nuo energijos $(\mathrm{d}Y/\mathrm{d}(h\nu))^{1/2}$ atvaizdavime remiantis formulėmis (2.7) to (2.9)

1.2.4 Tirtos medžiagos

Siekiant parodyti naujojo metodo galimybes, buvo ištirta keletas gerai žinomų medžiagų: bemetalis ftalocianinas (H_2Pc), titaniloftalocianinas (TiOPc), N, N′-is (3-metilfenil) -N, N′-difenilbenzidinas (TPD) iš „Sands Co.", regioreguliarus poliheksiltiofenas (P3HT) iš „Sigma Aldrich". Medžiagų cheminės formulės parodytos 9 pav. TiOPc ir H_2Pc milteliai buvo disperguoti THF tirpiklyje be rišamųjų medžiagų, dispersija buvo užlieta ant padėklų, susidedančių iš poliesterio plėvelės, padengtos laidžiu Al sluoksniu, ir ~ 0,5 μm storio polimero. TPD buvo ištirpintas THF ir padengtas ant padėklo. P3HT buvo ištirpintas chloroforme. Mėginiai buvo džiovinami 30 minučių kaitinant 60°C temperatūroje.
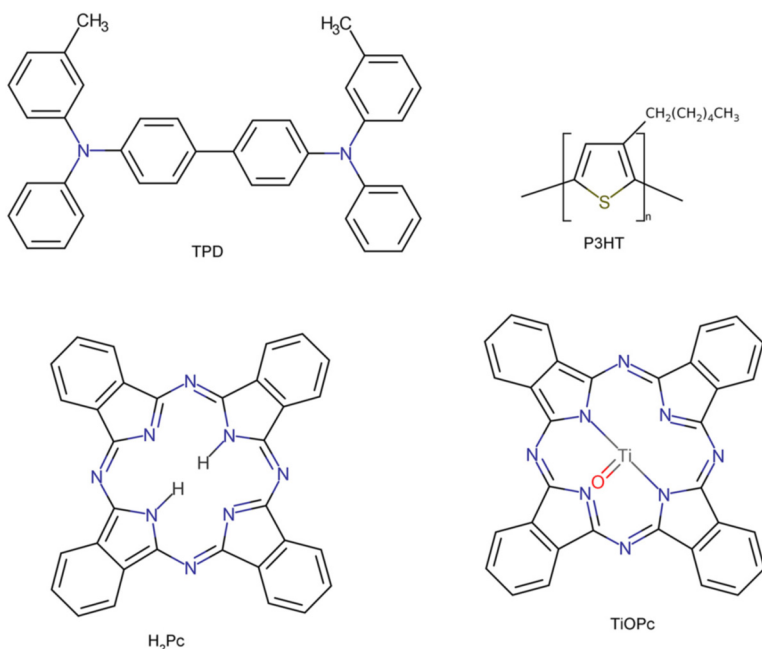
9 pav. Tirtų medžiagų struktūrinės formulės: TPD, P3HT, H_2Pc, TiOPc.

1.2.5 Rezulatai

10 pav. H_2Pc miltelių I_p buvo įvertintas naudojant $(dY/d(h\nu))^{1/2}$ priklausomybę. Spektrą galima suskirstyti į 3 sritis: iki x_1 = 4.95 eV yra tamsinė sritis, tarp x_1 = 4.95 eV ir x_2 = 5.15 eV (I_{p2}) yra antroji tiesinė sritis, ir nuo 5.15 eV seka trečioji tiesinė sritis.
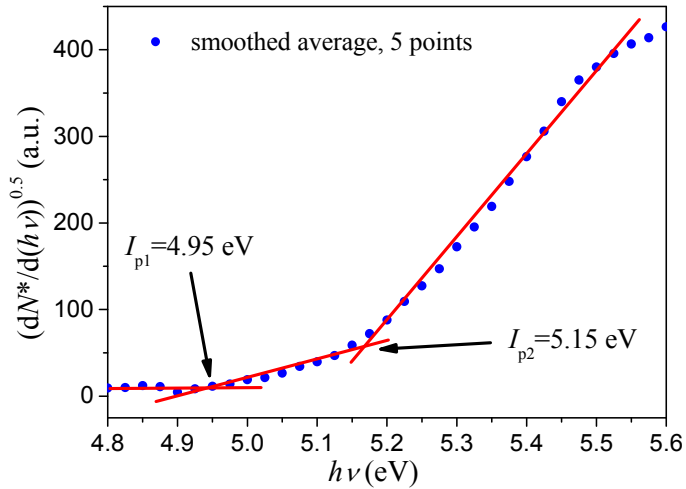
10 pav. H₂Pc fotoemisijos spektras.

10 pav. tie patys duomenys atvaizduoti pagal $Y^{1/n}$ priklausomybę ir logaritminėje skalėje.
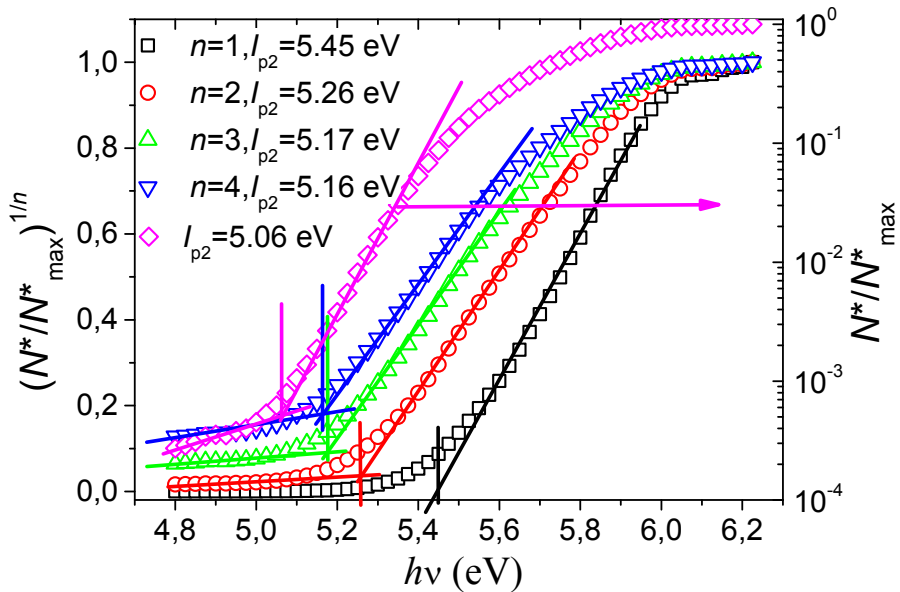
11 pav.: Normalizuotas H₂Pc fotoemisijos spektras įvairiuose atvaizdavimuose.

Apskaičiuotos I_p vertės svyruoja nuo 5.45 eV, kai $n = 1$ iki 5.16 eV, kai $n = 4$. Kai kurios vertės galėtų būti palyginamos su I_{p2}, tačiau nei viena vertė neindikuoja I_{p1} egzistavimo. $(dY/d(h\nu))^{1/2}$ metodas geriau atskleidžia spektro ypatumus bei leidžia įžiūrėti daugiau spektro polinkių.

Šiame skyriuje ištirtų ir aptartų medžiagų rezultatai apibendrinti lentelėje 4. Visais atvejais lūžio taškai pereina prie mažesnių energijų didėjant n.

Lentelė 4. I_p matavimų rezultatai elektronvoltais (eV).

Medžiaga	I_p (eV±0.05eV), kai				Log skalė	$(Der)^{0.5}$	
	$n = 1$	$n = 2$	$n = 3$	$n = 4$		I_{p1}	I_{p2}
TiOPc	5.61	5.47	5.40	5.36	5.3	5.25	5.41
H$_2$Pc	5.45	5.26	5.17	5.16	5.06	4.95	5.15
TPD	5.57	5.46	5.39	5.35	5.28	5.16	5.34
P3HT	4.83	4.72	4.67	4.65	4.61	4.40	4.66

5 lentelėje parodytas eksperimentinių rezultatų palyginimas su aprašytais literatūroje. Kaip matyti 4 lentelėje, apskaičiuotos I_p vertės pagal $(dY/d(h\nu))^{1/2}$ priklausomybę koreliuoja su vertėmis, apskaičiuotomis pagal $Y^{1/n}$, kai n yra 3 arba 4. I_p verčių skirtumą gali nulemti gamyba metodai, kristalinė ar amorfinė struktūra bandinio struktūra, matavimo įrenginio paklaidos arba vieta, kur mėginys buvo pagamintas ir matuotas: atmosferoje, inertinių dujų aplinkoje arba vakuume. Šiame eksperimente, jei nenurodyta kitaip, visi mėginiai buvo matuojami iškart po pagaminimo.

Lentelė 5. I_p matavimų rezultatai elektronvoltais (eV) ir jų palyginimas su publikuotais rezultatais

Medžiaga	PES/PYS	UPS	CV	KP	$I_{p1}/I_{p2,}$ (±0.05eV)
TiOPc	5.24* [61], [77]	5.2 [32]–[34]			5.25/5.41
H$_2$Pc	5.1* [78]	4.95-5.1 [29],[32],[70]		5.1 [80]	4.95/5.15
TPD	5.34** [43]	5.1-5.2 [29]–[31]	5.55 [41]		5.16/5.34
P3HT	4.54** [36], 4.75* [45]	4.6-4.85 [36], [37], [81], [82]	5.2 [83]		4.40/4.66
Au	4.78* [76]	5.10[75]			4.60***, 4.92****

*ore; **vakuume; ***po pagaminimo; ****po 7 dienų;

1.2.6 I_{p1} ir I_{p2} verčių reikšmė

Pirmąją silpną fotoemisiją, kurios pradžia yra $h\nu = I_{p1}$, gali sukelti įvairūs veiksniai, tokie kaip priemaišų buvimas tiriamame mėginyje, sluoksnių kristalizacija ar agregacija, adsorbuotos dujos ir kt. Tai, taip pat gali nulemti HOMO Gauso funkcijos „uodega" ir, bent jau kai kuriais atvejais, atspindi tikrąją jonizacijos potencialo vertę. Rezultatų palyginimas su UPS tyrimų rezultatais padeda tiksliau atsakyti į šį klausimą. TiOPc atveju jonizacijos potencialo arba HOMO lygio vertė, nustatyta UPS metodika [32]–[34], yra 5,2 eV, o I_{p1}= 5,25 eV yra labai artima šiai vertei. Todėl galime daryti išvadą, kad šiuo atveju I_{p1} vertė atitinka HOMO vertę. Tada reikšmė I_{p2} = 5,41 eV gali atitikti HOMO - 1. H_2Pc atveju UPS nustatyta vertė yra 4,95 eV [35] sutampa su I_{p1} = 4,95 eV, o I_{p2} = 5,15 eV yra artima 5,1 eV UPS vertei [79]. Su VB-UPS nustatyta H_2Pc 4,96 eV jonizacijos energija sutampa su I_{p1}= 4,95 eV. Tačiau nėra jokių požymių, kad būtų antrasis lūžio taškas, kuris yra ties 5,15 eV. TPD UPS matavimai parodė 5,1–5,2 eV vertes, kurios yra artimos I_{p1} = 5,16 eV reikšmei, todėl galime manyti, kad ši vertė atspindi HOMO. Tada antroji vertė - I_{p2} = 5,34 eV, gali būti laikoma HOMO - 1. P3HT atveju UPS vertė HOMO yra 4,6 - 4,85 eV, o tai yra artima I_{p2} = 4,66 eV vertei. Jei vertinsime šią vertę kaip HOMO, tada fotoemisijos, kurios pradžia yra I_{p1} = 4,40 eV, nebuvo arba ji buvo per silpna, kad būtų aptikta UPS eksperimentuose. Tai gali sukelti skirtingos eksperimento sąlygos - aukštas vakuumas UPS eksperimento metu ar dujų mišinys šiuo atveju. Kiti veiksniai, į kuriuos reikia atsižvelgti, yra šie: kaip mėginiai keičia savo paviršiaus savybes oro aplinkoje, kaip laikomos pradinės medžiagos (mūsų atveju visos medžiagos, išskyrus P3HT, laikomos ore) arba kada buvo matuojamas mėginys. Pvz. Au bandinio I_p vertė per savaitę pasikeičia iki 0,30 eV. Yra žinoma, kad Au bandiniai yra jautrūs užterštumui [56]. TPD, H_2Pc, TiOPc atveju, mėginius laikant ore vieną savaitę, I_p vertės pasikeitė tik paklaidos ribose.

1.3 Krūvininkų judrio nustatymas organinėms medžiagoms

1.3.1 Kserografis lėkio trukmės metodas (XTOF)

XTOF metodika leidžia matuoti bandinius tik su vienu elektrodu ir įvertinti krūvininkų judrį didelės varžos puslaidininkiuose [88]. Taip pat verta paminėti, kad XTOF matavimams bandiniai gali būti paruošti paprastu liejimo iš tirpalo metodu.

XTOF veikimo principas: įžemintas bandinys tamsoje įelektrinamas vainikiniu išlydžiu. Tuomet trumpas stipriai sugeriamos šviesos impulsas bandinio paviršiuje sugeneruoja elektronų-skylių poras. Šviesos bangos ilgis parenkamas taip, kad absorbcijos gylis būtų $\delta(\lambda) << d$, kur d yra bandinio storis. Tarkime, esant teigiamam paviršiaus potencialui, laisvos skylės yra traukiamos link laidaus pagrindo [88], [89]. Tokiu atveju, žinant trukmę, per kurią skylės pereis per bandinį t_{tr}, prijungtą įtampą U_0 bei bandinio storį d, pasinaudojus formule 1.8 galima apskaičiuoti skylių judrį μ_d. t_{tr} trukmė nustatoma iš krūvininkų dreifo dU/dt kinetikų.

$$t_{tr} = \frac{d^2}{\mu_d\, U_0}. \hspace{2cm} (1.8)$$

1.3.2 Rezultatai

Bandiniai su HTM1 - HTM5 buvo paruošti liejimo metodu. HTM buvo ištirpinti THF tirpiklyje. HTM sluoksnis suformuotas ant poliesterio plėvelės su laidžiu Al sluoksniu. Papildomai buvo pagaminti bandinai sumaišant HTM ir polikarbonatą (PC-Z) („Mitsubishi Gas Chemical Co.", polikarbonatas „Iupilon Z-200") 1: 1 masės dalimis THF tirpiklyje. Yra žinoma, kad paruoštų bandinių kokybė turi įtakos judrio matavimų rezultatams [91]: kiekviena molekulė turi skirtingas sluoksnio formavimo savybes, todėl, siekiant minimizuoti sluoksnio pagaminimo kokybės įtaką rezultatams, buvo atlikti papildomi XTOF matavimai HTM PC-Z matricoje. Absoliučios judrio vertės yra mažesnės, nes struktūroje yra nelaidaus polimero, tačiau struktūros ir savybių santykis yra geriau išreikštas.

Bandinių storiai buvo tarp 2 μm ir 6 μm. Bandinys įelektrinamas naudojant vainikinį išlydį. Krūvininkai sugeneruojami sluoksnio paviršiuje apšviečiant azoto lazerio impulsais (impulso trukmė 2 ns, bangos ilgis 337 nm). Tranzito trukmė t_{tr} buvo nustatyta pagal dU/dt krūvininkų dreifo kinetikas dvigubame logaritminiame mastelyje. Krūvininkų judris apskaičiuotas pagal formulę (1.8).

Krūvininkų dreifo kinetikos integraliniame režime parodė, kad visos tirtos organinės medžiagos yra skylinio laidumo (įskaitant ir bandinius su PC-Z).

12 (c ir d) paveiksluose parodyta grynos HTM2 medžiagos ir HTM2 + PC-Z mišinio dU/dt priklausomybė. Kreivėse matomas dispersiška skylių pernaša, o tai indikuoja apie stiprią judrio priklausomybę nuo elektrinio

lauko bei esančius prilipomo lygmenis. 12 pav. (e) atvaizduota μ priklausomybė nuo elektrinio lauko bandiniams su HTM2 ir HTM2 + PC-Z.
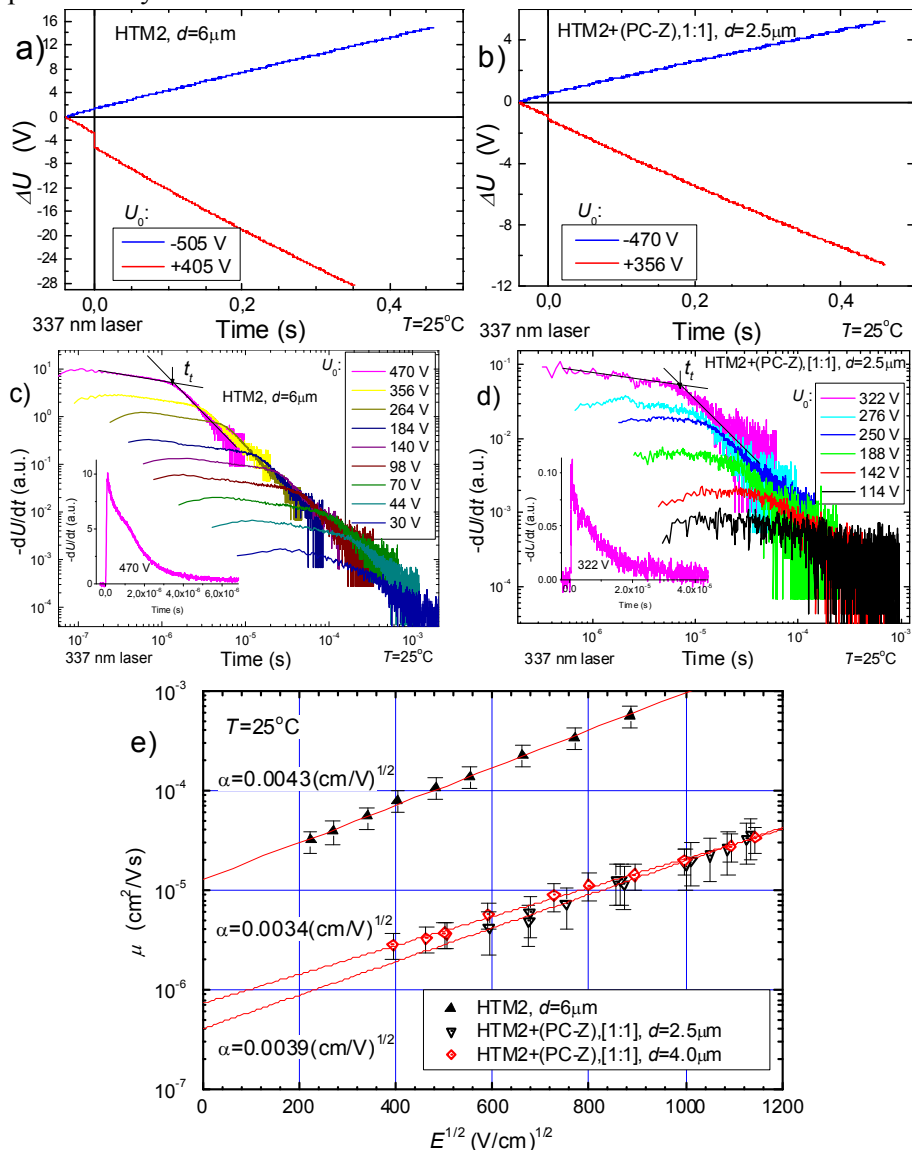
12 pav. a- HTM2 medžiagos krūvininkų dreifo kinetikos integraliniame režime ir b – mišinyje su PC-Z. c- HTM2 skylių pernašos dU/dt kinetikos. d- HTM2 + PC-Z skylių pernašos dU/dt kinetikos. e- μ priklausomybė nuo elektrinio lauko bandiniams su HTM2 ir HTM2+PC-Z.

Matavimų rezultatai apibendrinti 13 pav. ir 6 lentelėje. XTOF matavimai parodė, HTM1, HTM2, HTM4, HTM5 medžiagose skylių dreifinis judris

silpnuose elektriniuose laukuose yra apie $\sim 10^{-5}$ cm^2 V^{-1}s^{-1} ir $\sim 3 \times 10^{-4}$ cm^2 V^{-1}s^{-1}, kai elektrinio lauko stipris buvo 6.4×10^5 Vcm^{-1}. 13(b) paveiksle pateikti XTOF matavimai HTM1-HTM5 mišinyje PC-Z (1:1). μ vertės buvo maždaug viena eile mažesnės, esant lauko stiprumui 10^6 Vcm^{-1}. Tokios μ vertės yra palyginamos arba didesnės su Spiro-OMeTAD μ vertėmis.
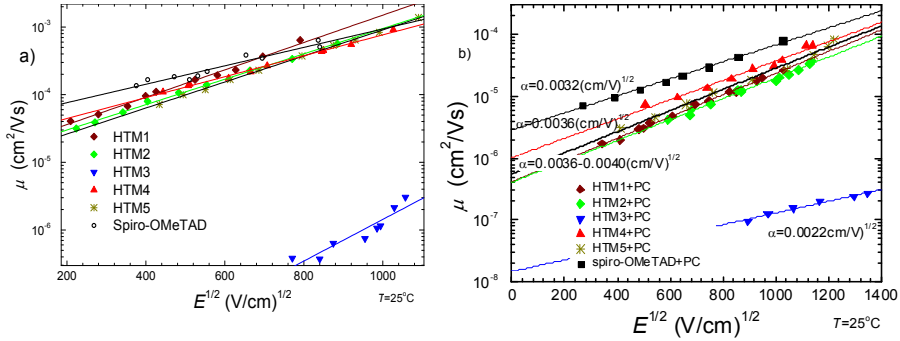
13 pav. μ priklausomybė nuo elektrinio lauko bandiniams su HTM1-5 (a) ir HTM1-5+PC-Z (b) bei Spiro-OMeTAD.

Lentelė 6. I_p grynose HTM, μ_0 ir μ grynose HTM ir mišinyje su PC-Z (1:1).

| Medžiagos	I_p, (eV)	μ_0 , (cm^2 V^{-1} s^{-1})	μ ,(cm^2 V^{-1} s^{-1})
HTM1	5.05	1.4×10^{-5}	5.9×10^{-4}
HTM2	5.00	1.3×10^{-5}	3.8×10^{-4}
HTM3	5.00	1×10^{-9}	3×10^{-7}
HTM4	4.92	2.2×10^{-5}	3.8×10^{-4}
HTM5	5.03	1.1×10^{-5}	3.8×10^{-4}
Spiro-OMeTAD	5.00	4.1×10^{-5}	5×10^{-4}
HTM1 + PC	-	3.9×10^{-7}	2.3×10^{-5}
HTM2 + PC	-	4.0×10^{-7}	1.9×10^{-5}
HTM3 + PC	-	1.5×10^{-8}	1.3×10^{-7}
HTM4 + PC	-	1.1×10^{-6}	3.7×10^{-5}
HTM5 + PC	-	5.8×10^{-7}	2.8×10^{-5}
Spiro-OMeTAD+PC	-	2.9×10^{-6}	6.8×10^{-5}

Prof. Sanghyun Paek ir prof. Michael Saliba pagamino ir išanalizavo perovskito SC su HTM1-5. SC PCE buvo nuo 9% iki 16,8% [63]. Toks rezultatų skirtumas, parodė ryšį tarp HTM cheminės struktūros ir fotoelektrinių savybių ir leido įvertinti, kaip netinkamoje vietoje esanti metilo

grupė gali pakenkti prietaiso veikimui. Perovskito SC struktūrą sudarė legiruotas alavo oksidas (FTO) / kompaktiškas TiO_2 / mezoporinis TiO_2 / perovskitas / HTM / Au. Vieno žingsnio perovskito tirpalas buvo paruoštas sumaišius 1,15 m PbI_2, 1,10 m FAI, 0,2 m $PbBr_2$, 0,2 m MABr DMF: DMSO tirpiklyje (tūrio santykis 4:1).

1.4 Skersaryšinami HTM

Pagrindiniai skersaryšinamų polimerų panaudojimo privalumai organiniams ar neorganiniams SC yra šie: a) morfologijos stabilizavimas [94], b) netirpumas - nereikia ortogonalaus tirpiklio ir tai atveria galimybę gaminti invertuotas SC [27], c - padidina atsparumą vandeniui , deguoniui, karščiui bei padidina atsparumą mechaniniam poveikiui [95].

Norint pagaminti pigius SC, terminis skersaryšinimas yra paprasčiausias metodas, nereikalaujantis jokių cheminių priedų ar specialios įrangos, kuri apsunkintų didelio ploto SC gamybą. Tačiau šis būdas turi vieną trūkumą - skersaryšinimo temperatūra dažnai viršija aukščiausią galimą perovskito atkaitinimo temperatūrą [96]. Vienas iš sprendimų yra gaminti perovskito SC su invertuota struktūra. Kauno technologijos universitete buvo susintetintos skylių pernašos medžiagos su fluoreno pagrindu. Medžiagų struktūrinės formulės pateiktos 14 pav.
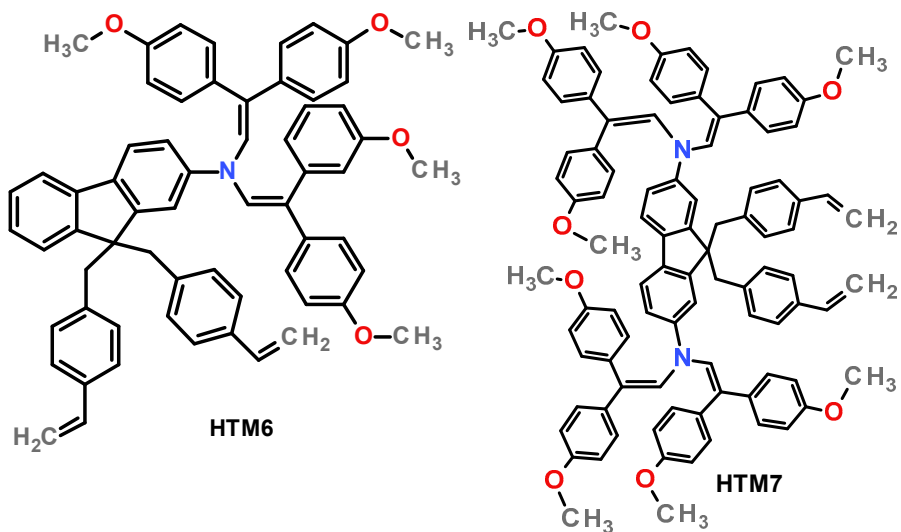
14 pav. HTM6 ir HTM7 medžiagų cheminės struktūrinės formulės.

N, N-bis [2,2-bis (4-metoksifenil) vinil] -9H-fluoren-2-aminas (HTM6) ir N^2, N^2, N^7, N^7-tetrakis [2,2-bis (4-metoksifenilas) vinilas] -9H-fluoren-2,7-

93

diaminas (HTM7) buvo ištirtos XTOF ir PYSA metodais. HTM6 ir HTM7 skersaryšinimas truko 45 minutes esant 230-240 °C temperatūrai.
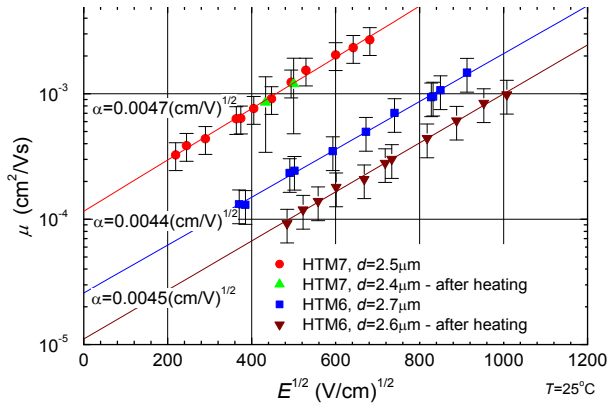
15 pav. μ priklausomybė nuo elektrinio lauko HTM6 ir HTM7 bandiniams prieš ir po kaitinimo.

15 pav. atvaizduota μ priklausomybė nuo elektrinio lauko HTM6 ir HTM7 bandiniams prieš ir po kaitinimo. HTM7 medžiagos μ prieš ir po kaitinimo buvo apie 10^{-3} cm^{2}V^{-1}s^{-1}, esant 3.6×10^5 Vcm^{-1} elektriniam laukui. HTM6 pademonstravo šiek tiek mažesnį skylių judrį - 3.5x10^{-4} cm^{2}V^{-1}s^{-1} ir 1.75x10^{-4} cm^{2}V^{-1}s^{-1} skersaryšintame sluoksnyje, kai elektrinio lauko stipris buvo 3.6×10^5 Vcm^{-1}. Šios vertės yra palyginamos ar net geresnės, nei daugelis dažniausiai naudojamų HTM perovskito SC.

PYSA rezultatai HTM6 ir HTM7 parodyti 16 pav. I_p vertės HTM6 ir HTM7 prieš kaitinimą buvo 5,26 ir 5,11 eV, o po kaitinimo - 5,39 ir 5,30 eV atitinkamai. Tokios vertės atitinka kitų HTM, naudojamų perovskito SC.
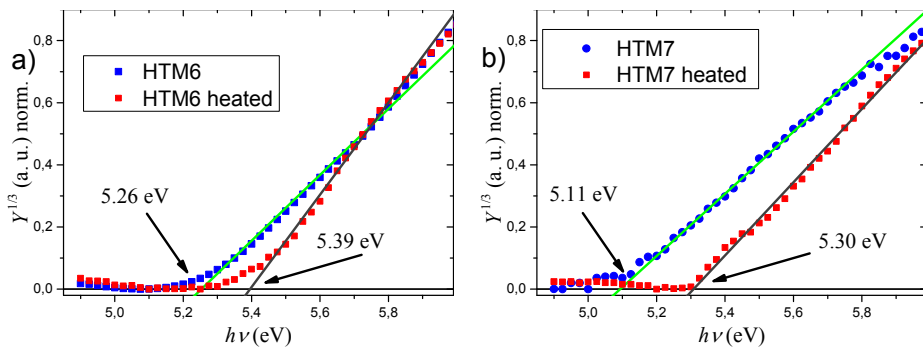
16 pav. Fotoemisijos spektrai HTM6 (a) ir HTM7 (b) medžiagų, prieš ir po kaitinimo.

Dr. Amran Al-Ashouri ir prof. Steve Albrecht pagamino invertuotas peroskito SC su HTM6 ir HTM7 medžiagomis. SC su HTM6 prieš ir po skersaryšinimą pasiekė ~ 14% PCE, o SC su HTM7 PCE prieš kaitinimą buvo ~ 15% ir po kaitinimo padidėjo iki 16%. SC struktūra buvo sudaryta iš ITO/HTM6-7/perovskito/C60/BCP/Ag. Perovskito tirpalo kopozicija buvo sudaryta iš $Cs_{0.05}(FA_{0.83}MA_{0.17})_{0.95}Pb(I_{0.83}Br_{0.17})_3$ [27].
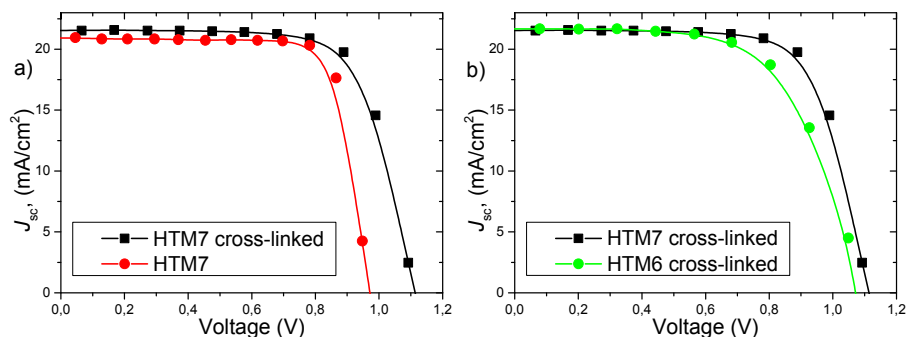
17 pav. Perovskito SC su HTM6 ir HTM7 VACh matavimai. a) SC palyginimas, kai HTM7 buvo neskersaryšinta ir skersaryšinta b) SC palyginimas, kai HTM6 ir HTM7 buvo skersaryšintos [27].

17 pav. perovskito SC su HTM6 ir HTM7 VACh matavimai. Po skersaryšinimo V_{OC} padidėjo abiems HTM. Tai galima paaiškinti tuo, kad suskersaryšinus šias medžiagas išauga jų I_p arba formuojant perovskito sluoksnį buvo pažeistas skylių pernašos sluoksnis ir dėl to išaugo paviršinė rekombinacija, kas galėjo nulemti mažesnę V_{OC} [97], [98]. Didesnį FF ir PCE galima būtų priskirti didesniam skylių judriui - pagerėjusiam krūvininkų transportavimui per sluoksnį [99].

1.5 CZTS SC

Perovskito SC yra efektyviausios trečiosios kartos saulės celės [100], tačiau perovskitai dažnai sudaryti iš toksiškų elementų, tokių kaip Sb, o SC ilgaamžiškumas vis dar yra problema. Mažiau aplinkai kenksmingos ir neturinčios toksiškų cheminių elementų, yra CZTSSe SC. Tačiau yra gana sudėtinga pagaminti aukštos kokybės CZTSSe sluoksnius, ypač invertuotos struktūros, nenaudojant vakuuminio nusodinimo technikų. Jei gamybos metodui būtų iškelti reikalavimai, tokie kaip didelis plotas ir naši gamyba - purškimas būtų vienas tinkamiausių gamybos būdų.

Toliau bus pristatyti CZTSSe SC, pagaminti naudojant purškimo metodą [101]. Vienas iš tikslų buvo pagaminti neorganinę SC struktūrą, kuri būtų

suderinama su tokiomis medžiagomis kaip HTM1-HTM7, tačiau buvo nuspręsta, kad pirmajame eksperimento etape turėtų būti naudojami gerai žinomi ir komerciškai prieinami HTM, todėl kaip HTM buvo pasirinkta Spiro-OMeTAD.

CZTS aktyviojo sluoksnio gamybos technika buvo tobulinama naudojant automatizuotą purškimo sistemą ir formuojant sluoksnius rankiniu purkštuku. Svarbu paminėti, kad geriausi CZTS sluoksniai buvo pagaminti naudojant rankinį purškimą. Tačiau rankinio purškimo esminis trūkumas yra tas, kad tokie parametrai, kaip atstumas tarp purkštuko ir bandinio, purkštuko judėjimo greitis virš bandinio, purškiamo tirpalo srautas ir kt. yra sunkiai kontroliuojami. Todėl pagrindinis automatizuoto purškimo tikslas buvo išbandyti skirtingus gamybos parametrus, juos modifikuoti ar formuoti sluoksnius iš skirtingų tirpalų identiškomis sąlygomis, kas yra beveik neįmanoma naudojant rankinį purškimą. Tuomet, pagal su automatizuota purškimo sistema nustatytus preliminarius parametrus, buvo formuojami sluoksniai naudojant rankinį purškimą.

1.5.1 Automatizuota purškimo sistema
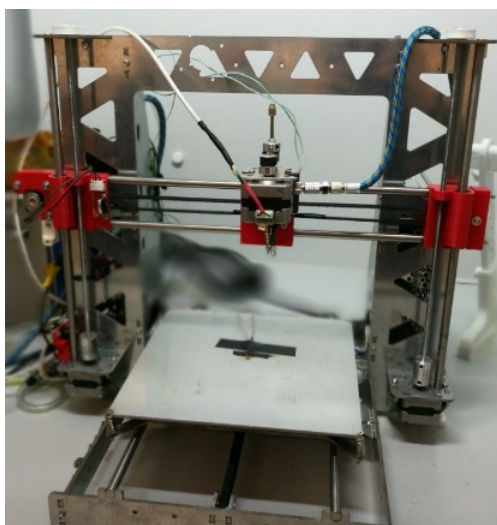
18 pav. Automatizuota purškimo sistema, skirta formuoti CZTS sluoksniams.
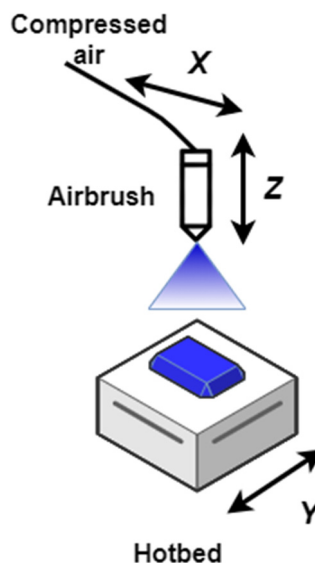
19 pav. Supaprastintas purškimo sistemos veikimo principas.

Purškimo sistema paremta „RepRap" stiliaus 3D spausdintuvu [102], modifikuota „Marlin" programine įranga [103] ir valdoma per „Arduino Mega 2560", siunčiant valdikliui G-CODE [104]. Tirpalo paskirstymui ant padėklų buvo naudojamas modifikuotas „Harder & Steenbeck" aerografas. Sistemos nuotrauka ir supaprastintas įrenginio veikimo principas parodytas 18 ir 19 paveiksluose. Sistemoje yra judanti platforma y ašimi, su kuria kartu juda kaitlentė, ant kurios dedamas bandinys. Aerografas gali judėti išilgai x ir z ašimi. Aerografo veikimas paremtas Bernoulli principu. Oro srautas sukuria skirtingo slėgio zonas ir sudaromos sąlygos siurbti tirpalą iš rezervuaro. Tirpalas patekęs į oro srautą suardomas į lašelius. Pradiniu oro srautu lašeliai pernešami ant padėklo. Oro srautas reguliuojamas purkštuko adatėlę traukiant į viršų ar į apačią. Adatėlė yra pritvirtinta prie žingsninio variklio, kurį valdo kompiuteris.

1.5.2 CZTS SC gamyba
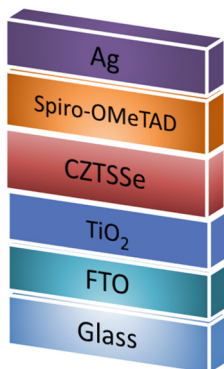
20 pav. CZTSSe SC struktūra.

20 pav. pavaizduota SC struktūra. SC buvo gaminamos ant laidžių fluoru legiruoto alavo oksido (FTO) padengtų stiklo pagrindų. 30–50 nm kompaktinis titano dioksido (TiO_2) sluoksnis buvo nusodintas ant FTO. Ant TiO_2 sluoksnio cheminėje vonelėje (CBD) nusodintas CdS buferinis sluoksnis. Po to suformuotas CZTS sluoksnis esant 340°C padėklo temperatūrai, naudojant purškimo pirolizę. Tirpalas buvo purškiamas per stiklinį antgalį (0,25 mm), naudojant suspaustą orą kaip nešančiąsias dujas, su pastoviu tirpalo srauto išpurškimo greičiu (~ 1 ml / min.). Purškimo procedūra buvo pakartota keletą kartų, kad susidarytų maždaug 1,5 μm sluoksnio storis. Susidaręs sluoksnis 1 valandą buvo kaitinamas 340 ° C temperatūroje. Susiformavęs CZTS sluoksnis buvo atkaitinamas grafito kameroje (tūris 20 cm³) su skirtingu Se kiekiu ir 5 mg Sn, Ar (99,999%) dujų atmosferoje.

Selenizavimo procesą sudarė du atkaitinimo etapai ir jie buvo atlikti per 20 minučių 540 ° C temperatūroje. Vėliau besisukančio stalelio metodu suformuotas Spiro-OMeTAD sluoksnis ir ant viršaus termiškai užgarintas 50 nm storio sidabro sluoksnis.
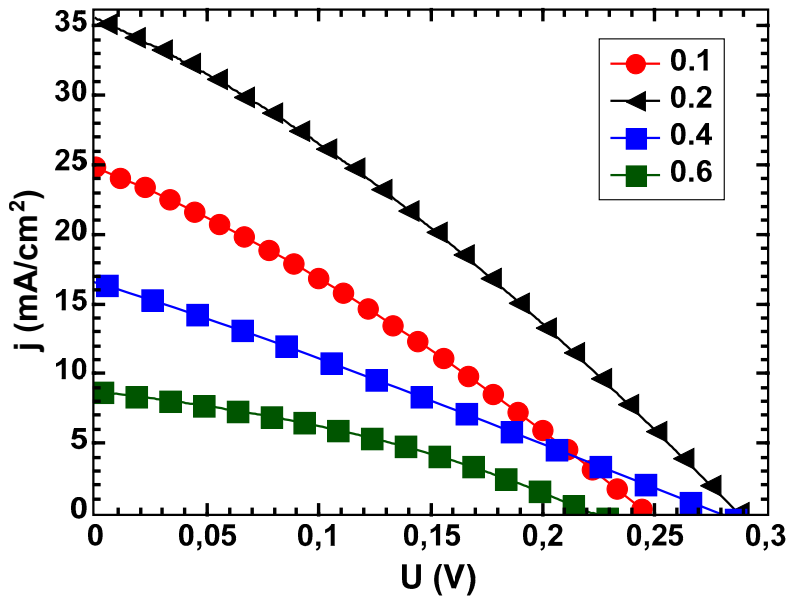
21 pav. CZTSSe SC VACH esant skirtingoms S/(S+Se) koncentracijoms.

21 pav. pateiktos CZTSSe SC VACh charakteristikos. *FF*, J_{sc}, PCE, V_{oc} buvo nustatyti ir atvaizduoti 22 (a-d) pav. Našiausia SC pagaminta naudojant S/(S+Se)=0.2 santykį ir pademonstravo PCE 3,1%. Invertuotos struktūros saulės elementas FTO/TiO₂/Cu₂ZnSnSe₃.₂S₀.₈/ Spiro-OMeTAD /Ag pademonstravo 3,1% efektyvumą, kuris, tuo metu tarp publikuotos literatūros, buvo didžiausias tarp purškimo būdu suformuotų ir invertuotų CZTSSe saulės elementų.
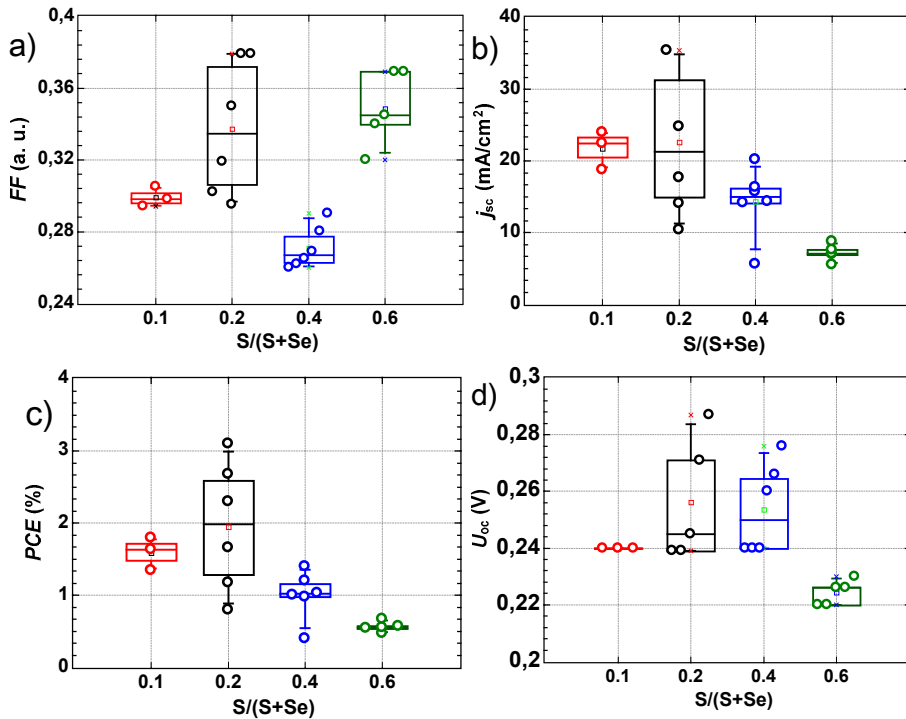
22 pav. Pagrindiniai CZTSSe SC parametrai, proklausomai nuo S/(S+Se) santykio: a- užpildos faktorius, b- trumpo jungimo srovė, c- efektyvumas, d- atviros grandinės įtampa.

23 pav. pavaizduota tipinės perovskito SC, CZTSSe ir suskersaryšintų HTM6 ir HTM7 sluoksnių energijų diagrama. Diagrama rodo, kad HTM6 ir HTM7 yra tinkami CZTSSe SC, kalbant apie energijos lygmenis. Be to, šie HTM yra iki 5 kartų pigesni nei Spiro-OMeTAD [27].
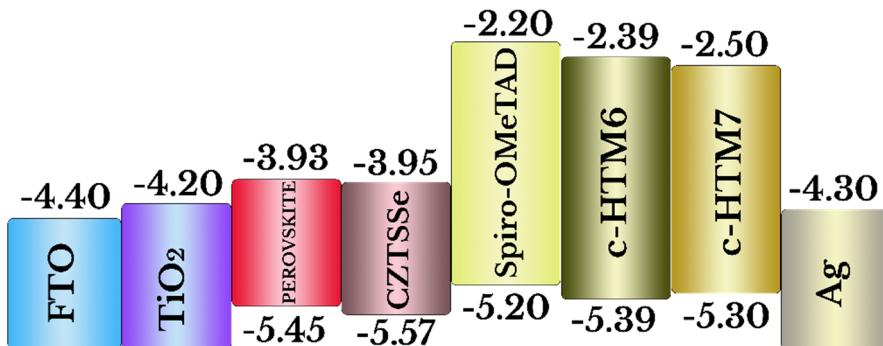
23 pav. Tipinė perovskitų SC, CZTSSe ir suskersaryšintų HTM6 ir HTM7 sluoksnių energijų diagrama [12], [106], [107].

1.6 Išvados

1. Sukurtas matavimo įrenginys, skirtas puslaidininkių ir metalo jonizacijos potencialo nustatymui oro, Ar ir CH$_4$ dujų mišinio aplinkoje. Įrenginys leidžia registruoti foto sroves iki 10^{-19}A. Toks fotojautris leidžia atlikti tikslesnius fotoemisijos spektro matavimus.

2. Fotoemisijos spektras pateiktas $(\mathrm{d}Y/\mathrm{d}(h\nu))^{1/2}$ atvaizdavime, yra informatyvesnis ir parodo daugiau spektro lūžio taškų nei dažniausiai naudojamas $Y^{1/n}$ atvaizdavimas. Naudojant fotoemisijos $(\mathrm{d}Y/\mathrm{d}(h\nu))^{1/2}$ priklausomybę apskaičiuotos I_p vertės yra tikslesnės, lyginant su rastomis vertėmis literatūroje.

3. Metoksidifenilaminu pakeisti fluoreno dariniai HTM1, HTM2, HTM4, HTM5 pademonstravo skylių judrį tarp 3.8×10^{-4} ir 5.9×10^{-4} cm^2 V^{-1} s^{-1}. Šios vertės yra panašios arba didesnės lyginant su dažnai naudojama skylių pernašos medžiaga Spiro-OMeTAD – 5.0×10^{-4} cm^2 V^{-1} s^{-1}. Tačiau, HTM1, HTM2, HTM4, HTM5 darinių sintezė vykdoma dvejais etapais vietoje penkių.

4. Nustatytas HTM1-HTM5 medžiagų jonizacijos potencialas buvo tarp 4.92-5.05 eV. Tokios jonizacinio potencialo vertės tinka pakeisti Spiro-OMeTAD (5.00 eV) perovskito saulės elementų struktūroje.

5. Polimerizacija turi minimalų poveikį krūvininkų pernašai fluoreno pagrindu susintetintoms ir skersaryšinamoms HTM6 ir HTM7 medžiagoms: prieš kaitinimą HTM7 skylių judris siekė $2\mathrm{x}10^{-3}$ cm^{2}V^{-1}s^{-1}, o HTM6 - $3.5\mathrm{x}10^{-4}$ cm^{2}V^{-1}s^{-1}, esant 3.6×10^5 Vcm^{-1} elektriniam lauku. Nustatytos HTM6 ir HTM7 jonizacinio potencialos vertės buvo 5.26 ir 5.11 eV prieš kaitinimą ir 5.39 ir 5.30 eV po kaitinimo. Tokios jonizacinio potencialo vertės yra suderinamos su CZTSSe energine struktūra. Šias suskersaryšintas medžiagas galima panaudoti invertuotoje perovskito saulės celės struktūroje, kaip apatinį skyles pernešantį sluoksnį.

6. Invertuotos struktūros saulės elementas FTO/TiO$_2$/Cu$_2$ZnSnSe$_{3.2}$S$_{0.8}$/ Spiro-OMeTAD /Ag pademonstravo 3,1% efektyvumą, kuris buvo didžiausias tarp publikuotų purškimo būdu suformuotų ir invertuotų CZTSSe saulės elementų.

References

[1]   Saliba, M., "Polyelemental, Multicomponent Perovskite Semiconductor Libraries through Combinatorial Screening," *Adv. Energy Mater.*, vol. 9, no. 25, pp. 1–8, 2019.

[2]   "No Title." [Online]. Available: https://www.nrel.gov/pv/cell-efficiency.html. [Accessed: 16-Jun-2020].

[3]   Bishop, J. E., C. D. Read, J. A. Smith, T. J. Routledge, and D. G. Lidzey, "Fully Spray-Coated Triple-Cation Perovskite Solar Cells," *Sci. Rep.*, vol. 10, no. 1, pp. 1–8, 2020.

[4]   Urbina, A., "The balance between efficiency, stability and environmental impacts in perovskite solar cells: a review," *J. Phys. Energy*, vol. 2, no. 2, p. 022001, 2020.

[5]   Wallace, S. K., D. B. Mitzi, and A. Walsh, "The Steady Rise of Kesterite Solar Cells," *ACS Energy Lett.*, vol. 2, no. 4, pp. 776–779, 2017.

[6]   Kumar, M., A. Dubey, N. Adhikari, S. Venkatesan, and Q. Qiao, "Strategic review of secondary phases, defects and defect-complexes in kesterite CZTS-Se solar cells," *Energy Environ. Sci.*, vol. 8, no. 11, pp. 3134–3159, 2015.

[7]   Walsh, A., S. Chen, S. H. Wei, and X. G. Gong, "Kesterite thin-film solar cells: Advances in materials modelling of Cu 2 ZnSnS 4," *Adv. Energy Mater.*, vol. 2, no. 4, pp. 400–409, 2012.

[8]   Tang, D., Q. Wang, F. Liu, L. Zhao, Z. Han, K. Sun, Y. Lai, J. Li, and Y. Liu, "An alternative route towards low-cost Cu2ZnSnS4thin film solar cells," *Surf. Coatings Technol.*, vol. 232, pp. 53–59, 2013.

[9]   Wang, W., M. T. Winkler, O. Gunawan, T. Gokmen, T. K. Todorov, Y. Zhu, and D. B. Mitzi, "Device characteristics of CZTSSe thin-film solar cells with 12.6% efficiency," *Advanced Energy Materials*, vol. 4, no. 7. 2014.

[10]   Yan, R., L. Kang, Y. Sun, and J. Zhang, "Solution-processed Cu2ZnSnS4thin film with mixed solvent and its application in superstrate structure solar cells," *RSC Adv.*, vol. 8, no. 21, pp. 11469–11477, 2018.

[11]   Wang, Z., N. Brodusch, R. Gauvin, and G. P. Demopoulos, "Nanoengineering of the Cu2ZnSnS4-TiO2interface: Via atomic layer deposition of Al2O3for high sensitivity photodetectors and solid state solar cells," *J. Mater. Chem. A*, vol. 6, no. 24, pp. 11507–11520, 2018.

[12]   Nazligul, A. S., M. Wang, and K. L. Choy, "Recent development in earth-abundant kesterite materials and their applications," *Sustain.*, vol. 12, no. 12, 2020.

[13]   Zhang, Y., C. Kou, J. Zhang, Y. Liu, W. Li, Z. Bo, and M. Shao, "Crosslinked and dopant free hole transport materials for efficient and stable planar perovskite solar cells," *J. Mater. Chem. A*, vol. 7, no. 10,

pp. 5522–5529, 2019.

[14] Atesin, T. A., S. Bashir, and J. L. Liu, *Nanostructured materials for next-generation energy storage and conversion: Photovoltaic and solar energy*. 2019.

[15] Tanaka, K., K. Minoru, G. Koichi, N. Yuya, and H. Uchiki, "Face-to-Face Annealing Process of Cu2ZnSnS4 Thin Films Deposited by Spray Pyrolysis Method.pdf," *Jpn. J. Appl. Phys.*, vol. 51, p. 10NC26, 2012.

[16] Yu, J., H. Deng, Q. Zhang, J. Tao, L. Sun, P. Yang, and J. Chu, "The role of tuning Se/(S + Se) ratio in the improvement of Cu2MnSn(S, Se)4 thin films properties and photovoltaic device performance," *Sol. Energy*, vol. 179, no. December 2018, pp. 279–285, 2019.

[17] Lin, X., J. Kavalakkatt, M. C. Lux-Steiner, and A. Ennaoui, "Inkjet-Printed Cu2ZnSn(S, Se)4Solar Cells," *Adv. Sci.*, vol. 2, no. 6, pp. 2–7, 2015.

[18] Zaki, M. Y., K. Nouneh, M. Ebn Touhami, R. A. Belakhmima, A. C. Galca, L. Pintilie, M. Enculescu, M. Baibarac, and M. Taibi, "Effect of mixing complexing agents on the properties of electrodeposited CZTS thin films," *Opt. Mater. (Amst).*, vol. 83, no. June, pp. 252–256, 2018.

[19] MIYAMOTO, E., Y. YAMAGUCHI, and M. YOKOYAMA, "Ionization Potential of Organic Pigment Film by Atmospheric Photoelectron Emission Analysis," *DENSHI SHASHIN GAKKAISHI (Electrophotography)*, vol. 28, no. 4, pp. 364–370, 1989.

[20] Daskevicience, M., V. Getautis, J. Grazulevicius, A. Stanisauskaite, J. Antulis, V. Gaidelis, V. Jankauskas, and J. Sidaravicius, "Crosslinkable carbazolyl-containing molecular glasses for electrophotography," *J. Imaging Sci. Technol.*, vol. 46, pp. 467–472, 2002.

[21] "Photoelectron spectrometer, Surface Analyzer." [Online]. Available: https://www.hitachi-hta.com/sites/default/files/product_manuals/AC-2%2BEPC5-0150.pdf. [Accessed: 25-Feb-2019].

[22] "Photoelectron Spectrophotometer in Air, Surface Analyzer." [Online]. Available: https://www.rkiinstruments.com/pdf/AC3.pdf. [Accessed: 25-Feb-2019].

[23] Saragi, T. P. I., T. Spehr, A. Siebert, T. Fuhrmann-Lieker, and J. Salbeck, "Spiro compounds for organic optoelectronics," *Chem. Rev.*, vol. 107, no. 4, pp. 1011–1065, 2007.

[24] Kim, H., K. G. Lim, and T. W. Lee, "Planar heterojunction organometal halide perovskite solar cells: Roles of interfacial layers," *Energy Environ. Sci.*, vol. 9, no. 1, pp. 12–30, 2016.

[25] Yu, Z. and L. Sun, "Recent Progress on Hole-Transporting Materials for Emerging Organometal Halide Perovskite Solar Cells," *Adv. Energy Mater.*, vol. 5, no. 12, p. 1500213, 2015.

[26] Kumar, M., A. Dubey, N. Adhikari, S. Venkatesan, and Q. Qiao, "Strategic review of secondary phases, defects and defect-complexes in kesterite CZTS-Se solar cells," *Energy Environ. Sci.*, vol. 8, no. 11, pp. 3134–3159, 2015.

[27] Vaitukaitytė, D., A. Al-Ashouri, M. Daškevičienė, E. Kamarauskas, J. Nekrasovas, V. Jankauskas, A. Magomedov, S. Albrecht, and V. Getautis, "Enamine-Based Cross-Linkable Hole-Transporting Materials for Perovskite Solar Cells," *Sol. RRL*, vol. 5, no. 1, p. 2170012, 2021.

[28] Reinert, F. and S. Hüfner, "Photoemission spectroscopy—from early days to recent applications," vol. 7, p. 97.

[29] Sugiyama, K., D. Yoshimura, T. Miyamae, T. Miyazaki, H. Ishii, Y. Ouchi, and K. Seki, "Electronic structures of organic molecular materials for organic electroluminescent devices studied by ultraviolet photoemission spectroscopy," vol. 83, no. 9, pp. 4928–4938.

[30] Ishii, H., K. Sugiyama, D. Yoshimura, E. Ito, Y. Ouchi, and K. Seki, "Energy-level alignment at model interfaces of organic electroluminescent devices studied by {UV} photoemission: trend in the deviation from the traditional way of estimating the interfacial electronic structures," vol. 4, no. 1, pp. 24–33.

[31] Murdey, R. J. and W. R. Salaneck, "Charge Injection Barrier Heights Across Multilayer Organic Thin Films," vol. 44, no. 6, pp. 3751–3756.

[32] Brumbach, M., D. Placencia, and N. R. Armstrong, "Titanyl Phthalocyanine/C $_{\textrm{60}}$ Heterojunctions: Band-Edge Offsets and Photovoltaic Device Performance," vol. 112, no. 8, pp. 3142–3151.

[33] Placencia, D., W. Wang, J. Gantz, J. L. Jenkins, and N. R. Armstrong, "Highly Photoactive Titanyl Phthalocyanine Polymorphs as Textured Donor Layers in Organic Solar Cells," vol. 115, no. 38, pp. 18873–18884.

[34] Placencia, D., W. Wang, R. C. Shallcross, K. W. Nebesny, M. Brumbach, and N. R. Armstrong, "Organic Photovoltaic Cells Based On Solvent-Annealed, Textured Titanyl Phthalocyanine/C $_{\textrm{60}}$ Heterojunctions," vol. 19, no. 12, pp. 1913–1921.

[35] Kimura, T., M. Sumimoto, S. Sakaki, H. Fujimoto, Y. Hashimoto, and S. Matsuzaki, "Electronic structure of lithium phthalocyanine studied by ultraviolet photoemission spectroscopy," vol. 253, no. 1, pp. 125–131.

[36] Grzibovskis, R. and A. Vembris, "Energy level determination in bulk heterojunction systems using photoemission yield spectroscopy: case of P3HT:{PCBM}," vol. 53, no. 10, pp. 7506–7515.

[37] Cascio, A. J., J. E. Lyon, M. M. Beerbom, R. Schlaf, Y. Zhu, and S. A. Jenekhe, "Investigation of a polythiophene interface using photoemission spectroscopy in combination with electrospray thin-

film deposition," vol. 88, no. 6, p. 62104.

[38] Zahn, D. R. T., G. N. Gavrila, and M. Gorgoi, "The transport gap of organic semiconductors studied using the combination of direct and inverse photoemission," vol. 325, no. 1, pp. 99–112.

[39] Deibel, C., D. Mack, J. Gorenflot, A. Schöll, S. Krause, F. Reinert, D. Rauh, and V. Dyakonov, "Energetics of excited states in the conjugated polymer poly(3-hexylthiophene)," vol. 81, no. 8.

[40] Bard, A. J. and L. R. Faulkner, *Electrochemical methods: fundamentals and applications*, 2nd ed. Wiley.

[41] Kim, J., S. Lee, J. Lee, E. Lim, and B. Jung, "3,3′-Bicarbazole-Based Host Molecules for Solution-Processed Phosphorescent {OLEDs}," vol. 23, no. 4, p. 847.

[42] Ishii, H., H. Kinjo, T. Sato, S. Machida, and Y. Nakayama, "Photoelectron Yield Spectroscopy for Organic Materials and Interfaces," Springer Japan, pp. 131–155.

[43] Fujikawa, H., S. Tokito, Y. Taga, Hisayoshi Fujikawa, Shizuo Tokito, and Yasunori Taga, "Energy structures of triphenylamine oligomers," *Synth. Met.*, vol. 91, no. 1–3, pp. 161–162, 1997.

[44] Ohmori, Y., A. Fujii, M. Uchida, C. Morishima, and K. Yoshino, "Fabrication and characteristics of 8-hydroxyquinoline aluminum/aromatic diamine organic multiple quantum well and its use for electroluminescent diode," vol. 62, no. 25, pp. 3250–3252.

[45] Huang, Y.-J., W.-C. Lo, S.-W. Liu, C.-H. Cheng, C.-T. Chen, and J.-K. Wang, "Unified assay of adverse effects from the varied nanoparticle hybrid in polymer–fullerene organic photovoltaics," vol. 116, pp. 153–170.

[46] Guo, Y., C. Liu, K. Inoue, K. Harano, H. Tanaka, and E. Nakamura, "Enhancement in the efficiency of an organic–inorganic hybrid solar cell with a doped P3HT hole-transporting layer on a void-free perovskite active layer," vol. 2, no. 34, pp. 13827–13830.

[47] Baikie, I. D., A. C. Grain, J. Sutherland, and J. Law, "Dual Mode Kelvin Probe: Featuring Ambient Pressure Photoemission Spectroscopy and Contact Potential Difference," vol. 60, pp. 48–56.

[48] Gutmann, S., M. A. Wolak, M. Conrad, M. M. Beerbom, and R. Schlaf, "Effect of ultraviolet and x-ray radiation on the work function of {TiO}2 surfaces," vol. 107, no. 10, p. 103705.

[49] Helander, M. G., M. T. Greiner, Z. B. Wang, and Z. H. Lu, "Pitfalls in measuring work function using photoelectron spectroscopy," vol. 256, no. 8, pp. 2602–2605.

[50] Yu-Ran Luo, *Handbook of Bond Dissociation Energies in Organic Compounds*, 1st ed. {CRC} Press.

[51] Yamashita, D., Y. Nakajima, A. Ishizaki, and M. Uda, "Photoelectron spectrometer equipped with open counter for electronic structures of organic materials," vol. 14, no. 4, pp. 433–436.

[52] Grigalevicius, S., G. Blazys, J. Ostrauskaite, J. V Grazulevicius, V. Gaidelis, V. Jankauskas, and E. Montrimas, "3,6-Di(N-diphenylamino)-9-phenylcarbazole and its methyl-substituted derivative as novel hole-transporting amorphous molecular materials," vol. 128, no. 2, pp. 127–131.

[53] M. Uda, Sh. Omiya, "Apparatus for detecting low-speed electrons," no. United States Patent: 4740730. .

[54] Ishii, H. and K. Seki, "Energy level alignment at organic/metal interfaces studied by {UV} photoemission: breakdown of traditional assumption of a common vacuum level at the interface," vol. 44, no. 8, pp. 1295–1301.

[55] Martin Pope and Charles E. Swenberg, *Electronic processes in organic crystals and polymers*, 2nd ed. Oxford University Press.

[56] Ishii, H., K. Kudo, T. Nakayama, and N. Ueno, *Electronic processes in organic electronics: bridging nanostructure, electronic states and device properties*, vol. 209. Springer.

[57] Berglund, C. N. and W. E. Spicer, "Photoemission studies of copper and silver: Theory," *Phys. Rev.*, vol. 136, no. 4A, pp. 1030–1044, 1964.

[58] Fowler, R. H., "The Analysis of Photoelectric Sensitivity Curves for Clean Metals at Various Temperatures," vol. 38, no. 1, pp. 45–56.

[59] Fan, H. Y., "Theory of photoelectric emission from metals," *Phys. Rev.*, vol. 68, no. 1–2, pp. 43–52, 1945.

[60] Nakayama, Y., S. Machida, T. Minari, K. Tsukagishi, Y. Noguchi, and H. Ishii, "Direct observation of the electronic states of single crystalline rubrene under ambient condition by photoelectron yield spectroscopy," vol. 93, no. 17, p. 173305.

[61] Honda, M., K. Kanai, K. Komatsu, Y. Ouchi, H. Ishii, and K. Seki, "Atmospheric effect on the ionization energy of titanyl phthalocyanine thin film as studied by photoemission yield spectroscopy," *J. Appl. Phys.*, vol. 455, no. 10, pp. 219–225, 2007.

[62] Masakatsu Kochi, Yoshiya Harada, Tomohiko Hirooka, Hiroo Inokuchi, M. Kochi, Y. Harada, T. Hirooka, and H. Inokuchi, "Photoemission from Organic Crystal in Vacuum Ultraviolet Region," *Bull. Chem. Soc. Jpn.*, vol. 43, no. 9, pp. 2690–2702, 1970.

[63] Tiazkis, R., S. Paek, M. Daskeviciene, T. Malinauskas, M. Saliba, J. Nekrasovas, V. Jankauskas, S. Ahmad, V. Getautis, and M. K. Nazeeruddin, "Methoxydiphenylaminesubstituted fluorene derivatives as hole transporting materials: Role of molecular interaction on device photovoltaic performance," *Sci. Rep.*, vol. 7, no. 1, pp. 1–9, 2017.

[64] Wang, X. *et al.*, "Hole-Transporting Materials Incorporating Carbazole into Spiro-Core for Highly Efficient Perovskite Solar Cells," *J. Mater. Sci. Technol.*, vol. 29, no. 35, pp. 1–8, 2019.

[65] Feng, J., X. Zhu, Z. Yang, X. Zhang, J. Niu, Z. Wang, S. Zuo, S. Priya,

S. (Frank) Liu, and D. Yang, "Record Efficiency Stable Flexible Perovskite Solar Cell Using Effective Additive Assistant Strategy," *Adv. Mater.*, vol. 30, no. 35, pp. 1–9, 2018.

[66] Dong, X., J. Tao, Y. Li, and H. Zhu, "Oriented single crystalline {TiO}2 nano-pillar arrays directly grown on titanium substrate in tetramethylammonium hydroxide solution," vol. 256, no. 8, pp. 2532–2538.

[67] Liu, Y., Y. Hu, X. Zhang, P. Zeng, F. Li, B. Wang, Q. Yang, and M. Liu, "Inhibited aggregation of lithium salt in spiro-OMeTAD toward highly efficient perovskite solar cells," *Nano Energy*, vol. 70, no. January, p. 104483, 2020.

[68] Hwang, J., A. Wan, and A. Kahn, "Energetics of metal–organic interfaces: New experiments and assessment of the field," vol. 64, no. 1, pp. 1–31.

[69] Nekrasovas, J., V. Gaidelis, E. Kamarauskas, M. Viliunas, and V. Jankauskas, "Photoemission studies of organic semiconducting materials using open Geiger-Müller counter," *J. Appl. Phys.*, vol. 126, no. 1, 2019.

[70] Knoll, G. F. and H. W. Kraner, *Radiation Detection and Measurement*, vol. 69, no. 4. 1981.

[71] Tsoulfanidis, N. and Nicholas Tsoulfanidis, *Measurement and detection of radiation*, 2nd ed. Taylor and Francis, 1995.

[72] C. Leroy, P, G. R., *Principles of Radiation Interaction in Matter and Detection*, 2nd editio. World Sciantific Publishing Co. Pte. Ltd, 2009.

[73] Sebenne, C. A., "High-resolution photoemission yield and surface states in semiconductors," *Nuovo Cim. B Ser. 11*, vol. 39, no. 2, pp. 768–780, 1977.

[74] Peek, F. W., *Dielectric phenomena in high-voltage engineering,*. New York: McGraw-Hill Book Company, Inc., 1929.

[75] Eastman, D. E., "Photoelectric Work Functions of Transition, Rare-Earth, and Noble Metals," vol. 2, no. 1, pp. 1–2.

[76] M.Uda, "Open Counter for Low Energy Electron Detection," vol. 24, no. S4, p. 284.

[77] Honda, M., K. Kanai, K. Komatsu, Y. Ouchi, H. Ishii, and K. Seki, "Atmospheric effect of air, N2, O2, and water vapor on the ionization energy of titanyl phthalocyanine thin film studied by photoemission yield spectroscopy," *J. Appl. Phys.*, vol. 102, no. 10, 2007.

[78] C. Adachi, T. Oyamada, Y. Nakajima, *Data Book on Work Function of Organic Thin Films*, 2nd ed. {CMC} International.

[79] Nardi, M. V., F. Detto, L. Aversa, R. Verucchi, G. Salviati, S. Iannotta, and M. Casarin, "Electronic properties of {CuPc} and H2Pc: an experimental and theoretical study," vol. 15, no. 31, p. 12864.

[80] Shintaku, N., M. Hiramoto, and S. Izawa, "Doping for Controlling Open-Circuit Voltage in Organic Solar Cells," vol. 122, no. 10, pp.

5248–5253.

[81] Xu, Z., L.-M. Chen, M.-H. Chen, G. Li, and Y. Yang, "Energy level alignment of poly(3-hexylthiophene): [6,6]-phenyl C61 butyric acid methyl ester bulk heterojunction," vol. 95, no. 1, p. 13301.

[82] Osikowicz, W., M. P. de Jong, and W. R. Salaneck, "Formation of the Interfacial Dipole at Organic-Organic Interfaces: C60/Polymer Interfaces," vol. 19, no. 23, pp. 4213–4217.

[83] Al-Ibrahim, M., "Flexible large area polymer solar cells based on poly(3-hexylthiophene)/fullerene."

[84] Brütting, W., *Physics of Organic Semiconductors*. 2006.

[85] Weiss, P. M. B. and D. S., *Organic Photoreceptors in Xerography*. New York: Marcel Dekker, Inc., 1998.

[86] Bässler, H., "Charge transport in disordered organic photoconductors a Monte Carlo simulation study," vol. 175, no. 1, pp. 15–56.

[87] Borsenberger, P. M. and H. Bässler, "Concerning the role of dipolar disorder on charge transport in molecularly doped polymers," *J. Chem. Phys.*, vol. 95, no. 7, pp. 5327–5331, 1991.

[88] Vaezi-Nejad, S. M., "Xerographic time of flight experiment for the determination of drift mobility in high resistivity semiconductors," *Int. J. Electron.*, vol. 62, no. 3, pp. 361–384, 1987.

[89] Chan, A. Y. C. and C. Juhasz, "Xerographic-mode transient charge technique for probing drift mobility in high-resistivity materials," *Int. J. Electron.*, vol. 62, no. 4, pp. 625–632, 1987.

[90] Vaezdi-Nejad, S. M., "Xerographic time of flight experiment for the determination of drift mobility in high resistivity semiconductors," vol. 62, no. 3, pp. 361–384.

[91] Bässler, H. and A. Köhler, "Charge transport in organic semiconductors.," *Top. Curr. Chem.*, vol. 312, pp. 1–65, 2012.

[92] Jeon, N. J., J. Lee, J. H. Noh, M. K. Nazeeruddin, M. Grätzel, and S. Il Seok, "Efficient Inorganic–Organic Hybrid Perovskite Solar Cells Based on Pyrene Arylamine Derivatives as Hole-Transporting Materials," vol. 135, no. 51, pp. 19087–19090.

[93] Rumer, J. W. and I. McCulloch, "Organic photovoltaics: Crosslinking for optimal morphology and stability," *Mater. Today*, vol. 18, no. 8, pp. 425–435, 2015.

[94] Kahle, F. J., C. Saller, A. Köhler, and P. Strohriegl, "Crosslinked Semiconductor Polymers for Photovoltaic Applications," *Adv. Energy Mater.*, vol. 7, no. 16, pp. 1–10, 2017.

[95] Wantz, G., L. Derue, O. Dautel, A. Rivaton, P. Hudhomme, and C. Dagron-Lartigau, "Stabilizing polymer-based bulk heterojunction solar cells via crosslinking," *Polym. Int.*, vol. 63, no. 8, pp. 1346–1361, 2014.

[96] Dualeh, A., N. Tétreault, T. Moehl, P. Gao, M. K. Nazeeruddin, and M. Grätzel, "Effect of annealing temperature on film morphology of

organic-inorganic hybrid pervoskite solid-state solar cells," *Adv. Funct. Mater.*, vol. 24, no. 21, pp. 3250–3258, 2014.

[97]   Stolterfoht, M., P. Caprioglio, C. M. Wolff, J. A. Márquez, J. Nordmann, S. Zhang, D. Rothhardt, U. Hörmann, Y. Amir, A. Redinger, L. Kegelmann, F. Zu, S. Albrecht, N. Koch, T. Kirchartz, M. Saliba, T. Unold, and D. Neher, "The impact of energy alignment and interfacial recombination on the internal and external open-circuit voltage of perovskite solar cells," *Energy Environ. Sci.*, vol. 12, no. 9, pp. 2778–2788, 2019.

[98]   Correa-Baena, J. P., W. Tress, K. Domanski, E. H. Anaraki, S. H. Turren-Cruz, B. Roose, P. P. Boix, M. Grätzel, M. Saliba, A. Abate, and A. Hagfeldt, "Identifying and suppressing interfacial recombination to achieve high open-circuit voltage in perovskite solar cells," *Energy Environ. Sci.*, vol. 10, no. 5, pp. 1207–1212, 2017.

[99]   Zhou, W., Z. Wen, and P. Gao, "Less is More: Dopant-Free Hole Transporting Materials for High-Efficiency Perovskite Solar Cells," *Adv. Energy Mater.*, vol. 8, no. 9, pp. 1–28, 2018.

[100]   "Best Research-Cell Efficiency Chart." [Online]. Available: https://www.nrel.gov/pv/assets/pdfs/best-research-cell-efficiencies.20200925.pdf. [Accessed: 30-Sep-2020].

[101]   Franckevičius, M. *et al.*, "Efficiency improvement of superstrate {CZTSSe} solar cells processed by spray pyrolysis approach.," vol. 185, pp. 283–289.

[102]   "RepRap project." [Online]. Available: https://en.wikipedia.org/wiki/RepRap_project. [Accessed: 29-Sep-2020].

[103]   "Marlin (firmware)." [Online]. Available: https://en.wikipedia.org/wiki/Marlin_(firmware). [Accessed: 01-Oct-2020].

[104]   "G-code." [Online]. Available: https://en.wikipedia.org/wiki/G-code. [Accessed: 01-Oct-2020].

[105]   Prochowicz, D., M. Franckevičius, A. M. Cieślak, S. M. Zakeeruddin, M. Grätzel, and J. Lewiński, "Mechanosynthesis of the hybrid perovskite CH3NH3PbI3: Characterization and the corresponding solar cell efficiency," *J. Mater. Chem. A*, vol. 3, no. 41, pp. 20772–20777, 2015.

[106]   Wang, X., D.-X. Kou, W.-H. Zhou, Z.-J. Zhou, S.-X. Wu, and X. Cao, "Cu2ZnSnSe4 nanocrystals capped with S2− by ligand exchange: utilizing energy level alignment for efficiently reducing carrier rec ombination," *Nanoscale Res. Lett.*, vol. 9, no. 1, p. 262, 2014.

[107]   Liu, F., S. Bi, X. Wang, X. Leng, M. Han, B. Xue, Q. Li, H. Zhou, and Z. Li, "Similar or different: the same Spiro-core but different alkyl chains with apparently improved device performance of perovskite solar cells," *Sci. China Chem.*, vol. 62, no. 6, pp. 739–745, 2019.

Ionization potential determination results for TPD, TiOPc and P3HT.
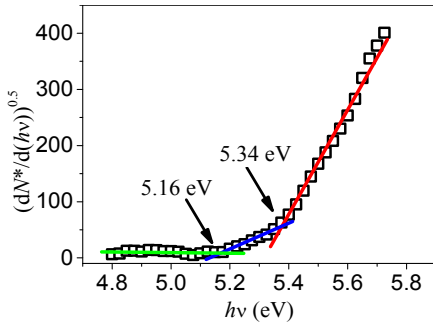
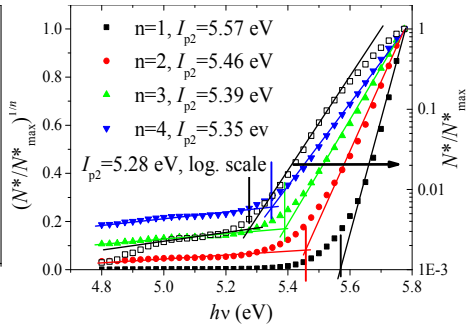

Fig. S1. Photoemission spectrum of TPD.

Fig. S2. Photoemission spectra of TPD in different presentation.
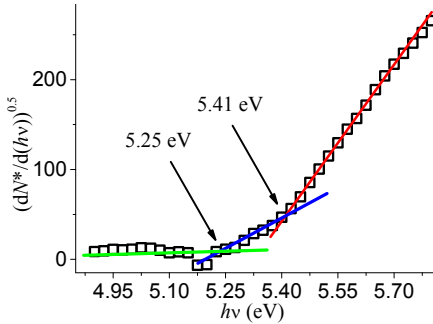
Fig. S3. Photoemission spectrum of TiOPc.
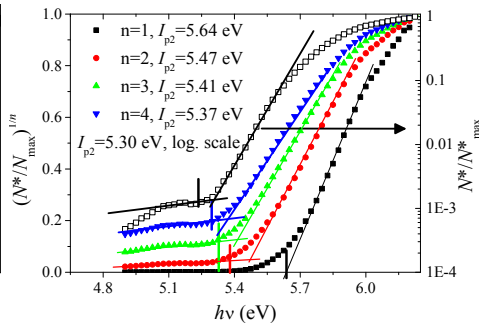
Fig. S4. Photoemission spectra of TiOPc in different presentation.
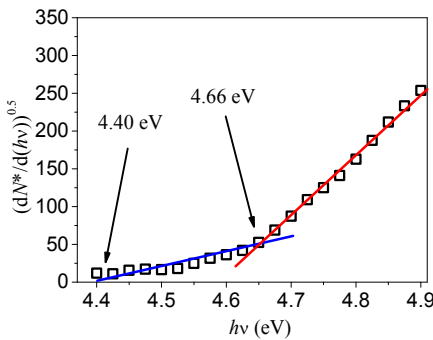
Fig. S5. Photoemission spectrum of P3HT.
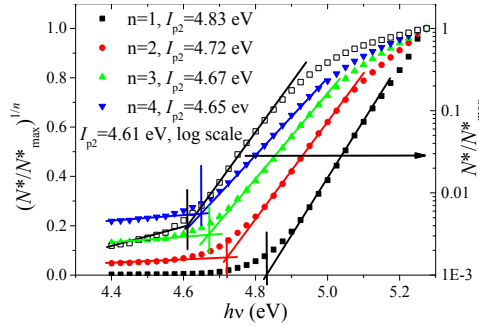
Fig. S6. Photoemission spectra of P3HT in different presentation.

APPENDIX II

Presentation of charge carriers drift kinetics in integral mode, dU/dt hole-transients, field dependent μ values of HTM3 with and without PC-Z.

Fig. S7. a- Charge carriers drift kinetics in integral mode of HTM3 and b – in mixture in PC-Z. c -dU/dt hole-transients of HTM1 in mixture in PC-Z. d - field dependent μ values with and without PC-Z of HTM3.

Presentation of charge carriers drift kinetics in integral mode, dU/dt hole-transients, field dependent μ values of HTM4 with and without PC-Z.
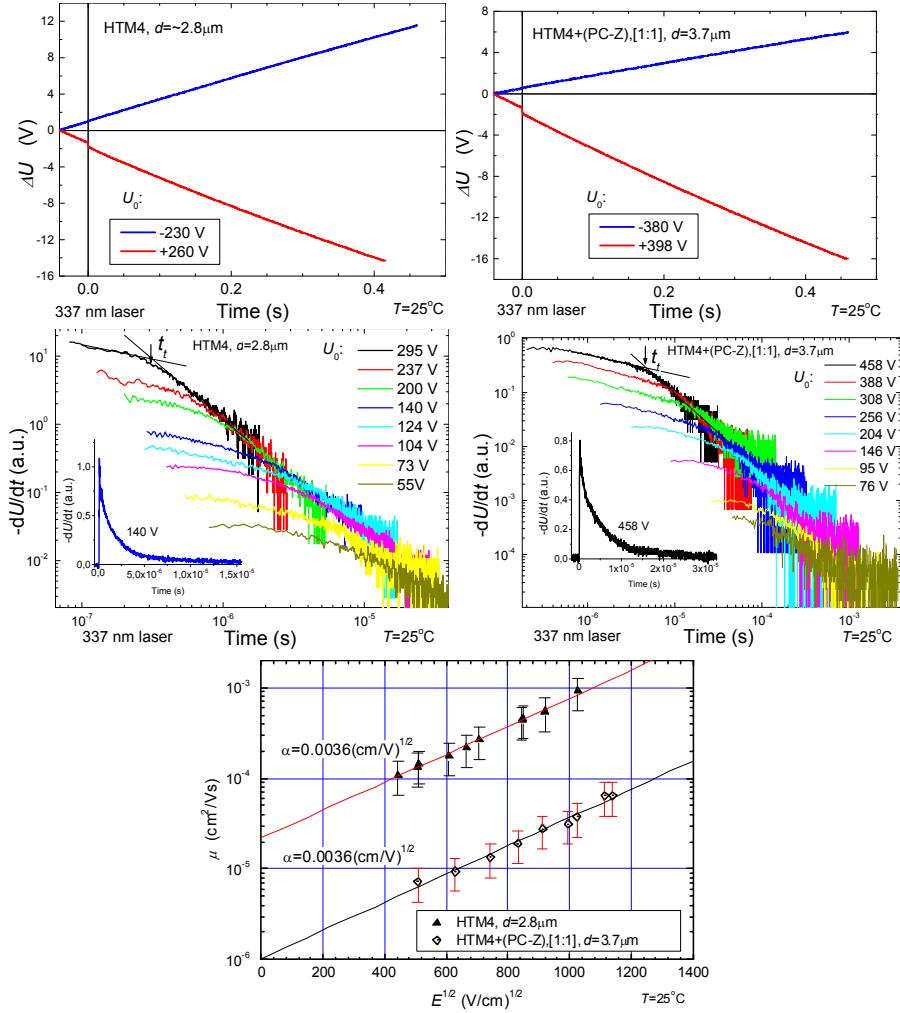
Fig. S8. a- Charge carriers drift kinetics in integral mode of HTM4 and b − in mixture in PC-Z. c- dU/dt hole-transients of HTM4. d- dU/dt hole-transients of HTM4 in mixture in PC-Z. e- field dependent μ values with and without PC-Z of HTM4.

Presentation of charge carriers drift kinetics in integral mode, dU/dt hole-transients, field dependent μ values of HTM5 with and without PC-Z.

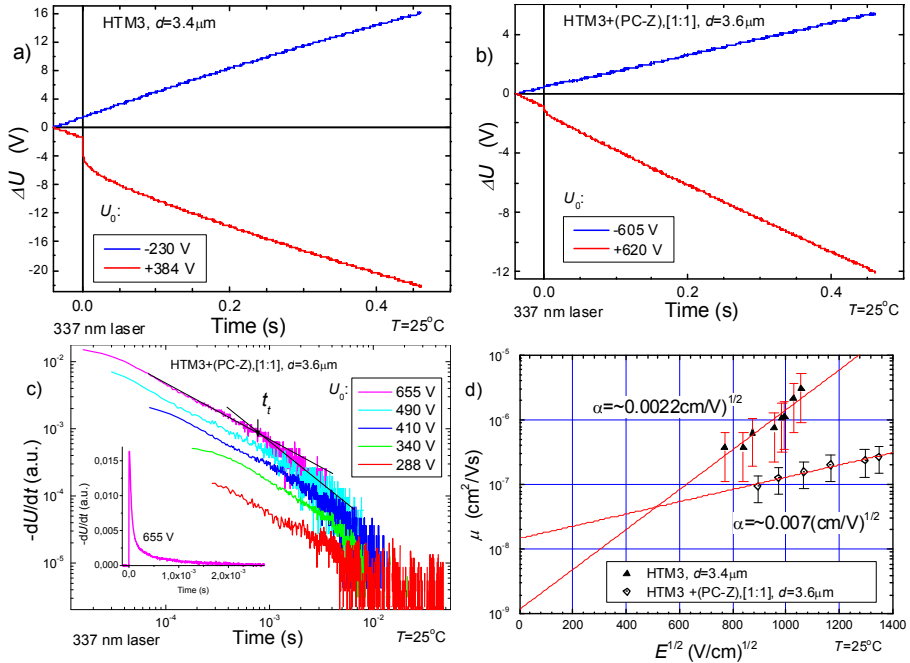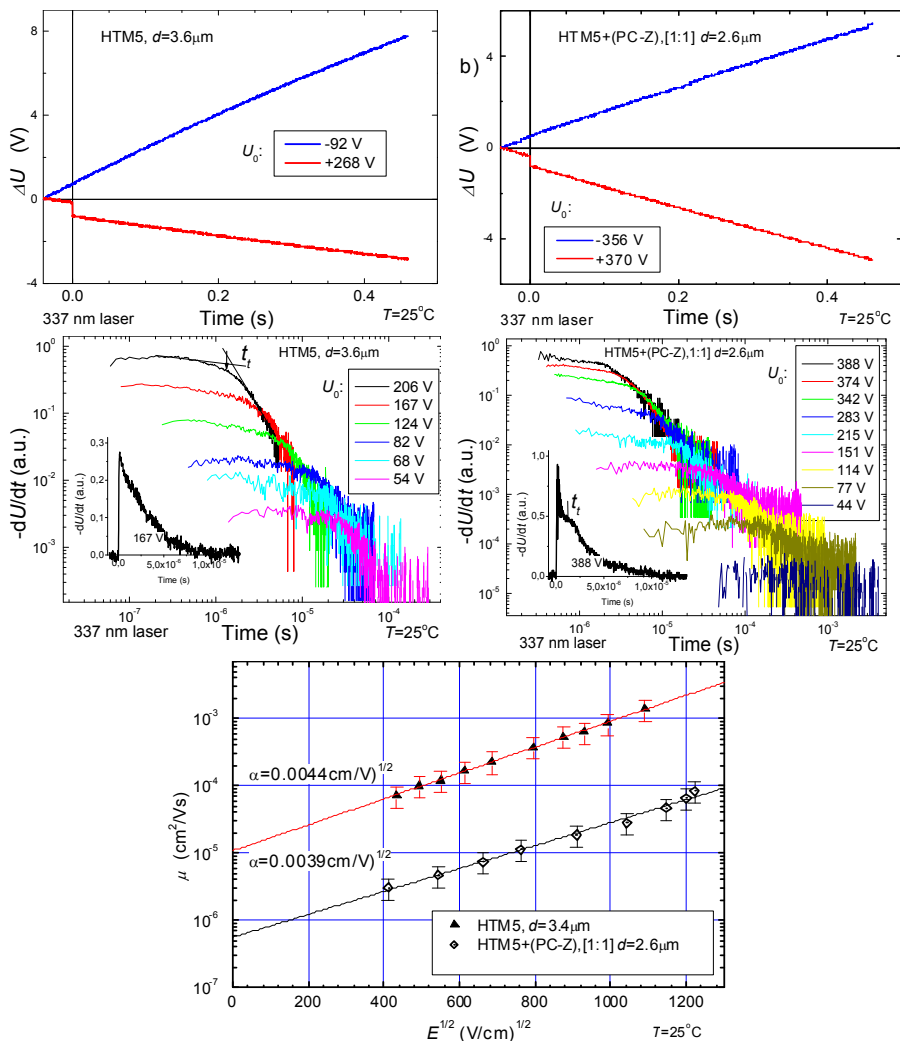Fig. S9. a- Charge carriers drift kinetics in integral mode of HTM5 and b – in mixture in PC-Z. c- dU/dt hole-transients of HTM5. d- dU/dt hole-transients of HTM5 in mixture in PC-Z. e- field dependent μ values with and without PC-Z of HTM5.

DSC measurements of HTM6 and HTM7 are depicted in Fig. S10. During the first DSC heating cycle the glass transition process was detected at 100 °C, followed by a melting process at 228 °C for HTM6. Directly after melting, an exothermic process was detected at 231 °C, suggesting that thermal polymerization occurs at this temperature. During the second heating cycle, no phase transitions were observed, confirming formation of the cross-linked polymer. For HTM7 with higher molecular weight, a slightly higher T_g of 136 °C was detected and no melting process was observed. The cross-linking process started at 190 °C, with a peak at around 239 °C.
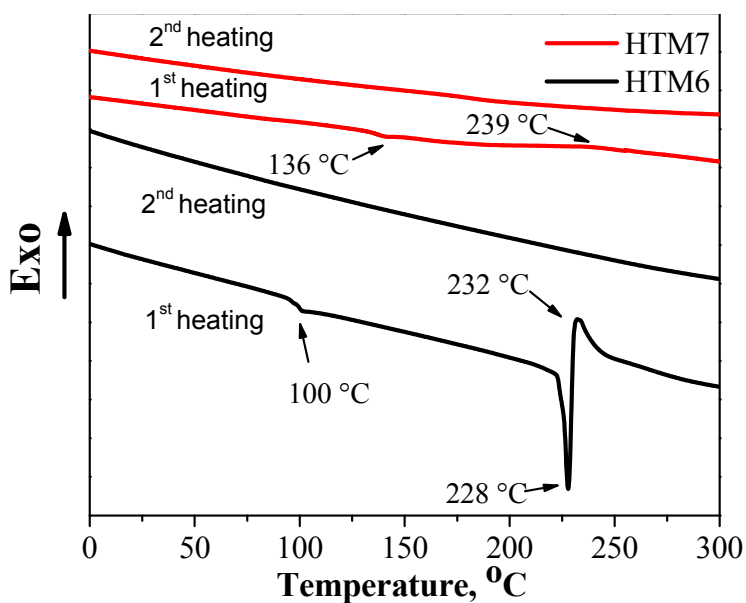
Fig. S10. DSC measurements of HTM6 and HTM7.

Curriculum vitae

Name, Surname	Jonas Nekrasovas
Date of birth	1989 08 031
Place of birth	Lithuania
Nationality	Lithuanian
Address	Saulėtekio al. 3, Vilnius
Phone nr.	+370 65634153
e-mail	jonas.nekrasovas@ff.vu.lt

Education:	
1996 - 2008	Vievis gymnasium
2008 - 2012	Vilnius university, Bachelor of Modern technology physics and management, Physics
2012 - 2014	Vilnius university, Master of Physical technologies and management, Physics
Work experience:	
2012 - 2015	Technician, Vilnius university
2015-2021	Junior researcher, Vilnius university
Internship:	
2013	Tor Vergata university, Rome (Italy)
2013 – 2014	Augsburg university, Ausgburg (Germany)

List of publications (Publikacijų sąrašas ir jų kopijos)

1. R. Tiazkis, P. Sanghyun, M. Daškevičienė, T. Malinauskas, M. Saliba, J. Nekrasovas, V. Jankauskas, Sh. Ahmad, V. Getautis, M. K. Nazeeruddin. "Methoxydiphenylamine-substituted fluorene derivatives as hole transporting materials: role of molecular interaction on device photovoltaic performance", *SCIENTIFIC REPORTS*, Volume 7, 150, DOI: 10.1038/s41598-017-00271-z (2017).

2. M. Franckevičius, V. Pakštas, G. Grincienė, E. Kamarauskas, R. Giraitis, J. Nekrasovas, A. Selskis, R. Juškėnas, G. Niaura. "Efficiency improvement of superstrate CZTSSe solar cells processed by spray pyrolysis approach", *Solar Energy*, Volume 185, June 2019, Pages 283-289. DOI: 10.1016/j.solener.2019.04.072 (2019).

3. J. Nekrasovas, V. Gaidelis, E. Kamarauskas, M. Viliūnas, V. Jankauskas. "Photoemission studies of organic semiconducting materials using open Geiger-Muller counter", *Journal of Applied Physics*, 126, 015501. DOI: 10.1063/1.5096070 (2019).

4. D. Vaitukaitytė, A. Al-Ashouri, M. R. Juškėnas, E. Kamarauskas, J. Nekrasovas, V. Jankauskas, A. Magomedov, S. Albrecht, V. Getautis, "Enamine-Based Cross-Linkable Hole-Transporting Materials for Perovskite Solar Cells", *SOLAR RRL*, Volume: 5 Issue: 1, 2000597, DOI: 10.1002/solr.202000597 (2021).

1ˢᵗ publication / 1-oji publikacija

Methoxydiphenylamine-substituted fluorene derivatives as hole transporting materials: role of molecular interaction on device photovoltaic performance
R. Tiazkis, P. Sanghyun, M. Daškevičienė, T. Malinauskas, M. Saliba, J. Nekrasovas, V. Jankauskas, Sh. Ahmad, V. Getautis, M. K. Nazeeruddin

Methoxydiphenylamine-substituted fluorene derivatives as hole transporting materials: role of molecular interaction on device photovoltaic performance

Robertas Tiazkis[1], Sanghyun Paek[2], Maryte Daskeviciene[1], Tadas Malinauskas[1], Michael Saliba[2], Jonas Nekrasovas[3], Vygintas Jankauskas[3], Shahzada Ahmad[4], Vytautas Getautis[1] & Mohammad Khaja Nazeeruddin[2]

The molecular structure of the hole transporting material (HTM) play an important role in hole extraction in a perovskite solar cells. It has a significant influence on the molecular planarity, energy level, and charge transport properties. Understanding the relationship between the chemical structure of the HTM's and perovskite solar cells (PSCs) performance is crucial for the continued development of the efficient organic charge transporting materials. Using molecular engineering approach we have constructed a series of the hole transporting materials with strategically placed aliphatic substituents to investigate the relationship between the chemical structure of the HTMs and the photovoltaic performance. PSCs employing the investigated HTMs demonstrate power conversion efficiency values in the range of 9% to 16.8% highlighting the importance of the optimal molecular structure. An inappropriately placed side group could compromise the device performance. Due to the ease of synthesis and moieties employed in its construction, it offers a wide range of possible structural modifications. This class of molecules has a great potential for structural optimization in order to realize simple and efficient small molecule based HTMs for perovskite solar cells application.

Hybrid organic-inorganic perovskite materials have shown great potential for use not only in photovoltaics but also in lasers, plasmonics, light-emitting diodes, tandems with silicon, photodetectors and sensors[1–4]. Recently, perovskite solar cells (PSCs) have attracted considerable attention due to extremely large and rapid performance progress. In 2009, Kojima *et al*. demonstrated that methylammonium lead iodide (MAPbI$_3$) perovskite can work as a solar cell material with 3.8% power conversion efficiency (PCE)[5]. Since then published values leaped to 21.6%[6] in only five years with a currently certified record PCE of 22.1%[7]. Such values are already exceeding commercialized polycrystalline silicon solar cells and rapidly approach crystalline silicon solar cells with record efficiency around 25.6%[8].

In the PSC perovskite light absorber layer, either with or without mesoporous scaffold, is positioned between the electron and hole transport layers. By precisely manipulating charge carriers along the entire pathway from the absorber to both electrodes, an increase in the power conversion efficiency could be achieved. Although research is conducted on each layer, the biggest progress has been made in the area of perovskite film processing and relevant material design. Several reports show stability, performance and reproducibility improvements for the perovskite materials using mixtures of multiple cations, i.e. methylammonium, formamidinium and Cs,

[1]Department of Organic Chemistry, Kaunas University of Technology, Radvilenu pl. 19, 50254, Kaunas, Lithuania. [2]Group for Molecular Engineering of Functional Materials, Institute of Chemical Sciences and Engineering, École Polytechnique Fédérale de Lausanne, Rue de l'Industry 17, CH-1951, Sion, Switzerland. [3]Department of Solid State Electronics, Vilnius University, Sauletekio 9, 10222, Vilnius, Lithuania. [4]Abengoa Research, C/Energía Solar n° 1, Campus Palmas Altas, 41014, Sevilla, Spain. Correspondence and requests for materials should be addressed to V.G. (email: vytautas.getautis@ktu.lt) or M.K. (email: mdkhaja.nazeeruddin@epfl.ch)

instead of single methylammonium[9, 10]. Tuning the halide composition, by using an increased amount of bromide instead of iodide, has also been reported to improve thermal and humidity stability[11].

Although a number of new hole transporting materials (HTM) has been developed and investigated[12], the field is still dominated by costly 2,2′,7,7′-tetrakis(*N*,*N*-di-*p*-methoxyphenylamine)-9-9′-spirobifluorene (Spiro-OMeTAD) and even more expensive poly[bis(4-phenyl)(2,4,6-trimethylphenyl)amine] (PTAA)[13–15]. The main factors contributing to the high cost of these materials are multistep synthesis procedures, expensive reagents and costly purification methods used[16]. For example, sublimation-grade Spiro-OMeTAD is needed in order to obtain high-performance devices. A significant effort has been made to develop less costly and easier to synthesize HTMs with performance comparable or better than that of Spiro-OMeTAD or PTAA[17–21]. One promising avenue for simplification of the HTM synthesis procedure is substitution of the difficult to obtain 9,9′-spirobifluorene core with a simpler alternative. Methoxydiphenylamine-substituted fluorene and triphenylamine derivatives have demonstrated their effectiveness as HTMs for number of applications and they form a basis of two most effective HTMs used for PSC construction, Spiro-OMeTAD and PTAA[6, 15, 18, 22]. Therefore, it's appropriate to test the combination of the two as a new class of HTMs for application in PSCs. Additionally, it was demonstrated that structure of the HTMs has a significant influence on the molecular planarity, energy level and charge transport properties[23]. Understanding the relationship between the chemical structure of the HTMs and the photovoltaic performance is crucial in continued development of the more efficient organic charge transporting materials and is imperatively needed[24]. Numerous investigations are being carried out aimed at enhancement of hole drift mobility; however, until now only a few tangible recommendations have been made with regard to molecular structure modifications[25–27].

In this report a new type of HTMs (Fig. 1), based on methoxydiphenylamine-substituted fluorene and triphenylamine fragments is reported. Using molecular engineering approach, *i.e.* influencing conformation and packing of the molecules in the film *via* changing angle of rotation between fluorene and triphenylamine moieties with the help of additional methyl groups or by placing different aliphatic substituents at the *para* positions of the triphenylamine fragments, we have constructed a series of HTMs in order to investigate the relationship between the chemical structure of the HTMs and the photovoltaic performance. PCEs in the range of 9% to 16.8% was measured utilizing these HTMs, highlighting the importance of the optimal chemical structure, as an inappropriately placed methyl group could compromise device performance.

Results

Synthesis of new type of hole transporting molecules involves condensation of 2,7-dibromofluorene with corresponding formyltriphenylamine, followed by a palladium-catalysed C–N cross coupling reaction with 4,4′-dimethoxydiphenylamine (Fig. 2). More detailed information on the synthesis can be found in the Supporting Information.

Thermogravimetric analysis (TGA) reveals very good thermal stability of the investigated HTMs, the fluorene derivatives start to decompose at temperatures above 410 °C (Fig. 3a, Table 1 and Supplementary Figs S1–S4).

During differential scanning calorimetry (DSC) scans it was determined that investigated materials are fully amorphous. Only the glass to liquid transition is detected and it is in the range between 85 and 109 °C (Fig. 3b, Table 1 and Supplementary Figs S5–S8). This is desired in order to form homogeneous HTM films in SC devices. T_g of **HTM1–3** are similar to that of Spiro-OMeTAD (126 °C), while presence of aliphatic substituents in *para* positions of the tripenylamine fragment in **HTM4** and **HTM5** reduce the glass transition temperature by ~20 °C.

The UV-vis absorption bands of the investigated **HTM1–5** are shown in Fig. 4a. All studied derivatives are based on the same principal structure, *i.e.* fluorene core with attached 4,4′-dimethoxydiphenylamine fragments connected with a triphenylamine unit; therefore, their UV-vis spectra bear significant similarities.

Presence of a fluorene fragment with attached 4,4′-dimethoxydiphenylamine moieties, the same as in Spiro-OMeTAD, results in a comparable UV-Vis absorption spectra. The π–π* absorption bands for **HTM1–5** are observed at around 383 nm, indicating a similar sized π–conjugated system as that of Spiro-OMeTAD. Presence of the triphenylamine fragment results in the increase in size of the π–conjugated system and an additional absorption shoulder at 430 nm is observed[28]. Position of the methyl group in the triphenylamine segment has a noticeable influence on the intensity of the shoulder. Methyl group in the *meta* position of the triphenylamine fragment in **HTM3** causes it to be more twisted out of the plain. As a consequence shoulder at 430 nm is less intense, compared with other investigated HTMs, indicating that methyl group at this position restricts π–electron conjugation in the molecule and limits the ability of the π–electrons of triphenylamine moiety to join the common system. On the other hand, alkyl groups at *para* positions of the triphenylamine moiety (**HTM4**, **HTM5**) have a positive effect on the intensity of the absorption band at 430 nm. UV-Vis-NIR absorbance spectra, upon chemical oxidation of **HTM4** and Spiro-OMeTAD by the silver bis(trifluoromethanesulfonyl)imide (AgTFSI)[29], are shown in the Fig. 4b.

Similarly as Spiro(TFSI)$_2$, chemically oxidized HTM4TFSI demonstrated absorption bands at around 460 nm, 650 nm and 1470 nm indicating formation of the oxidized species. The lower intensity of the HTM4TFSI absorption maxima could be attributed to the fact that the transition is accompanied by a smaller change in the electronic charge distribution upon excitation as **HTM1–5** have one less methoxydiphenylamine-substituted fluorene fragment available for oxidation.

Cyclic voltammetry (CV) was used to determine the ground-state oxidation potentials of the HTMs (Table 2). Quasi-reversible oxidation signals are observed for all investigated materials (Supplementary Figs S12–16) and differences in the CV results are quite small, although, there are some slight variations in the energy levels. A slight increase of E_{HOMO}, compared with **HTM1**, is observed for **HTM2**, **HTM4**, **HTM5** due to presence of additional alkyl groups and stronger interactions between methoxydiphenylamine-substituted fluorene and triphenylamine fragments. **HTM3** on the other hand, doesn't follow a similar pattern as methyl group in the *meta* position
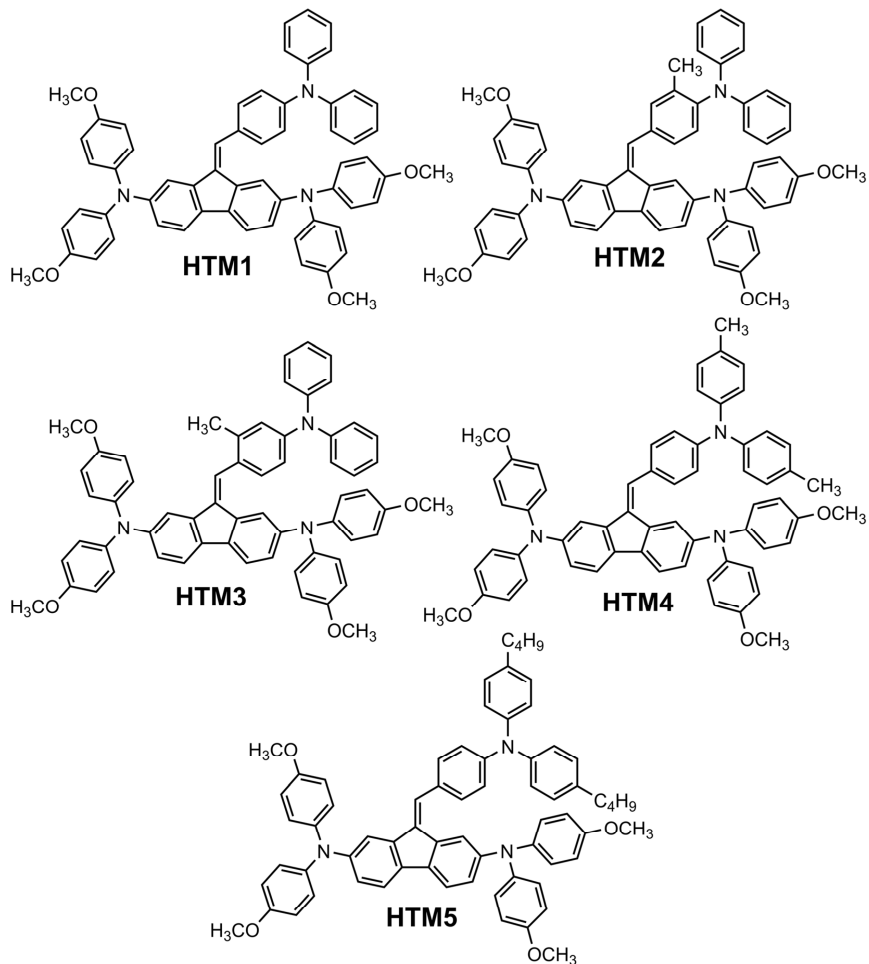
118

Figure 1. Structures of the investigated hole transporting materials **HTM1–5**.

of the triphenylamine moiety restricts π–electron conjugation in the molecule, these results correlate well with the UV-vis absorption data.

The solid-state ionization potential (I_p), was measured by photoelectron spectroscopy in air (PESA) method in the films of the undoped HTMs (Supplementary Figs S9 and S10 and Table 2). The structure/energy level dependency is less clearly defined in tightly packed films compared with the solvated molecules. Measured I_p values are slightly lower than the HOMO levels found in the CV experiments and the difference may arise from different measurement methods and conditions (solution in CV and solid film in the photoemission method) used. Overall from the ionization potential data presented in the Table 2 it can be stated that I_p values of the HTMs containing alkyl substituents in the triphenylamine fragment are lower as compared to the parent derivative **HTM1.** The most noticeable decrease in I_p is observed for **HTM4** with two methyl groups in *para* positions of the triphenylamine moiety. PESA and CV measurements reveal that solid-state I_p and oxidation potentials in solution of the investigated compounds are similar to those of the Spiro-OMeTAD, as all of them share the same methoxydiphenylamine-substituted fluorene main fragment.

Charge-transporting properties of the investigated HTMS were determined by the xerographic time-of-flight (XTOF) technique. Supplementary Fig. S17a demonstrates representative dU/dt hole-transients for the thin film of **HTM3**. It exhibits a dispersive hole-transport; which, along with the strong electric-field mobility dependence, suggests the trap-dominant charge transport in this material. Nevertheless, well-defined transit times (t_t) established from the intersection points of two asymptotes of double-logarithmic plots provided hole-drift mobility at respective applied fields. Similar performance was also established for **HTM2**, **HTM4**, and **HTM5**. Hole transport
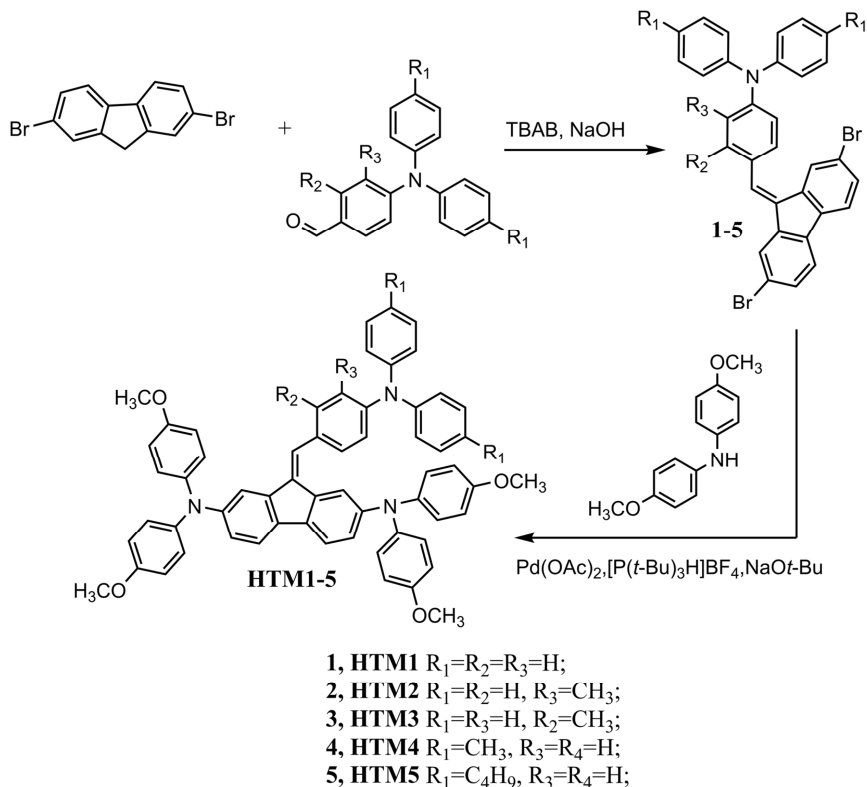
119

Figure 2. Synthetic route to hole transporting materials **HTM1–5**.

1, HTM1 $R_1=R_2=R_3=H$;
2, HTM2 $R_1=R_2=H$, $R_3=CH_3$;
3, HTM3 $R_1=R_3=H$, $R_2=CH_3$;
4, HTM4 $R_1=CH_3$, $R_3=R_4=H$;
5, HTM5 $R_1=C_4H_9$, $R_3=R_4=H$;

of **HTM1** is Gaussian and transit time is defined in linear plot of transients (Supplementary Fig. S17b). Examples of mobility field dependencies are given in the Supplementary Fig. S11. In all cases investigated mobility μ may be well approximated by the formula:

$$\mu = \mu_0 \exp(\alpha\sqrt{E})$$

here μ_0 is the zero field mobility, α is Pool-Frenkel parameter and E is electric field strength. Such mobility dependence is explainable by terms of the Borsenberger and Weiss[30], and Borsenberger et al.[31] disorder formalism. The mobility defining parameters μ_0 and α values as well as the mobility value at the 6.4×10^5 V cm^{-1} field are given in Table 2.

As seen from the results, synthesized HTMs demonstrated competitive charge mobility. XTOF measurements of the films prepared from **HTM1**, **HTM2**, **HTM4**, **HTM5** indicate that the hole-drift mobility is $\sim 10^{-5}$ cm^2 V^{-1}s^{-1} at weak electric fields and $\sim 3 \times 10^{-4}$ cm^2 V^{-1}s^{-1} at a field strength of 6.4×10^5 Vcm^{-1}. The hole mobility of these HTMs is comparable to that of Spiro-OMeTAD, while **HTM3** demonstrates several orders of magnitude lower results. Most likely methyl group in the *meta* position of the triphenylamine fragment causes it to be more twisted out of the plain which prevents tight packing of the molecules and makes it more difficult for the charge to hop between sites.

It is well known that quality of the prepared films can have significant impact on the results of mobility measurements[32]. Every molecule has different film forming properties, therefore in order to mitigate film quality influence on mobility results we have also performed XTOF measurements with HTMs dispersed in polycarbonate (PC) polymeric matrix which minimizes HTM molecule dependent film quality variations (Fig. 5 and Table 2). Naturally, absolute mobility values are lower due to the presence of large portion of nonconductive polymer; however structure/properties relation is much better expressed in this case. Methyl group in the *meta* position of the triphenylamine fragment in **HTM3** causes significant negative changes in the molecule's conformation which translates into lowest charge mobility. While mobility in **HTM4**, **HTM5**, with alkyl groups at *para* positions of the triphenylamine moiety, is up to two orders of magnitude higher due to better optimized structure. XTOF measurement results in the HTM:polycarbonate mixtures also correlate well with the UV-Vis spectroscopy data.
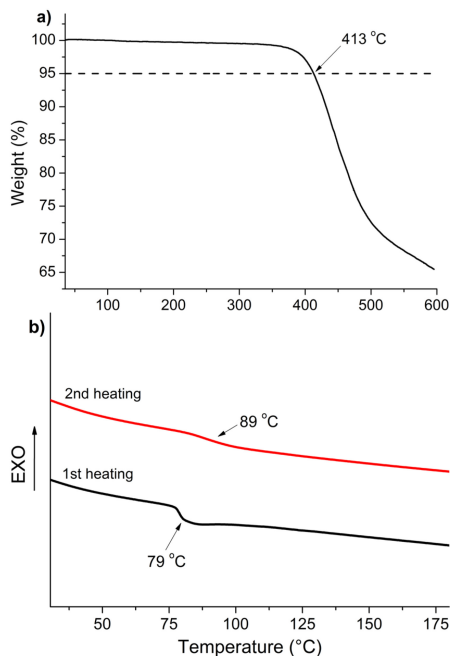
120

Figure 3. Thermogravimetric (**a**) and differential scanning calorimetry (**b**) heating curves of **HTM4** (heating rate 10 K min^{-1}, N$_2$ atmosphere).

Compound	T_m (°C)	T_g [a] (°C)	T_{dec} (°C)	Abs$_{max}$ [b] (nm)	ε (M^{-1} cm^{-1})
HTM1	—	108	416	382	5.5×10^4
HTM2	—	104	419	383	5.8×10^4
HTM3	—	104	418	383	5.5×10^4
HTM4	—	89	413	383	5.2×10^4
HTM5	—	85	413	385	5.4×10^4
Spiro	245	126	449	387	6.9×10^4

Table 1. Thermal and optical properties of the Spiro-OMeTAD, **HTM1–5**. [a]Determined by DSC: scan rate, 10 K min^{-1}; N$_2$ atmosphere; second run. [b]Measured in 10^{-4} M THF solution.

The new semiconductors **HTM1–5** were tested as HTMs in perovskite solar cells using a device stack of fluorine doped tin oxide(FTO)/compact TiO$_2$/mesoporous TiO$_2$/perovskite/HTM/Au.

Position of the methyl groups in the molecule had a noticeable impact on the performance of the semiconductors in the PSC. Arrangement of the molecules into conformations less favourable for the charge transport in **HTM3** had a visible negative impact on charge mobility. Expectedly, decreased mobility had a negative effect on the performance of the HTM in the PSC as the PCE was only 9.15% (Fig. 6 and Supplementary Table S1). Change of the methyl group position from *meta* to *ortho* (**HTM2**) or its removal (**HTM1**) increases the mobility and also performance of the HTM in the PSC, PCE jumps to ~14–15%. The best results were obtained with structures containing aliphatic substituents in the *para* position of the triphenylamine moiety (**HTM4, HTM5**) which incidentally also demonstrated highest mobility in HTM:polycarbonate mixtures. PCE of 16.8% under AM 1.5 G illumination was recorded in the PSC with HTM4 (Table S1). The open-circuit voltage (V_{oc}) was determined to be 1052 mV, current density (J_{sc}) 21.3 mA cm^{-2} and fill factor 0.75 (Fig. 6). Similar PCE (16.5%) was also showed by **HTM5**. The best device prepared following the same device fabrication procedure, but using Spiro-OMeTAD as hole transporter, exhibited PCE of 17.88%.

Conclusion

In conclusion, a new group of small-molecule hole transporting materials, based on methoxydiphenylamine-substituted fluorene and triphenylamine fragments, is demonstrated. These HTMs are synthesized in two steps from commercially available materials. Relationship between the chemical structure of
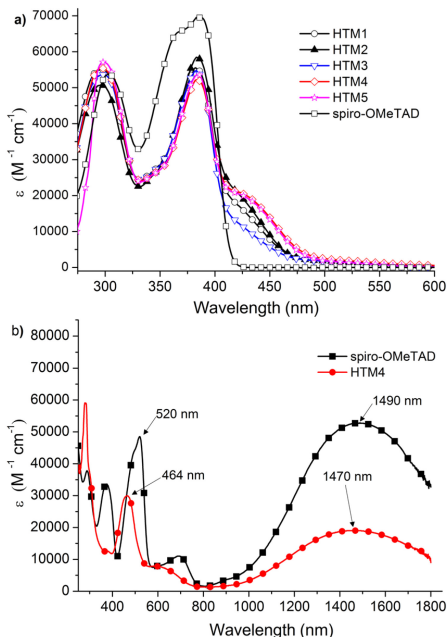
121

Figure 4. UV–vis absorption spectra of **HTM1−5**, Spiro-OMeTAD (**a**) and oxidized Spiro(TFSI)$_2$, HTM4TFSI (**b**) in THF (c $= 10^{-4}$ M).

Compound	E_{HOMO}[a] (eV)	I_p[b] (eV)	μ_0[c] (cm^2 V^{-1} s^{-1})	μ[d] (cm^2 V^{-1} s^{-1})
HTM1	−5.13	5.05	1.4×10^{-5}	5.9×10^{-4}
HTM2	−5.05	5.00	1.3×10^{-5}	3.8×10^{-4}
HTM3	−5.14	5.00	1×10^{-9}	3×10^{-7}
HTM4	−5.05	4.92	2.2×10^{-5}	3.8×10^{-4}
HTM5	−5.08	5.03	1.1×10^{-5}	3.8×10^{-4}
Spiro	−5.12	5.00	4.1×10^{-5}	5×10^{-4}
HTM1 + PC	—	—	3.9×10^{-7}	2.3×10^{-5}
HTM2 + PC	—	—	4.0×10^{-7}	1.9×10^{-5}
HTM3 + PC	—	—	1.5×10^{-8}	1.3×10^{-7}
HTM4 + PC	—	—	1.1×10^{-6}	3.7×10^{-5}
HTM5 + PC	—	—	5.8×10^{-7}	2.8×10^{-5}
Spiro + PC	—	—	2.9×10^{-6}	6.8×10^{-5}

Table 2. Electrochemical characteristics, I_p, hole mobility for Spiro-OMeTAD, **HTM1−5**. [a]CV measurements were carried out at a glassy carbon electrode in dichloromethane solutions containing 0.1 M tetrabutylammonium hexafluorophosphate as electrolyte and Pt wire as the reference electrode. Each measurement was calibrated with ferrocene (Fc). Conversion factors: ferrocene in DCM vs SCE 0.46[34], SCE vs SHE: 0.244[35], SHE vs. vacuum: 4.43[36]. [b]Ionization potential was measured by the photoemission in air method from films. [c]Mobility value at zero field strength. [d]Mobility value at 6.4×10^5 V cm^{-1} field strength.

the HTMs and the photovoltaic performance has been investigated using molecules with strategically placed aliphatic substituents. It was found that the structure of the HTMs play an important role in their hole extraction in PSCs and can have a significant influence on the molecular planarity, charge transport properties and device characteristics. We have observed that aliphatic substituents in *meta* position of the triphenylamine fragment cause it to be more twisted out of the plain and severely reduce charge transport properties of the HTM and overall device characteristics of the perovskite solar cells. In general, altering the structure of the phenyl ring connecting the fluorene and triphenylamine moieties produces undesirable conformational changes in the molecule and reduces its overall performance of the HTM in the PSC. On the other hand, positive effect on the performance of the hole
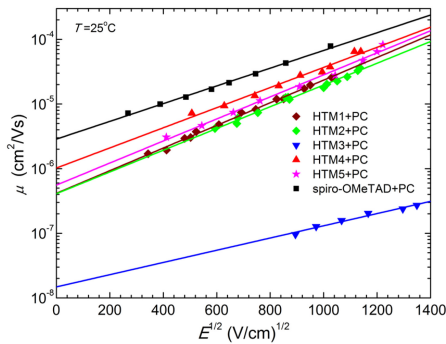
Figure 5. Electric-field dependencies of the hole drift mobilities in charge-transport layers of **HTM1–5** dispersed in polycarbonate polymeric matrix.
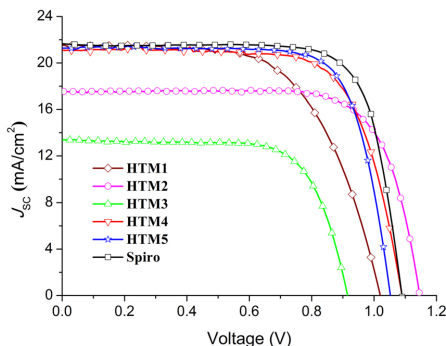

Figure 6. Current (J)-voltage (V) curves of the solar cells with **HTM1–5**, and **Spiro-OMeTAD** (control) recorded under AM 1.5 conditions (100 mW/cm^2).

transporting materials is observed after substitution at *para* position of the triphenylamine moiety. The overall efficiency of the investigated HTM in perovskite-based solar cells was in a range of 9% to 16.8% demonstrating the importance of the optimal molecular structure. Due to the ease of synthesis and moieties employed in its construction, it offers a wide range of possible structural modifications. The reported class of molecules has a great potential for further structure optimization in order to realize simple and efficient small molecular HTMs applied in perovskite solar cells.

Methods

Photovoltaic device preparation. Chemically eched FTO glass (Nippon Sheet Glass) was sequentially cleaned by sonication in a 2% Helmanex solution, acetone and ethanol for 30 min each, followed by a 15 min UV-ozone treatment. To form a 30 nm thick TiO$_2$ blocking layer, diluted titanium diisopropoxide bis(acetylacetonate) (TAA) solution (Sigma-Aldrich) in isopropanol was sprayed at 450 °C. For the 200 nm mesoporous TiO$_2$ layer, mesoporous-TiO$_2$ layers were made by spin-coating a commercially available TiO$_2$ paste (Dyesol 30NRD). Substrates were baked at 500 °C for 30 min. Then, Li-doping of mesoporous TiO$_2$ is treated by spin coating a 0.1 M solution of Li-TFSI in acetonitrile at 3000 rpm for 20 min before the deposition of the perovskite layer. Mixed-perovskite precursor was prepared by mixing 1.15 m PbI$_2$, 1.10 m FAI, 0.2 m PbBr$_2$, 0.2 m MABr in a mixed solvent of DMF:DMSO = 4:1 (volume ratio). Perovskite solutions are successively spin-coated in the glovebox as follows: first, 2000 rpm for 10 s with a ramp-up of 200 rpm s^{-1}; second, 6000 rpm for 30 s with a ramp-up of 2000 rpm s^{-1}[33]. Chlorobenzene (CB, 100 μl) was dropped on the spinning substrate during the second spin-coating step 20 s before the end of the procedure. Films were annealed at 100 °C for 90 min. The hole-transporting materials were applied from a 60 mM solution in chlorobenzene. All HTMs were doped with bis(trifluoromethylsulfonyl)imide lithium salt (Li-TFSI, Sigma-Aldrich), tris(2-(1H-pyrazol-1-yl)-4-tert-butylpyridine)- cobalt(III) tris(bis(trifluoromethylsulfonyl)imide) (FK209, Dynamo) and 4-tert-Butylpyridine (TBP, Sigma-Aldrich). The molar ratio of additives for the HTMs where: 0.5, 0.03 and 3.3 for Li-TFSI, FK209 and TBP respectively. The HTM solutions were spin-coated onto the perovskite layers at 4000 rpm for 30 s. The gold electrodes were deposited by thermal evaporation of 80 nm gold in high vacuum conditions.

123

Photovoltaic device testing. The solar cells were measured using a 450 W xenon light source (Oriel). The spectral mismatch between AM1.5 G and the simulated illumination was reduced by the use of a Schott K113 Tempax filter (Präzisions Glas & Optik GmbH). The light intensity was calibrated with a Si photodiode equipped with an IR-cutoff filter (KG3, Schott), and it was recorded during each measurement. Current-voltage characteristics of the cells were obtained by applying an external voltage bias while measuring the current response with a digital source meter (Keithley 2400). The voltage scan rate were 5 and $10\,mV\,s^{-1}$ and no device preconditioning, such as light soaking or forward voltage bias applied for long time, was applied before starting the measurement. The starting voltage was determined as the potential at which the cells furnish 1 mA in forward bias, no equilibration time was used. The cells were masked with a black metal mask ($0.16\,cm^2$) to fix the active area and reduce the influence of the scattered light.

References

1. Mitzi, D. B. Synthesis, Structure, and Properties of Organic-Inorganic Perovskites and Related Materials In *Progress in Inorganic Chemistry* (ed. K. D. Karlin) Volume 48, 1–121 (John Wiley & Sons, 1999).
2. Saliba, M. *et al.* Structured organic–inorganic perovskite toward a distributed feedback laser. *Adv. Mater.* **28**, 923–929 (2016).
3. Saliba, M. *et al.* Plasmonic-induced photon recycling in metal halide perovskite solar cells. *Adv. Funct. Mater.* **25**, 5038–5046 (2015).
4. Albrecht, S. *et al.* Monolithic perovskite/silicon-heterojunction tandem solar cells processed at low temperature. *Energy Environ. Sci.* **9**, 81–88 (2016).
5. Kojima, A., Teshima, K., Shirai, Y. & Miyasaka, T. Organometal halide perovskites as visible-light sensitizers for photovoltaic cells. *J. Am. Chem. Soc.* **131**, 6050–6051 (2009).
6. Saliba, M. *et al.* Incorporation of rubidium cations into perovskite solar cells improves photovoltaic performance. *Science* **354**, 206–209 (2016).
7. NREL research cell record efficiency chart http://www.nrel.gov/pv/assets/images/efficiency_chart.jpg (accessed 2016. 11. 24).
8. Masuko, K. *et al.* Achievement of more than 25% conversion efficiency with crystalline silicon heterojunction solar cell. *Ieee. J. Photovolt.* **4**, 1433–1435 (2014).
9. Yi, C. *et al.* Entropic stabilization of mixed A-cation ABX3 metal halide perovskites for high performance perovskite solar cells. *Energy Environ. Sci.* **9**, 656–662 (2016).
10. Li, Z., Yang, M., Park, J.-S., Wei, S.-H., Berry, J. J. & Zhu, K. Stabilizing perovskite structures by tuning tolerance factor: formation of formamidinium and cesium lead iodide solid-state alloys. *Chem. Mater.* **28**, 284–292 (2016).
11. Noh, J. H., Im, S. H., Heo, J. H., Mandal, T. N. & Seok, S. I. Chemical management for colorful, efficient, and stable inorganic–organic hybrid nanostructured solar cells. *Nano Lett.* **13**, 1764–1769 (2013).
12. Calio, L., Kazim, S., Grätzel, M. & Ahmad, S. Hole-transport materials for perovskite solar cells. *Angew. Chem. Int. Ed.* **55**, 14522–14545 (2016).
13. Yang, W. S. *et al.* High-performance photovoltaic perovskite layers fabricated through intramolecular exchange. *Science* **348**, 1234–1237 (2015).
14. Yu, Z. & Sun, L. Recent progress on hole-transporting materials for emerging organometal halide perovskite solar cells. *Adv. Energy Mater.* **5**, 1500213 (2015).
15. Kim, H., Lim, K.-G. & Lee, T.-W. Planar heterojunction organometal halide perovskite solar cells: roles of interfacial layers. *Energy Environ. Sci.* **9**, 12–30 (2016).
16. Saragi, T. P. I., Spehr, T., Siebert, A., Fuhrmann-Lieker, T. & Salbeck, J. Spiro compounds for organic optoelectronics. *Chem. Rev.* **107**, 1011–1065 (2007).
17. Saliba, M. *et al.* A molecularly engineered hole-transporting material for efficient perovskite solar cells. *Nat. Energy* **1**, 15017 (2016).
18. Bi, D. *et al.* Facile synthesized organic hole transporting material for perovskite solar cell with efficiency of 19.8%. *Nano Energy* **23**, 138–144 (2016).
19. Molina-Ontoria, A. *et al.* Benzotrithiophene-Based Hole-Transporting Materials for 18.2% Perovskite Solar Cells. *Angew. Chem. Int. Ed.* **55**, 6270–6274 (2016).
20. Zhang, J. *et al.* Constructive Effects of Alkyl Chains: A Strategy to Design Simple and Non-Spiro Hole Transporting Materials for High-Efficiency Mixed-Ion Perovskite Solar Cells. *Adv. Energy Mater.* 1502536 (2016).
21. Li, H. *et al.* A simple 3,4-ethylenedioxythiophene based hole-transporting material for perovskite solar cells. *Angew. Chem. Int. Ed.* **53**, 4085–4088 (2014).
22. Shirota, Y. & Kageyama, H. Charge carrier transporting molecular materials and their applications in devices. *Chem. Rev.* **107**, 953–1010 (2007).
23. Zhang, J. B. *et al.* Constructive effects of alkyl chains: a strategy to design simple and non-spiro hole transporting materials for high-efficiency mixed-ion perovskite solar cells. *Adv. Energy Mater.* 1502536 (2016).
24. Salado, M. *et al.* Interface play between perovskite and hole selective layer on the performance and stability of perovskite solar cells. *ACS Appl. Mater. Interfaces*, 10.1021/acsami.6b12236 (2016).
25. Jeon, N. J. *et al.* o-Methoxy substituents in spiro-ometad for efficient inorganic–organic hybrid perovskite solar cells. *J. Am. Chem. Soc.* **136**, 7837–7840 (2014).
26. Rakstys, K. *et al.* Triazatruxene based hole transporting materials for highly efficient perovskite solar cells. *J. Am. Chem. Soc.* **137**, 16172–16178 (2015).
27. Tomkute-Luksiene, D. *et al.* Molecular engineering of the hole-transporting material spiro-OMeTAD via manipulation of alkyl groups. *RSC Adv.* **6**, 60587–60594 (2016).
28. Lukes, V. *et al.* Structure, electronic and optical characterization of oligothiophenes terminated with (9H-fluoren-9-ylidene)methyl chromophores. *Synth. Met.* **157**, 770–778 (2007).
29. Nguyen, W. H., Bailie, C. D., Unger, E. L. & McGehee, M. D. Enhancing the hole-conductivity of spiro-OMeTAD without oxygen or lithium salts by using spiro(TFSI)$_2$ in perovskite and dye-sensitized solar cells. *J. Am. Chem. Soc.* **136**, 10996–11001 (2014).
30. Borsenberger, P. M. & Weiss D. S. *Organic Photoreceptors for Imaging Systems* (Marcel Dekker, 1993).
31. Borsenberger, P. M., Pautmeier, L. & Bässler, H. Charge transport in disordered molecular solids. *J. Chem. Phys.* **94**, 5447–5454 (1991).
32. Bässler, H. & Köhler, A. Charge transport in organic semiconductors. *Top. Curr. Chem.* **312**, 1–65 (2012).
33. Bi, D. *et al.* Efficient luminescent solar cells based on tailored mixed-cation perovskites. *Sci. Adv.* **2**, e1501170 (2016).
34. Connelly, N. & Geiger, W. Chemical redox agents for organometallic chemistry. *Chem. Rev.* **96**, 877–910 (1996).
35. Pavlishchuk, V. & Addison, A. Conversion constants for redox potentials measured versus different reference electrodes in acetonitrile solutions at 25 °C. *Inorg. Chim. Acta* **298**, 97–102 (2000).
36. Reiss, H. & Heller, A. The absolute potential of the standard hydrogen electrode: a new estimate. *J. Phys. Chem.* **89**, 4207–4213 (1985).

124

Acknowledgements

Author Contributions

V.G., M.K.N. conceived the initial idea and supervised the research. S.A. contributed to design, discussion, and improvement of all experiments. R.T. conducted the synthesis and structural characterization of the compounds. P.S., M.S. performed fabrication and characterisation of solar cells. M.D., T.M. carried out the DSC, TGA, CV, UV-Vis-NIR lights absorption measurements. J.N., V.J. carried out the ionization potential and mobility measurements. All authors contributed in writing this paper.

Additional Information

Supplementary information accompanies this paper at doi:10.1038/s41598-017-00271-z

Competing Interests: The authors declare that they have no competing interests.

Publisher's note: Springer Nature remains neutral with regard to jurisdictional claims in published maps and institutional affiliations.

2nd publication / 2-oji publikacija

M. Franckevičius, V. Pakštas, G. Grincienė, E. Kamarauskas, R. Giraitis,
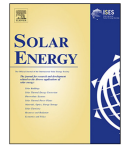J. Nekrasovas, A. Selskis, R. Juškėnas, G. Niaura

Efficiency improvement of superstrate CZTSSe solar cells processed by spray pyrolysis approach

Marius Franckevičius[a,*], Vidas Pakštas[a], Giedrė Grincienė[a], Egidijus Kamarauskas[a,b], Raimondas Giraitis[a], Jonas Nekrasovas[b], Algirdas Selskis[a], Remigijus Juškėnas[a], Gediminas Niaura[a]

[a] Center for Physical Sciences and Technology, Sauletekio 3, Vilnius 10257, Lithuania
[b] Department of Solid State Electronics, Vilnius University, Sauletekio 9, Vilnius 10222, Lithuania

A B S T R A C T

In this work, the influence of Se proportion on structural and photovoltaic characteristics of the spray pyrolysis deposited CZTSSe film, and superstrate solar cell device are reported. We observe that the sulfur to selenium ratio significantly impacts the crystallinity and concomitant electrical properties of CZTSSe films. The higher amount of Se leads to better device performance. We found that the superstrate solar cell devices with S/(S + Se) ratio of about 0.2 achieved a power conversion efficiency (PCE) of 3.1%, which is among the highest for the spray pyrolysis deposited solid state CZTSSe solar cells of superstrate architecture.

1. Introduction

The quaternary direct bandgap semiconductors such as copper zinc tin sulfide (CZTS), selenide (CZTSe) and mixed chalcogenide (Cu_2ZnSn ($S_xSe_{1-x})_4$) (CZTSSe) are considered as promising materials for the production of efficient and inexpensive solar cells (Kumar et al., 2015; Wallace et al., 2017). These materials are composed of Earth-abundant and non-toxic chemical elements and possess excellent intrinsic properties such as high absorption coefficients of about $10^{-4}\,cm^{-1}$, tunable band-gap (1–1.5 eV) and easy processability (Walsh et al., 2012). To date, most of the kesterite solar cells were made with regular device architecture where semiconductor absorber is formed between Mo back contact and the top buffer layer (CdS or ZnS), and transparent conducting oxide bi-layer (Tang et al., 2013; Wang et al., 2014). However, this architecture has some limitations when it comes to cost, stability, and application for tandem solar cells (Dalapati et al., 2017; Redinger et al., 2011; Scragg et al., 2013). Scragg et al. suggested that CZTS(e) and Mo interface is chemically unstable during thermal processing, resulting in decomposition of the CZTS layer into secondary phases, including Cu_2S, ZnS and SnS, and growth of MoS_2 (Scragg et al., 2012). To overcome these drawbacks, kesterite solar cells have been processed in superstrate configuration as an alternative. In this architecture back contact is transparent conductive glass (FTO or ITO) electrode, onto which all electron transporting, photoactive CZTS and hole collecting layers are deposited (Wang et al., 2018a; Yan et al., 2018).

CZTS layer can be formed employing vacuum or non-vacuum deposition methods. Both methods have their strengths and weaknesses. The vacuum deposition techniques allow obtaining a high quality CZTS films, but they are expensive, some materials are unstable at high deposition temperatures, and it is also difficult to control the ratio of elements. On the other hand, non-vacuum growing techniques such as spray pyrolysis (Tanaka et al., 2012), spin coating (Yu et al., 2019), ink printing (Lin et al., 2015), and electrochemical deposition (Zaki et al., 2018), are versatile, straightforward and relatively low cost. Thus, currently it is huge challenge to fabricate high quality CZTS films for the superstrate configuration using non-vacuum deposition methods. However, using these methods it is more difficult to control the quality of the coatings because it strongly depends on the precursor solution (Grincienė et al., 2018), film annealing temperature (Wang et al., 2018a), composition of the CZTS(Se) film (Jadhav et al., 2016) and other conditions.

Optimization of the buffer layer structure, absorber deposition methods, and annealing conditions have already accelerated an increase in the CZTS device quality and subsequent power conversion efficiency. Very recently Wang et al. improved the quality of spin coated CZTS via Li doping what allowed to achieve PCE of about 5% (Wang et al., 2018b). The CZTS formation using the hot injection method gave PCE of 4.7% (Bai et al., 2016). Electrodeposition methods showed slightly lower PCE with the highest to date achieved value of 3.5% (Berruet et al., 2017). CZTS solar cell of superstrate configuration,

fabricated using spray pyrolysis technique showed PCE of 6.4%; however in this case liquid electrolyte solar cell was employed (Swami et al., 2014). Meanwhile, the solid state CZTS solar cells yielded significantly lower PCE values among all of solution approach methods with the current highest efficiency of only 1.13% (Tanaka et al., 2013). The main reason for this is poor film quality due to vigorous evaporation of the precursor solvent resulting in the nonhomogeneous coating and presence of the cracks. Nevertheless, among all the of non-vacuum deposition methods, spray pyrolysis seems to be one of the easiest adaptable methods for the large-area coating, which is essential for mass production. Thus, the device fabrication process needs further improvements to boost the PCE of the CZTS solar cells.

In this work, we fabricated CZTS thin film precursors by spray pyrolysis deposition technique, then the films were annealed in Se vapor to form CZTSSe films of different S/Se values, which were later used in the solar cell devices. We explore the influence of Se content on the structural, optical and photovoltaic characteristics and demonstrate the advantage of Se content on the device performance.

2. Experimental

2.1. Device fabrication

The devices were prepared on conductive fluorine-doped tin oxide (FTO) coated glass substrates. The substrates were cleaned by sonication for 30 min in Hellmanex (2% by volume in water) and then rinsed by deionized water and isopropanol. A compact titanium dioxide (TiO$_2$) layer of about 30–50 nm was deposited as described previously (Prochowicz et al., 2015). On top of this layer, CdS as a buffer layer was formed at 65 °C for 15 min by chemical bath deposition (CBD) method. Thereafter the CZTS thin films were deposited at 340 °C using spray pyrolysis a stock solution containing mixture of copper chloride 0.08 M, tin chloride 0.04 M, zinc chloride 0.6 M, and thiourea 0.4 M in dimethylformamide (DMF). The precursor solution was sprayed through the glass nozzle (0.25 mm) using compressed air as carrier gas with a constant flow rate (~1 ml/min). The spraying procedure was repeated several times in a 30 s drying interval to build up a precursor film thickness of approximately 1.5 μm. The formed layer was heated at 340 °C for 1 h. The formed CZTS films were annealed in a graphite box (volume 20 cm^3) with different content of Se and 5 mg of Sn under atmospheric pressure Ar (99,999%) gas atmosphere. The selenization process consisted of two annealing steps and was completed in 20 min at temperature of 540 °C. Subsequently, hole transporting material was deposited on the top of CZTSSe film by spin coating of Spiro-MeOTAD dissolved in chlorobenzene at the concentration of 0.06 M at spinning rate of 3000 r.p.m. for 20 s while keeping solutions at ambient environment during the whole procedure. Devices were finalized by thermal evaporation of 50 nm thick silver layer on the top of hole transporting material.

2.2. Characterization

A SEM/FIB workstation Helios Nanolab 650 with an energy dispersive X-ray (EDX) spectrometer INCA Energy 350 X-Max 20 was employed for imaging of the surface morphology, cross section view and measurement of chemical composition.

XRD patterns of the CZTSSe films were measured using an X-ray diffractometer SmartLab (Rigaku) equipped with 9 kW rotating Cu anode X-ray tube. Grazing incidence (GIXRD) method was used in 2θ range 5–70°. An angle between parallel beam of X-rays and a specimen surface (ω angle) was adjusted to 0.5° degrees. Phase identification was performed using software package PDXL (Rigaku) and ICDD powder diffraction data-base PDF-4+ (2018 release).

The optical properties of materials were recorded using a Jasco V-670 spectrophotometer in the visible-NIR spectral range from 400 to 1500 nm.

Raman spectra were recorded using a confocal microspectrometer inVia (Renishaw, UK) equipped with thermoelectrically cooled (−70 °C) CCD camera and microscope. Raman spectra were excited with lasers emitting 325, 442, 532 and 785 nm wavelength light. The 50x/0.50 NA long working distance objective was used for excitation and collection of the Raman spectra observed with 442, 532, and 785 nm wavelengths. The 15×/0.12 NA objective was used in the case of 325 nm excitation. The overall integration time was 400. Position of the Raman bands on the wavenumber axis was calibrated by the polystyrene film standard spectrum. Parameters of the bands were determined by fitting the experimental spectra with Gaussian-Lorentzian shape components using GRAMS/A1 8.0 (Thermo Scientific) software assuming linear baseline.

The J-V characteristics of the CZTSSe devices were measured under simulated AM1.5G (100 mW/cm^2) illumination (Oriel, Model 9119, Newport). The current–voltage characteristics of the devices were obtained by applying external potential bias to the cell while recording the generated photocurrent using a Keithley (Model 2420) digital source meter. Voltage was scanned from −0.5 to 0.5 V with a step size of 10 mV. The active area of solar cells was 0.10 cm^2.

3. Results and discussion

The chemical composition of the as-deposited CZTS films was determined by EDX spectroscopy. The obtained CZTS films contained a low amount of copper Cu/(Zn + Sn) = 0.84 and sulfur S/(Cu + Zn + Sn) = 0.92, whereas the Zn content was higher than the stoichiometric (Zn/Sn = 1.14). Previous studies showed that solar cell efficiency is usually higher for those CZTS chemical compositions in which initial content of zinc is slightly higher and that of copper lower than the stoichiometric one (Liu et al., 2015; Werner et al., 2015). However, this nonstoichiometric composition can promote the formation of the secondary phases in CZTS films during the thermal treatment (Feng et al., 2015). To further gain more details about the phase composition and crystalline structure of the as-deposited CZTS films, the X-ray diffraction measurement was employed. The obtained XRD patterns of CZTS precursor films are shown in Fig. 1a. All the XRD peaks matched to the tetragonal Cu$_2$ZnSnS$_4$ (kesterite) phase (ICDD # 00-026-0575). These diffraction peaks are rather broad, indicating that the deposited films are composed of small crystallites with an average size of about 1.8 ± 0.3 nm. However, using XRD it is difficult to distinguish between kesterite and secondary phases such as ZnS, Cu$_3$SnS$_4$ or Cu$_2$SnS$_3$, since the most intensive peaks of these compounds overlap. As an alternative, we employed Raman spectroscopy to facilitate detection of the secondary phases in as-deposited CZTS films (Fig. 1b). The obtained Raman spectrum reveals the main peak at 338 cm^{-1} and three additional vibration bands at 268, 303, 368 cm^{-1}. Based on previous studies, the presence of these peaks discards the occurrence of other undesirable phases confirming that as-deposited CZTS films exhibit kesterite structure (Dimitrievska et al., 2014a,b; Paris et al., 2014; Swami et al., 2014). To be sure that the CZTS layer does not contain ZnS phase, Raman spectra were measured with 325 nm wavelength laser light. An absence ZnSe was verified by measuring Raman spectra using 442 nm wavelength laser light (see Fig. S1 in the Supplementary Material). Thus, neither ZnS nor ZnSe was found in any case.

Fig. 1c shows absorption spectra of the as-deposited CZTS films. These films show a broad absorption spectrum over the entire visible region with the absorption onset at about 1.45 eV. This additionally confirms that the as-deposited CZTS films do not have secondary phases, which is also consistent with previous studies (Grinciene et al., 2018; Valdés et al., 2014). The typical top surface SEM image of as-deposited CZTS film (Fig. 1d) indicates that the film is porous and presents rather small grains, which composed of even smaller particles. The performed analysis of as-deposited CZTS films allowed us to identify that CZTS films are phase-pure and have optimal chemical composition for further processing.
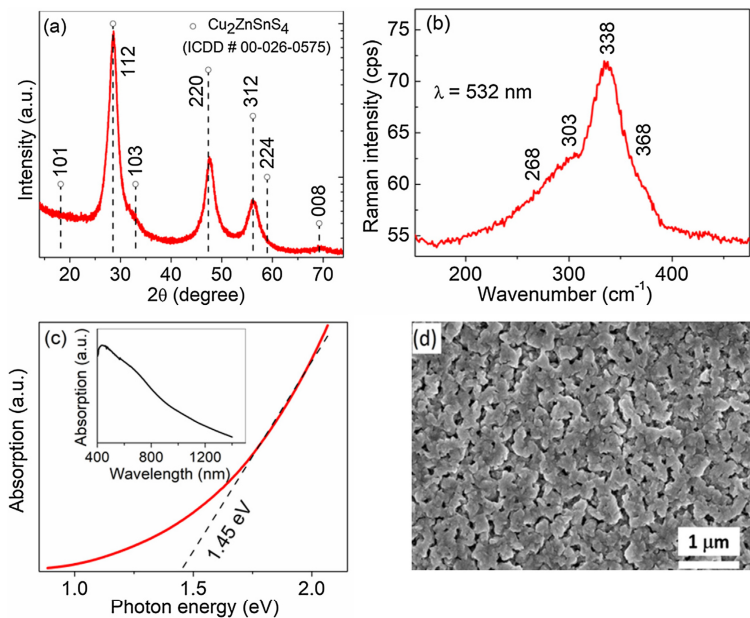
Fig. 1. CZTS precursor film deposited by spray pyrolysis at temperature of 340 °C. (a) Grazing incidence XRD pattern. (b) Raman spectrum observed at 532 nm excitation wavelength in the spectral region of 150–475 cm^{-1}. (c) UV–Vis absorption spectrum. (d) SEM image of the surface morphology.
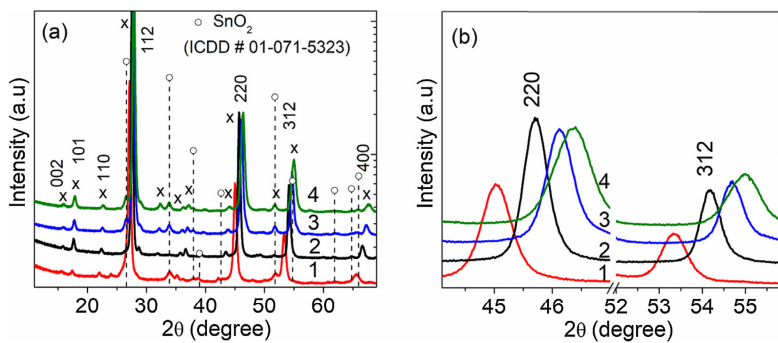

Fig. 2. (a) XRD patterns of the CZTSSe films after annealing with different Se quantity for 30 min. at temperature of 540 °C. The CZTSSe peaks are marked with "x". (b) Fragments of XRD patterns depicting the displacement of XRD peaks 220 and 312 at different S/(S + Se) ratios: 0.1 (1), 0.2 (2), 0.4 (3), and 0.6 (4) respectively.

Table 1
The CZTSSe stoichiometric composition, ICDD card number, lattice constants and crystallites size calculated from the XRD patterns using Halder-Wagner method for the films with different S/(S + Se) ratios.

S/(S + Se)	Composition	ICDD No.	a, Å	c, Å	Cryst. size, nm
0.1	$Cu_2ZnSnSe_{3.6}S_{0.4}$	04-019-1847	5.67	11.31	18.6
0.2	$Cu_2ZnSnSe_{3.2}S_{0.8}$	04-019-1848	5.64	11.24	22.8
0.4	$Cu_2ZnSnSe_{2.4}S_{1.6}$	04-019-1850	5.59	11.14	17.1
0.6	$Cu_2ZnSnSe_{1.6}S_{2.4}$	04-019-1852	5.52	11.02	15.5

To understand the impact of the Se proportion on the film and device characteristics, a different content of sulfur (S) was replaced by selenium (Se) during the CZTS annealing in selenium vapor. The selenization results in the formation of a new composition $Cu_2ZnSn(S_{1-x}Se_x)_4$ absorber layer, in which, the S to Se (S/(S + Se)) ratio plays a major role in film characteristics. To estimate the effect of Se on phase and chemical composition several different techniques such as XRD, Raman and EDX spectroscopies were employed. Fig. 2a shows XRD patterns of CZTS thin films annealed with different Se quantity at temperature of 540 °C. The systematic shift of all XRD peaks towards lower diffraction angles upon increasing the amount of selenium reflects a clear change in the film composition. Because the size of the
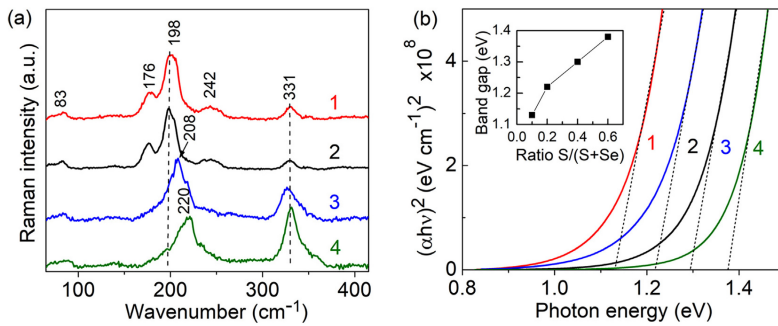
129

Fig. 3. (a) Raman spectra of CZTSSe samples with different S/(S + Se) ratio in the spectra region of 65–420 cm^{-1}: (1) sample S/(S + Se) ratio – 0.09, (2) sample – 0.16, (3) sample – 0.37, and (4) sample – 0.57. Excitation wavelength is 532 nm (0.06 mW). (b) The Tauc plots of $(\alpha h\nu)^2$ as a function of the photon energy for the CZTSSe films with different S/(S + Se) ratios: (1) – 0.1, (2) – 0.2, (3) – 0.4, (4) – 0.6 after selenization at a temperature of 540 °C. The insert shows the estimated band gap energies for the CZTSSe films with different Se content.

ions in the lattice determines the lattice constant of kesterite (Yu and Carter, 2015), the CZTSSe has the larger lattice constant than CZTS due to larger ionic radius of selenium (0.198 nm) compared to that of sulfur (0.184 nm). Thus, the shift of diffraction peaks may result from the formation of the CZTSSe phase containing different Se content and allows us to deduce lattice parameters of the new compositions. As there is a clear correlation between the lattice constants and Se proportion (Jadhav et al., 2016), from the shift of the 220 and 312 diffraction peaks (Fig. 2b) we can additionally determine the S/(S + Se) ratio in kesterite phase Cu$_2$ZnSn(S$_{1-x}$Se$_x$)$_4$ (0 < x < 1). The size of crystallites calculated using Halder-Wagner method, lattice parameters and S/(S + Se) ratio are summarized in Table 1.

Raman spectra additionally approved the shifts of diffraction peaks depending on the CZTSSe composition. Fig. 3a compares 532 nm excited Raman spectra of CZTSSe films in the spectral range from 65 to 420 cm^{-1}. The bands due to dominant Se and S vibrations are visible in the frequency regions of 170–205 cm^{-1} and 280–400 cm^{-1}, respectively. While mixed Se and S vibrational modes appear in the frequency region of 205–280 cm^{-1} (Dimitrievska et al., 2015, 2014a, 2014b). It is apparent that the changes in the composition of the samples result in evident alterations of the relative intensities and peak positions of the bands. Thus, Raman spectroscopy provides an additional possibility to determine the S/(S + Se) anion ratio (Dimitrievska et al., 2015):

$$\frac{S}{S + Se} = k \frac{A_S}{A_{S,Se} + A_S} + C$$

(1)

where $k = 1.26(3)$, $C = -0.046(17)$, A_S is the integrated intensity of Raman bands related with the vibration of S atom in the frequency range 270–380 cm^{-1}, and $A_{S,Se}$ is the integrated intensity of Raman bands related with Se and mixed S and Se vibrational modes in the frequency region of 150–260 cm^{-1}. The anion content S/(S + Se) values determined from Raman spectroscopy for different composition CZTSSe films are presented in Table 2. This table additionally compares

Table 2

S/(S + Se) ratios derived from XRD, Raman and EDX. Elemental ratios of the CZTSSe established by EDX.

S/(S + Se)			Elemental ratios			
XRD	Raman	EDX	Cu/(Zn + Sn)	Zn/Sn	Cu/Sn	(metal)/(S + Se)
0.1	0.09	0.12	0.84	1.10	1.76	1.08
0.2	0.16	0.18	0.83	1.10	1.75	1.05
0.4	0.37	0.39	0.85	1.11	1.80	1.06
0.6	0.56	0.58	0.86	1.12	1.83	1.06

the S/(S + Se) ratio obtained using XRD, Raman and EDX techniques. The estimated S/(S + Se) ratios using different methods are quite similar indicating that selenium was effectively incorporated into the CZTS lattice. We should also note that the position of the prominent band near 198–220 cm^{-1} shifts to higher wavenumbers with increasing the S/(S + Se) ratio in the sample. This band is associated with vibrations of both S and Se anions in the lattice and can also be used for determination of composition of anions (Dimitrievska et al., 2014b), however, because of overlap with other vibrational modes, the calculations based on integrated intensity ratios were find to be more correct (Dimitrievska et al., 2015).

Because the annealing process may cause a slight material loss, Table 2 also presents the ratios of other elements in the CZTSSe films obtained after the selenization of the CZTS precursor at a temperature of 540 °C. As the Se content increases, the ratio of all other elements remains more or less the same suggesting that the selenization did not change the crystal structure and the phase composition. Moreover, these ratios are very similar to those obtained by other authors, which has been proven beneficial for high-efficiency CZTSSe devices (Guo et al., 2016).

To understand the impact of the Se content on the surface morphology of the CZTSSe films, the high magnification surface morphology SEM images of the selenized CZTSSe films were undertaken (see Fig. S3) where the as-deposited CZTS layer is also presented for clarity. The CZTSSe layer acquired a granular shape after high temperature annealing with selenium. The size of the granules slightly increased with proportion of Se in the layer up to S/(S + Se) value of 0.2 (Fig. S3d). Further increase in the Se content in the CZTSSe film resulted in slight decrease in the grain size. These results are consistent with data on the variation of the crystallites size obtained from XRD measurements (Table 1).

The absorption spectra of the CZTSSe films containing different S/(S + Se) ratios are presented in Fig. S4. The comparative analysis of absorption spectra shows significant dependence on S/(S + Se) ratio. As the Se content increases the absorption onset shifts towards higher wavelengths. We used Tauc plots to determine the optical band gap of the prepared films (Fig. 3b). The insert in Fig. 3b shows the estimated band gap energies obtained from extrapolation of the linear part of the Tauc plots. It is evident that the band gap decreases linearly by increasing Se content, where it equals to 1.38 eV for S/(S + Se) = 0.6 and to 1.13 eV when S/(S + Se) ratio is 0.1. As discussed latter, we prove that the reduced band gap of CZTSSe only slightly contributes to a higher photocurrent generation, while the most significant contribution comes from the crystal quality.

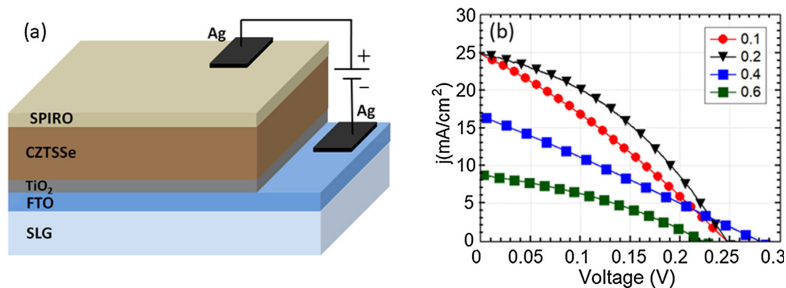To identify the influence of Se content on the device performance,

Fig. 4. (a) Schematic device architecture of investigated CZTSSe solar cells. (b) Current-voltage characteristics of the best CZTSSe solar cells containing different S/(S + Se) ratios.
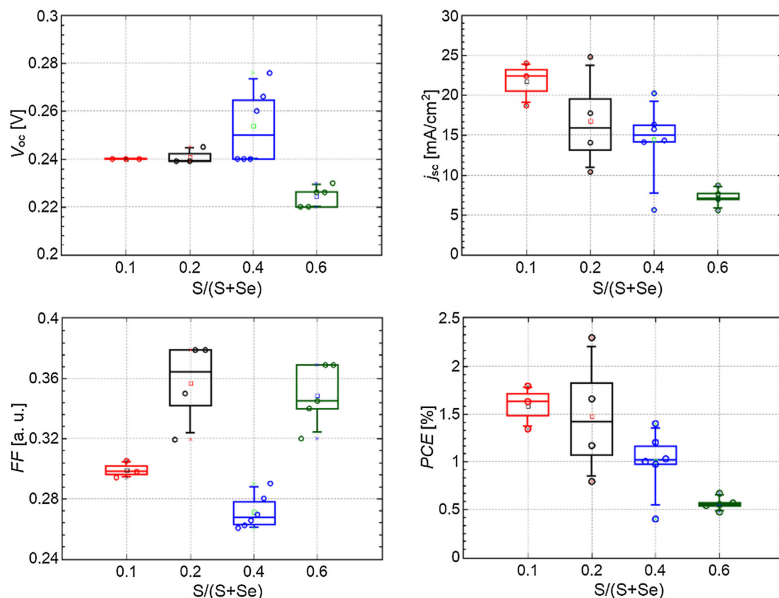

Fig. 5. Distributions of main photo-voltaic parameters as a function of different S/(S + Se) ratios.

we fabricated solid state CZTSSe solar cells of superstrate configuration using the following device architecture: FTO/TiO$_2$/CdS/Cu$_2$ZnSn $(S_{1-x}Se_x)_4$/SPIRO/Ag (where $0 < x < 1$). The schematic representation of this structure is shown in Fig. 4a. The current density-voltage (J-V) characteristics of the best performing devices are presented in Fig. 4b. The statistical distribution of the photovoltaic parameters as a function of (S/S + Se) ratio is shown in Fig. 5. The larger amount of selenium in solar cells leads to higher current densities as well as higher efficiencies. However, open circuit voltage almost does not depend on S/(S + Se) ratio and fill factors are distributed in the interval between 0.26 and 0.37, thus showing any noticeable influence of an amount of Se. Therefore, the significant increase in PCE is associated with increase in current densities. The best device generated a PCE of 3.1% with a short circuit photocurrent density of 36.5 mA/cm^2 and open-circuit voltage of 290 mV and fill factor of 38%. Though the best photovoltaic performances was obtained for device with S/(S + Se) = 0.2, the average power conversion efficiency was found to increase by increasing the content of Se. One could assume that the enhancement in photocurrent density might be associated with the band gap lowering. However, more than twice increased photocurrent is unlikely to be only due to band gap narrowing. To ascertain the contribution of the wavelengths that are responsible for the current generation, we measured the incident photon to electron conversion efficiency (IPCE). The corresponding IPCE spectra of the device containing different amount of Se are shown in Fig. S5. Importantly, the onsets of IPCE spectra (with experimental accuracy) is only slightly shifted to the longer wavelengths for the CZTSSe solar cells containing higher Se content and thus can hardly result in such a steep current increase. The highest IPCE resulted from the solar cells containing the largest Se content, whereas IPCE becomes lower when the Se content decreases which is also in line with the observed photocurrent densities (Fig. 4b). Thus, we can conclude that the photocurrent increase could be undoubtedly related to
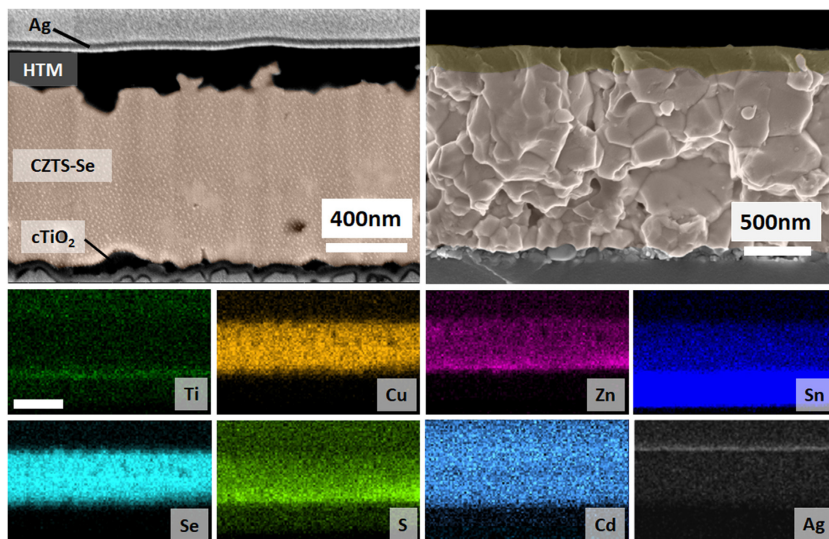
131

Fig. 6. SEM images of cross-sections made by FIB and fractured (upper left and right micrographs, respectively) of the solar cell device with S/(S + Se) = 0.2 ratio. The lower images depict EDX mapping of the FIB made cross-section (scale bar 1 μm). The chemical element, for which the map corresponds, is indicated on the image.

the improved crystal quality rather than the band gap narrowing due to Se content, which can only slightly contribute to the total photocurrent.

The solar cell with highest efficiency was chosen to further analyze its chemical composition. Fig. 6 shows SEM images of cross-sections made by FIB and fractured (upper left and right micrographs, respectively) of the solar cell device with S/(S + Se) = 0.2 ratio. The lower images depict EDX mapping of the FIB made cross-section and chemical element, for which the map corresponds is indicated on the image.

The solar cell consists of 1.5 μm thick CZTSSe absorbing layer, which is deposited between TiO_2 layer of several nm thickness and top hole transporting layer. We have chosen Spiro-MeOTAD as the HTM because it has decent carrier mobility, provides good coverage, smooth and pinhole-free films, and most importantly it also shows decent performance when applied both for CZTS solar cells (Wang et al., 2018a, 2017). The hole transporting layer penetrates into the pores and smooths the surface making it suitable for the deposition of silver electrode. The EDX maps of the cross section show that all the elements (Cu, Zn, Sn, S and Se) comprising CZTSSe film are uniformly distributed over the entire layer thickness. This suggests that during the annealing Se distributes homogeneously in the kesterite layer and replace the sulfur in the CZTS crystal lattice. Other clearly distinguished regions represent the presence of electron and hole transporting layer and also silver contact.

A more precise examination of interface CdS/CZTSSe revealed that Cd diffused into kesterite during the annealing since the CdS layer was absent in the EDX mapping of the FIB-made cross-section while it was quite evident before the annealing (see Fig. S6). The diffusion of Cd into CZTSSe absorber should be beneficial as CZTSSe or CZTS alloying by Cd yields increased grain size, decreased density of antisite defects and consequently improved photovoltaic performance (Sun et al., 2017). However, CdSe could be detrimental to device performance. To get the evidence that CdSe did not form during the selenization of glass/FTO/TiO2/CdS/CZTS structure we deposited CdS layer (~40 nm in thickness) on glass/FTO/TiO2 and performed the selenization. The XRD measurement confirmed that CdS transformed into CdSe. Raman

spectrum with the excitation wavelength of 532 nm was measured through the glass (Fig. S2 a, blue spectrum). Strong bands visible at 209 and 415 cm^{-1} belong to CdSe longitudinal optical (LO) phonon and its overtone (2LO) modes, respectively [Plotnichenko and Mityagin, 1977; Xi et al., 2008]. Since the spectrum was obtained through the glass substrate, strong and broad glass bands are visible at 559 and 614 cm^{-1}. The intensity of 2LO mode considerably decreases in the 785 nm excited spectrum, confirming the operation of resonance enhancement effect in the case of 532 nm excitation. The resonant Raman spectroscopy makes it possible to detect a very small quantity of investigated material.

Fig. S2 b compares Raman spectra of thin CdSe film (blue spectrum) already presented in Fig. S1 a and of CZTSe sample (red spectrum) obtained through the glass substrate since absorption of CZTSSe layer is much stronger than that of glass/FTO/TiO2. The LO mode of CdSe appears in the frequency range occupied by other vibrational modes of CZTSSe; thus this mode is not useful for the detection of the CdSe phase. However, the strong overtone mode (2LO) appears in the relatively free spectral region and can serve as an excellent Raman marker band for analysis of CdSe. The absence of the band in the vicinity of 415 cm^{-1} for 532 nm excited spectrum of glass/FTO/TiO2/CZTSSe sample confirms that the CdSe phase had not formed.

The increase in efficiency of our superstrate solar cell could be attributed to an improvement of the crystalline structure of the absorber layer with the increase in Se proportion in the layer. The largest crystallite size (Table 1, the last column) was measured in the samples with S/(S + Se) ratio of 0.2. The best crystalline structure of this samples is also evidenced by the sample Raman spectrum presenting the narrowest bands width (Fig. 3a). The imperfect crystallinity or amorphous structure is one of the reasons to occur shallow and deep defect levels within the bandgap, which are detrimental for solar cell efficiency (Kim et al., 2018). Results obtained imply that there is a lot of space to improve the crystalline structure of our CZTSSe absorber and consequently the efficiency of solar cell.

4. Conclusions

The role of Se content on the structural and optical characteristics of CZTSSe films and the superstrate solar cell performance were investigated. We found that selenium successfully incorporates into the CZTS lattice via selenium-sulfur substitution without changing the ratios of other elements. The increase of Se content reduces the optical band gap from 1.38 eV to 1.13 eV. The solar cell of superstrate configuration $FTO/TiO_2/Cu_2ZnSnSe_{3.2}S_{0.8}/SPIRO/Ag$ demonstrated a record PCE of 3.1% which, to the best of our knowledge, is the highest value reported for spray pyrolysis deposited the superstrate solar cells.

Appendix A. Supplementary material

Supplementary data to this article can be found online at https://doi.org/10.1016/j.solener.2019.04.072.

References

Bai, B., Kou, D., Zhou, W., Zhou, Z., Tian, Q., Meng, Y., 2016. Quaternary Cu 2 ZnSnS 4 quantum dot-sensitized solar cells: synthesis, passivation and ligand exchange. J Power Sources 318, 35–40. https://doi.org/10.1016/j.jpowsour.2016.04.009.

Berruet, M., Di Iorio, Y., Pereyra, C.J., Marotti, R.E., Vázquez, M., 2017. Highly-efficient superstrate Cu2ZnSnS4solar cell fabricated low-cost methods. Phys. Status Solidi – Rapid Res. Lett. https://doi.org/10.1002/pssr.201700144.

Dalapati, G.K., Zhuk, S., Masudy-Panah, S., Kushwaha, A., Seng, L., Chellappan, V., Suresh, V., Su, Z., Batabyal, S.K., 2017. Impact of molybdenum out diffusion and interface quality on the performance of sputter grown CZTS based solar cells. Sci. Rep. 1–12. https://doi.org/10.1038/s41598-017-01605-7.

Dimitrievska, M., Fairbrother, A., Pérez-Rodríguez, A., Saucedo, E., Izquierdo-Roca, V., 2014a. Raman scattering crystalline assessment of polycrystalline Cu2ZnSnS4thin films for sustainable photovoltaic technologies: Phonon confinement model. Acta Mater. 70, 272–280. https://doi.org/10.1016/j.actamat.2014.02.035.

Dimitrievska, M., Gurieva, G., Xie, H., Carrete, A., Cabot, A., Saucedo, E., Pérez-Rodríguez, A., Schorr, S., Izquierdo-Roca, V., 2015. Raman scattering quantitative analysis of the anion chemical composition in kesterite Cu2ZnSn(SxSe1−x)4 solid solutions. J. Alloys Compd. 628, 464–470. https://doi.org/10.1016/J.JALLCOM.2014.12.175.

Dimitrievska, M., Xie, H., Fairbrother, A., Fontané, X., Gurieva, G., Saucedo, E., Pérez-Rodríguez, A., Schorr, S., Izquierdo-Roca, V., 2014b. Multiwavelength excitation Raman scattering of Cu2ZnSn(SxSe1-x)4(0 ≤ x ≤ 1) polycrystalline thin films: vibrational properties of sulfoselenide solid solutions. Appl. Phys. Lett. 105. https://doi.org/10.1063/1.4891333.

Feng, Y., Yu, B., Cheng, G., Lau, T., Li, Z., Yin, L., Song, Q., Yang, C., Xiao, X., 2015. Searching for a fabrication route of efficient Cu < inf > 2 < / inf > ZnSnS < inf > 4 < /inf > solar cells by post-sulfuration of co-sputtered Sn-enriched precursors. J. Mater. Chem. C 3, 9650–9656. https://doi.org/10.1039/c5tc02486b.

Grinciené, G., Franckevičius, M., Kondrotas, R., Giraitis, R., Juškénas, R., Niaura, G., Naujokaitis, A., Juodkazyté, J., Tamašauskaité-Tamašiūnaité, L., Pakštas, V., 2018. Spray pyrolysis approach to CZTSSe thin fi lms. Influence of solvents on film characteristics. Semicond. Sci. Technol. 33, 095013. https://doi.org/10.1088/1361-6641/aad5d0.

Guo, J., Zhou, W.H., Pei, Y.L., Tian, Q.W., Kou, D.X., Zhou, Z.J., Meng, Y.N., Wu, S.X., 2016. High efficiency CZTSSe thin film solar cells from pure element solution: a study of additional Sn complement. Sol. Energy Mater. Sol. Cells 155, 200–215. https://doi.org/10.1016/j.solmat.2016.06.021.

Jadhav, Y.A., Thakur, P.R., Haram, S.K., 2016. Solar energy materials & solar cells voltammetry investigation on copper zinc tin sulphide/selenide (CZTS x Se 1–x) alloy nanocrystals: estimation of composition dependent band edge parameters. Sol. Energy Mater. Sol. Cells 155, 273–279. https://doi.org/10.1016/j.solmat.2016.06.030.

Kim, S.Y., Rana, T.R., Kim, J.H., Son, D.H., Yang, K.J., Kang, J.K., Kim, D.H., 2018. Limiting effects of conduction band offset and defect states on high efficiency CZTSSe solar cell. Nano Energy 45, 75–83. https://doi.org/10.1016/j.nanoen.2017.12.031.

Kumar, M., Dubey, A., Adhikari, N., Venkatesan, S., Qiao, Q., 2015. Strategic review of secondary phases, defects and defect-complexes in kesterite CZTS-Se solar cells. Energy Environ. Sci. 8, 3134–3159. https://doi.org/10.1039/c5ee02153g.

Lin, X., Kavalakkatt, J., Lux-Steiner, M.C., Ennaoui, A., 2015. Inkjet-printed Cu2ZnSn(S, Se)4solar cells. Adv. Sci. 2, 2–7. https://doi.org/10.1002/advs.201500028.

Liu, F., Shen, S., Zhou, F., Song, N., Wen, X., Stride, J.A., Sun, K., Yan, C., Hao, X., 2015. Kesterite Cu2ZnSnS4 thin film solar cells by a facile DMF-based solution coating process. J. Mater. Chem. C 3, 10783–10792. https://doi.org/10.1039/c5tc01750e.

Paris, M., Choubrac, L., Lafond, A., Guillot-Deudon, C., Jobic, S., 2014. Solid-state NMR and Raman spectroscopy to address the local structure of defects and the tricky issue of the Cu/Zn disorder in Cu-poor, Zn-rich CZTS materials. Inorg. Chem. 53, 8646–8653. https://doi.org/10.1021/ic5012346.

Plotnichenko, V.G., Mityagin, Yu.A., 1977. Investigation of fundamental vibrations in CdSe by Raman scattering and infrared methods. Sov. Phys. Solid State 19, 1584.

Prochowicz, D., Franckevičius, M., Cieślak, A.M., Zakeeruddin, S.M., Grätzel, M., Lewiński, J., 2015. Mechanosynthesis of the hybrid perovskite CH 3 NH 3 PbI 3: characterization and the corresponding solar cell efficiency. J. Mater. Chem. A 20772–20777. https://doi.org/10.1039/C5TA04904K.

Redinger, A., Berg, D.M., Dale, P.J., Siebentritt, S., 2011. The consequences of kesterite equilibria for efficient solar cells. J. Am. Chem. Soc. 133, 3320–3323. https://doi.org/10.1021/ja111713g.

Scragg, J.J., Kubart, T., Wätjen, J.T., Ericson, T., Linnarsson, M.K., Platzer-Björkman, C., 2013. Effects of back contact instability on Cu2ZnSnS4devices and processes. Chem. Mater. 25, 3162–3171. https://doi.org/10.1021/cm4015223.

Scragg, J.J., Wa, J.T., Edo, M., Ericson, T., Kubart, T., Platzer-bjo, C., 2012. A detrimental reaction at the molybdenum back contact in Cu2ZnSn(S, Se)4 thin-film solar cells. J. Am. Chem. Soc. 134, 19330–19333. https://doi.org/10.1021/ja308862n.

Sun, R., Zhuang, D., Zhao, M., Gong, Q., Scarpulla, M., Wei, Y., Ren, G., Wu, Y., 2017. Beyond 11% efficient Cu2ZnSn(Se, S)4 thin film solar cells by cadmium alloying. Sol. Energy Mater. Sol. Cells 174, 494–498. https://doi.org/10.1016/j.solmat.2017.09.043.

Swami, S.K., Chaturvedi, N., Kumar, A., Chander, N., Dutta, V., Kumar, D.K., Ivaturi, A., Senthilarasu, S., Upadhyaya, H.M., 2014. Spray deposited copper zinc tin sulphide (Cu 2 ZnSnS 4) film as a counter electrode in dye sensitized solar cells. Phys. Chem. Chem. Phys. 16, 23993–23999. https://doi.org/10.1039/C4CP03312D.

Tanaka, K., Kurokawa, M., Moriya, K., Uchiki, H., 2013. Surface morphology improvement of three-dimensional solar cell. J. Alloys Compd. 571, 98–102. https://doi.org/10.1016/j.jallcom.2013.03.060.

Tanaka, K., Minoru, K., Koichi, G., Yuya, N., Uchiki, H., 2012. Face-to-face annealing process of Cu2ZnSnS4 thin films deposited by spray pyrolysis method.pdf. Jpn. J. Appl. Phys. 51, 10NC26.

Tang, D., Wang, Q., Liu, F., Zhao, L., Han, Z., Sun, K., Lai, Y., Li, J., Liu, Y., 2013. An alternative route towards low-cost Cu2ZnSnS4thin film solar cells. Surf. Coatings Technol. 232, 53–59. https://doi.org/10.1016/j.surfcoat.2013.04.052.

Valdés, M., Santoro, G., Vázquez, M., 2014. Spray deposition of Cu2ZnSnS4thin films. J. Alloys Compd. 585, 776–782. https://doi.org/10.1016/j.jallcom.2013.10.009.

Wallace, S.K., Mitzi, D.B., Walsh, A., 2017. The steady rise of kesterite solar cells. ACS Energy Lett. 2, 776–779. https://doi.org/10.1021/acsenergylett.7b00131.

Walsh, A., Chen, S., Wei, S.H., Gong, X.G., 2012. Kesterite thin-film solar cells: advances in materials modelling of Cu 2 ZnSnS 4. Adv. Energy Mater. 2, 400–409. https://doi.org/10.1002/aenm.201100630.

Wang, W., Winkler, M.T., Gunawan, O., Gokmen, T., Todorov, T.K., Zhu, Y., Mitzi, D.B., 2014. Device characteristics of CZTSSe thin-film solar cells with 12.6% efficiency. Adv. Energy Mater. https://doi.org/10.1002/aenm.201301465.

Wang, Z., Brodusch, N., Gauvin, R., Demopoulos, G.P., 2018a. Nanoengineering of the Cu2ZnSnS4-TiO2interface: Via atomic layer deposition of Al2O3 for high sensitivity photodetectors and solid state solar cells. J. Mater. Chem A 6, 11507–11520. https://doi.org/10.1039/c8ta02966k.

Wang, Z., Brodusch, N., Gauvin, R., Demopoulos, G.P., 2018b. Lithium-doped Cu2ZnSnS4superstrate solar cells with 5% efficiency – an alternative to thin film kesterite photovoltaics. Nano Energy 53, 130–134. https://doi.org/10.1016/j.nanoen.2018.08.049.

Wang, Z., Gauvin, R., Demopoulos, G.P., 2017. Nanostructural and photo-electrochemical properties of solution spin-coated Cu2ZnSnS4-TiO2 nanorod forest films with an improved photovoltaic performance. Nanoscale 9, 7650–7665. https://doi.org/10.1039/c7nr01422h.

Werner, M., Romanyuk, Y.E., Tiwari, A.N., 2015. 8.3 % ef fi cient Cu 2 ZnSn (S, Se) 4 solar cells processed from sodium-containing solution precursors in a closed reactor. Thin Solid Films 582, 308–312. https://doi.org/10.1016/j.tsf.2014.10.043.

Xi, L., Lam, Y.M., Xu, Y.P., Li, L.-J., 2008. Synthesis and characterization of one dimensional CdSe by a novel reverse micelle assisted hydrothermal method. J. Colloid Interface Sci. 320, 491–500. https://doi.org/10.1016/j.jcis.2008.01.048.

Yan, R., Kang, L., Sun, Y., Zhang, J., 2018. Solution-processed Cu2ZnSnS4thin film with mixed solvent and its application in superstrate structure solar cells. RSC Adv. 8, 11469–11477. https://doi.org/10.1039/c8ra01095a.

Yu, J., Deng, H., Zhang, Q., Tao, J., Sun, L., Yang, P., Chu, J., 2019. The role of tuning Se/ (S + Se) ratio in the improvement of Cu2MnSn(S, Se)4 thin films properties and photovoltaic device performance. Sol. Energy 179, 279–285. https://doi.org/10.1016/j.solener.2018.12.076.

Yu, K., Carter, E.A., 2015. A strategy to stabilize kesterite CZTS for high-performance solar cells. Chem. Mater. 27, 2920–2927. https://doi.org/10.1021/acs.chemmater.5b00172.

Zaki, M.Y., Nouneh, K., Ebn Touhami, M., Belakhmima, R.A., Galca, A.C., Pintilie, L., Enculescu, M., Baibarac, M., Taibi, M., 2018. Effect of mixing complexing agents on the properties of electrodeposited CZTS thin films. Opt. Mater. 83, 252–256. https://doi.org/10.1016/j.optmat.2018.06.030.

3rd publication / 3-oji publikacija

Photoemission studies of organic semiconducting materials using open
Geiger-Muller counter
J. Nekrasovas, V. Gaidelis, E. Kamarauskas, M. Viliūnas, V. Jankauskas

Photoemission studies of organic semiconducting materials using open Geiger-Müller counter

View Online   Export Citation   CrossMark

Jonas Nekrasovas,[a] Valentas Gaidelis, Egidijus Kamarauskas, Mindaugas Viliūnas, and Vygintas Jankauskas

AFFILIATIONS

Institute of Chemical Physics, Vilnius University, Sauletekio av. 3, LT-10257 Vilnius, Lithuania

[a]**Author to whom correspondence should be addressed:** jonas.nekrasovas@ff.vu.lt

ABSTRACT

We investigated an open ionization cell based on the Geiger-Müller counter principle in a gas mixture at atmospheric pressure and demonstrated that the photoemission signals as weak as 1 electron per second are detectable. This finding allowed us to investigate more accurately the photoemission spectrums, especially in the vicinity of the photoemission threshold. Using such a cell, we investigated a number of organic semiconductor materials, tested various ways to analyze the results of the measurements of photoemission spectrums, and demonstrated an efficient way to determine ionization potential by using the square root of the derivative of the yield dependence on the light quanta energy $(\mathrm{d}Y_1/\mathrm{d}(h\nu))^{1/2}$. This method leads to more evident graphical representation of the measurement results and better I_p estimation in comparison to the results estimated by using the traditional method of plotting $Y^{1/n}$ dependence on the quanta energy $h\nu$.

I. INTRODUCTION

The electron photoemission is an important tool to investigate energetic levels of semiconducting materials, especially organic compounds, which are widely used in the development of electronic devices, such as solar cells, light emitting diodes, field effect transistors, and electrophotography photoreceptors. In all the cases mentioned, the knowledge of the energetic levels of the materials is essential for making the right choice from the wide variety of existing materials or to synthesize new materials with desired characteristics. The key question in the evaluation of energetic levels is the measurement of the ionization potential (I_p). Various methods are used for this purpose, such as ultraviolet photoemission spectroscopy (UPS)[1–10] and its modification valence band UPS (VB-UPS),[11,12] electrochemical method of cyclic voltammetry (CV),[13,14] the photoelectron yield spectroscopy (PYS) method,[9,15–19] and dual-mode Kelvin probe ambient pressure Photoemission Spectroscopy (PES) method, which enables one to measure both contact potential difference between the material investigated and the tip electrode of the apparatus as well as the ionization potential.[20] The UPS method is widely used for investigations of both metals and nonmetals. However, this method has some drawbacks related to the need of performing experiments in high vacuum and charging-up of the sample as discussed in Refs. 21 and 22. Another problem arises from the light sources used in the UPS equipment.

The cold cathode capillary discharge in He light source UV illumination with quanta energies of 21.2 and 40.8 eV is usually used, which may cause negative effects on the specimens investigated. The bond dissociation energy in organic molecules is around 6.4 eV (or around 618 kJ/mol in the case of the C–H bonds and around 338 kJ/mol for C–C bonds);[23] therefore, the energy of the light quanta in the UPS apparatus far exceeds the dissociation of the molecules limit and may cause photochemical reactions to change the characteristics of samples. In the case of TiO_2, the work function change of 0.5 eV was found as a result of UV illumination during measurement by the UPS method.[21]

The electrochemical method is performed with the materials dissolved in an organic solvent, while in the electronic devices the same materials are used as solids. Therefore, the CV measurements are useful for comparison of different materials between themselves, but in fact they give little information on possible behavior of the materials in the devices. Photoelectron yield spectroscopy (PYS) is based on the measurement of the quantity of photoelectrons released from the sample as a function of the light quanta energy. PYS experiments may be performed either in vacuum or in a gas atmosphere, including air. The methods based on the photoemission in air are relatively easy to perform and are widely used for the evaluation of the ionization potential of semiconducting materials or work function of metals.[15,24–27] The authors of the article[24] for

the measurement of the photoemission yield used an open electron counter, while in Ref. 25 an electrometer was used, which measured the electric potential buildup as a result of incoming photoelectrons in the capacitance of the input of the electrometer. Our experience shows that the sensitivity of the available electrometers, which is around 10^{-16} A, is not always sufficient for accurate measurement. A photoemission current near the threshold may be lost due to the noise of the equipment. In such cases, the quanta energy, at which the current reaches the noise level, may be regarded as the photoemission threshold, and this leads to an inaccurate evaluation of the ionization potential. In order to increase the sensitivity of measurement, we conducted experiments with an open ionization cell working on the principal of Geiger–Müller counter and estimated that at calm geomagnetic conditions photoemission current as low as about one electron per second, or around 10^{-19} A, may be detected. We developed a setup for the I_p measurement. Investigations of the photoemission yield in a gas mixture under atmospheric pressure were performed on a number of materials, some of which are described in this article.

Another question discussed in this article is the method of processing and graphical presentation of the PYS results in order to show in detail the peculiarities of the photoemission spectrums. Fowler showed how to estimate work function for metals using the yield function of photoemission.[28] Usually for organic materials, the photoemission yield Y results are plotted as $Y^{1/n}$ dependence on the quanta energy $h\nu$ with the n values varying from 1 to 4.[9,15,29,30] In general, for metal samples $n = 2$ and for most organic materials, $n = 3$ values are used. The rule of this method is to find the n value in order to achieve the best linearity of plotted curve. Kochi et al. reported the experimental results for tetracene, where good linearity was achieved for the values $n = 1, 2, 3, 4$.[16] We propose to calculate the square root of the derivative of the yield dependence on the light quanta energy $(dY/d(h\nu))^{1/2}$. In literature, the derivatives of the yield spectrum are used to evaluate the density of states (DOS) in the energy bands of the materials investigated,[24] we estimated that the square root plots of the derivatives are a good tool to evaluate the I_p value. The graphical representation of this function is more informative and straightforward than the other presentations used.

II. EXPERIMENTAL SETUP

For the investigation of photoemission at the atmospheric pressure, we used the scheme working on the principal of Geiger–Müller counter.[31] Our home built slow electron counter consisting of the cylinder shape ionization cell with a slit along one side of the cylinder for the electrons to enter from the surrounding space (Fig. 1). A thin wire runs along the axis of the cylinder, and a high positive voltage is applied to the wire during cell operation. The voltage of the wire is maintained somewhat lower than the corona discharge initiation voltage and creates around 10^5 V/cm electric field at the wire surface. When slow electron enters the interior of the cylinder, it is affected by the electric field and drifts toward the wire. The avalanche develops in the vicinity of the wire, where ionization of the gas molecules takes place in a strong electric field. The swift multiplication of the charge carriers increases their number up to around 10^9. The avalanche process ends when positive ions

form space charge in the vicinity of the wire; thus, the electric field is weakened. Subsequently, positive ions drift toward the cathode, where they lose their charge. The molecules become neutral and excited.[31] Some gases, such as Ar or N_2, lose the excitation energy emitting quanta of UV light;[31] these quanta may ionise other gas molecules, thus creating secondary free electrons, which approach the anode and initiate new undesirable avalanches. In order to diminish these avalanches, we used high purity mixture of gases, containing 5% methane and 95% argon together with air at around 1:1 ratio. The molecules of methane lose the energy by dissociation, working as an effective quencher of the formation of secondary electrons and false signal pulses.

The electric scheme of the electron counter is shown in Fig. 1. It consists of a high voltage source (HV), an ionization cell and a special sample's holder placed in a closed measurement camera as well as amplifier and comparator with optional threshold level adjustment. The high voltage value is set by U_{SET}. The pulse counter and the experiment are controlled by microcontroller, which is operated by PC. The monochromatic light enters into the camera through quartz window. If light quanta are absorbed by the sample and electron is emitted into the cell, the avalanche discharge takes place. A short current pulse runs through the cell and the input resistor of the amplifier R_{IN}. The rising part of the pulse less than $1\,\mu s$ long is determined by the processes inside the cell and bandwidth of amplifier while the falling part, which lasts around $25\,\mu s$, is determined by the capacitances of the cell, connecting wires, input capacitance of amplifier, and resistor R_{IN}. After the pulse, the voltage in the cell increases up to the initial value. The duration of the voltage recovery is limited by R_{HV} and the capacitance of the cell and connecting wires, with the time constant close to the $20\,\mu s$. The registration of the number of signal pulses is mostly limited by the time of the electric field redistribution in the cell and other phenomena, such as warming up of the gases around the wire; therefore, the upper limit is around 1000 pulses per second. The magnitude of the signal pulses depends on the atmospheric pressure, high voltage, and gas mixture composition. Typical signal height of registered pulses was around 4 V, and the threshold of the minimum signal height was set to 2 V (U_{TH}). The sample was illuminated with monochromatic light from the
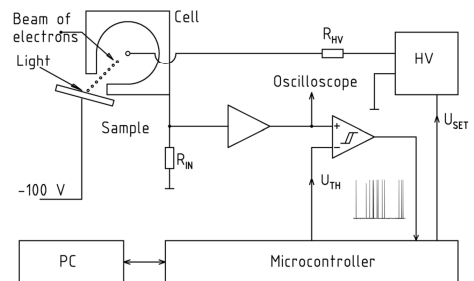

FIG. 1. Electric scheme of electron counter.

deuterium light source through the Newport CS260 grating mono-chromator. The slit width of the monochromator is 0.2 mm, and the reciprocal resolution was 6.4 nm/mm. The calculation gives the spectral width of the light beam 0.040 eV at 6.2 eV quanta energy and 0.026 eV at 5.0 eV.

In comparison to commercially available photoelectron spec-trometers, like Riken-Keiki's AC-2 and AC-3,[32,33] our system does not use quenching and suppressor grids along with pulse genera-tors; instead, we use commercially available 95% of argon and 5% methane mixture and this solves the problem of quenching and false pulses. An absence of the quenching pulses is one of the merits of our counter. The electrons, reaching the counter, cannot be detected while these pulses are applied; thus, 3 ms long waiting periods arise; as a result, considerably less than 300 electrons can be detected per second.[32,33] These 3 ms are dead time of the counter. In our case, the counter recovers with the time constant $25 \mu s$, hence in about $100 \mu s$. This enables to detect up to 1000 electrons per second.

III. INVESTIGATED MATERIALS AND PREPARATION OF THE SAMPLES

In order to demonstrate the capabilities of the new method, the photoemission spectra of some well-known materials were investigated: metal-free phthalocyanine (H_2Pc), titanyl phthalocya-nine (TiOPc), N, N^t-Bis(3-methylphenyl)-N,N^t-diphenylbenzidine (TPD) from Sands Co., regioregular polyhexyltiophene from Sigma Aldrich. Chemical formulas of the materials are shown in Fig. 2. TiOPc and H_2Pc powders were dispersed in (Tetrahydrofuran)

without any binding material, and the dispersion was casted on the substrates consisting of polyester film coated with Al conductive layer and around $0.5 \mu m$ thick layer of a copolymer of methylmeta-crylate and metacrylic acid, coated from the 2.5% solution in 1:1 mixture of ethanol and acetone. TPD was dissolved in THF and coated on the substrate. P3HT was dissolved in chloroform. The samples were dried by heating them at 60 °C for 30 min.

IV. GRAPHICAL PRESENTATION OF THE RESULTS AND EVALUATION OF I_p

For the interpretation of the measurement results and finding the correct value of the ionization potential, a proper graphical pre-sentation of the photoemission spectrums, clearly revealing their peculiarities, is needed. Usually, in the PYS method, I_p is evaluated by using $Y^{1/n}$ dependence on the quanta energy graphs at the n values 1–4[9,15,29] with the recommendation to find the n value, at which the best linearity is achieved. However, it is not always easy to do this evaluation correctly, since the estimated I_p value consid-erably depends on n.

Secondly, in publications on the UPS investigations of organic materials, as in Refs. 11, 12, and 34, it is stated that the distribution of the density of states (DOS) is a Gaussian function. This function is used in both—theoretical calculations and interpretation of experimental results, but in a sense of finding I_p value, it raises a question—how to define and to find experimentally photoemission threshold correctly? The Gaussian function smoothly decreases down toward zero all the way. If we draw a straight line, best fitting
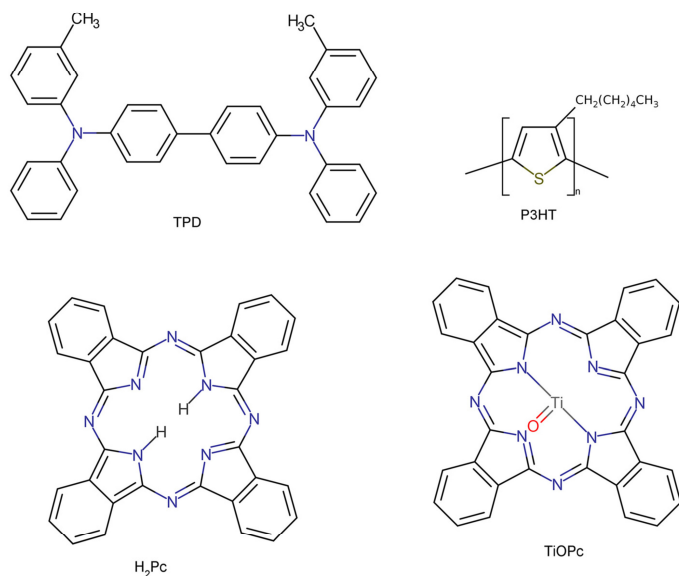
137

the slope of the Gaussian function, then it intersects the abscissa at the point where the function value is about 10% of the maximum value. The values near to this are present in the results of UPS investigations.[11,12,34] Thus, the weak photoemission present in the gap may be caused by the tails of HOMO. $Y^{1/n}$ method eliminates possible detection of weak DOS in HOMO-LUMO energy gap. The weak photoemission at the quanta energies less than the estimated I_p values is reported in the literature.[15,24,29]

Mathematical modeling helps to decide which of the possible methods of the graphical data presentation and processing is better for the evaluation of I_p. It is assumed that the dependence of yield Y for semiconductors is proportional to the cube of the difference between the incident quanta energy $h\nu$ and ionization potential I_p.[15,35] It is evident that in the simple case, when there is only one photoemission band, the square root of the derivative of Y on the quanta energy is linear.

Let us consider a model, in which there are two photoemission bands: the first weak band and the second strong band accordingly characterized by the thresholds I_{pR1} and I_{pR2}. Further, we suppose that there may be a weak nearly constant photoemission of yield C caused by the background radiation, scattered light or other phenomena. Yield Y can be presented as follows:

$$Y = C, \quad \text{if } x < I_{pR1}, \qquad (1)$$

$$Y = C + A \cdot (x - I_{pR1})^3, \quad \text{if } I_{pR1} < x \leq I_{pR2}, \qquad (2)$$

$$Y = C + A \cdot (x - I_{pR1})^3 + (x - I_{pR2})^3, \quad \text{if } x > I_{pR2}. \qquad (3)$$

Here, x means the quanta energy. The parameter $A < 1$ means the intensity of the first band while the intensity of the second band is 1.
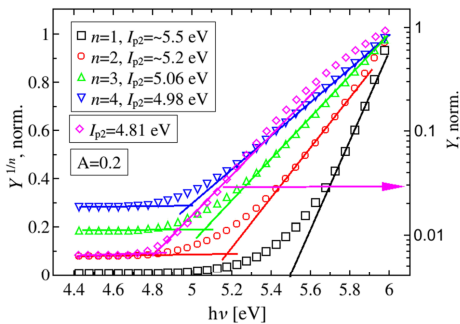

FIG. 3. Results of calculation plotted as $Y^{1/n}$ dependencies on x (representing light quanta energy) on linear and logarithm scales (pink diamond). The values of Y were calculated using formulas (1), (2), and (3) with these parameters: $I_{pR1} = 4.6$, $I_{pR2} = 5$, $C = 0.01$, and $A = 0.2$.

The plot of Y values is shown in Fig. 3 as $Y^{1/n}$ dependencies on x. Y values were calculated using (1), (2) and (3) formulas. The straight lines approximating the sections of the curves were drawn in order to find the crossing points. The x coordinate of the intersection point is considered as I_{p2}. It is necessary to note that it is practically impossible to find satisfactorily linear sections in the cases of $n = 1$ or 2; thus, the "best visual fit" was chosen. The linearity of the curves improves at $n = 3$ or 4. In the case of $n = 1$, the dependence was plotted both in linear and logarithm scale, and we found the crossing point in the latter case. The values of the parameter I_{p2} defined as x at the crossing points are given in Table I. In the case of the linear plot, these values decrease with an increase of n, but the lowest value is estimated on the logarithm scale curve at $n = 1$. Almost in all the cases estimated, the I_{p2} value significantly differs from the real value $I_{pR2} = 5$. Moreover, it is problematic to decide how to find the real value of I_{p1}, which is 4.6 eV, on these graphs.

We explored the way for solving above described issues based on the calculation and plotting of the square root of the derivative of the dependence of Y on the quanta energy. Differentiation of (2) to (4) gives

$$dY/dx = 0, \quad \text{if } x \leq I_{pR1}, \qquad (4)$$

$$dY/dx = 3A(x - I_{pR1})^2, \quad \text{if } I_{pR1} < x \leq I_{pR2}, \qquad (5)$$

$$dY/dx = 3A(x - I_{pR1})^2 + 3(x - I_{pR2})^2, \quad \text{if } x > I_{pR2}. \qquad (6)$$

In Fig. 4, there are the dependencies of the square roots of Y calculated by the formulas from (4) to (6) at $I_{pR1} = 4.6$ eV and $I_{pR2} = 5$ eV. The derivatives were calculated digitally from Y data, similarly as it is done with the experiment results. Each dependence in Fig. 4 may be approximated by pairs of straight lines, and the crossing points of these lines shift to higher x values with the increment of parameter A, but this shift is smaller than in the power law presentations.

Differentiation of the expression (3) is superior in comparison with the calculation of the power law expressions or logarithm, because each component of the expression is differentiated individually; thus, there is a possibility to evaluate each component in Eq. (6).

TABLE I. Values of the parameter I_{p2} defined as x values at the crossing points.

	I_{p2} (eV)		
n	$A - 0.05$	$A - 0.2$	$A - 0.5$
1	~5.6	~5.5	~5.5
2	~5.3	~5.2	~5.2
3	5.15	5.06	4.93
4	5.04	4.98	4.86
1, log scale	5.04	4.81	4.74
Derivative	5.05	5.08	5.11
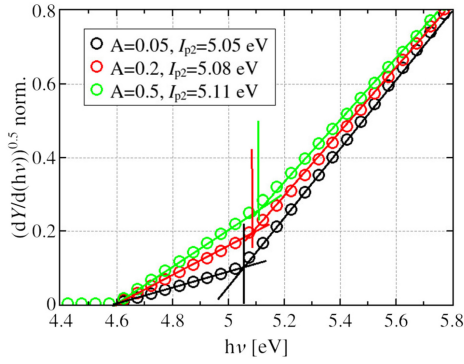
FIG. 4. Dependencies of the square root of the derivatives of Y according to the formulas (4)–(6).

FIG. 6. Effect of the spectrum data smoothing before calculating the square root of the derivative. Black squares for raw data and blue dots for smoothed data. Photoemission spectrum of H_2Pc.

V. MEASUREMENTS AND DATA PROCESSING

A. Backround signal

Some signal pulses are detected even in the case when the sample is not illuminated (Fig. 5). To evaluate the multitude of these pulses, a series of the counting cycles were made, each lasting 20 s. The numbers of these pulses were from 0 to 17, and the average was 4.9 pulses per 20 s or $0.245\,s^{-1}$. For comparison, when the H_2Pc sample was illuminated with 4.95 eV and 5.15 eV monochromatic light, the average numbers of the pulses of four experiments were $4.4\,s^{-1}$ and $24.4\,s^{-1}$, respectively. The signal to dark noise ratio was about 18 and 100, respectively. The pulses registered in the dark may be caused by the radiation background or other
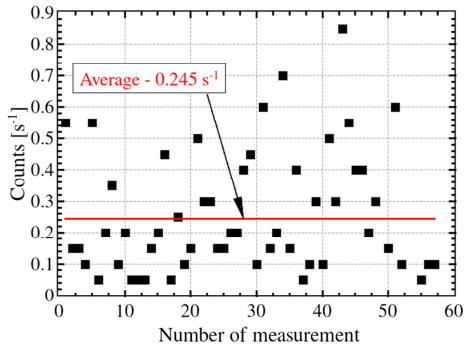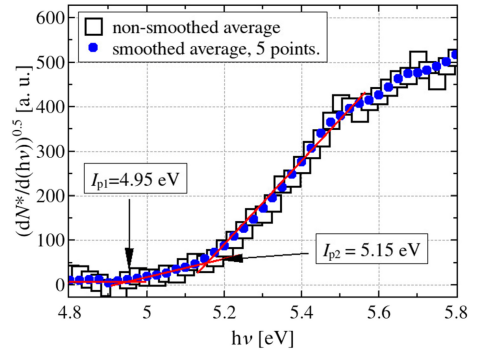
factors not related to the photoemission. Those pulses can hinder the investigation of the photoemission spectrums near to the threshold, where the numbers of pulses are relatively small. We investigated some possibilities to reduce the negative influence of these pulses. The numbers, that were considerably higher than the average of the near interval of the spectrum, were replaced by the average of the two adjacent counts. Then, as seen in Fig. 6, the smoothing by the 3 to 5 point methods made the results less scattered.

B. Data processing

Finally, the photoemission spectrums were scanned for 2–4 times and then the considerably higher numbers than the average of the near interval of the spectrum were replaced by the average of the two adjacent counts. The results for all the scans were averaged, smoothed by the 3 or 5 points methods, divided by the normalized intensity of monochromatic light reaching the sample; thus, the corrected pulse numbers N` were calculated for the case of equal energy spectrum, and the result was considered as the photoemission yield Y. The yield was normalized by dividing its values by the highest value in the spectrum. The spectrums of the derivative Der of Y on the quanta energy hν and the square root of derivative were calculated.

C. I_p estimation

In order to retain the negative values of derivative in the square root of the derivative graphs, the following quantity was calculated:

$$(Der)^{0.5^*} = (|(Der)|)^{0.5} \cdot |(Der)|/(Der), \qquad (7)$$

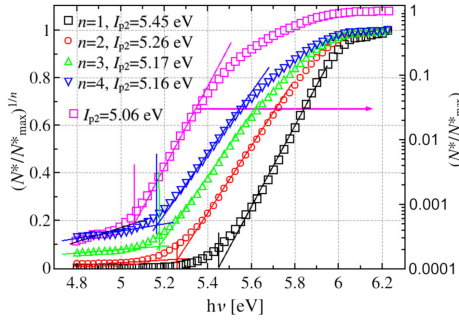where (Der) is $(dN*/d(h\nu))$. In the cases of positive derivative, the

FIG. 5. Numbers of the signal pulses when a sample is not illuminated.

FIG. 7. Normalized photoemission spectrum of the H$_2$Pc powder in various presentations.

TABLE II. Results of the I_p measurements in electronvolts.

Material	I_p (eV), when				Log scale	$(Der)^{0.5}$	
	$n=1$	$n=2$	$n=3$	$n=4$		I_{p1}	I_{p2}
TiOPc	5.61	5.47	5.40	5.36	5.3	5.25	5.41
H$_2$Pc	5.45	5.26	5.17	5.16	5.06	4.95	5.15
TPD	5.58	5.40	5.32	5.28	5.23	5.16	5.34
P3HT	4.83	4.72	4.67	4.65	4.61	4.40	4.66

$(Der)^{0.5*}$ coinciding with the usual square root but at the negative (Der) the $(Der)^{0.5*}$ value is also negative.

The plot of the square root of the derivative for H$_2$Pc powder sample is shown in Fig. 6 (blue dots). There is nearly linear part up to the quanta energy of $x_1 = 4.95$ eV (I_{p1}). Between $x_1 = 4.95$ eV and $x_2 = 5.15$ eV (I_{p2}), there is a second linear region and above 5.15 eV follows the third linear region.

The I_{p2} value of 5.15 eV found that this way is close to the values found by using the $n = 3$ (5.17 eV) and $n = 4$ (5.16 eV) in power low plots, but it only reveals one threshold of the spectrum and the I_{p1} value of 4.95 eV is lost. The square root of the derivative plot is preferable because it reveals the peculiarities of the spectrum most clearly, and more break points are seen on these plots.

VI. RESULTS

In Fig. 7, normalized photoemission spectrum of the metal-free phthalocyanine powder is presented in various forms. The picture is very similar to the one shown in Fig. 3 representing the results of the mathematical considerations. There are the regions on these dependencies, which may be approximated as straight lines; the crossing points of these lines may be considered as I_p

values. If the power law function is used, then estimated values vary from 5.45 eV at $n = 1$ to 5.16 eV at $n = 4$. In Fig. 7, the case of $n = 1$ is also plotted in logarithm scale and the break point may be found on this plot at 5.06 eV.

The results of investigated samples are summarized in Table II. In all the cases, the breaking points shift to lower energies at increasing n. Usually I_p values estimated on the plots at $n = 3$ or 4 are close to the values found on the square root of derivative plot. $n = 1$ plots in logarithm scale give the lowest I_p value.

Table III shows the comparison of the results of our experiments to those reported in the literature. As seen in Table II, estimated I_p values on $(dY_1/d(hv))^{1/2}$ plots correlate with the values estimated on $Y^{1/n}$ plots, when n is 3 or 4. The difference in I_p values can be caused by fabrication techniques, crystalline modification or amorphous state of the sample, apparatus error range, or where the sample was made and measured: in atmosphere, in inert gases environment or in vacuum. In our case, if it is not mentioned otherwise, all samples were measured right after fabrication. Moreover, in some cases, it is not clear how actually the final value of I_p was estimated or $n = 3$ was chosen by default. The errors of UPS measurements of published results could be found up to 0.1 eV, in the case of H$_2$Pc.[2] The error of our system is around 0.1 eV. Additionally, we made some thermally evaporated Au samples and measured them right after deposition as well as one week and two weeks later, estimating I_p values of 4.60 eV, 4.92 eV, and 4.88 eV, respectively. Usually, Au I_p value found by UPS is 5.10 eV,[36] though when Au samples are measured in air, estimated I_p value tends to decrease to 4.78 eV.[37]

What is the meaning of the values I_{p1} and I_{p2}? The first weak photoemission band with the beginning at h$\nu = I_{p1}$ may be caused by various factors, such as the presence of impurities in the sample

TABLE III. Ionization potential values in electrovolts found in various literature sources.

Material	PES/PYS	UPS	CV	Kelvin probe	I_{p1}/I_{p2}
TiOPc	5.24[a] (Refs. 29 and 38)	5.2 (Refs. 5–7)			5.25/5.41
H$_2$Pc	5.1[a] (Ref. 39)	4.95–5.1 (Refs. 8, 11, and 40)		5.1 (Ref. 41)	4.95/5.15
TPD	5.34[b] (Ref. 16)	5.1–5.2 (Refs. 2–4)	5.55 (Ref. 14)		5.16/5.34
P3HT	4.54[b] (Ref. 9), 4.75[a] (Ref. 18)	4.6–4.85 (Refs. 9, 10, 42, and 43)	5.2 (Ref. 44)		4.40/4.66
Au	4.78[a] (Ref. 37)	5.10 (Ref. 36)			4.60[c], 4.92[d]

[a]In air.
[b]In vacuum.
[c]After deposition.
[d]1 week after deposition.

investigated, crystallization or aggregation of the molecules, adsorbed gases, and other factors. It may also be caused by the tail of the HOMO Gaussian function and, at least in some cases, represent the real value of the ionization potential. Comparison of our results with the results of UPS studies helps us to answer this question. In the case of TiOPc, the value of ionization potential, or highest occupied molecular orbital level (HOMO), found by the UPS method[5–7] is 5.2 eV, and $I_{p1} = 5.25$ eV found by us is very close to this value. Therefore, we can conclude that in this case, the value of I_{p1} corresponds to the HOMO value. Then, the value $I_{p2} = 5.41$ eV may correspond to HOMO-1. In the case of H_2Pc, the UPS value of 4.95 eV[8] matches with the $I_{p1} = 4.95$ eV and $I_{p2} = 5.15$ eV is close to the UPS value of 5.1 eV.[40] The ionization energy of 4.96 eV for H_2Pc found in Ref. [11] by the VB-UPS method coincides with our value of $I_{p1} = 4.95$ eV. However, there is no indication of the presence of the second break point, found by us at 5.15 eV. The UPS measurements for TPD give values 5.1–5.2 eV that are close to the value $I_{p1} = 5.16$ eV; thus, we can assume this value as representing HOMO. Then, the second value, $I_{p2} = 5.34$ eV, may be regarded as HOMO-1. In the case of P3HT, the UPS value for HOMO is 4.6–4.85 eV, which is close to our $I_{p2} = 4.66$ eV value. If we regard this value as HOMO, then the photoemission band with the beginning at $I_{p1} = 4.40$ eV was probably absent or too weak to be detected in the UPS experiments. This may be caused by different experiment conditions—high vacuum in UPS experiment and the gas mixture in our case.

Other factors to consider are these: how the samples tend to change their surface properties in air environment, how initial materials were stored (in our case, all materials except P3HT were kept in air), or when the sample was measured. As mentioned previously, I_p value from Au sample changes up to 0.30 eV in one week. It is known that Au samples are sensitive in terms of contamination.[45] In the case of TPD, H_2Pc, and TiOPc, after being kept one week in air, I_p values changed only within the error range.

It is almost impossible to approximate weak photoemission linearly on $Y^{1/n}$ plot and to choose the right n value; thus, we prefer to use $(dY_1/d(h\nu))^{1/2}$ plot. $(dY_1/d(h\nu))^{1/2}$ plot allows us to analyze photoemission spectrums in more detail.

VII. CONCLUSIONS

We demonstrated an apparatus to measure I_p of semiconductor materials in a gas mixture at atmospheric pressure by using the PYS method. The apparatus is able to detect electron photoemission signals down to a single electron per second (10^{-19} A). The high sensitivity detector enabled us to accurately detect weak electron emissions out of the samples at photoemission spectrum threshold. This led us to the new way of estimating I_p values, which is to calculate the square root of the derivative of the yield dependence on the light quanta energy $(dY_1/d(h\nu))^{1/2}$. This method is supported by the mathematical consideration and provides more precise estimation of I_p in comparison to the results plotted as $Y^{1/n}$ dependence on the quanta energy $h\nu$. The graphical presentation of this function is more informative than the other used presentations and clearly shows multiple thresholds in the photoemission spectrum. Our experiments were carried out and I_p values measured for four well-known materials (TPD, TiOPc, H_2Pc, P3HT) and Au.

The high sensitivity detector and the new method of data interpretation allowed us to estimate I_p values more precisely in comparison to the PYS results that were found in the literature.

REFERENCES

[1] F. Reinert and S. Hüfner, "Photoemission spectroscopy—From early days to recent applications," New J. Phys. 7, 97–97 (2005).

[2] K. Sugiyama, D. Yoshimura, T. Miyamae, T. Miyazaki, H. Ishii, Y. Ouchi, and K. Seki, "Electronic structures of organic molecular materials for organic electroluminescent devices studied by ultraviolet photoemission spectroscopy," J. Appl. Phys. 83(9), 4928–4938 (1998).

[3] H. Ishii, K. Sugiyama, D. Yoshimura, E. Ito, Y. Ouchi, and K. Seki, "Energy-level alignment at model interfaces of organic electroluminescent devices studied by UV photoemission: Trend in the deviation from the traditional way of estimating the interfacial electronic structures," IEEE J. Sel. Top. Quantum Electron. 4(1), 24–33 (1998).

[4] R. J. Murdey and W. R. Salaneck, "Charge injection barrier heights across multilayer organic thin films," Jpn. J. Appl. Phys. 44(6), 3751–3756 (2005).

[5] M. Brumbach, D. Placencia, and N. R. Armstrong, "Titanyl phthalocyanine/C_{60} heterojunctions: Band-edge offsets and photovoltaic device performance," J. Phys. Chem. C 112(8), 3142–3151 (2008).

[6] D. Placencia, W. Wang, J. Gantz, J. L. Jenkins, and N. R. Armstrong, "Highly photoactive titanyl phthalocyanine polymorphs as textured donor layers in organic solar cells," J. Phys. Chem. C 115(38), 18873–18884 (2011).

[7] D. Placencia, W. Wang, R. C. Shallcross, K. W. Nebesny, M. Brumbach, and N. R. Armstrong, "Organic photovoltaic cells based on solvent-annealed, textured titanyl phthalocyanine/C_{60} heterojunctions," Adv. Funct. Mater. 19(12), 1913–1921 (2009).

[8] T. Kimura, M. Sumimoto, S. Sakaki, H. Fujimoto, Y. Hashimoto, and S. Matsuzaki, "Electronic structure of lithium phthalocyanine studied by ultraviolet photoemission spectroscopy," Chem. Phys. 253(1), 125–131 (2000).

[9] R. Grzibovskis and A. Vembris, "Energy level determination in bulk heterojunction systems using photoemission yield spectroscopy: Case of p3ht:PCBM," J. Mater. Sci. 53(10), 7506–7515 (2018).

[10] A. J. Cascio, J. E. Lyon, M. M. Beerbom, R. Schlaf, Y. Zhu, and S. A. Jenekhe, "Investigation of a polythiophene interface using photoemission spectroscopy in combination with electrospray thin-film deposition," Appl. Phys. Lett. 88(6), 062104 (2006).

[11] D. R. Zahn, G. N. Gavrila, and M. Gorgoi, "The transport gap of organic semiconductors studied using the combination of direct and inverse photoemission," Chem. Phys. 325(1), 99–112 (2006).

[12] C. Deibel, D. Mack, J. Gorenflot, A. Schöll, S. Krause, F. Reinert, D. Rauh, and V. Dyakonov, "Energetics of excited states in the conjugated polymer poly (3-hexylthiophene)," Phys. Rev. B 81(8), 085202 (2010).

[13] A. J. Bard and L. R. Faulkner, Electrochemical Methods: Fundamentals and Applications, 2nd ed. (Wiley, 2001).

[14] J. Kim, S. Lee, J. Lee, E. Lim, and B. Jung, "3,3′-bicarbazole-based host molecules for solution-processed phosphorescent OLEDs," Molecules 23(4), 847 (2018).

[15] H. Ishii, H. Kinjo, T. Sato, S.-I. Machida, and Y. Nakayama, "Photoelectron yield spectroscopy for organic materials and interfaces," Electron. Process. Organic Electron. 209, 131–155 (2015).

[16] H. Fujikawa, S. Tokito, and Y. Taga, "Energy structures of triphenylamine oligomers," Synth. Met. 91(1), 161–162 (1997).

[17] Y. Ohmori, A. Fujii, M. Uchida, C. Morishima, and K. Yoshino, "Fabrication and characteristics of 8-hydroxyquinoline aluminum/aromatic diamine organic multiple quantum well and its use for electroluminescent diode," Appl. Phys. Lett. 62(25), 3250–3252 (1993).

[18] Y.-J. Huang, W.-C. Lo, S.-W. Liu, C.-H. Cheng, C.-T. Chen, and J.-K. Wang, "Unified assay of adverse effects from the varied nanoparticle hybrid

in polymer–fullerene organic photovoltaics," Solar Energy Mater. Solar Cells **116**, 153–170 (2013).

[19]Y. Guo, C. Liu, K. Inoue, K. Harano, H. Tanaka, and E. Nakamura, "Enhancement in the efficiency of an organic–inorganic hybrid solar cell with a doped p3ht hole-transporting layer on a void-free perovskite active layer," J. Mater. Chem. A **2**(34), 13827–13830 (2014).

[20]I. D. Baikie, A. C. Grain, J. Sutherland, and J. Law, "Dual mode kelvin probe: Featuring ambient pressure photoemission spectroscopy and contact potential difference," Energy Procedia **60**, 48–56 (2014).

[21]S. Gutmann, M. A. Wolak, M. Conrad, M. M. Beerbom, and R. Schlaf, "Effect of ultraviolet and x-ray radiation on the work function of TiO$_2$ surfaces," J. Appl. Phys. **107**(10), 103705 (2010).

[22]M. Helander, M. Greiner, Z. Wang, and Z. Lu, "Pitfalls in measuring work function using photoelectron spectroscopy," Appl. Surf. Sci. **256**(8), 2602–2605 (2010).

[23]Y.-R. Luo, *Handbook of Bond Dissociation Energies in Organic Compounds*, 1st ed. (CRC Press, 2002).

[24]D. Yamashita, Y. Nakajima, A. Ishizaki, and M. Uda, "Photoelectron spectrometer equipped with open counter for electronic structures of organic materials," J. Surf. Anal. **14**(4), 433–436 (2008).

[25]S. Grigalevicius, G. Blazys, J. Ostrauskaite, J. Grazulevicius, V. Gaidelis, V. Jankauskas, and E. Montrimas, "3,6-di(n-diphenylamino)-9-phenylcarbazole and its methyl-substituted derivative as novel hole-transporting amorphous molecular materials," Synth. Met. **128**(2), 127–131 (2002).

[26]M. Uda and Sh. Omiya, "Apparatus for detecting low-speed electrons." U.S Patent 4,740,730 (26 April 1988).

[27]H. Ishii and K. Seki, "Energy level alignment at organic/metal interfaces studied by UV photoemission: Breakdown of traditional assumption of a common vacuum level at the interface," IEEE Trans. Electron Devices **44**(8), 1295–1301 (1997).

[28]R. H. Fowler, "The analysis of photoelectric sensitivity curves for clean metals at various temperatures," Phys. Rev. **38**(1), 45–56 (1931).

[29]M. Honda, K. Kanai, K. Komatsu, Y. Ouchi, H. Ishii, and K. Seki, "Atmospheric effect of air, N$_2$, O$_2$, and water vapor on the ionization energy of titanyl phthalocyanine thin film studied by photoemission yield spectroscopy," J. Appl. Phys. **102**(10), 103704 (2007).

[30]M. Kochi, Y. Harada, T. Hirooka, and H. Inokuchi, "Photoemission from organic crystal in vacuum ultraviolet region," Bull. Chem. Soc. Jpn. **43**(9), 2690–2702 (1970).

[31]N. Tsoulfanidis, *Measurement and Detection of Radiation*, 2nd ed. (Taylor and Francis, 1995).

[32]Photoelectron spectrophotometer in air, surface analyzer.

[33]Photoelectron spectrometer, surface analyzer.

[34]J. Hwang, A. Wan, and A. Kahn, "Energetics of metal–organic interfaces: New experiments and assessment of the field," Mater. Sci. Eng. R **64**(1), 1–31 (2009).

[35]M. Pope and C. E. Swenberg, *Electronic Processes in Organic Crystals and Polymers*, 2nd ed. (Oxford University Press, 1999).

[36]D. E. Eastman, "Photoelectric work functions of transition, rare-earth, and noble metals," Phys. Rev. B **2**(1), 1–2 (1970).

[37]M. Uda, "Open counter for low energy electron detection," Jpn. J. Appl. Phys. **24**, 284 (1985).

[38]M. Honda, K. Kanai, K. Komatsu, Y. Ouchi, H. Ishii, and K. Seki, "Atmospheric effect on the ionization energy of titanyl phthalocyanine thin film as studied by photoemission yield spectroscopy," Mol. Cryst. Liq. Cryst. **455**(1), 219–225 (2006).

[39]C. Adachi, T. Oyamada, and Y. Nakajima, *Data Book on Work Function of Organic Thin Films*, 2nd ed. (CMC International, 2006).

[40]M. V. Nardi, F. Detto, L. Aversa, R. Verucchi, G. Salviati, S. Iannotta, and M. Casarin, "Electronic properties of CuPc and h2pc: An experimental and theoretical study," Phys. Chem. Chem. Phys. **15**(31), 12864 (2013).

[41]N. Shintaku, M. Hiramoto, and S. Izawa, "Doping for controlling open-circuit voltage in organic solar cells," J. Phys. Chem. C **122**(10), 5248–5253 (2018).

[42]Z. Xu, L.-M. Chen, M.-H. Chen, G. Li, and Y. Yang, "Energy level alignment of poly(3-hexylthiophene): [6,6]-phenyl C$_{61}$ butyric acid methyl ester bulk heterojunction," Appl. Phys. Lett. **95**(1), 013301 (2009).

[43]W. Osikowicz, M. de Jong, and W. Salaneck, "Formation of the interfacial dipole at organic-organic interfaces: C$_{60}$/polymer interfaces," Adv. Mater. **19**(23), 4213–4217 (2007).

[44]M. Al-Ibrahim, "Flexible large area polymer solar cells based on poly (3-hexylthiophene)/fullerene," Solar Energy Mater. Solar Cells **85**, 13–20 (2005).

[45]H. Ishii, K. Kudo, T. Nakayama, and N. Ueno, *Electronic Processes in Organic Electronics: Bridging Nanostructure, Electronic States and Device Properties* (Springer, 2015), Vol. 209.

4ᵗʰ publication / 4-oji publikacija

Enamine-Based Cross-Linkable Hole-Transporting Materials for
Perovskite Solar Cells
D. Vaitukaitytė, A. Al-Ashouri, M. R. Juškėnas, E. Kamarauskas,
J. Nekrasovas, V. Jankauskas, A. Magomedov, S. Albrecht, V. Getautis

Enamine-Based Cross-Linkable Hole-Transporting Materials for Perovskite Solar Cells

Deimantė Vaitukaitytė, Amran Al-Ashouri, Marytė Daškevičienė, Egidijus Kamarauskas, Jonas Nekrasovas, Vygintas Jankauskas, Artiom Magomedov, Steve Albrecht, and Vytautas Getautis*

The development of the simple synthesis schemes of organic semiconductors can have an important contribution to the advancement of related technologies. In particular, one of the fields where the high price of the hole-transporting materials may become an obstacle toward successful commercialization is perovskite solar cells. Herein, enamine-based materials that are capable of undergoing cross-linking due to the presence of two vinyl groups are synthesized. It is shown that new compounds can be thermally polymerized, making the films resistant to organic solvents. This can allow the use of a wet-coating process for the deposition of the perovskite absorber film, without the need for orthogonal solvents. Cross-linked films are used in perovskite solar cells, and, upon optimization of the film thickness, the highest power conversion efficiency of 18.1% is demonstrated.

1. Introduction

Perovskite solar cells (PSCs) have recently demonstrated efficiencies comparable to those of the best Si-based technologies.[1] Among other things, further advancement of PSCs depends on the development of novel materials that can serve as efficient hole transporters.[2] However, the choice of organic hole-transporting materials (HTMs) that are able to deliver competitive performance

D. Vaitukaitytė, Dr. M. Daškevičienė, Dr. A. Magomedov, Prof. V. Getautis
Department of Organic Chemistry
Kaunas University of Technology
Radvilenu pl. 19, Kaunas LT-50254, Lithuania
E-mail: vytautas.getautis@ktu.lt

A. Al-Ashouri, Prof. S. Albrecht
Young Investigator Group Perovskite Tandem Solar Cells
Helmholtz-Zentrum Berlin
Kekuléstraße 5, 12489 Berlin, Germany

Dr. E. Kamarauskas, J. Nekrasovas, Dr. V. Jankauskas
Institute of Chemical Physics
Vilnius University
Sauletekio al. 3, Vilnius LT-10257, Lithuania

Prof. S. Albrecht
Faculty of Electrical Engineering and Computer Science
Technical University Berlin
Marchstraße 23, 10587 Berlin, Germany

The ORCID identification number(s) for the author(s) of this article can be found under https://doi.org/10.1002/solr.202000597.

is still limited. Therefore, it is important to search for promising new organic materials.

As an additional constraint, to keep the transition from lab to fab as fast as possible, it is advantageous to maintain the simplicity of the organic materials as one of the highest priorities. It is thus necessary to use simple and short synthesis pathways because it was recently shown that multistep schemes lead to extremely high materials costs.[3] In addition, it is better to avoid the use of metal-catalyzed reactions, as metal traces are known to have detrimental effects on the performance of optoelectronic devices,[4] and therefore additional purification processes (e.g., sublimation[5]) are required, which further increases the price of the final material. In this context, condensational chemistry is giving possibilities to increase the π-conjugated system of the molecules in a simple way, with water as the only byproduct. The simplicity of the synthesis and purification can promote wider application of such materials.

One of the semiconducting material classes that fulfill the aforementioned requirements is enamines. Typically, they are synthesized from aromatic amine and aromatic ketone/aldehyde. First studies of their charge-transporting abilities were reported in the 1980s,[6–8] and since then they have been successfully incorporated in electrophotographic devices[9] and organic light-emitting diodes,[10] and recently they have been reported to show good performance in PSCs.[11–13]

Depending on the order of the layers in the final device, PSCs are commonly divided into two large groups. Currently, the highest certified efficiency, published in peer-reviewed journals (22.7%), was achieved in a so-called regular or n–i–p configuration, where the HTM is deposited on top of the perovskite absorber layer.[14] As an alternative, in recent years, also p–i–n (or "inverted") configuration of PSCs was established, with efficiencies getting close to those of the best PSCs (highest published certified value of 22.3%),[15] and in addition, having advantages in tandem applications.[16,17] In the case of p–i–n devices, solution processing of the perovskite absorber layer adds additional constraints on the choice of HTMs, as it usually should withstand a mixture of polar dimethylformamide: dimethyl sulfoxide (DMF:DMSO) solvents. The perovskite precursor solution has significantly lower ability to dissolve organic HTMs (Table S1, Supporting Information); however, it is enough to reduce the scope of the applicable materials. Therefore, so far

the most popular choice of organic HTMs for such devices is polymers, such as poly[bis(4-phenyl)(2,4,6-trimethylphenyl) amine][18] and poly(3,4-ethylenedioxythiophene) polystyrene sulfonate.[19] Recently, different small-molecule HTMs for p–i–n have been reported, such as MPA-BTTI,[20] BTF4,[21] and BDPSO;[22] however, their number is still rather limited due to the aforementioned restriction. Therefore, as an alternative, several strategies have been reported, e.g., change of the perovskite precursor solvent,[23] use of self-assembled monolayers,[24] and use of soluble precursors that are subsequently transformed into insoluble films.[25] In addition, recently cross-linkable HTMs were introduced into inverted devices, resulting in relatively high performance.[26] However, it was achieved using palladium-catalyzed reactions.

In this work, enamine-based cross-linkable HTMs, containing two vinyl groups, were synthesized and investigated. We show that new materials can undergo thermal polymerization, forming solvent-resistant films. The polymerization process has a negligible effect on the electrical properties of the materials. As a proof of concept, PSCs of p–i–n configuration were constructed, and devices with polymerized V1187 showed a promising power conversion efficiency (PCE) of 18.14%, showing the great potential of the presented class of dopant-free organic HTMs.

2. Results and Discussion

For the target materials to undergo in situ cross-linking, it is required to incorporate at least two groups that can undergo polymerization into the structure of the final compounds. To do so, commercially available fluorene amines were chosen as the starting compounds, and following a simple two-step reaction scheme (Scheme S1 and S2, Supporting Information), two final compounds V1162 and V1187 were obtained (**Figure 1**). Detailed synthesis procedures are reported in the Supporting Information. In brief, during the first step, starting amines were condensed with 2,2-bis(4-methoxyphenyl)acetaldehyde, following a previously published procedure,[11] and intermediate compounds 1 and 2 were isolated via crystallization in 47% and 94% yields, respectively. During the second step, intermediate compounds were alkylated by 4-vinylbenzylchloride, to obtain final compounds V1162 and V1187 with good yields (74% and 59%, respectively). Structures of the synthesized compounds were confirmed by means of NMR and elemental analysis.

Following a previously published procedure,[3] the costs of the materials used for the synthesis were evaluated (detailed calculations can be found in the Supporting Information). The calculated price of the materials is 13.56 and 16.34€ g^{-1} for V1162 and V1187, respectively, which is somewhat higher than the lowest reported costs of organic HTMs (e.g., V950 ≈6€ g$^{-1[11]}$ and EDOT–amide–TPA ≈5$ g$^{-1[27]}$); however, it is significantly lower than that of the most popular HTM Spiro-OMeTAD (93$ g$^{-1[28]}$).

To evaluate the optical properties of the synthesized compounds, UV–vis and photoluminescence (PL) spectra were recorded from the solutions, and the results are shown in Figure S2, Supporting Information. The enamine V1162 has an absorption maximum (λ_{max}) in the UV range at 370 nm, with only negligible absorption in the visible range of electromagnetic
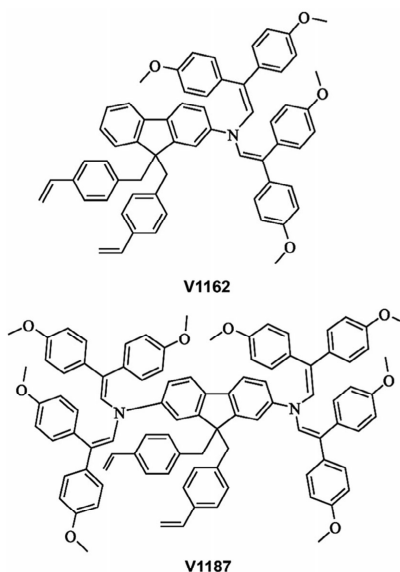

Figure 1. Molecular structures of the synthesized cross-linkable HTMs V1162 and V1187.

radiation. The compound V1187 with its additional enamine branch has a bathochromically shifted λ_{max} of 406 nm due to the larger π-conjugated electrons system, giving a slightly stronger light absorption in the visible range. This might reduce the performance of the p–i–n PSC, where the light first passes through the HTM layer; however, if the film thickness is small, the drop in J_{sc} should not be significant. In addition, from the PL spectra, it can be seen that the emission of the V1187 is slightly redshifted by 7 nm, compared to that of V1162, which is consistent with the increased π-conjugated electron system.

For the evaluation of the thermal stability of the materials and their ability to undergo a cross-linking process, thermal properties were studied by means of differential scanning calorimetry (DSC) and thermogravimetric analysis (TGA). For the V1162, during the first DSC heating cycle (**Figure 2**), the glass transition process was detected at 100 °C, followed by a melting process at 228 °C, showing that the material after purification has a mixture of amorphous and crystalline states. Directly after melting, an exothermic process was detected at 231 °C, suggesting that thermal polymerization occurs at this temperature. During the second heating cycle, no phase transitions were observed, confirming formation of the cross-linked polymer. For V1187, with higher molecular weight, a slightly higher T_g of 136 °C was detected and no melting process was observed, suggesting that V1187 was isolated as an amorphous material. The cross-linking process started at ≈190 °C, with a peak at around 239 °C. Again, during the second heating cycle, no phase transitions were detected. In addition, both compounds showed excellent thermal stability, with a T_d of 396 °C for V1162 and
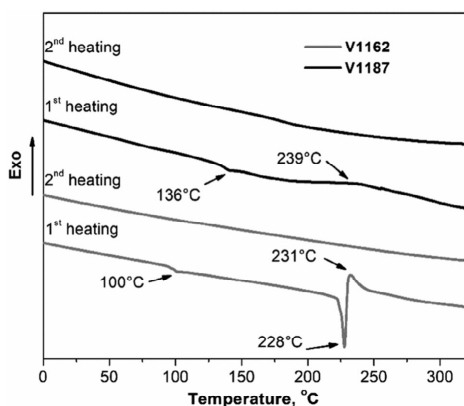
Figure 2. First and second scan heating curves of V1162 and V1187 (heating rate 10 °C min⁻¹; the y-axis is showing a heat flux).

393 °C for V1187, as can be seen from TGA analysis (Figure S1, Supporting Information).

To evaluate the cross-linking ability of the thin films of the new HTMs, they were analyzed by evaluating the amount of washed material from the spin-coated film, by means of UV–vis spectroscopy (detailed cross-linking procedure can be found in the Supporting Information). The results are shown in **Figure 3**. After heating the HTM films at 231 °C, already after 15 min the majority of the monomer was cross-linked into an insoluble polymer. A very similar behavior was observed for both the V1162 and V1187 materials, and the process of cross-linking was complete roughly after 45 min of heating. The cross-linked films have shown to be resistant to the DMF:DMSO (4:1)
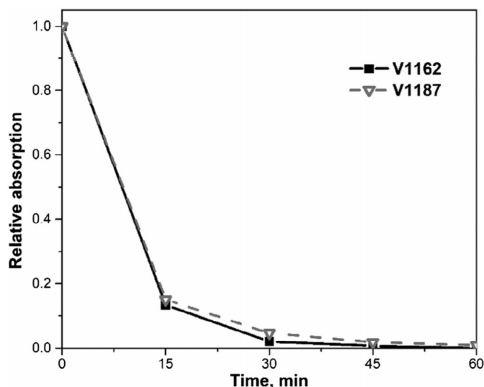

Figure 3. Cross-linking experiment of the V1162 and V1187 films. The absorption (at 370 nm for V1162 and at 406 nm for V1187) of the solutions, prepared by dipping spin-coated HTM films into THF after heating at 231 °C for the respective times, relative to the absorption of the solution, prepared by dipping of the non-cross-linked film.

solvents, as after exposure to them the UV–vis absorption spectra of the films remained almost the same (Figure S4 and S5, Supporting Information). As an additional indication of the conversion of the vinyl groups, fourier-transform infrared spectroscopy were recorded (Figure S6, Supporting Information). After annealing, the characteristic peaks of the vinyl groups at the 988–991 and 904–908 cm⁻¹ disappeared, which were previously reported to show a complete cross-linking.[29,30] Next, to study the electrical properties of the synthesized HTMs, the hole drift mobility was measured with the xerographic time-of-flight (XTOF) technique (**Figure 4**). V1187 showed very good charge-transporting properties, reaching 10^{-3} cm² V⁻¹ s⁻¹ at strong electrical fields. The simpler compound V1162 showed slightly lower hole drift mobilities, yet still comparable to those of popular HTMs for PSCs. As the cross-linking process does not affect the chromophoric system of the HTMs, it had only a minor influence on the hole drift mobility. For V1187, the value stayed virtually the same, whereas for V1162 after cross-linking mobility became roughly two times lower (Figure 4). In addition to charge-transporting properties, ionization potentials were measured through photoelectron spectroscopy in air (PESA). The values were 5.11 and 5.26 eV for V1187 and V1162, respectively. Such values are consistent with the values reported for other HTMs used in PSCs.

To evaluate the performance of the materials acting as hole-selective layers in PSCs, devices with the p–i–n architecture were fabricated and characterized. As an absorber material, triple-cation perovskite was used,[31] with a nominal precursor solution composition of $Cs_{0.05}(FA_{0.83}MA_{0.17})_{0.95}Pb(I_{0.83}Br_{0.17})_3$ (see Figure S8, Supporting Information, for the top-view and cross-section scanning electron microscopy images of the best device). The films of the organic HTMs were prepared by spin coating from toluene, and afterward, they were annealed in a nitrogen atmosphere at 230 °C for 45 min for the cross-linking, as was determined previously. The J/V curves are reported in reverse (from open to short circuit) direction, as the devices have shown only a minor hysteresis (Figure S11, Supporting Information). A detailed description of the fabrication and
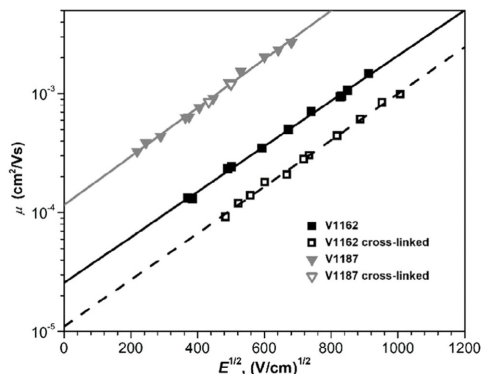

Figure 4. Electric-field dependencies of the hole drift mobilities in films of V1162 and V1187 before and after thermal cross-linking.
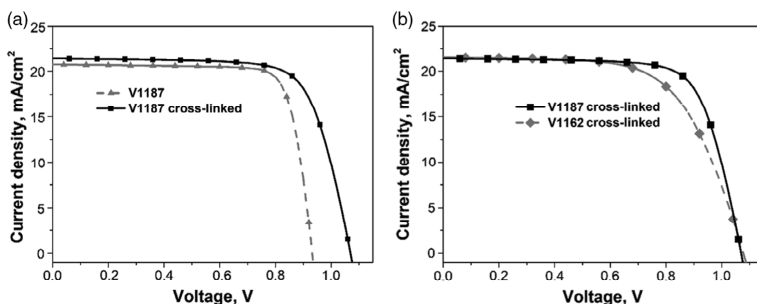
Figure 5. J/V measurements of the PSCs prepared with the new HTMs (reverse scan, from open to short circuit). a) Comparison of the devices, prepared with the neat HTM versus cross-linked HTM; b) comparison of the performances of the two cross-linked HTMs.

Table 1. Average performance parameters of the PSCs with new HTMs (prepared from 2 mg mL^{-1} in toluene). Data extracted from J/V scans, including the standard errors and the best performance parameters (in brackets). The statistics are based on six to ten cells on different substrates.

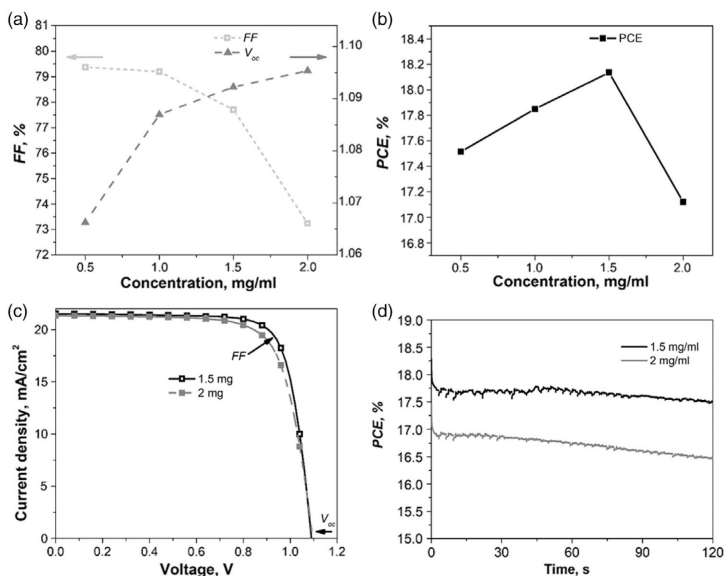| Compound	J_{sc} [mA cm^{-2}]	V_{oc} [V]	FF [%]	PCE [%]
V1162	21.19 ± 0.12 (21.60)	0.846 ± 0.013 (0.878)	75.8 ± 0.2 (76.4)	13.60 ± 0.25 (14.49)
V1162 cross-linked	21.55 ± 0.14 (21.51)	1.036 ± 0.014 (1.077)	61.7 ± 0.8 (63.5)	13.78 ± 0.35 (14.71)
V1187	21.34 ± 0.16 (20.73)	0.891 ± 0.020 (0.932)	79.3 ± 0.4 (80.3)	15.08 ± 0.35 (15.51)
V1187 cross-linked	21.95 ± 0.15 (21.40)	1.040 ± 0.012 (1.069)	71.1 ± 1.8 (73.3)	16.21 ± 0.35 (16.77)

Figure 6. PSC analysis of cross-linked V1187 films. a) Dependence of the FF and V_{oc} and b) PCE on the concentration of the V1187 solution. c) Comparison of representative J/V characteristics (reverse scan, from open to short circuit) of V1187-based devices prepared from solutions with different concentrations and d) respective maximum power point tracking.

Table 2. Average performance parameters of the PSCs with the V1187 films, prepared from solutions with different concentrations. Data extracted from J/V scans, including the standard errors and the best performance parameters (in brackets). The statistics are based on six to ten cells on different substrates.

Compound	Concentration [mg ml^{-1}]	J_{sc} [mA cm^{-2}]	V_{oc} [V]	FF [%]	PCE [%]
V1187 cross-linked	0.5	20.98 ± 0.09 (21.18)	1.039 ± 0.013 (1.066)	73.3 ± 2.1 (79.4)	15.95 ± 0.47 (17.51)
	1.0	21.42 ± 0.12 (21.64)	1.057 ± 0.014 (1.070)	72.7 ± 3.4 (79.2)	16.48 ± 0.88 (17.74)
	1.5	21.39 ± 0.09 (21.61)	1.075 ± 0.009 (1.092)	71.4 ± 2.5 (77.7)	16.44 ± 0.68 (18.14)
	2.0	21.31 ± 0.10 (21.67)	1.077 ± 0.007 (1.095)	69.2 ± 1.2 (73.2)	15.88 ± 0.33 (17.12)

characterization of the devices can be found in the Supporting Information.

First, to check the influence of the cross-linking on the performance of the devices, we compared thermally cross-linked HTM films with the the neat films. Via profilometry, we measured no significant surface morphology differences after the cross-linking process (Figure S3, Supporting Information). As shown in **Figure 5** and **Table 1**, both V1162 and V1187 devices with monomer films showed low open-circuit voltages (V_{oc}) (0.85 V for V1162 and 0.89 V for V1187 on average). It can be attributed to the formation of a direct contact between the perovskite and indium tin oxide (ITO), due to the damage of the HTM film during solution processing of the perovskite film. This in turn leads to increased interfacial recombination, which reduces V_{oc}.[32,33] In contrast, for both materials after thermal polymerization, V_{oc} was significantly improved up to 1.04 V on average. Quite a different trend can be observed for the full factor (FF), where higher values were obtained for neat films (75.8% for V1162 and 79.3% for V1187 on average), which can be attributed to the high conductivity of the ITO, and as a consequence fast transport of charges. This result is supporting the previous statement that after cross-linking the HTM films have improved resistance against solvents.

V1187 allowed for higher FFs than V1162 (Figure 5), and as a consequence, the highest PCE of 16.8%. As the films are used without oxidizing dopants, such improvement can be attributed to the higher values of the hole drift mobilities,[34] and as a result better transport of the charges through the film.

To further optimize the HTM film, the concentration of the V1187 starting solution was varied from 2 mg mL^{-1} down to 0.5 mg mL^{-1} in toluene. As expected, the lower concentration led to the improved FF, but at the cost of reduced V_{oc} (**Figure 6, Table 2**). Steady-state PL measurements of the perovskite films on this concentration series revealed a reduced intensity of the emission with lower concentration (Figure S9, Supporting Information). As the extraction abilities of the material should be independent of the concentration, such a behavior can be attributed to insufficient coverage of the ITO substrate and increased direct contact between the perovskite and ITO.[35] As a result of increased interface recombination, the reduction in V_{oc} is observed. Overall, an optimized PCE of 18.1% for the cross-linked films prepared from the 1.5 mg mL^{-1} solutions was achieved.

3. Conclusion

In conclusion, in this work, two new enamine-based HTMs were synthesized and investigated. Due to the presence of two vinyl groups, materials V1162 and V1187 are able to undergo thermal cross-linking during heating at 230 °C. After ≈45 min, the deposited films became resistant toward organic solvents. It was further shown that polymerization leads only to minor changes in hole drift mobilities; therefore, the materials are suitable for application in p–i–n PSCs. As a result, devices with the thermally cross-linked films have shown advantageous performance, mainly due to the higher open-circuit voltage. After further optimization of the concentration of the V1187 solution, PSCs have shown over 18% power conversion efficiency, demonstrating the great promise of the presented strategy.

Supporting Information

Supporting Information is available from the Wiley Online Library or from the author.

Conflict of Interest

The authors declare no conflict of interest.

Keywords

cross-linking, enamines, hole-transporting materials, perovskite solar cells

[1] Best Research-Cell Efficiency Chart, https://www.nrel.gov/pv/cell-efficiency.html (accessed: August 2020).
[2] A. K. Jena, A. Kulkarni, T. Miyasaka, *Chem. Rev.* **2019**, *119*, 3036.
[3] T. P. Osedach, T. L. Andrew, V. Bulović, *Energy Environ. Sci.* **2013**, *6*, 711.
[4] C. Bracher, H. Yi, N. W. Scarratt, R. Masters, A. J. Pearson, C. Rodenburg, A. Iraqi, D. G. Lidzey, *Org. Electron.* **2015**, *27*, 266.

[5] K. Rakstys, M. Saliba, P. Gao, P. Gratia, E. Kamarauskas, S. Paek, V. Jankauskas, M. K. Nazeeruddin, *Angew. Chem., Int. Ed.* **2016**, *55*, 7464.

[6] S. L. Rice, R. D. Balanson, R. Wingard, *J. Imaging Sci.* **1985**, *29*, 7.

[7] J. A. Sinicropi, J. R. Cowdery-Corvan, E. H. Magin, P. M. Borsenberger, *Chem. Phys.* **1997**, *218*, 331.

[8] Y. Morishita, Y. Sugimoto, H. Ishikawa, S. Hayashida, T. Okamoto, N. Hayashi, *Synth. Met.* **1991**, *41*, 1231.

[9] A. Matoliukstyte, E. Burbulis, J. V. Grazulevicius, V. Gaidelis, V. Jankauskas, *Synth. Met.* **2008**, *158*, 462.

[10] R. Paspirgelyte, R. Zostautiene, G. Buika, J. V. Grazulevicius, S. Grigalevicius, V. Jankauskas, C. C. Chen, Y. C. Chung, W. B. Wang, J. H. Jou, *Synth. Met.* **2010**, *160*, 162.

[11] M. Daskeviciene, S. Paek, Z. Wang, T. Malinauskas, G. Jokubauskaite, K. Rakstys, K. T. Cho, A. Magomedov, V. Jankauskas, S. Ahmad, H. J. Snaith, V. Getautis, M. K. Nazeeruddin, *Nano Energy* **2017**, *32*, 551.

[12] D. Vaitukaityte, Z. Wang, T. Malinauskas, A. Magomedov, G. Bubniene, V. Jankauskas, V. Getautis, H. J. Snaith, *Adv. Mater.* **2018**, *30*, 1803735.

[13] M. Steponaitis, M.-G. La-Placa, İ. C. Kaya, G. Bubniene, V. Jankauskas, M. Daskeviciene, M. Sessolo, T. Malinauskas, H. J. Bolink, V. Getautis, *Sustainable Energy Fuels* **2020**, *4*, 5017.

[14] E. H. Jung, N. J. Jeon, E. Y. Park, C. S. Moon, T. J. Shin, T. Y. Yang, J. H. Noh, J. Seo, *Nature* **2019**, *567*, 511.

[15] X. Zheng, Y. Hou, C. Bao, J. Yin, F. Yuan, Z. Huang, K. Song, J. Liu, J. Troughton, N. Gasparini, C. Zhou, Y. Lin, D. J. Xue, B. Chen, A. K. Johnston, N. Wei, M. N. Hedhili, M. Wei, A. Y. Alsalloum, P. Maity, B. Turedi, C. Yang, D. Baran, T. D. Anthopoulos, Y. Han, Z. H. Lu, O. F. Mohammed, F. Gao, E. H. Sargent, O. M. Bakr, *Nat. Energy* **2020**, *5*, 131.

[16] J. Xu, C. C. Boyd, Z. J. Yu, A. F. Palmstrom, D. J. Witter, B. W. Larson, R. M. France, J. Werner, S. P. Harvey, E. J. Wolf, W. Weigand, S. Manzoor, M. F. A. M. Van Hest, J. J. Berry, J. M. Luther, Z. C. Holman, M. D. McGehee, *Science* **2020**, *367*, 1097.

[17] Y. Hou, E. Aydin, M. De Bastiani, C. Xiao, F. H. Isikgor, D. J. Xue, B. Chen, H. Chen, B. Bahrami, A. H. Chowdhury, A. Johnston, S. W. Baek, Z. Huang, M. Wei, Y. Dong, J. Troughton, R. Jalmood, A. J. Mirabelli, T. G. Allen, E. Van Kerschaver, M. I. Saidaminov, D. Baran, Q. Qiao, K. Zhu, S. De Wolf, E. H. Sargent, *Science* **2020**, *367*, 1135.

[18] M. Stolterfoht, C. M. Wolff, J. A. Márquez, S. Zhang, C. J. Hages, D. Rothhardt, S. Albrecht, P. L. Burn, P. Meredith, T. Unold, D. Neher, *Nat. Energy* **2018**, *3*, 847.

[19] W. Nie, H. Tsai, R. Asadpour, J. C. Blancon, A. J. Neukirch, G. Gupta, J. J. Crochet, M. Chhowalla, S. Tretiak, M. A. Alam, H. L. Wang, A. D. Mohite, *Science* **2015**, *347*, 522.

[20] Y. Wang, W. Chen, L. Wang, B. Tu, T. Chen, B. Liu, K. Yang, C. W. Koh, X. Zhang, H. Sun, G. Chen, X. Feng, H. Y. Woo, A. B. Djurišić, Z. He, X. Guo, *Adv. Mater.* **2019**, *31*, 1902781.

[21] X. Sun, Q. Xue, Z. Zhu, Q. Xiao, K. Jiang, H. L. Yip, H. Yan, Z. Li, *Chem. Sci.* **2018**, *9*, 2698.

[22] R. Shang, Z. Zhou, H. Nishioka, H. Halim, S. Furukawa, I. Takei, N. Ninomiya, E. Nakamura, *J. Am. Chem. Soc.* **2018**, *140*, 5018.

[23] C. Wang, J. Hu, C. Li, S. Qiu, X. Liu, L. Zeng, C. Liu, Y. Mai, F. Guo, *Sol. RRL* **2019**, *4*, 1900389.

[24] A. Magomedov, A. Al-Ashouri, E. Kasparavičius, S. Strazdaite, G. Niaura, M. Jošt, T. Malinauskas, S. Albrecht, V. Getautis, *Adv. Energy Mater.* **2018**, *8*, 1801892.

[25] K. Rakstys, M. Stephen, J. Saghaei, H. Jin, M. Gao, G. Zhang, K. Hutchinson, A. Chesman, P. L. Burn, I. Gentle, P. E. Shaw, *ACS Appl. Energy Mater.* **2020**, *3*, 889.

[26] Y. Zhang, C. Kou, J. Zhang, Y. Liu, W. Li, Z. Bo, M. Shao, *J. Mater. Chem. A* **2019**, *7*, 5522.

[27] M. L. Petrus, K. Schutt, M. T. Sirtl, E. M. Hutter, A. C. Closs, J. M. Ball, J. C. Bijleveld, A. Petrozza, T. Bein, T. J. Dingemans, T. J. Savenije, H. Snaith, P. Docampo, *Adv. Energy Mater.* **2018**, *8*, 1801605.

[28] M. L. Petrus, T. Bein, T. J. Dingemans, P. Docampo, *J. Mater. Chem. A* **2015**, *3*, 12159.

[29] Z. Li, Z. Zhu, C.-C. Chueh, J. Luo, A. K.-Y. Jen, *Adv. Energy Mater.* **2016**, *6*, 1601165.

[30] S. Abraham, G. P. T. Ganesh, S. Varughese, B. Deb, J. Joseph, *ACS Appl. Mater. Interfaces* **2015**, *7*, 25424.

[31] M. Saliba, T. Matsui, J.-Y. Seo, K. Domanski, J.-P. Correa-Baena, M. K. Nazeeruddin, S. M. Zakeeruddin, W. Tress, A. Abate, A. Hagfeldt, M. Grätzel, *Energy Environ. Sci.* **2016**, *9*, 1989.

[32] M. Stolterfoht, P. Caprioglio, C. M. Wolff, J. A. Márquez, J. Nordmann, S. Zhang, D. Rothhardt, U. Hörmann, Y. Amir, A. Redinger, L. Kegelmann, F. Zu, S. Albrecht, N. Koch, T. Kirchartz, M. Saliba, T. Unold, D. Neher, *Energy Environ. Sci.* **2019**, *12*, 2778.

[33] J. P. Correa-Baena, W. Tress, K. Domanski, E. H. Anaraki, S. H. Turren-Cruz, B. Roose, P. P. Boix, M. Grätzel, M. Saliba, A. Abate, A. Hagfeldt, *Energy Environ. Sci.* **2017**, *10*, 1207.

[34] W. Zhou, Z. Wen, P. Gao, *Adv. Energy Mater.* **2018**, *8*, 1702512.

[35] E. M. Hutter, T. Kirchartz, B. Ehrler, D. Cahen, E. Von Hauff, *Appl. Phys. Lett.* **2020**, *116*, 100501.